



TECHNISCHE  
UNIVERSITÄT  
WIEN

Dissertation

**Anwendungen von Eigenschaften  
szintillierender Gase in optisch ausgelesenen  
GEM-basierten Detektoren**

zur Erlangung des akademischen Grades  
**Doktor der Technischen Wissenschaften**

unter der Leitung von  
**Ao.Univ.Prof. Dipl.-Ing. Dr.techn. Christina Strelj**  
Atominstitut (E141)

eingereicht an der Fakultät für Physik  
der Technischen Universität Wien

von  
**Dipl.-Ing. Florian Maximilian Brunbauer, BSc**  
Matrikelnummer 1125221  
Peuerbachstraße 1  
4040 Linz  
Österreich

und begutachtet von  
**Prof. Dr. João Veloso und Dr. Paul Colas**





Dissertation

# **Applications of gas scintillation properties in optically read out GEM-based detectors**

submitted in partial fulfillment of the requirements for the degree of  
**Doktor der Technischen Wissenschaften**

under supervision of

**Ao.Univ.Prof. Dipl.-Ing. Dr.techn. Christina Strelt**  
Institute of Atomic and Subatomic Physics (E141)

to the Faculty of Physics  
at Technische Universität Wien

by

**Dipl.-Ing. Florian Maximilian Brunbauer, BSc**  
Matriculation number 1125221  
Peuerbachstraße 1  
4040 Linz  
Austria

and reviewed by

**Prof. Dr. João Veloso and Dr. Paul Colas**



## Abstract

Strong signal amplification, high achievable spatial resolution and low material budget as well as applicability in high-rate environments as key advantages of micropattern gaseous detectors make them an attractive candidate for radiation detection and imaging. Reading out scintillation light emitted during electron avalanche multiplication with modern imaging sensors provides accurate visualisations of incident radiation. The adjustable gain of amplification structures such as Gaseous Electron Multipliers (GEMs) enables radiation detection over a wide range of energies from minimum ionising particles to single low-energy X-ray photons and highly ionising radiation. Scintillation characteristics of gas mixtures for optically read out GEM-based detectors were investigated. Light yield and scintillation spectra of the emitted scintillation light in a range of operating conditions with variable amplification fields and different gas mixtures were studied to determine optimum operation conditions for optically read out detectors. Long term sealed mode operation of optically read out GEM-based detectors was achieved with a minimal degradation of signal strength. The presented gas scintillation studies and detector concepts based on optically read out GEMs effectively pave the way for applications ranging from radiation imaging to high energy physics and hadron therapy. Optically read out GEM-based detectors optimised and employed for X-ray radiography and tomography were developed. Operating in a proportional high-sensitivity regime, single X-ray photon sensitivity could be used for X-ray fluorescence imaging and material distinction with 2D resolution. Augmenting images of particle tracks with timing information, which can be obtained with fast photon detectors or complementary electronic readout, 3D reconstructed trajectories in an optically read out Time Projection Chamber (TPC) could be obtained. A transparent multi-pad anode was developed to combine simultaneous optical and electronic readout to extend the track reconstruction capabilities of optically read out TPCs. A planispherical GEM-based detector employing radially focused field lines in the conversion volume to minimise parallax-induced broadening was developed and shown to permit significantly improved spatial resolution for X-ray fluorescence applications of gaseous detectors with thick conversion layers. Taking advantage of the high spatial resolution achievable with optical readout and the low material budget of gaseous detectors, a proton beam monitoring detector was developed. 2D dose imaging as well as accurate beam profile and intensity monitoring were demonstrated at a clinical proton therapy facility.



# Kurzfassung

Starke Signalverstärkung, hohe Ortsauflösung und niedriges Materialbudget zählen neben der Anwendbarkeit in Umgebungen mit hohen Teilchenflüssen zu den wichtigsten Vorteilen von gasbasierten Detektoren und machen diese zu einer attraktiven Technologie für die Messung von Strahlung und für bildgebende Verfahren. Die Auslese von Szintillationslicht, welches während der lawinenhaften Vervielfachung von Elektronen emittiert wird, mittels moderner Bildsensoren liefert akkurate Visualisierungen der einfallenden Strahlung. Die anpassbaren Signalverstärkungsfaktoren von Strukturen wie gasbasierten Elektronenvervielfachern (GEMs) erlauben die Messung von Strahlung über einen weiten Bereich von Energien von minimal ionisierenden Teilchen bis zu niedrigerenergetischen Röntgenstrahlen und stark ionisierender Strahlung. Die Szintillationseigenschaften von Gasmischungen für optisch ausgelese GEM-basierte Detektoren wurden untersucht. Die Lichtausbeute und Szintillationsspektren des emittierten Szintillationslichtes wurden in verschiedenen Konfigurationen mit unterschiedlichen Gasmischungen und elektrischen Signalverstärkungsfeldern gemessen um die optimalen Parameter für optisch ausgelesene Detektoren zu bestimmen. Optisch ausgelesene GEM-basierte Detektoren wurden über längere Zeiträume hinweg geschlossen betrieben, wobei sich die Intensität der gemessenen Signale nur minimal verminderte. Die präsentierten Untersuchungen der Szintillationseigenschaften und darauf basierender Detektorkonzepte ebnen den Weg für Anwendungen in bildgebenden Verfahren bis hin zu Kernphysik und Hadronentherapie. Optisch ausgelesene GEM-basierte Detektoren optimiert für Röntgenaufnahmen und Tomografie wurden entwickelt. Der Betrieb in einem proportionalen Bereich der Signalverstärkung und ausreichende Sensitivität zur Aufnahme einzelner Röntgenstrahlen ermöglichten die Aufnahme von Röntgenfluoreszenz und die darauf basierende Unterscheidung verschiedener Materialien mit 2D Auflösung. In Verbindung mit Interaktionszeitinformationen, welche von schnellen Photonendetektoren oder von ergänzenden elektronischen Ausleseverfahren stammen können, wurden Teilchenbahnen in einer optisch ausgelesenen Zeitprojektionskammer (TPC) aufgenommen und zu 3D Repräsentationen rekonstruiert. Eine optisch transparente, segmentierte Anode wurde entwickelt um die simultane Anwendung von optischen und elektronischen Ausleseverfahren zu erlauben und die Rekonstruktion von komplexen Teilchenbahnen in der optisch ausgelesenen TPC zu ermöglichen. Ein planisphärischer GEM-basierter Detektor mit radial fokussierten Feldlinien im aktiven Detektionsvolumen wurde entwickelt um Parallaxe zu minimieren und die deutlich verbesserte Ortsauflösung von Detektoren mit dicken Detektionsvolumen basierend auf diesem Konzept für Anwendungen in der Röntgenfluoreszenzanalyse und Kristallographie wurde demonstriert. Die gute Ortsauflösung, welche mit optischer Auslese erreicht werden kann, und das niedrige Materialbudget gasbasierter Detektoren wurden für einen Detektor für Protonenstrahlen kombiniert. Die Möglichkeiten der Aufnahme von 2D Profilen der deponierten Dosis sowie der Beobachtung der Profile und Intensität von Protonenstrahlen wurden in einer klinischen Einrichtung für Protonentherapie demonstriert.

# Acknowledgement

The invaluable support and contributions of many people over the past years made the work and results presented within this thesis possible.

I am grateful to you, Christina Strel, for accepting to be my supervisor and for accompanying me throughout the work as doctoral student. Thank you for helping me navigate the requirements of the doctoral programme and balance studies at Technische Universität Wien with experimental work at CERN.

I would like to express my deepest appreciation and gratitude to you, Leszek Ropelewski, for providing me with the unique opportunity to work in the gaseous detector development group at CERN and for creating and nourishing a wonderful atmosphere of appreciation for novel ideas and experimental progress. I greatly value your guidance as supervisor of my work as doctoral student at CERN and your honest input and patience in solving the most demanding challenges.

I would also like to thank you, João Veloso, and you, Paul Colas, for agreeing to review and assess my thesis and for joining the examination committee at the doctoral defence of the thesis. I value your input and comments and appreciate your help in compiling a comprehensive presentation of the conducted experimental work.

I would like to extend my deepest gratitude to you, Eraldo Oliveri, and to you, Filippo Resnati, for your dedication and exceptional diligence in introducing me to the field of gaseous detector development and for transferring your enthusiasm for experimental work to me. Your enduring support and uncompromising willingness to help and answer countless questions made working in the gaseous detector development lab a real pleasure and I greatly appreciate your invaluable contribution to the presented work. From the time I joined the group as summer student and throughout the time as doctoral student you have always offered me inspiration, guidance and help and I am happy to know you as the kind and exceptional persons you are.

My gratitude also goes to all other colleagues in the gaseous detector development group for making this group a wonderful place to work and enjoy experimental detector development. Thank you, Michael Lupberger, Hans Müller, Dorothea Pfeiffer, Patrik Thuiner, and many others for your help and for many inspiring, insightful and enjoyable discussions. Thank you, Gábor Galgóczi and Tero Korkalainen, for your important contributions to the event reconstruction in the optically read out TPC.

Thank you, Miranda van Stenis, for your help in designing, manufacturing and assembling numerous detector prototypes and for your patience in making things fit just right. Your support in going from an idea to a fully assembled and operational detector made the multitude of detector concepts covered within this thesis possible and it was a pleasure working with you. I would also like to thank you, Christophe Bault, for your assistance in designing and manufacturing intricate parts of various detector prototypes.

I would like to thank you, Fabio Sauli, for triggering the exciting development of the planispherical GEM concept and for your input and help in various other projects and presentations of the conducted work.

Thank you, Diego Gonzalez Diaz, for starting the work on the optically read out TPC and for challenging me to make the most of it.



I would also like to thank you, Francisco Ignacio Garcia Fuentes, for the interesting idea of using transparent anodes in the optically read out TPC and for your support in the realisation of this project. Thank you, Alois Lugstein and Markus Schinnerl, for your assistance and support in manufacturing transparent anodes.

I am grateful for the opportunity to perform the presented developments of gaseous detectors within the RD51 collaboration and for the valuable input and support from colleagues in the collaboration.

I truly enjoyed living with you, Alejandra Tschudi-Spiropulo and Pierre-Alain Tschudi, in Meyrin while working at CERN. Although we sometimes did not see each other much, I always felt at home and welcome at your place.

Throughout the time working at CERN, I am happy to have been able to stay in touch with friends and family back home and I am grateful to be able to call you, Franz Fellingner, Maximilian Lerchbaumer, Christian Fuchs, Matthias Bartmann, Klaus Vogelmayr and many others, my friends. Thank you for wonderful moments spent together and for being there for me.

My deepest gratitude goes to my parents, Margareta Brunbauer and Gernot Brunbauer, and my sister, Christina Brunbauer. Thank you for being the wonderful family you are, for all the time spent together, for giving me strength and for everything else.

Thank you, Maximilian Kaiser, for forming my enthusiasm for technology and science, for many inspiring and motivating discussions and for supporting me in pursuing the path I chose.

I am grateful to be able to count on all of you, Maximilian Kaiser, Werner and Erika Brunbauer and Karin and Magdalena Kaiser during enjoyable as well as challenging times and greatly appreciate all you have done for me and all you mean to me.

Thank you, Kerstin Hinterndorfer, for helping me accomplish things I am enthusiastic about and for your enduring support throughout the work on this thesis. I greatly value all the wonderful moments and adventures spent together. Thank you for being the wonderful person you are.

# Publications

**The results of this thesis were published in the following peer-reviewed journal articles:**

F. M. Brunbauer et al., "The planispherical chamber: A parallax-free gaseous X-ray detector for imaging applications", Nuclear Instruments and Methods in Physics Research Section A: Accelerators, Spectrometers, Detectors and Associated Equipment, vol. 875, pp. 16-20, 2017

F. M. Brunbauer et al., "Live event reconstruction in an optically read out GEM-based TPC", Nuclear Instruments and Methods in Physics Research Section A: Accelerators, Spectrometers, Detectors and Associated Equipment, vol. 886, pp. 24-29, 2018

F. M. Brunbauer et al., "Combined Optical and Electronic Readout For Event Reconstruction in a GEM-based TPC", IEEE Transactions on Nuclear Science, vol. 65, no. 3, 2018

F. M. Brunbauer et al., "Radiation imaging with optically read out GEM-based detectors", Journal of Instrumentation, vol. 13, T02006, 2018

**The results of this thesis were presented at the following conferences, workshops, meetings, and seminars:**

F. M. Brunbauer et al., "Progress towards optically read out GEM-based TPC", RD51 collaboration meeting, March 8-11, 2016

F. Resnati et al., "Developments of an optical readout for imaging Micro-Pattern-Gas-Detectors", CERN Detector Seminar, April 29, 2016. CERN, Geneva, Switzerland  
Presented by F. Resnati

F. M. Brunbauer et al., "Optically read out GEM detector in H4 test beam", RD51 mini-week, June 6-9, 2016, CERN, Geneva, Switzerland

F. M. Brunbauer et al., "Optically Read Out Planispherical GEM Detector for Minimizing Parallax Error", Workshop MPGD Applications Beyond Fundamental Science, September 15-16, 2016, Aveiro, Portugal  
Presented by F. Sauli

F. M. Brunbauer et al., "Live Event Reconstruction and Scintillation Studies in an Optically Read Out GEM-Based TPC", IEEE NSS/MIC 2016, October 29 - November 5, 2016, Strasbourg, France

F. M. Brunbauer et al., "Example of a RD51 generic R&D - Optically Read Out GEM-Based TPC", Workshop on Neutrino Near Detectors based on gas TPCs, 8-9 November 2016, CERN, Geneva, Switzerland

F. M. Brunbauer et al., "GEM-based TPC optically read out for R&D purposes", 8th Symposium on Large TPCs for Low Energy Rare Events, 5th-7th of December 2016, Paris, France

F. M. Brunbauer et al., "Optical readout of GEM-based detectors: concepts and applications", CERN EP-DT Training Seminar, May 11, 2017, CERN, Geneva, Switzerland

F. M. Brunbauer et al., "Online Dose Imaging and Beam Monitoring Detector for Hadron Therapy based on Optically Read Out GEM", 5th EIROforum School on Instrumentation, June 19-23, DESY, Hamburg, Germany

Received best student poster award

F. M. Brunbauer et al., "Optical readout of MPGDs: Techniques and applications", 5th International Conference on Micro-Pattern Gas Detectors, May 22-26, 2017, Philadelphia, Pennsylvania, United States of America

F. M. Brunbauer et al., "Combined Optical and Electronic Readout for Event Reconstruction in a GEM-based TPC", IEEE NSS/MIC, October 21-28, 2017, Atlanta, Georgia, United States of America

Second place in student paper competition

F. M. Brunbauer et al., "Combined Optical and Electronic Readout for Event Reconstruction in a GEM-based TPC", RD51 mini-week, December 13-15, 2017, CERN, Geneva, Switzerland

F. M. Brunbauer et al., "Low material budget beam monitoring with optically read out GEMs", 6th Beam Telescopes and Test Beams Workshop 2018, January 16-19, 2018, Zurich, Switzerland

# Contents

<b>1</b>	<b>Interaction of radiation with matter</b>	<b>1</b>
1.1	Interaction of charged particles with matter	1
1.1.1	Ionisation and excitation	2
1.1.2	Emission of bremsstrahlung	3
1.1.3	Cherenkov and transition radiation	3
1.2	Interaction of photons with matter	4
1.2.1	Photoelectric effect	5
1.2.2	Scattering	6
1.2.3	Pair production	7
<b>2</b>	<b>Radiation detection with gaseous detectors</b>	<b>9</b>
2.1	Charge conversion in gaseous detectors	10
2.2	Charge transport in gases	10
2.2.1	Drift	11
2.2.2	Diffusion	13
2.3	Charge amplification in gases	15
2.4	MicroPattern Gaseous Detectors	18
2.5	Gaseous Electron Multipliers	21
2.6	Readout of MPGDs	24
2.6.1	Electronic readout of MPGDs	25
2.6.2	Optical readout of MPGDs	28
2.7	Applications of MPGDs	29
<b>3</b>	<b>Light production and detection in gaseous detectors</b>	<b>31</b>
3.1	Light production mechanisms	31
3.1.1	Scintillation of Ar/CF <sub>4</sub> mixtures	33
3.2	Photon detection devices	34
3.2.1	PMTs	35
3.2.2	CCD sensors	36
3.2.3	EMCCD sensors	37
3.2.4	CMOS sensors	38
3.2.5	Comparison of sensitivity of imaging sensors	39
3.3	Optically read out detector applications	40
<b>4</b>	<b>Scintillation studies</b>	<b>43</b>
4.1	Secondary scintillation spectra	43
4.1.1	Scintillation of Ar	45

4.1.2	Scintillation of $\text{CF}_4$ . . . . .	45
4.1.3	Scintillation of $\text{Ar}/\text{CF}_4$ gas mixtures . . . . .	46
4.1.4	Scintillation of $\text{He}/\text{CF}_4$ gas mixtures . . . . .	48
4.1.5	Scintillation of $\text{Ne}/\text{CF}_4$ gas mixtures . . . . .	49
4.2	Light yield . . . . .	50
4.2.1	Light yield of $\text{Ar}/\text{CF}_4$ , $\text{He}/\text{CF}_4$ and $\text{Ne}/\text{CF}_4$ gas mixtures . . . . .	53
4.2.2	Trend of light yield in sealed detector . . . . .	54
<b>5</b>	<b>Optically read out detector concepts</b>	<b>57</b>
5.1	Radiation imaging with optically read out GEM-based detectors . . . . .	57
5.1.1	Detector concept and operation . . . . .	57
5.1.2	X-ray radiography . . . . .	58
5.1.3	X-ray fluoroscopy . . . . .	61
5.1.4	X-ray tomography . . . . .	62
5.1.5	X-ray fluorescence . . . . .	63
5.1.6	Radiation imaging . . . . .	66
5.2	Minimising parallax error with planispherical GEM . . . . .	69
5.2.1	Detector concept . . . . .	70
5.2.2	Minimisation of parallax error . . . . .	71
5.3	Event reconstruction in an optically read out TPC . . . . .	76
5.3.1	Detector concept . . . . .	77
5.3.2	Detector operation . . . . .	78
5.3.3	Live event reconstruction . . . . .	79
5.3.4	Combined optical and electronic readout . . . . .	83
5.4	Dose imaging detector for hadron therapy . . . . .	92
5.4.1	Detector concept and operation . . . . .	95
5.4.2	Material budget . . . . .	97
5.4.3	Detector response . . . . .	98
5.4.4	Beam profile monitoring . . . . .	102
5.4.5	Dose depth curve measurement . . . . .	103
5.4.6	Dose imaging . . . . .	105
<b>6</b>	<b>Conclusions</b>	<b>109</b>
<b>A</b>	<b>Experimental details</b>	<b>113</b>
A.1	Quantum efficiency of CCD, EMCCD and CMOS imaging sensors . . . . .	113
A.2	GEM gain measurement . . . . .	113
A.3	Photon detection efficiency . . . . .	115
A.4	PMT dynamic range . . . . .	117
A.5	PMT single photon response . . . . .	118
A.6	Residual gas analyser setup . . . . .	119



## CHAPTER 1

# Interaction of radiation with matter

Radiation can interact with and deposit energy in traversed matter by a variety of mechanisms depending on the characteristics of the particles and the medium. Depending on properties such as charge, energy or substructure, the dominant interaction principles may differ significantly and the observed effect of radiation on target materials must be considered as the composite of all possible interaction channels. The detection of radiation relies on the deposition of energy in the detector material by the investigated radiation and careful engineering of detector properties is necessary to tune detection capabilities to cover the range of interest.

Possible ways of interaction of radiation with matter include ionisation and excitation of the target material by charged particles, scattering and absorption of photons, pair production, emission of photons as bremsstrahlung, Cherenkov radiation, transition radiation, hadronic interactions with nuclei and interactions mediated by the weak force. Energy deposition by incident radiation in the target material by ionisation and excitation processes as well as the absorption of photons are the dominant interaction channels for the presented studies. The energy of particles can be either deposited in a specific location or over an extended range. The absorption of low-energy photons typically leads to the full energy of individual photons being deposited in a single interaction. The photons which have undergone interaction are consequently removed from the photon beam, which results in an exponential decrease of the intensity of a low-energy photon beam with penetration depth in a material as shown in figure 1a. Charged particles, on the other hand, may deposit their energy in multiple interactions over an extended range while traversing matter. The energy loss profile with a pronounced peak of the energy loss in a certain depth of material results in a rather localised drop of beam intensity at a specific depth as shown in figure 1b [1].

## 1.1 Interaction of charged particles with matter

Charged particles dissipate their energy when traversing a medium primarily through interactions with the electrons of the target atoms mediated by the electromagnetic force. The probabilities for atomic excitation, ionisation and other interaction channels depend on the energy and the mass of the charged particles and the nature of the traversed medium. Energy deposited in the target material by scattering or absorption of incident particles can be subsequently emitted through dissipative processes such as photon emission.

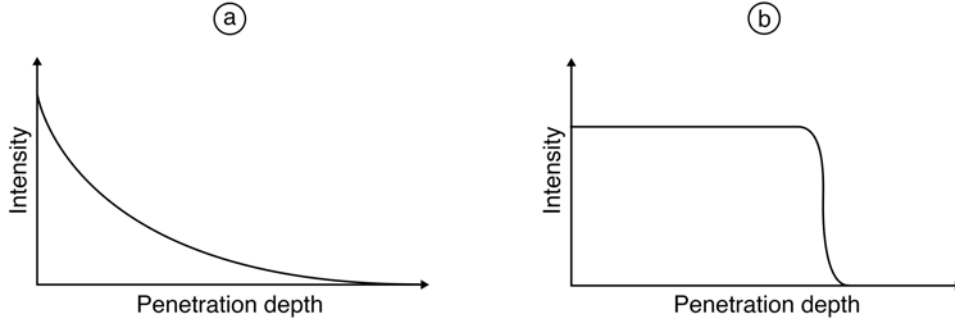


**Figure 1.** Intensity drop of photons and charged particles: (a) Photons interacting with the target material deposit their full energy and are removed from the beam resulting in an exponential decrease in photon beam intensity with penetration depth. (b) Charged particles deposit their energy throughout their path in the target material with maximum energy transfer in a certain depth resulting in a localised drop in intensity of a particle beam penetrating a target material. Adapted from [1].

### 1.1.1 Ionisation and excitation

During ionisation processes, charged particle radiation transfers sufficient energy to bound electrons in the target material to lift them out of the potential well binding them to the atoms and thus produces free charge carriers leaving behind positive ions. The so-called primary electrons may be used for detection of the incident charged particle and their number and momenta depend on the energy deposited by the incident particle. The initially created free charge carriers may have high energies and can ionise further atoms releasing some of their excess energy in secondary ionisation events. Ionisation is an interaction channel for charged particle detection utilised in detectors with gaseous or liquified gas active media as well as in semiconductor based detectors. The threshold energy for ionisation to take place depends on the energy states of the active detector material. This so-called ionisation energy can range from a few eV in semiconductor-based detectors, where it depends on the band gap between valence and conduction bands [2], to tens of eV in gaseous detectors. If the released energy does not reach the ionisation energy, the target material can be excited. When excited atoms or molecules return to their ground states, the excess energy can be released by the emission of scintillation light, which can also be used for detection of the incident radiation.

The linear stopping power  $S$  of charged particles traversing matter is expressed as the energy loss  $dE$  per unit distance  $dx$  as  $S = \frac{dE}{dx}$ . For charged particles much heavier than the electron rest mass, the linear stopping power can be expressed by the Bethe formula accounting for energy loss due to excitation and ionisation. The relativistic Bethe formula expresses the average stopping power for a particle with charge  $z$  and velocity  $v$  traversing a target medium as

$$-\left\langle \frac{dE}{dx} \right\rangle = \frac{4\pi}{m_e c^2} \frac{n_e z^2}{\beta^2} \frac{e^2}{4\pi\epsilon_0} \left[ \ln\left(\frac{2m_e c^2 \beta^2}{I(1-\beta^2)}\right) - \beta^2 \right] \quad (1.1)$$

with electron mass  $m_e$ , speed of light  $c$ ,  $\beta = \frac{v}{c}$ , electron number density of the target material  $n_e$ , electron charge  $e$ , vacuum permittivity  $\epsilon_0$  and mean ionisation potential  $I$ . The electron number density  $n_e$  of the target medium depends on the atomic number  $Z$  of the target material, its atomic mass  $A$  and its density  $\rho$  and can be written as

$$n_e = \frac{N_A Z \rho}{A M_u} \quad (1.2)$$



with the Avogadro constant  $N_A$  and the Molar mass constant  $M_u$ . The mean ionisation potential can be approximated by  $I \approx 10Z$  and is determined empirically.

As a function of the energy expressed as the product  $\beta\gamma$ , with the Lorentz factor  $\gamma = \frac{1}{\sqrt{1-\beta^2}}$ , the Bethe formula accurately describes the stopping power of heavy charged particles in the range of  $\beta\gamma \approx 0.1$  to  $\beta\gamma \approx 100$ . In this range, the energy losses by ionisation and excitation dominate, while at higher energies radiative losses such as bremsstrahlung contribute significantly to the energy loss of charged particles. At low energies, the energy loss of charged particles is proportional to  $\frac{1}{\beta^2}$  until it reaches a minimum at  $\beta\gamma \approx 3$ . Particles with an energy around  $\beta\gamma \approx 3$  are called Minimum Ionising Particles (MIPs) as their energy loss per unit length is minimal. At higher energies, the energy loss increases logarithmically until radiative losses start to dominate at even higher energies.

The Bethe formula expresses the average energy loss per unit length of a heavy charged particle traversing a target medium due to ionisation and excitation and does not account for event by event fluctuation of the energy loss. The formula does not accurately describe the energy loss of light charged particles such as electrons as they can be easily deflected by the target material and might move at relativistic speeds. Furthermore, in the case of electrons colliding with the shell electrons of the target material the interaction occurs between particles which are quantum mechanically indistinguishable and has to be treated accordingly.

### 1.1.2 Emission of bremsstrahlung

Charged particles emit electromagnetic radiation termed bremsstrahlung when accelerated or decelerated. Bremsstrahlung is also emitted when charged particles are deflected in the presence of other charged particles. The high-energy photons emitted as bremsstrahlung may be used to detect incident charged particles and present a major contribution to the energy spectrum of X-ray tubes. The energy loss of charged particles due to this radiation is strongly dependent on the mass of the charged particles and is significantly higher for lighter particles. The radiative energy loss is approximately proportional to  $\frac{E}{m^2}$  with the energy  $E$  and the mass  $m$  of the incident particles. The residual energy  $E(x)$  of a charged particle after traversing a certain thickness  $x$  of the target material while emitting bremsstrahlung can be expressed as

$$E(x) = E_0 e^{-\frac{x}{X_0}} \quad (1.3)$$

with the initial energy  $E_0$  of the particle and the radiation length  $X_0$ . The radiation length describes the distance over which the energy of the particle is reduced to  $\frac{1}{e}$  of the initial energy.

### 1.1.3 Cherenkov and transition radiation

Photons can also be emitted as Cherenkov or transition radiation. Cherenkov radiation is a low-intensity, low-energy photon production mechanism occurring when particles move through matter with a velocity higher than the velocity of light in the traversed medium. Thus, Cherenkov light is emitted only when

$$v > \frac{c}{n} \quad (1.4)$$

is fulfilled with the velocity  $v$  of the incident particle and the refractive index  $n$  of the target material. The light is emitted coherently and conically in the direction of movement with an opening angle  $\theta_c$  dependent on the particle velocity and the refractive index of the material as

$$\cos(\theta_c) = \frac{1}{\beta n} \quad (1.5)$$

Similarly to the electromagnetic wave of rapidly moving particles leading to Cherenkov radiation, charged particles passing the boundary between materials with different dielectric constants emit transition radiation. Resulting from the different extents of the electric fields of the moving charge in materials with low or high dielectric constants and the movement of charges when traversing boundaries between materials, transition radiation is emitted conically in the direction of particle movement with an opening angle depending on the speed of the particle. The angle  $\theta_t$  under which transition radiation photons are mainly emitted can be expressed as

$$\cos(\theta_t) = \frac{1}{\gamma} \quad (1.6)$$

and the intensity of the emitted radiation is proportional to  $\gamma$  as well as to the second power of the atomic charge of the traversed medium. Therefore, transition radiation of detectable intensity is only emitted in certain materials by highly energetic particles and may be used for particle identification.

## 1.2 Interaction of photons with matter

Photons may interact with traversed target material by the photoelectric effect, different forms of scattering such as elastic scattering or inelastic Compton scattering or pair production. The relative significance of these processes depends on the target material composition as well as the photon energy as shown for Ar in figure 2.

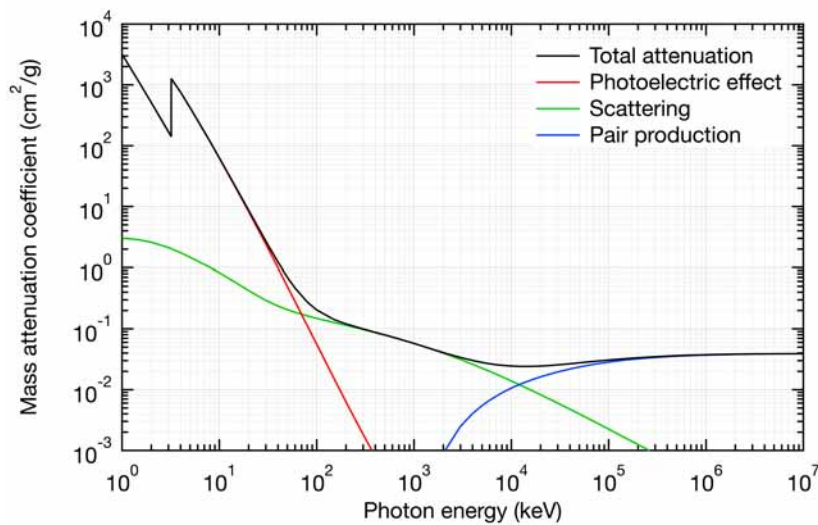


**Figure 2.** Mass attenuation coefficient in Ar: For low-energy photons, the photoelectric effect is the dominant contribution to the total attenuation of a photon beam in Ar. At intermediate energies, Compton scattering becomes significant while pair production dominates for high photon energies. Data from [3].

Typically, the photoelectric effect dominates for low-energy photons while pair production is the most significant interaction process for highly energetic photons with Compton scattering dominating in the intermediate energy range. Compton scattering changes the energy of the incident photons but does not remove them from the photon beam, while the photoelectric effect and pair production lead to the complete absorption of photons and their removal from the photon beam. The photoelectric effect and pair production therefore lead to an exponential decay of beam intensity with increasing depth and the intensity  $I(x)$  at a certain depth  $x$  can be expressed as

$$I(x) = I_0 e^{-\mu x} \quad (1.7)$$

with the initial intensity  $I_0$  and the attenuation coefficient  $\mu$ . The attenuation coefficient  $\mu$  contains all processes relevant for the attenuation of the intensity of a photon beam traversing a target material and can be calculated by

$$\mu = \frac{N_A \rho}{A} \sum_i \sigma_i \quad (1.8)$$

with the interaction cross section  $\sigma_i$  of a certain process.

### 1.2.1 Photoelectric effect

The photoelectric effect describes the absorption of an incident photon by an electron in the shell of a target atom and the subsequent liberation of an electron from the atom. In the case of incident photons with high energies, predominantly electrons from the innermost shells will be emitted. The kinetic energy  $E_e$  of the released electron is defined by the excess energy of the incident photon over the energy threshold required for ionisation and can be expressed as

$$E_e = E_\gamma - E_b \quad (1.9)$$

with the energy  $E_\gamma$  of the incident photon and the binding potential  $E_b$  of the released electron. The kinetic energy of the emitted electron might be high enough to trigger subsequent ionisation events. A schematic representation of the photon absorption and subsequent electron emission by the photoelectric effect is shown in figure 3a.

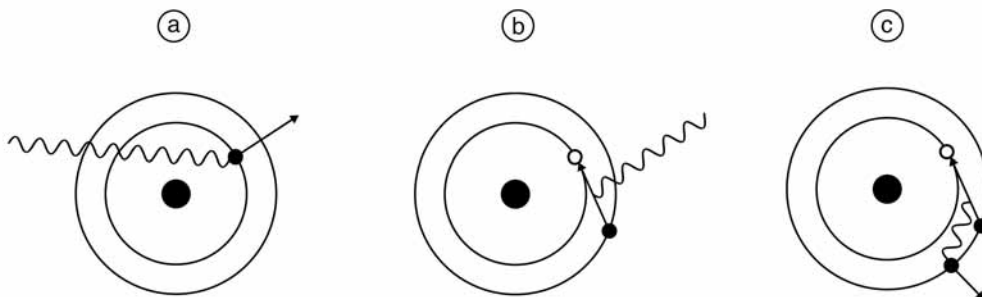


**Figure 3.** Ionisation by incident radiation: (a) The photoelectric effect describes the emission of bound electrons from an atom following the deposition of energy by an incident photon. (b) Electrons from higher shells can fill vacancies in lower shells and the excess energy is emitted as photon. (c) In radiation-less transitions, the excess energy available when an electron from a higher shell fills a lower shell vacancy is reabsorbed by another electron, which is in turn emitted as a so-called Auger electron.

The liberated electron leaves behind a hole in the shell of the atom, which can be filled by an electron from a higher shell. As the binding energy of inner shells is higher, an electron transitioning from a higher shell to fill a vacancy left in a lower one will emit its excess energy as a photon. These photons may be directly absorbed by another electron in a higher shell of the same atom leading to the liberation of a so-called Auger electron as shown in figure 3c. Alternatively, such photons carrying the energy difference between the two involved shells can be emitted from the atom as shown in figure 3b and contribute to further photon absorption or scattering processes in other atoms. The emission of characteristic photons and the emission of Auger electrons are competing processes and their relative yields depend on the atomic number of the target material. The Auger effect dominates at low atomic numbers while the emission of photons becomes dominant for target materials with higher atomic numbers. The cross section  $\sigma_{\text{ph}}$  of the photoelectric effect strongly depends on the atomic number  $Z$  of the target material and can be expressed as

$$\sigma_{\text{ph}} \propto \frac{Z^5}{E_{\gamma}^3} \quad (1.10)$$

with the energy of the incident photon  $E_{\gamma}$ .

The total number  $N$  of electron-ion pairs created by the photoelectron emitted by an incident photon interacting in a target material can be calculated by dividing the total deposited energy  $\Delta E$  by the average energy needed to create an electron-ion pair,  $W_i$ , as

$$N = \frac{\Delta E}{W_i} \quad (1.11)$$

and varies between 20 eV and 40 eV for most gases [4].

The observed fluctuation  $\sigma N$  of the number of created electron-ion pairs is lower than the one expected due to Poisson statistics due to limitations on the ionisation process imposed by the energy of the incident photon as an upper bound for the available energy for ionisation and the presence of discrete energy levels in the electron shells of the involved atoms. The Fano factor  $F$  describes such energy loss mechanisms which are not purely statistical and is used to define the fluctuation in the number of created electron-ion pairs as

$$\sigma N = \sqrt{FN} \quad (1.12)$$

## 1.2.2 Scattering

Photons may be scattered elastically or inelastically depending on their energy and the target material. Elastic scattering processes such as Thomson scattering or Rayleigh scattering do not change the energy of incident photons and may occur by photons interacting with electrons or atoms. If the energy of incident photons is large compared to the binding energy of the electrons in the target material, photons may be scattered inelastically on weakly bound electrons of the target material as shown in the Feynman diagram representation in figure 4a.

This process known as Compton scattering changes the wavelength of the incident photons and depends on the scattering angle  $\theta$  between the incident and the scattered photons as shown in figure 4b. The change in wavelength  $\Delta\lambda = \lambda' - \lambda$  due to Compton scattering can be expressed as

$$\Delta\lambda = \frac{h}{m_e c} [1 - \cos(\theta)] \quad (1.13)$$

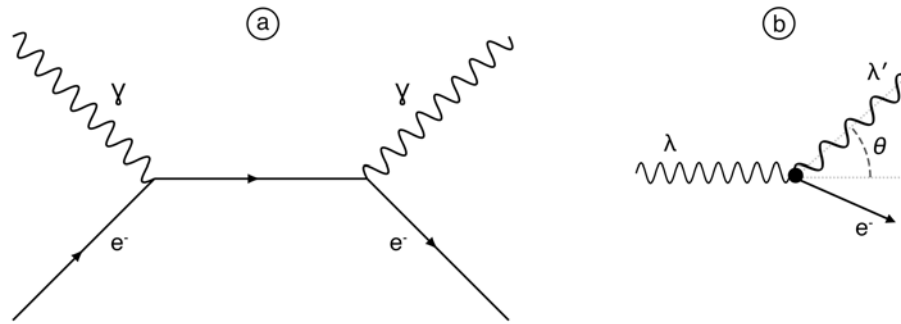


**Figure 4.** Compton scattering: (a) An incident photon is scattered on an electron of the target material. (b) The scattering angle  $\theta$  determines the change in wavelength between the incident and scattered photons.

with the Planck constant  $h$ . While for a scattering angle of  $0^\circ$  no energy is transferred and the wavelength of the photon does not change, the maximum energy is transferred for backscattering with a scattering angle of  $180^\circ$ .

### 1.2.3 Pair production

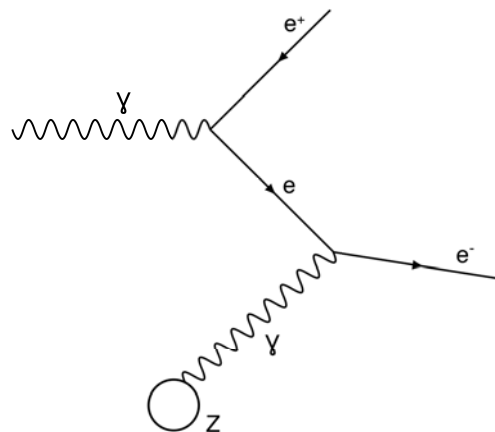


**Figure 5.** Pair production: A photon of sufficient energy may produce an electron-positron pair.

At even higher photon energies, photons passing the fields of nuclei or electrons can create electron-positron pairs as shown in the Feynman diagram representation in figure 5. The threshold photon energy for this pair production process is the sum of the rest masses of the electron and the positron of 511 keV each. Therefore, pair production only occurs at photon energies above  $2 \times 511 \text{ keV} = 1.022 \text{ MeV}$ . The excess energy of the incident photon above this threshold is transferred to the created electron-positron pair as kinetic energy. At high photon energies, electrons and positrons are preferably emitted in the forward direction of the incident photon. The cross section for pair production depends on the atomic number of the target material and only increases slowly with incident photon energy. However, since the cross sections of the photoelectric effect and Compton scattering decrease with increasing incident photon energy, pair production is the dominant interaction process for highly energetic incident photons. The mean free path for pair production by highly energetic photons  $\lambda_{\text{pair}}$  can be related to the radiation length  $X_0$  by

$$\lambda_{\text{pair}} = \frac{9}{7} X_0 \quad (1.14)$$



## CHAPTER 2

# Radiation detection with gaseous detectors

The detection of radiation is of paramount importance for a wide range of applications in fields ranging from science and industry to medical imaging and treatment, to name but a few. Taking advantage of the different channels of interaction of radiation with matter, numerous detector concepts adapted for specific requirements and delivering information about different properties of the studied radiation have been developed and used. Depending on the desired applications, radiation detectors should provide information about the properties of incident radiation such as type and energy of particles, 2D or 3D information of individual incident particles or particle beams or time of arrival information among others. To achieve resolution and accuracy requirements in the determination of the properties of radiation of a certain type, which are of the highest interest in a specific use case, different detector technologies might be better suited than others. Detector technologies such as semiconductor-based detectors, scintillators or gaseous detectors all come with strengths and weaknesses and in many situations a combination of different technologies is necessary to achieve the desired radiation detection capabilities. While semiconductor-based detectors provide high detection efficiencies and good energy resolution, they may suffer significantly from radiation damage and large-sized semiconductor-based detectors may be uneconomical. Scintillators can provide fast timing information and are ideal time tagging detectors but provide only limited spatial information and may degrade due to various ageing mechanisms. Gaseous detectors, on the other hand, allow for radiation detection with minimal material budget by using gases or gas mixtures as the active medium for detection. The low density of gases compared to liquids or solids minimises the impact on the incident radiation but may also result in lower detection efficiencies as the interaction probability of the incident radiation may be significantly lower than in the cases of liquid or solid active detection materials. In addition, gaseous detectors are compatible with high-rate environments [5, 6] and can be scaled up to cover large areas [7].

With minimal material budget, good radiation tolerance, cost-effective scalability to large area coverage and the possibility to operate in high-rate environments, gaseous detectors have gained popularity in fields such as high energy physics, nuclear physics and radiation monitoring. Relying on the interaction of incident radiation with the gas used as target material for detection, gaseous detectors make use of primary electrons produced by the ionisation of gas atoms by the incident radiation. If the number of primary electrons is sufficient, they can be used directly for the detection of incident radiation. Alternatively, the primary electrons generated by incident radiation can be multiplied by subsequent secondary ionisation processes to increase the effectively available charge in the detector and permit detection with increased signal-to-noise ratios. While various different gaseous detector

concepts exist and are in use, they all rely on the same basic principles for the production of free electrons and their movement in gases. The drift and diffusion behaviour of electrons in electrical fields in gases determines the characteristics of gaseous detectors and the achievable detection capabilities.

## 2.1 Charge conversion in gaseous detectors

Primary electrons created when incident radiation interacts with the active gas volume of gaseous detectors are used for radiation detection. While charged particles directly produce primary electrons when traversing the active volume by ionising gas atoms or molecules, neutral particles can be detected when they undergo nuclear reactions such as inelastic scattering, which produce charged particles or other products which can be detected directly. Low-energy photons interacting in the gas volume produce electrons by the photoelectric effect. The number of primary electrons produced by incident radiation in the gas depends on the energy threshold for the creation of free electrons in the gas, which is the energy required to create an electron-ion pair, and the energy deposited by the incident radiation. To achieve high signal-to-noise ratios in radiation detection, a possibly high number of primary electrons is desirable. Charged particles such as alpha particles may deposit a large amount of energy in the active volume of a detector resulting in high numbers of primary electrons and consequently a high achievable signal-to-noise ratio. In the case of large amounts of deposited energy, the initially created electrons might have sufficient energies to ionise further gas atoms or molecules contributing to the total number of electrons created by ionisation.

However, gaseous detectors are not readily suitable for the detection of some types of radiation such as highly energetic photons or neutral particles as the probability for interaction of such particle radiation with the gas acting as target material for detection is very low resulting in low detection efficiencies. The detection efficiency can be improved by increasing the gas pressure in gaseous detectors, effectively increasing the density of the active medium. Alternatively, the detection efficiency for a wide range of particles and particle energies can be significantly increased by using suitable converters. Neutron detection with gaseous detectors becomes feasible when employing converters such as Gd or B, which emit directly detectable radiation as a reaction to incident neutrons [8]. The same principle can be applied for the detection of highly energetic photons, which barely interact with gases typically used as target materials. As the cross section for the interaction of photons strongly depends on the atomic number of the target material, high-Z materials present effective converters for highly energetic photons and can be used to significantly increase detection efficiencies for such photons in gaseous detectors.

## 2.2 Charge transport in gases

Primary electrons created in the target gas volume of a gaseous detectors can subsequently be used for the detection of incident radiation. To record signals based on these primary electrons, they have to be efficiently collected and amplified to produce significantly strong signals for detection as the numbers of primary electrons are typically too low. With the average energy needed to create an electron-ion pair,  $W_i$ , of several tens of eV, the number of primary electrons created by incident low-energy photons is typically in the range of several



hundreds. For example, 5.9 keV photons emitted by a radioactive  $^{55}\text{Fe}$  source interacting in an Ar-based gas mixture release around 200 primary electrons, which is not enough for direct detection with commonly used readout electronics. Therefore, primary electrons must be transported to an amplification structure used in gaseous detectors to undergo charge amplification processes. Moving under the influence of electric fields, electrons will undergo drift and diffusion processes when moving through the gas volume of a gaseous detector until eventually undergoing avalanche multiplication processes by ionisation of gas atoms or molecules in high electric field regions which produce further electrons and ions.

### 2.2.1 Drift

Due to their electric charge, electrons will move under the influence of an external electric field against the direction of electric field vectors. This leads to a drift movement of electrons in the presence of an electric field in a gas volume and is used to transport primary electrons from the conversion region where they are created to amplification structures. The velocity of electrons when drifting in an electric field depends on the frequency of collisions with gas molecules and the strength of the electric field which accelerates the electrons. The drift velocity  $w^-$  of electrons can be expressed as

$$w^- = k \frac{eE}{m} \tau \quad (2.1)$$

with a constant  $k$  describing the energy distribution of electrons, the electron charge  $e$ , the electric field strength  $E$  and the mean time between collisions with gas molecules  $\tau$ . Therefore, the electron drift velocity depends on both the electric field and the mean time between collisions since electrons lose energy when colliding with gas molecules and can gain energy when being accelerated by the applied electric field between collisions. Electron drift velocities vary significantly between different gas species and electric field strengths and are typically in the order of several  $\text{cm}/\mu\text{s}$ . While for gases such as Ar or Xe the electron drift velocities at atmospheric pressure increase approximately linearly with the electric field strength up to at least  $10\text{ kV}/\text{cm}$  and remain below  $5\text{ cm}/\mu\text{s}$  at  $10\text{ kV}/\text{cm}$ , the drift velocities in some molecular gases such as  $\text{CF}_4$  or  $\text{CO}_2$  reach much higher values already at lower electric field strengths [4]. The electron drift velocity as a function of the electric field for different pure gases is shown in figure 6.

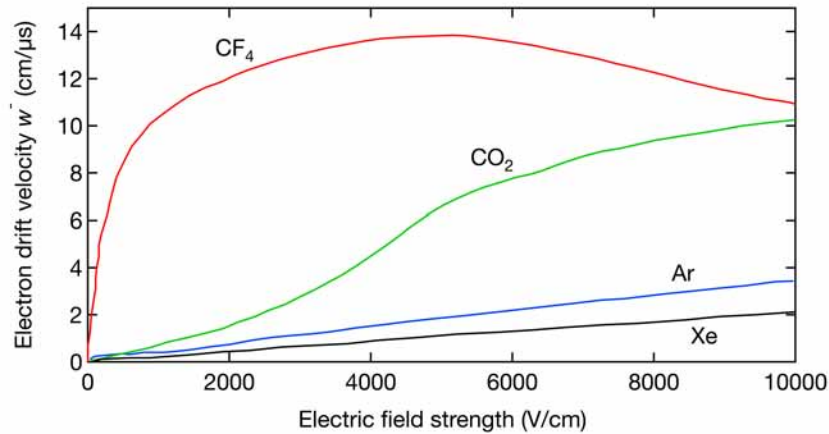


**Figure 6.** Computed electron drift velocities: The electron drift velocities in different pure gases at 1 bar vary greatly with the electric field strength. Adapted from [4].

In noble gases, electrons colliding with the gas atoms can only interact by elastic scattering, excitation or ionisation. As there are no bound molecules but only individual gas atoms, there are no other degrees of freedom such as vibrational or rotational states which could be excited by electrons interacting with the atoms of noble gases. Therefore, electrons might reach high energies, while the most probable energies in gas mixtures with molecular gases such as  $\text{CO}_2$  are much lower as shown in figure 7.

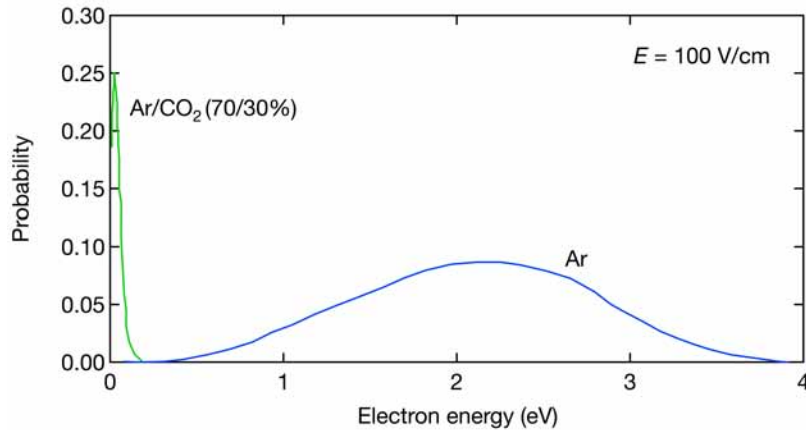


**Figure 7.** Computed electron energy distribution: In pure noble gases such as Ar, electrons are significantly more likely to reach higher energies than in gas mixtures with molecular gases such as  $\text{CO}_2$ . Adapted from [4].

For electrons with kinetic energies below the threshold for excitation or ionisation, elastic scattering at gas atoms causes electrons to repeatedly change their direction while moving through the gas. For electrons which are accelerated by the electric field and consequently reach higher velocities, the cross section for elastic scattering increases and leads to a higher probability for faster electrons to be scattered and slowed down by gas atoms before reaching energies sufficient for excitation or ionisation processes. The dependence of the cross section for elastic scattering on the electron velocity therefore leads to a non-uniform behaviour of the electron drift velocity  $w^-$  with the electric field and limits the achievable electron drift velocity in monatomic gases. As the electron drift velocity  $w^-$  is proportional to the mean time between collisions, which is in turn proportional to the mean free path between collisions, a higher probability for elastic scattering leads to a decreased electron drift velocity.

In gaseous detectors, high electron drift velocities are desirable to optimise the timing response of detectors by quickly transporting primary electrons from the conversion region to multiplication structures. Using molecular gases, significantly higher electron drift velocities can be reached. Since molecular gases feature additional degrees of freedom such as rotational or vibrational states of gas molecules, electrons may transfer their energy to gas molecules through other means than elastic scattering even for energies below the threshold for excitation or ionisation. As a result, the mean energy of electrons is reduced for molecular gases in comparison to monatomic gases as electrons can transfer their energy to gas molecules more efficiently. Lower electron energies lead to a decreased total cross section for interaction with gas atoms or molecules and therefore an increased mean free path and mean time  $\tau$  between collisions. An increased mean time between collisions results in an increased drift velocity  $w^-$  for electrons. Even small quantities of molecular gases added to noble gases can significantly increase the electron drift velocity by providing additional

channels for electrons to transfer their kinetic energy. Gas mixtures of noble gases with admixtures of molecular gases are therefore commonly used in gaseous detectors to achieve optimised electron drift behaviours.

The drift velocity  $w^+$  of ions under the influence of an electric field can be described by

$$w^+ = \mu E \quad (2.2)$$

with the ion mobility  $\mu$  and the electric field strength  $E$ . At atmospheric pressure, the drift velocities of ions are several orders of magnitude lower than electron drift velocities and typically in the order of  $10^{-2}$  cm/ $\mu$ s or  $10^{-3}$  cm/ $\mu$ s for electric field strengths of 0.1 kV/cm or 1 kV/cm, respectively [4]. The average energy of ions remains largely independent of the electric field up to very high field strengths, which leads to an ion mobility which is independent on the electric field but depends on the type of ions moving in a specific gas and on the pressure and the temperature of the gas [4]. The ion mobility can be related to the diffusion coefficient for ions by the Nernst-Townsend formula as

$$\frac{D}{\mu} = \frac{kT}{e} \quad (2.3)$$

with the diffusion coefficient  $D$ , the Boltzmann constant  $k$ , the temperature  $T$  and the electron charge  $e$ . For gas mixtures consisting of  $N$  different gas species  $G_1, G_2, \dots, G_N$ , the ion mobility  $\mu_i$  for ions of the gas species  $G_i$  in the gas mixture can be calculated by

$$\frac{1}{\mu_i} = \sum_{j=1}^N \frac{p_j}{\mu_{ij}} \quad (2.4)$$

with the volume concentration  $p_j$  of the gas species  $G_j$  in the gas mixture and the mobility  $\mu_{ij}$  of ions of the species  $G_i$  in pure gas of species  $G_j$ .

## 2.2.2 Diffusion

Undergoing collisions with gas molecules due to thermal movement, ions and electrons undergo diffusion even in the absence of electric fields. An initially localised distribution of particles will diffuse symmetrically with time and the fraction  $\frac{dN}{N}$  of the number of particles in a segment  $dx$  at distance  $x$  from the initial position can be calculated by

$$\frac{dN}{N} = \frac{1}{\sqrt{4\pi Dt}} e^{-\frac{x^2}{4Dt}} dx \quad (2.5)$$

with the diffusion coefficient  $D$  and the time  $t$ . The diffusion coefficient  $D$  depends on the gas species, temperature and pressure and is used to quantify the diffusion behaviour in a specific gas at defined environmental parameters. Diffusion also leads to a widening of the density distribution of particles. The standard deviation  $\sigma$  of diffusing particles can be described as

$$\sigma_x = \sqrt{2Dt} \quad (2.6)$$

with the standard deviation of the distribution of particles in one direction  $\sigma_x$  [4]. In three dimension, the standard deviation of the distribution in a volume,  $\sigma_V$ , can be expressed as

$$\sigma_V = \sqrt{3}\sigma_x = \sqrt{6Dt} \quad (2.7)$$

For drifting charges, longitudinal diffusion leads to a spread of an initially well-localised distribution along the drift direction while transversal diffusion leads to a widening of the charge distribution with the drifted distance, which also depends on the electric field strength. The magnitude of the transversal diffusion of electrons after a drift distance of 1 cm in different gases at atmospheric pressure expressed as the standard deviation  $\sigma_T$  as a function of the electric field strength is shown in figure 8.

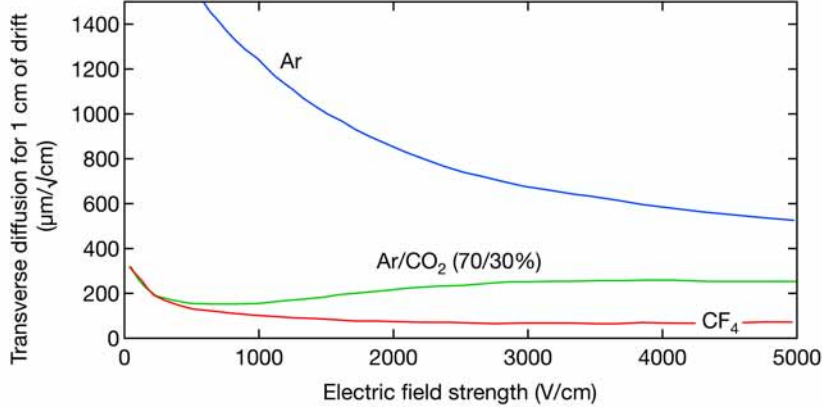


**Figure 8.** Computed transverse diffusion in different gases: The transverse diffusion of electrons after a drift distance of 1 cm varies with the gas species and the electric field strength. Adapted from [4].

In the absence of an electric field, the velocity of electrons and ions leading to their diffusion depends on their thermal energy. The distribution of the energies of particles at a specific temperature is described by the Maxwell-Boltzmann law and can be expressed as

$$F(\epsilon) = 2 \sqrt{\frac{\epsilon}{\pi(kT)^3}} e^{-\frac{\epsilon}{kT}} \quad (2.8)$$

with the probability  $F(\epsilon)$  for a particle having a specific energy  $\epsilon$ , the Boltzmann constant  $k$  and the temperature  $T$ . The distribution of energies does not depend on the mass of the described particles. The energy distribution can be used to express the distribution of velocities for particles with a specific mass  $m$  as

$$f(v) = 4\pi \left(\frac{m}{2\pi kT}\right)^{\frac{3}{2}} v^2 e^{-\frac{mv^2}{2kT}} \quad (2.9)$$

with the probability  $f(v)$  for particles to have a velocity  $v$ .

In the presence of an electric field, electrons drift against the direction of the electric field vectors and diffuse as a result of collisions with gas molecules. This combination of electron drift and diffusion leads to a movement and spreading of an initially localised electron cloud. As the electric field accelerates electrons and leads to an increase in the mean electron energy, the diffusion behaviour of electrons moving in an electric fields strongly depends on the electric field strength  $E$  in addition to the gas species, pressure and temperature. The Nernst-Townsend formula (2.3) can be modified to relate the mobility of electrons to the gas-dependent diffusion coefficient  $D$  and a characteristic energy  $\epsilon_k$  as

$$\frac{D}{\mu} = \frac{\epsilon_k}{e} \quad (2.10)$$

with the electron mobility  $\mu$  and the electron charge  $e$ . The characteristic energy  $\epsilon_k$  is a phenomenological quantity taking into account the increased average electron energy due

to the acceleration by an external electric field. This quantity can be used to express the linear diffusion of electrons in one direction,  $\sigma_e$ , over the distance  $x$  as

$$\sigma_e = \sqrt{\frac{2\epsilon_k x}{eE}} \quad (2.11)$$

Due to their much higher mass, ions are not accelerated by the electric field as strongly as electrons and their energy is not significantly modified by an external electric field. Therefore, the diffusion of ions in an electric field can be expressed without the need for a characteristic energy as in the case of electrons. The linear space diffusion  $\sigma_i$  of ions moving under the influence of an external electric field can be written as

$$\sigma_i = \sqrt{\frac{2kTx}{eE}} \quad (2.12)$$

and depends only on the temperature  $T$  of the gas and the electric field  $E$ .

### 2.3 Charge amplification in gases

Electrons drifting in an electric field are accelerated by the field and their energy is increased. With increasing energy, electrons can interact with gas atoms and molecules through inelastic processes and excitation or ionisation processes. The cross sections for different possible interaction processes depend on the energy as shown in figure 9 for the electron-molecule cross section for Ar.

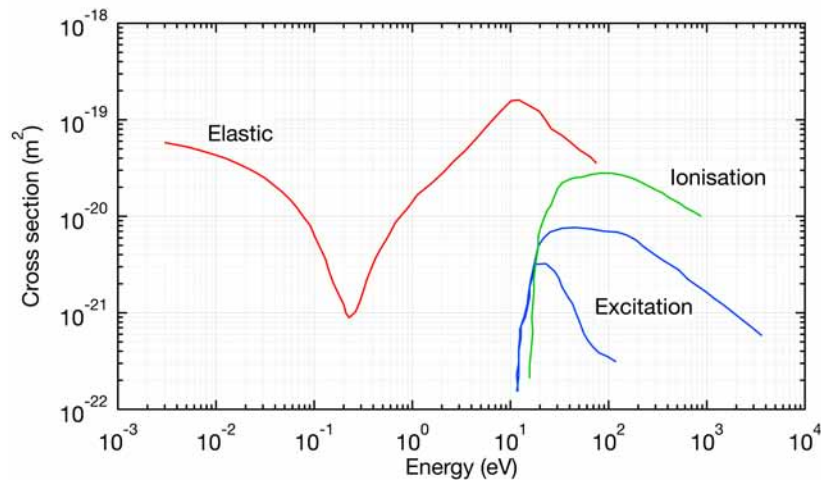


**Figure 9.** Electron-molecule cross section for Ar: While only elastic processes can occur at low energies, ionisation and excitation processes set in at higher energies. Adapted from [4].

If electron energies exceed the ionisation potential of present gas species, electrons might ionise gas atoms or molecules. Ionisation processes lead to the creation of pairs of electrons and ions, which are also subject to the electric field and will be accelerated by it. In sufficiently strong electric fields, electrons created during ionisation processes can be quickly accelerated by the electric field and gain enough energy to trigger subsequent ionisation processes creating further electron-ion pairs. The average number of electron-ion pairs created per unit length by consecutive ionisations initiating from a single electron drifting in a high electric field is expressed by the first Townsend coefficient  $\alpha$  and can be calculated by

$$\alpha = N\sigma_1 \quad (2.13)$$

with the number of gas molecules per unit volume  $N$  and the ionisation cross section  $\sigma_1$ . The increase  $dn$  in the number of electrons due to successive ionisations over a drift distance  $dx$  can be expressed with the first Townsend coefficient as

$$dn = n\alpha dx \quad (2.14)$$

with the number of electrons  $n$  at a given location. Integrating this expression, the number  $n(x)$  of electrons after a drift distance  $x$  is given by

$$n(x) = n_0 e^{\alpha x} \quad (2.15)$$

with the initial number of electrons  $n_0$  for a constant Townsend coefficient  $\alpha$ . Therefore, successive ionisation events triggered by electrons accelerated in high electric field regions lead to an exponential increase in the number of electrons. This mechanism is exploited for signal amplification in gaseous detectors. The magnitude of amplification is expressed by the gain factor  $G$  defined as the ratio between the number of electrons after multiplication,  $n$ , over a distance  $x$  and the number of primary electrons before multiplication,  $n_0$ , as

$$G = \frac{n}{n_0} = e^{\alpha x} \quad (2.16)$$

This exponential increase in the number of electrons leads to the development of electron avalanches and is used to achieve high charge amplification factors. In addition to secondary electrons being created in successive ionisation events, electron collisions with gas molecules might also lead to excited atoms and molecules. Photons emitted during de-excitation of excited gas atoms and molecules might be absorbed in the gas volume of the detector and create additional free electrons, which might contribute to the overall observed signal intensity and constitute a feedback mechanism which can lead to discharges in gaseous detectors. If the number of photons emitted during electron avalanche multiplication is high enough to create a significant number of free electrons which are subsequently amplified as well, the overall charge in the detector might increase and lead to discharges due to excessive charge densities. The efficiency of photon emission processes during charge amplification is described by the second Townsend coefficient. The risk for discharges due to photon feedback may be reduced and mitigated by limiting the range of photons in the gas volume. This can be achieved by adding so-called quenching gases to the gas mixture used in a detector which diminish the transparency of the gas mixture to the photons emitted by de-excitation processes during avalanche multiplication or quench scintillation photon emission.

At excessive electric fields in gaps between two electrodes, feedback mechanisms might lead to breakdown by avalanche multiplication. If the electric field is strong enough, ions produced during electron avalanche multiplication of primary electrons might extract additional secondary electrons upon impact on the cathode, which trigger subsequent electron avalanches. If the number of secondary electrons exceeds the number of primary electrons, breakdown by avalanche multiplication can set in. The first Townsend coefficient  $\alpha$  can be used to express the condition required for the ignition of self-sustained discharges, which is referred to as the Townsend criterion for gap breakdown, as

$$\gamma(e^{\alpha d} - 1) = 1 \quad (2.17)$$

with the secondary ionisation coefficient  $\gamma$  and the gap thickness  $d$  [9]. In the case of  $\gamma(e^{\alpha d} - 1) \geq 1$ , self-sustained discharges due to significant feedback mechanisms may occur and cause gaseous detectors to enter unstable operation regimes.

Depending on the electric field used for charge multiplication in gaseous detectors, different operation modes of gaseous detectors are distinguished. While the electric field ranges for different operation modes depend on gas parameters and detector geometry, a universal classification of operational regimes valid for all gaseous detectors can be performed as shown in figure 10.

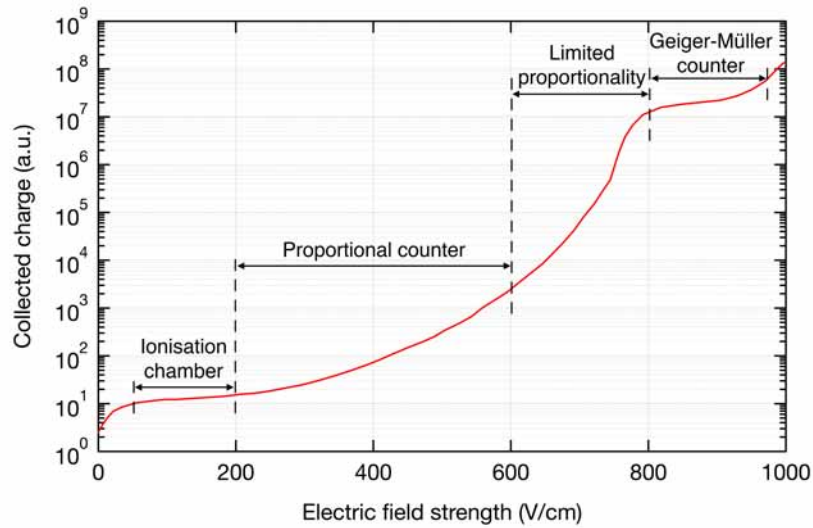


**Figure 10.** Operation regimes of gaseous detectors: Depending on the electric field strength in gaseous detectors, different operation regimes can be distinguished. Adapted from [10].

At very low electric fields, primary electrons created in the conversion gas volume by incident radiation cannot be efficiently transported and collected. In this recombination regime, primary electrons are lost to recombination processes before they can reach a multiplication structure or collection anode and cannot be used for incident radiation detection.

At electric drift fields sufficiently strong for primary electrons to be separated from positive ions and be transported in the gas, gaseous detectors are operating in an ionisation chamber mode. Primary electrons are transported from the location of interaction of the incident radiation towards an anode electrode and collected there. The current reaching the anode can be monitored and used to measure the amount of energy deposited by radiation in the gas region between cathode and anode electrodes. In this operation mode, electric fields are too low to trigger charge multiplication by successive ionisation processes and only primary electrons are available for detection. This limits the applicability of ionisation chambers as the number of primary electrons created by ionising radiation may in some cases be insufficient for detection with readout electronics.

When the electric field in a gaseous detector is high enough for primary electrons to be significantly accelerated between collisions with gas molecules and gain energies above the threshold for ionisation, charge multiplication by ionisation takes place. The amplified signal amplitude after charge multiplication is proportional to the number of primary electrons as long as the significance of photon feedback remains limited and charge multiplications oc-

curs over a constant and well-defined distance. In this case, a gaseous detector is operating in the proportional mode and the amount of energy deposited by the incident radiation can be deduced from the amount of charge detected after the multiplication stage.

At even higher electric fields, significant photon feedback leads to gain factors of avalanche multiplication to become dependent on the primary charge and gaseous detectors enter a regime of limited proportionality. Therefore, the recorded secondary charge after multiplication is not directly proportional to the amount of primary charge anymore. In the case of strong photon feedback, incident radiation might trigger discharges which propagate throughout the whole detector. In this so-called Geiger-Müller mode [11], the secondary charge does not depend on the primary charge anymore and is predominantly a function of the capacitance of the gaseous detector. While unsuitable for proportional radiation detection, this operation mode is used when particle counting is sufficient.

## 2.4 MicroPattern Gaseous Detectors

Primary electrons created when incident radiation ionises gas atoms in the active gas volume of an ionisation chamber are transported by an applied electric field in the conversion region and collected on an anode electrode for detection. However, individual events cannot be identified by this approach as the energy deposited by individual interactions of incident particle radiation is typically not sufficient to be detectable without charge amplification.

An early concept of a gaseous detector taking advantage of charge amplification in a high electric field region is the single wire proportional chamber, which consists of a thin anode wire surrounded by a cathode electrode with a gas-filled gap used for detection of incident radiation between the wire and the cathode.

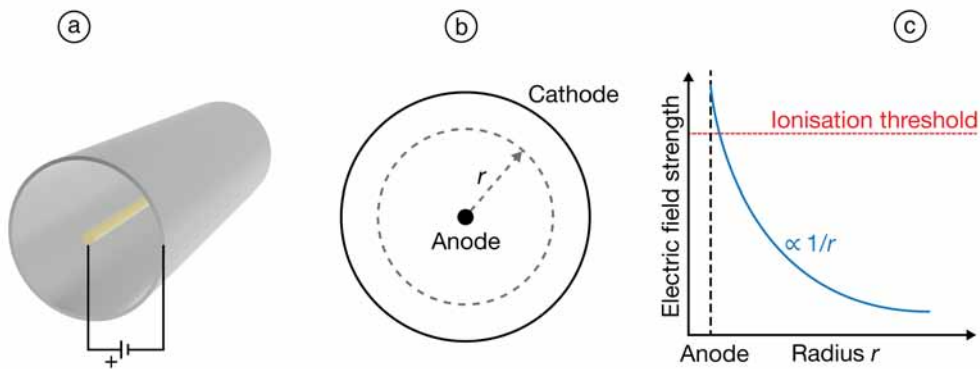


**Figure 11.** Single wire proportional counter: (a) Schematic view of coaxial single wire proportional counter with anode wire and cylindrical cathode. (b) A negatively biased cathode contains a thin positively biased wire with the electric field strength increasing towards the wire in the centre. Adapted from [4]. (c) In the vicinity of the anode wire, the electric field strength can surpass the threshold for ionisation to occur and electron avalanche multiplication towards the anode wire can take place. Adapted from [4].

In this detector concept as shown schematically in figure 11, primary electrons from ionisation occurring in the gas gap between the anode wire and the cathode are accelerated towards the positively biased anode wire. In the vicinity of the wire, the electric field strength increases significantly. At a certain distance from the anode wire, the electrical field strength surpasses the critical field strength needed to trigger secondary ionisation events as electrons undergo avalanche charge multiplication in the high electric field region around the anode wire. Therefore, even events with low numbers of primary electrons can be detected.



Extending this concept from a single wire to a multitude of wires individually connected to read out electronics, a multi-wire proportional chamber provides position information of the incident radiation as well as energy information by operating in a proportional charge amplification mode [12]. Multi-wire proportional chambers enabled a revolution in data acquisition by employing a fully electronic readout approach and paved the way for modern gaseous detector technologies and electronic data acquisition and analysis.

While the multiple wires of multi-wire proportional chambers could provide moderate spatial information of radiation events, the achievable spatial resolution was limited by the mechanical precision in manufacturing these detectors with a high number of thin wires with a fine pitch. Moving towards planar structures with anode, cathode and readout electrodes structured on substrates by micro-fabrication techniques such as photolithography, much smaller detector structures could be achieved. These so-called MicroPattern Gaseous Detectors (MPGDs) are capable of achieving much better spatial resolutions due to the inherent scale of the employed electrode structures.

MPGD-based detectors share a separation of charge conversion and amplification regions, which allows the achievement of good energy resolutions. Incident radiation interacts in a low electric field region and produces primary free electrons. Keeping the electric field strength in this drift region well below the threshold for avalanche multiplication, no charge multiplication occurs and electrons merely drift towards the multiplication region under the influence of the so-called drift field in the conversion region. This results in the number of electrons reaching the multiplication region to depend only on the energy deposited in the gas in the conversion region by the incident radiation. As there is no charge multiplication in the conversion region, the number of electrons reaching the multiplication region does not depend on the depth of interaction of the incident radiation in the conversion layer, which would adversely reflect on the achievable energy resolution. Signal amplification by electron avalanche multiplication occurs only in a thin, well-defined amplification region formed by micrometer-scale electrodes, which features a high electric field strength sufficient for secondary ionisation to occur. As all primary electrons produced in the conversion layer traverse the same distance in the high electric field amplification region, they are amplified by a constant factor, the so-called gain of a gaseous detector. The total number of electrons after charge multiplication is therefore proportional on the number of primary electrons and reflects the amount of energy deposited by the incident radiation.

Profiting from continuing advances in micro-fabrication techniques and many similarities with industrial Printed Circuit Board (PCB) manufacturing, various MPGD concepts have been developed over the past decades since the introduction of the first MPGD, the Micro-Strip Gas Counter (MSGC), by A. Oed in 1988 [13]. The inherent capability to operate these detectors in high-radiation-rate environments made them a valuable tool in high energy physics experiments [14] and other applications such as thermal neutron detection [15]. MSGCs consist of alternating cathode and anode strips with widths and pitches on the scale of tens to hundreds of micrometers structured on a planar substrate as shown in figure 12.

Operating this structure in a gas volume and biasing the electrodes with alternating positive and negative polarity, high electric field regions between neighbouring electrodes capable of achieving electron avalanche multiplication are created and electrical signals from the strips are read out by dedicated readout electronics. With the same micro-patterned electrodes being used for defining the amplification field and for signal readout, MSGCs are sensitive to discharges, which may damage or destroy the strip electrodes. By sepa-

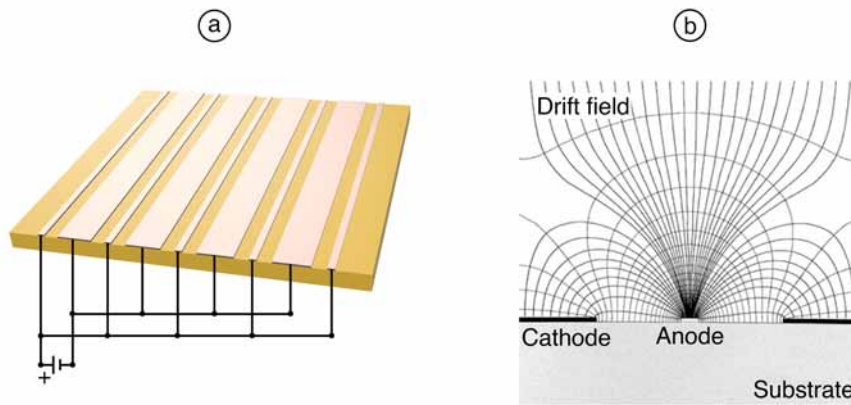


**Figure 12.** Micro-strip gas counter: (a) Schematic view of MSGC with alternating cathode and anode strips. (b) The electric field map shows the electric field lines between cathode and anode strips in a cross section of a MSGC. High electric field regions in the vicinity of the anode strips are used for signal amplification and electron collection. Adapted from [4].

rating the electrodes used for amplification and signal readout, other MPGD-based detectors could overcome this issue. While numerous MPGD concepts have been developed and used in a range of applications, two MPGD technologies stand out as having achieved widespread popularity and application. Micro-Mesh Gaseous Structures (Micromegas) have been proposed in 1992 by Y. Giomataris et al. [16] and employ a high electric field region for charge multiplication between a micro-mesh suspended on pillars on top of a planar anode electrode. Coupling a conversion region between a planar cathode and the micro-mesh to the thin amplification region between the suspended micro-mesh and the anode electrode, Micromegas-based detectors as shown in figure 13 can sustain high radiation rates and provide good energy resolution.

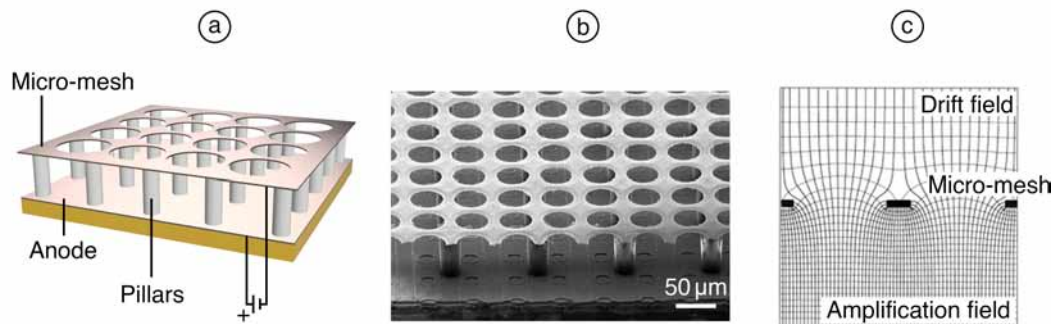


**Figure 13.** Micro-Mesh Gaseous Structures: (a) Schematic view of Micromegas with an amplification region between a micro-mesh suspended by pillars and an anode electrode. (b) SEM image of typical Micromegas geometry in a detector read out with readout electronics integrated in the substrate. Adapted from [17]. (c) The electric field map shows the high electric field in the amplification region between the micro-mesh and the anode electrode. Adapted from [4].

The thickness of the amplification region of typically around  $100\ \mu\text{m}$  permits high electric field regions and consequently high charge gain factors of up to  $10^5$ . The signal induced by the large number of electrons after avalanche multiplication is read out from the anode electrode or dedicated readout electrodes separated from the anode electrode. This single amplification stage concept limits the maximum achievable gain of Micromegas-based detectors.

Gaseous Electron Multipliers (GEMs), another MPGD technology, rely on high electric field regions inside well-defined holes for charge avalanche multiplication and permit multi-stage amplification structures.

## 2.5 Gaseous Electron Multipliers

Based on perforated foils consisting of two electrodes separated by an insulating layer, GEMs are multiplication structures used for charge amplification by electron avalanche multiplication within high electric field regions. First introduced in 1997 by F. Sauli [18], this technology has since gained popularity for various applications in radiation detection and large-area detectors based on GEMs have been realised [19]. While GEMs exist in many varieties and the dimensions and employed materials of the structures vary, typical GEM foils are made up of a 50  $\mu\text{m}$  thick insulating polyimide layer with 5  $\mu\text{m}$  thick Cu layers as electrodes on both sides, as shown schematically in figure 14.

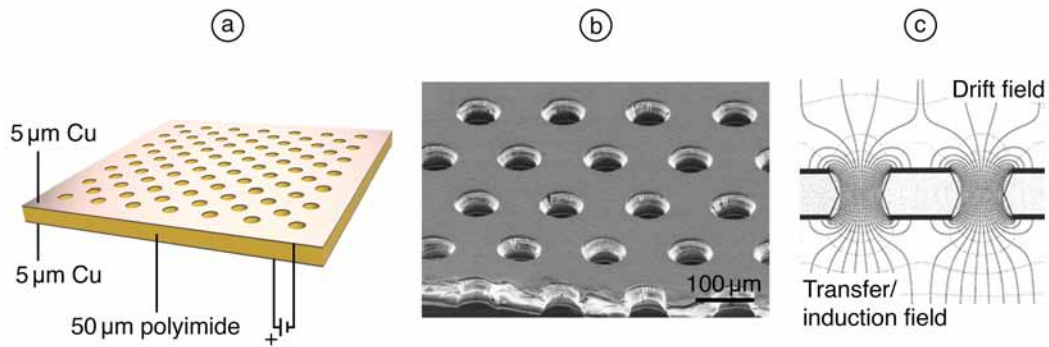


**Figure 14.** Gaseous electron multiplier: (a) Schematic view of GEM consisting of a perforated foil with two Cu electrodes separated by an insulating layer. (b) SEM image of typical GEM foil with 70  $\mu\text{m}$  diameter holes with a pitch of 140  $\mu\text{m}$ . Adapted from [4]. (c) The electric field map shows the high electric field in the holes of a GEM which permits electron avalanche multiplication. [4].

In this multi-layer foil, holes with a diameter of commonly 70  $\mu\text{m}$  and a pitch of 140  $\mu\text{m}$  in a hexagonal pattern are structured by photolithographic techniques and etching. Depending on structuring and etching techniques, the geometry of the cross section of the holes can vary from cylindrical to double conical shapes. The two Cu layers used as electrodes can be individually biased. By applying electrical potentials with a difference of several hundred volts on the two electrodes, high electric field regions with field strengths of several  $10^4$  V/cm in the holes of the GEM foil are obtained. Due to the geometry of the holes, electric field lines between the two electrode are concentrated in well-defined regions within the holes as shown in figure 14c. The holes in the GEM foils must be structured with high precision and care to achieve smooth surfaces as any exposed or sharp metallic edges on the electrodes or around the circumference of the GEM holes lead to concentrated electrical field lines and may trigger destructive discharges.

Electrons drifting towards a GEM foil will follow the electric field lines and are channeled into the holes of the GEM in appropriate electric field configurations. A high electric field strength inside of the holes created by biasing the bottom electrode of a GEM foil more positively than the top one by several hundred volts results in electrons being strongly accelerated within the GEM holes and permits them to gain enough energy to ionise further gas atoms thus creating additional electron-ion pairs. While ions move towards the cathode

under the influence of the electric field, the secondary electrons can gain sufficient energy from the high electric field region within the holes and create further electrons leading to electron avalanche multiplication. The high number of secondary electrons created within GEM holes will move out of the holes and follow electric field lines below the GEM foil. The created electrons from a GEM-based multiplication stage can be read out directly or transferred to further multiplication stages. The fact that electrons are available for subsequent multiplication steps after undergoing electron avalanche multiplication in the holes of a GEM foil is an outstanding feature of GEMs and can be used to achieve very high charge gain factors in multi-stage amplification structures. Commonly, multiple GEM foils are operated in series with each one multiplying the number of electrons arriving from the previous one. In a typical triple-layer GEM structure, primary electrons from ionisation in a drift region above the GEM stack are multiplied by the first GEM in the stack and transferred by an electric transfer field to the second GEM, where the arriving electrons are multiplied again. Subsequently, they are transferred to the third GEM in the stack and undergo a third stage of avalanche multiplication. This approach permits high charge gain factors of up to  $10^6$  while still operating the detector in a stable regime as each amplification stage is only responsible for a fraction of the total charge gain. A typical gaseous detector buildup based on a triple-GEM charge multiplication stage is shown schematically in figure 15.

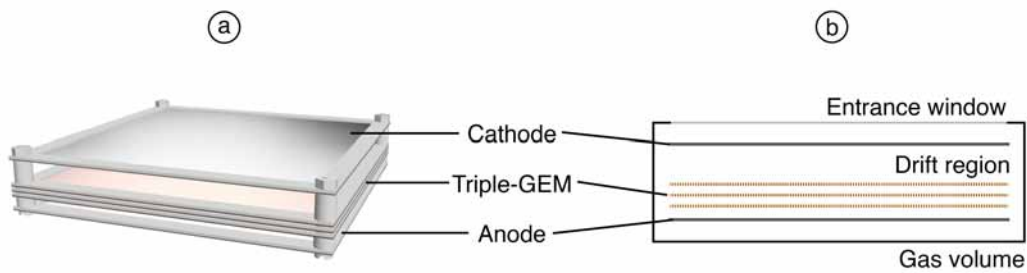


**Figure 15.** Triple-GEM setup: (a) Gaseous detector with triple-GEM multiplication stage and cathode and anode electrodes. (b) Schematic cross-sectional view of gaseous detector based on triple-GEM multiplications stage in a gas volume with an entrance window for incident radiation.

The active volume for incident interaction is formed between the cathode electrode and the top electrode of the first GEM in the triple-GEM stack. In this region, incident radiation produces primary electrons by ionisation of gas atoms. Since energy deposited by incident radiation is converted to primary electrons, which are subsequently used for detection, this region is called the conversion region. In the electric field created between the cathode and the top electrode of the first GEM, the created primary electrons drift towards the GEM. The conversion region of a gaseous detector is therefore also commonly called the drift region of the detector. The electric field in the drift region must be sufficiently strong to effectively allow primary electrons to reach the multiplication stage. If the drift field is too weak, primary electrons might undergo recombination with positive ions to neutral atoms which makes them unavailable for the electron avalanche multiplication process in the charge amplification stage. In addition, primary electrons might become attached to electronegative impurities such as  $O_2$  [9] in the gas volume of the detector if they move too slowly as a result of a weak drift field. These processes might lead to a decrease in signal amplitude and therefore limit the achievable signal-to-noise ratio. Depending on detector geometry, operation principle and gas purity, typical drift field strengths of several hundred up to a few thousand V/cm are used. Drift region thicknesses of several millimetres are common

for GEM-based detectors, which is sufficient to achieve reasonable detection efficiencies for MIPs, although detector concepts such as Time Projection Chambers (TPCs) may use significantly thicker drift regions with optional field shaping electrodes to ensure a possibly uniform electric field throughout the drift region.

After the multiplication in the first GEM of a multi-GEM multiplication structure, electrons need to be transferred from one GEM to the next one. Transfer gaps of a few millimetres between individual GEM foils in a multi-GEM stack are typically used. The electric field in the transfer region between GEMs, the so-called transfer field, plays an important role in the operation and efficiency of a multi-GEM multiplication stage. The transfer field must be chosen such that electrons are efficiently extracted from the holes of the first GEM and can be well collected into the holes of the second GEM. The correct choice of transfer fields is therefore important to maximise the effective total charge gain of a GEM-based multiplication stage in order to achieve possibly high signal-to-noise ratios.

The gain of a GEM-based multiplication stage depends on the voltage drop across the GEM as well as on operating conditions such as gas composition, temperature and pressure. Even with a single GEM, gain values exceeding  $10^3$  may be reached, although the onset of electron avalanche multiplication and the maximum achievable voltage before entering unstable operating conditions depend on the employed gas mixtures and compositions. The gain of a single GEM was measured in different gas mixtures with varying  $\text{CF}_4$  fractions as a function of the voltage drop across the GEM as described in detail in section A.2. High gain factors over three orders of magnitude could be reached with some of the investigated gas mixtures at atmospheric pressure as shown in figure 16 as a function of the voltage drop across a single GEM. The voltage drop across the GEM was increased up to a maximum of 500 V. At this voltage drop the GEM was still in a stable condition in all investigated gas mixtures.

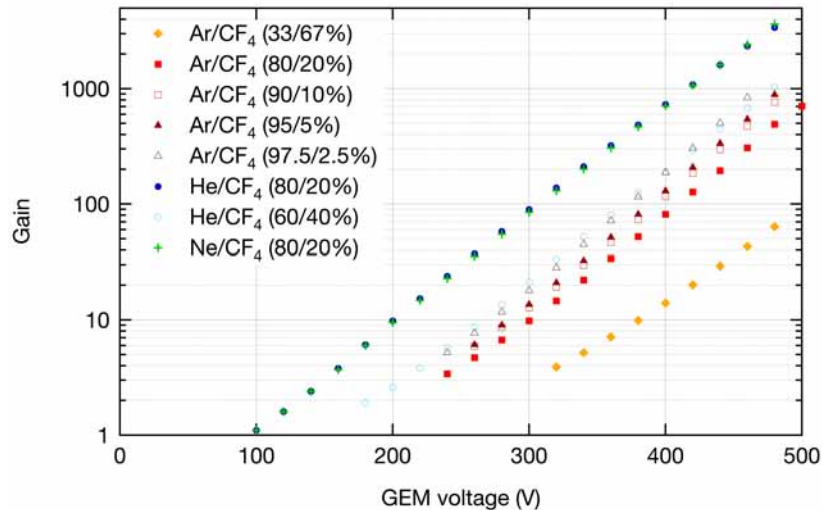


**Figure 16.** Single GEM gain: The gain of a single GEM operated in different gas mixtures at atmospheric pressure may be varied over three orders of magnitude by changing the voltage drop across the GEM. The onset of electron avalanche multiplication and the gain for a certain GEM voltage vary with gas composition.

GEMs are compatible with high particle rates [6] and are therefore well-suited for applications in detectors used in high energy physics. While ions created in the holes of the GEMs during avalanche multiplication distort electric fields due to their charge, their effect on the

response of a GEM-based multiplication stage is small. The so-called space charge region composed of ions slowly moving towards the cathode presents a problem only in extreme operating conditions and GEMs can readily cope with particle fluxes commonly encountered in most applications outside of high energy physics. Distortions of the electric fields used in GEM-based detectors due to space charge regions can be minimised for the case of long drift distances by employing gating structures to block ions from drifting towards the cathode and remove them from the active volume of the detector [20]. This requires structures which combine possibly high transparencies for electrons with minimal transparencies for ions. Gating meshes as well as high-aperture GEMs [21] have been developed to block ions, while graphene layers covering the holes of the GEMs present another promising approach, which may potentially work well to block ions while being transparent to electrons [6].

The low material budget of gaseous detectors such as GEMs permits the development of detectors for applications such as non-invasive beam monitoring, which require a minimisation of the material in the path of the beam. The low density of gas used as target material for incident radiation makes gaseous detectors ideally suited for applications requiring low material budgets. With 5  $\mu\text{m}$  thick Cu electrodes on both sides of a 50  $\mu\text{m}$  thick insulating foil, the typically used GEM geometry is already well-suited to fulfil low material budget requirements. In order to minimise the material budget further, the GEM geometry can be optimised by thinning down the metallic electrodes and using either thin Cu electrodes [22] or very thin layers of Cr [23] on both sides of an insulating foil as electrodes.

Presenting a cost-efficient solution for large-area detectors, GEM foils with active areas ranging from several square millimetres up to more than 1  $\text{m}^2$  are manufactured to meet experimental requirements. For small-scale detectors and detector development prototypes, a standard GEM foil geometry with an active area of  $10 \times 10 \text{ cm}^2$  has been defined and is widely used. Employing a double mask photolithography process, the production of these standard GEM foils with holes with a diameter of 70  $\mu\text{m}$  at a pitch of 140  $\mu\text{m}$  has been standardised and industrialised.

Different variation of GEMs and GEM-like multiplication structures have been developed and operated. Some examples include thick GEMs, glass GEMs and Thick-COBRA detectors. Thick GEM-like hole multipliers with typical thicknesses and hole diameters on the scale of millimetres have been shown to permit high single-stage gains and are proposed for photon detection and low-pressure operation [24]. Glass GEMs potentially offering superior outgassing properties have been manufactured and successfully operated for imaging applications [25] and high-resolution X-ray tomography [26]. Thick-COBRA detectors combine structured electrodes as found in micro-hole and strip plates with thick GEM geometries and aim at high gains and increased robustness [27]. Amplification structures based on high electric field regions in well-defined holes have also been integrated directly onto substrates to realise so-called WELL [28] or resistive-plate WELL [29] gaseous detectors.

## 2.6 Readout of MPGDs

Gaseous detector technologies such as Micromegas and GEMs are used to amplify electrical signals by electron avalanche multiplication. For the detection of incident radiation, the amplified electronic signals must be read out from the detector. This requires the coupling of a suitable readout technology to the amplification structure. Ranging from single-channel readout by planar anodes to high-resolution readout by electrical or optical signals, a multi-

tude of readout concepts meeting different experimental requirements and limitations have been developed and are employed for acquiring signals from gaseous detectors.

### 2.6.1 Electronic readout of MPGDs

An anode electrode below the last GEM in a multi-GEM multiplication stage as shown in figure 15 can be used for directly reading out the produced secondary charge by monitoring the electric current reaching the anode. The electric field strength between the bottom electrode of the GEM and the anode must be sufficiently high to efficiently extract electrons from the holes of the GEM and collect them on the anode. By connecting the anode electrode to ground with an ammeter in series or biasing it through an ammeter, the current reaching the anode can be recorded. This readout concept based on current monitoring is applicable only when an integrated reading of the secondary charge is sufficient. As electronic signals are typically on time scales too fast for the detection of individual signals by standard ammeters, the read out current results from an average of numerous signals and provides information about the average amount of charge arriving in a defined time interval. The current  $I$  at the anode depends on the average number of electrons per event reaching the anode and the rate of events and can be calculated by  $I = en_1R$  with the electron charge  $e$ , the average number of secondary electrons reaching the anode per event  $n_1$  and the rate of events  $R$  in Hz. When the average number of secondary electrons reaching the anode or the event rate are low, highly sensitive ammeters and optimised noise attenuation are required. Reading out the current from the anode of a GEM-based detector can be used to determine the effective charge gain of the multiplication stage. The effective charge gain  $G$  defines the factor by which the number of secondary electrons reaching the anode after electron avalanche multiplication is larger than the number of primary electrons. It differs from the inherent gain of the multiplication stage as it also takes into account possible losses of electrons due to a limited electron transparency of the GEM. Therefore,  $n_0$  primary electrons entering the multiplication stage will result in  $n_1 = n_0G$  secondary electrons reaching the anode. The effective charge gain of the detector,  $G = \frac{n_1}{n_0}$ , can be determined for a known current, event rate and number of primary electrons by the expression

$$G = \frac{I}{en_0R} \quad (2.18)$$

To read out events individually, electrical signals induced by secondary electrons moving in the induction gap between the last GEM and an anode electrode can be exploited. According to the Shockley-Ramo theorem, the high number of secondary electrons leaving the multiplication stage after electron avalanche multiplication induces an electrical signal, which can be used for the detection and the determination of the energy deposited by individual events. Induced electrical signals can be read out from the anode as well as from other electrodes in the detector such as the bottom electrode of the last GEM in a multi-GEM stack. To optimise the achievable signal-to-noise ratio in the readout of induced electrical signals and be able to read out signals from events with a low number of primary electrons created, a chain of readout electronics consisting of a combination of amplifiers, signal shaping electronics and filters can be used. Typically, a pre-amplifier connected to the electrode used for reading out induced electrical signals is used as a first signal conditioning stage. By connecting a pre-amplifier with a possibly short connection to the readout electrode, signals are quickly amplified to minimise the significance of electronic noise which may be picked up along the path of the read out signals. The signal produced in the pre-amplifier is typically

further amplified and shaped by an integrating and differentiating shaping amplifier before being acquired. Signal shaping parameters such as integration time and differentiation time have to be optimised to minimise the significance of electronic noise by an increased signal integration time while maintaining a possibly fast detector response. To achieve high signal-to-noise ratios in electronically read out detectors, electronic noise must be minimised as effectively as possible. The noise contribution from the power supplies used for biasing the detector elements including the multiplication stage can be minimised by employing low-pass filters in the bias lines between the power supply channels and the biased electrodes. A simple low-pass filter consisting of a series resistor and a capacitor to ground or a combination of multiple low-pass filter stages can effectively decrease electronic noise originating from the power supply. Noise picked up by the connection between the readout electrode and the first stage of the signal conditioning chain presents a significant contribution to the overall noise level and has to be minimised effectively. Using coaxial cables with a properly grounded shielding around the centre conductor used for transmitting signals can greatly decrease the level of picked up electrical noise. Furthermore, grounding all metallic components of a detector which can act as additional shielding, such as the detector vessel, boxes containing filtering circuits and read out electronics, can also limit the picked up noise and result in an improved signal-to-noise ratio.

Using signals induced by moving secondary electrons instead of collecting charge directly allows more intricate readout geometries, which can provide additional spatial information and can be used for 2D position sensitive electrical readout. Electrons can be collected by an anode used to define the induction field while the signal is read out from electrodes electrically insulated from the anode. These so-called readout electrodes are used to pick up the signal induced by the moving secondary electrons but do not collect charge themselves in an AC-coupled configuration. Decoupling the anode used for charge collection from the readout electrodes and relying on induced electrical signals permits detector geometries with higher tolerance to discharges. The destructiveness of discharges can be limited by using a resistive material as anode electrode for charge collection instead of a fully conductive metallic electrode. The separation of the readout electrodes from the anode electrode used for charge collection also decreases the effect of discharges on the readout electrodes. A schematic view of a resistive readout geometry consisting of resistive anode strips and top and bottom readout strips providing 2D spatial information separated by insulating layers is shown in figure 17. This technique is widely used to protect Micromegas and so-called resistive Micromegas, which employ a resistive anode electrode, are used particularly in high-rate environments [30, 31]. A resistive anode layer also permits a complete decoupling of charge collection and readout electrodes. In so-called Piggyback Micromegas, charge is collected on a resistive layer on a ceramic substrate while signals are capacitively coupled to pads, which are placed outside of the detector volume [32].

Using segmented readout electrodes to obtain spatial information from induced electrical signals, position sensitive detectors can be realised. Common geometries for segmented readout electrodes used for 2D readout include pixels and crossed strips. Pixelated readout electrodes consist of a large number of individually read out pads across the active area of the detector. The position of the incident radiation can be directly obtained by registering which pixel recorded an electrical signal. Pixelated readout requires the readout of a high number of individual channels and a connection from each pixel to the readout electronics. In the case of a high number of pixels, this may lead to difficulties in signal routing and may



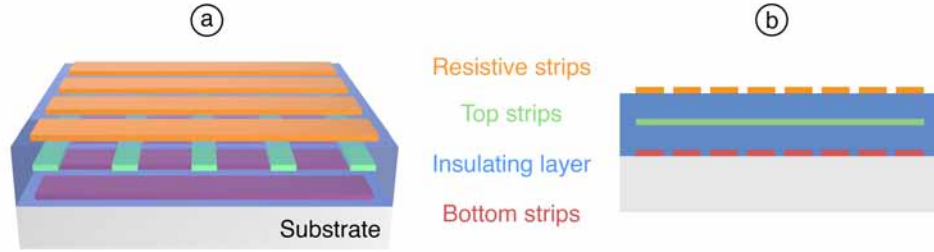


**Figure 17.** Resistive strip readout: (a) Schematic view of readout geometry consisting of resistive strips and top and bottom readout strips separated by insulating layers. (b) Cross section of the readout geometry with resistive strips parallel to bottom readout strips and top readout strips in between.

require multi-layer PCBs. Using a combination of GEM detectors and the Timepix readout chip, spatial resolutions below  $30\ \mu\text{m}$  have been achieved with pixelated readout [33].

Alternatively, 2D spatial resolution can also be obtained from crossed strip electrodes. In this geometry, the location of signals can be obtained by registering each event in multiple strips in different directions. In cartesian readout strip geometries, strip electrodes in one layer provide X-axis coordinates of detected signals while another layer of strips rotated by  $90^\circ$  with respect to the other one provides Y-axis coordinates of detected signals. By combining information about hit strips in the X-direction and in the Y-direction, the 2D position of events can be determined. Hit strips can be identified by checking the amplitude of the read out signal against a binary threshold. To achieve better spatial resolution, positions can be determined from a centre of gravity fit of the amplitudes of several neighbouring hit strips. This approach has been used to achieve spatial resolutions in the order of tens of  $\mu\text{m}$  in GEM-based detectors read out by crossed readout strips. A readout structure with crossed readout strips can be realised in a multi-layer structure by metallic readout strips in different directions electrically insulated from each other. As shown in figure 18, a bottom layer of strips is used for signal readout in one dimension while a second layer of strips on top of the first layer and separated by an insulating layer below the top strips is used for readout in a second dimension.

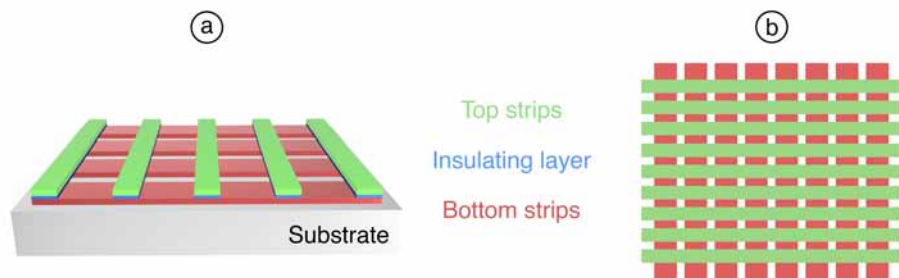


**Figure 18.** 2D strip readout: (a) Anode consisting of top and bottom strips in X and Y-directions separated by insulating layer. (b) Schematic view of cartesian readout strips drawn to scale with width and pitch of strips optimised for balanced charge sharing between layers.

As the top layer of readout strips partially covers the bottom layer of strips, the signal amplitude picked up by strips on the different layers may vary. To split the signal amplitude for top and bottom readout strips in a well-balanced way, the charge sharing ratio between the top and bottom layers of readout strips can be optimised by tuning the widths and pitches of the readout strips on both layers. In a readout strip geometry with bottom strips with a width of  $w_b$  and a pitch of  $p_b$  and top strips with a width of  $w_t$  and a pitch of  $p_t$ , the charge

sharing ratio  $r_c$  of the uncovered areas of the top and bottom strips can be calculated as  $r_c = w_t \rho_b (w_b \rho_t - w_t w_b)$  [34]. For the same strip pitch on both layers, the bottom strips must be wider than the top strips for equal charge sharing as they are partially covered by the top strips. The expression given above is true for the case of a negligibly thin insulating layer between the two layers of strips. If the insulating layer on which the top strips sit has non-negligible thickness, the fact that the bottom strips are not on the same plane as the top strips has to be taken into account in determining the required strip widths and pitches for balanced charge sharing between the layers. While 2D readout with crossed strips requires less readout channels than pixelated readout, it is more susceptible to ghost hits in high-rate environments. If two events hitting a total of four readout strips occur within a very short time interval and are recorded by the readout electronics simultaneously, the precise location of the events cannot be determined unambiguously and so-called ghost hits are recorded. However, some of these ambiguities might be resolved by correlating signal amplitudes of signals recorded on two layers of strips [35]. Crossed strip readout is widely used for the electrical readout of MPGDs due to its ease in implementation and simple routing from readout strips to readout electronics. The spatial resolution of 2D strip readout without centre of gravity fitting is on the scale of the pitch between strips. With centre of gravity fitting to determine the hit position with higher precision, spatial resolutions well below  $100 \mu\text{m}$  have been achieved [31]. If spatial information in a single direction is sufficient, 1D strips can be used. This approach has been employed in a GEM-based TPC for the Super-FRS tracking of heavy ions at FAIR [36] as well as in Micromegas-based detectors, where a spatial resolution of less than  $20 \mu\text{m}$  has been achieved [37].

Gaseous amplification stages such as GEMs or Micromegas can also be coupled to solid state pixel sensors. Due to the low capacitance of individual readout pixels and the high gain factors achievable by the amplification stages, these hybrid devices can be sensitive to single primary electrons released in the gas and perform tracking of high-multiplicity events as so-called micro-TPC devices [38]. Sub-millimetre spatial resolution in the 3D reconstruction of MIPs was achieved by coupling a triple-GEM to Timepix readout chips with a total of  $512 \times 512$  pixels in a so-called GEMPix hybrid detector [39]. Similarly, Micromegas-like amplification structures have also been combined with Complementary Metal-Oxide-Semiconductor (CMOS) pixel chips to so-called GridPix hybrid detectors [40] and high efficiencies for detecting single electrons with this concept have been demonstrated [41].

## 2.6.2 Optical readout of MPGDs

MPGD-based detectors can be also read out optically by recording the scintillation light emitted during electron avalanche multiplication. Using suitable gas mixtures with emission spectra matching the wavelength-dependent efficiency of photodetectors, emitted scintillation light can provide information about the energy of events and position sensitive photon detectors such as imaging sensors can provide images of events with high granularity and spatial resolution. Taking advantage of technical advances in the development of imaging sensors in recent years, Charge-Coupled Devices (CCD) and CMOS imaging sensors with a high number of low-noise pixels are available and can be used to optically read out gaseous detectors. The signal-to-noise ratios achievable by optical readout depend on the readout noise of the imaging sensor and the intensity of emitted and detected scintillation light. Inherently insensitive to electronic noise, optical readout provides an attractive alternative to electronic readout of MPGDs and high spatial resolution can be achieved by high-granularity

imaging sensors and matching optical lenses. However, the maximum frame rate in the order of 100 Hz achievable by modern imaging sensors limits optical readout with imaging sensors to an integrating data acquisition mode in many cases. The intuitive way of obtaining visual representations of events without the need for extensive image reconstruction algorithms is a key advantage of optical readout. GEMs are ideally suited for optical readout due to the high charge multiplication and the resulting strong scintillation light intensity in multi-GEM multiplication structures. Additionally, in comparison to other MPGD technologies like Micromegas, which are built on a substrate which may inhibit the readout of scintillation light, the perforated foil structure of GEMs permits emitted scintillation light to be readily recorded with photon detectors or imaging sensors placed below them.

## 2.7 Applications of MPGDs

The low material budget, radiation hardness and high-rate capability as well as scalability to large-area detectors have led to applications of MPGDs in many fields ranging from high energy physics to tomography and medical applications. Notable examples of applications of MPGDs in high energy physics include upgrades of the ATLAS, CMS and ALICE detectors at the Large Hadron Collider (LHC) at CERN, which will be installed during a shutdown of the LHC. The ATLAS collaboration has chosen Micromegas for the New Small Wheel (NSW) upgrade for the forward muon detectors. Employing a 2D strip readout with a dedicated Application-Specific Integrated Circuit (ASIC) developed for this purpose, the NSW will feature several planes of Micromegas-based detectors with a total detector area of 1200 m<sup>2</sup> [42]. The CMS collaboration is installing triple-GEM-based detectors as part of a muon chamber upgrade in the outer region of the detector. Individual modules with GEM foils with dimensions of up to 44.5 × 120.9 cm<sup>2</sup> are combined to cover a total active area of approximately 27 m<sup>2</sup> [43]. The ALICE collaboration is upgrading the readout of the endcaps of the main TPC used in the experiment with quad-GEM-based detectors. In order to reduce ion backflow and minimise distortions by space charge effects, each quad-GEM-based detector uses two GEM foils with a hole pitch of 140 μm and two GEM foils with a hole pitch of 280 μm [44].

Gaseous detectors are also used in muon tomography to acquire images of massive objects such as cave systems [45] or pyramids to analyse their homogeneity and search for concealed cavities. While the low detection efficiency of gaseous detectors limits their suitability for medical imaging applications in which radiation dose exposures to patients have to be minimised, GEM-based detectors may present a viable solution for beam monitoring detectors used for machine parameter and patient treatment plan verification in radiotherapy and hadron therapy facilities. Similar to commonly employed ionisation chambers in hadron therapy facilities, MPGD-based detectors may permit online beam monitoring due to their low material budget.

Gaseous detectors present an attractive approach to radiation detection and are ideally suited for applications demanding a low material budget or radiation hardness. While limited efficiency due to the low density of the active medium used for radiation detection may not be acceptable for some applications like medical imaging, the high achievable charge gain factors enable detection of weakly ionising radiation. Additionally, the ability to tune the effective charge gain of employed amplification structures permits detectors with radiation detection capabilities ranging from MIPs to highly ionising particles.



## CHAPTER 3

# Light production and detection in gaseous detectors

Radiation detection by optical readout relies on the emission of photons triggered by an incident particle traversing the active detector material and depositing energy. Different light production mechanisms are distinguished by the processes involved in the emission of photons. Primary and secondary scintillation and electroluminescence are dominant light production mechanisms used for particle detection.

### 3.1 Light production mechanisms

Scintillation is a type of luminescence, which is based on the excitation of atoms or molecules as a result of the deposition of energy by incident radiation. The light production mechanism of scintillation describes the emission of photons when excited atoms or molecules return to lower energy states and the excess energy between the excited state and the lower energetic one is emitted as photons. Depending on energy level structures of involved atoms and molecules, scintillation light emission might occur during direct transitions from an excited state to an energetic ground state or involve more complex processes. De-excitation processes resulting in the emission of scintillation photons with specific energies can be preceded or succeeded by other transitions of the excited atoms or molecules which might or might not emit photons themselves. Several energy level transitions, which do not trigger the emission of photons and are therefore called radiation-less transitions might take place before scintillation photons are emitted. In that case, the energy of emitted photons is lower than the one of the previously absorbed incident photons, which is described by the Stokes-shift to longer wavelengths for emitted scintillation photons.

Light emission by scintillation can occur in a multitude of materials including gases, liquids, organic and inorganic crystals and glasses. Depending on the time constants of the emission of scintillation light after the absorption of incident radiation, fluorescence and phosphorescence are distinguished as two classes of scintillation mechanisms. While fluorescence leads to the prompt emission of photons, phosphorescence describes scintillation processes in which the emission of photons occurs with some time delay after the absorption of incident radiation. The re-emission of absorbed energy may be delayed by up to several hours as a result of quantum mechanically forbidden transitions in the energy level spectra of some materials. In gaseous radiation detectors employing signal amplification structures, primary and secondary scintillation are distinguished. Light emitted as a result of the interaction of incident radiation with the target material of the detector is called primary

scintillation light as its emission coincides with the creation of primary electrons. Secondary scintillation light is emitted during the creation of secondary electrons as a result of electron avalanche multiplication in charge amplification structures. While different energy levels might be involved in the emission of primary and secondary scintillation light, these terms are solely used to distinguish the light produced by the primary interaction and during charge multiplication processes.

Light may also be emitted by a process called electroluminescence. In gaseous detectors, this process can result in photon emission when electrons with intermediate energies, which are below the threshold for ionisation but sufficient for excitation, excite gas atoms or molecules. The intensity of this photon production mechanism is proportional to the number of involved electrons, the electric field strength and the length of the path of the electrons. In semiconductors, electron-hole pairs might be created by highly energetic electrons striking atoms or by doping in semiconductor junctions. In high electric field regions, electrons might be accelerated sufficiently to create electron-hole pairs when striking atoms and thus trigger light production by electroluminescence. Light may also be emitted in a number of other luminescence processes in which energy is provided by different sources such as mechanical action, sound waves, or chemical reactions, to name but a few. While electroluminescence is an important process in semiconductor devices, light production in gaseous detectors is dominated by primary and secondary scintillation.

The amount of emitted light is an important parameter determining the achievable signal-to-noise ratio in an optically read out detector. For primary and secondary scintillation, the emitted light intensity may depend strongly on parameters such as gas pressure and electric field strength [46]. A careful tuning of these parameters is necessary to maximise the light yield in order to reach possibly high detection efficiencies and signal-to-noise ratios. Wavelength-resolved absolute irradiance measurements can be used to quantify and compare scintillation light emission intensities. Absolute irradiance is defined as the radiant flux passing through or hitting a surface area and can be reported in units of power per unit area per unit wavelength ( $\mu\text{W}/\text{cm}^2/\text{nm}$ ).

In the case of gaseous detectors, the number of primary scintillation photons emitted in the conversion gas volume depends on the amount of energy deposited by incident radiation as well as the gas composition and the pressure and electric field strength in the conversion region. In order to be useful for radiation detection by optical readout, emitted scintillation light must be possibly intense in a wavelength range compatible with the employed photon detection devices. While numerous gases and gas mixtures feature ample scintillation light emission in the UltraViolet (UV) or deep-UV wavelength ranges, technical considerations such as opaqueness of many materials in this short wavelength range have to be taken into account. To take advantage of readily available photon detectors and imaging sensors, wavelength-shifting materials such as tetraphenyl butadiene [47] or gases with significant scintillation light emission in the visible (VIS) wavelength range are necessary. Gas mixtures with admixtures of tetrafluoromethane (carbon tetrafluoride,  $\text{CF}_4$ ) have been found to feature ample scintillation light emission [48] with a pronounced emission peak in the VIS wavelength range. Such gas mixtures typically emit in the order of 0.1 to 0.3 secondary scintillation photons per secondary electron during electron avalanche multiplication. Therefore, mixtures based on noble gases with some fraction of  $\text{CF}_4$  have gained popularity for optically read out gaseous detectors and have been used extensively [49, 50, 51]. In addition to intense scintillation light emission,  $\text{CF}_4$  also permits high charge gain factors and values as high as  $1.6 \times 10^4$  have been achieved with single GEMs operated in pure  $\text{CF}_4$  at atmo-

spheric pressure [52]. As the use of Ar is much more economic than Ne, He or Xe, Ar/CF<sub>4</sub> gas mixtures are widely used for optically read out GEM-based detectors.

### 3.1.1 Scintillation of Ar/CF<sub>4</sub> mixtures

The scintillation light spectrum of an Ar/CF<sub>4</sub> gas mixture with 20 % of CF<sub>4</sub> (by volume) is shown in figure 19a. A dominant broad emission band centred around a wavelength of 630 nm is accompanied by a number of sharp emission lines in the Near-InfraRed (NIR) range between 720 nm and 820 nm and a UV emission band. The emission spectrum is a result of ionisation, excitation, charge transfer, dissociation and de-excitation processes occurring upon electron impact on Ar atoms and CF<sub>4</sub> molecules.

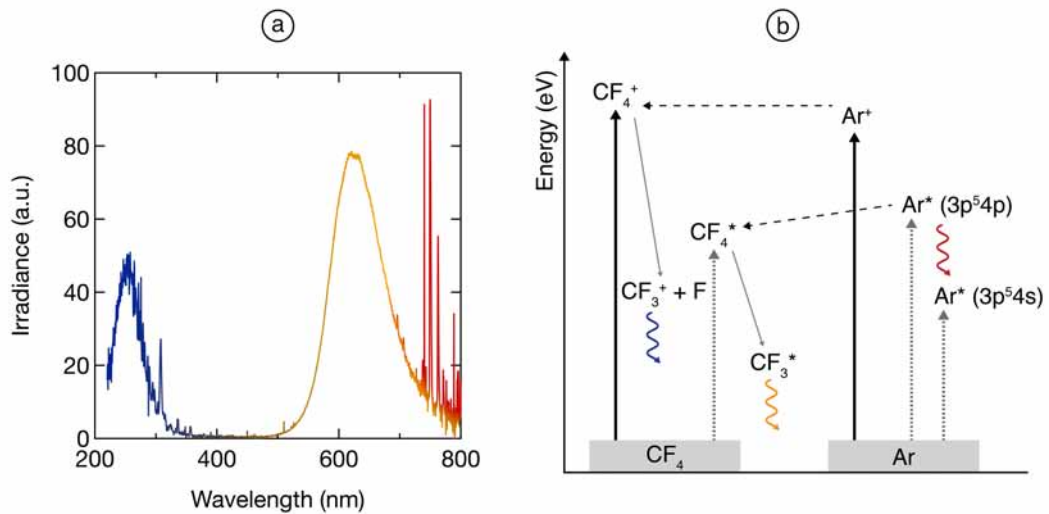


**Figure 19.** Scintillation of Ar/CF<sub>4</sub> gas mixture: (a) The scintillation spectrum of an Ar/CF<sub>4</sub> gas mixture with 20 % of CF<sub>4</sub> displays UV and VIS scintillation bands and sharp emission lines in the NIR range. (b) Scintillation mechanisms contributing to the Ar/CF<sub>4</sub> scintillation spectrum. Solid black lines represent ionisation processes and dashed grey lines denote excitation processes. Dashed black lines represent charge transfer between atoms and molecules and solid grey lines represent dissociation. Emission of photons in the UV band (blue), in the VIS band (orange) and in the NIR range (red) is shown by wavy arrows. Image adapted from [53].

Both Ar and CF<sub>4</sub> might be ionised to Ar<sup>+</sup> and CF<sub>4</sub><sup>+</sup> atoms, respectively, if impacting electrons transfer sufficient energy for ionisation. CF<sub>4</sub><sup>+</sup> ions dissociate to CF<sub>3</sub><sup>+</sup> ions and atomic F with a short half life and high probability [54] and CF<sub>3</sub><sup>+</sup> emission may contribute to the UV scintillation band in the emission spectrum of the gas mixture [55]. Alternatively, ionised and excited CF<sub>4</sub><sup>+</sup> may also contribute to the observed UV emission band [50, 56, 57].

Besides ionisation, electron impact may also lead to the excitation of CF<sub>4</sub> molecules and scintillation light emission in the VIS wavelength range from the de-excitation of CF<sub>3</sub><sup>+</sup> [50]. As the intensity of the VIS wavelength band does not change significantly with changing fractions of CF<sub>4</sub> in Ar/CF<sub>4</sub> gas mixtures, the direct excitation of CF<sub>4</sub> is not considered to be the only channel leading to light emission from CF<sub>3</sub><sup>+</sup> [50]. Ionised Ar atoms also contribute to the number of produced CF<sub>4</sub><sup>+</sup> ions and subsequent photon emission through charge transfer processes from Ar<sup>+</sup> ions to CF<sub>4</sub> molecules [58].

Transitions between different excited Ar states lead to the emission of the sharp atomic emission lines in the spectrum shown in figure 19b in the wavelength range between 720 nm and 820 nm [50]. For different ratios of Ar and CF<sub>4</sub> in the gas mixture, the relative intensity

of these emission lines to the broad emission band at lower wavelengths is modified. Mixtures with higher fractions of Ar feature more pronounced atomic emission lines attributed to emission resulting from the transfer between different excited states of Ar atoms. As Ar only features translational and electronic excited states due to its monatomic nature, the energy difference between excited states is well-defined and leads to sharp emission lines. Excited Ar states may also decay through two-body collisions with other atoms or molecules, which do not contribute to the scintillation light yield [53].

Excited  $\text{CF}_4^*$  molecules dissociate to excited  $\text{CF}_3^*$  molecules and F atoms with a short life time [59]. These excited  $\text{CF}_3^*$  fragments emit photons in the VIS wavelength range and are responsible for the broad VIS emission band between 720 nm and 820 nm in the emission spectra of Ar/ $\text{CF}_4$  gas mixtures [56, 60, 50]. In addition, charge transfer processes between excited  $\text{Ar}^*$  atoms and  $\text{CF}_4^*$  molecules might also contribute to the VIS scintillation light emission from  $\text{CF}_3^*$  molecules [50, 53].

## 3.2 Photon detection devices

Optical readout of radiation detectors relies on the detection of light emitted as a result of incident radiation interacting in the detector. The scintillation or electroluminescence light produced in detectors can be detected with a variety of photon detection devices. Light detection can be accomplished by taking advantage of a variety of interaction mechanisms of photons with the active media in photon detection devices such as the photoelectric effect, photovoltaic effects, polarisation changes or the increase of thermal energy. In the field of optical readout of radiation detectors, semiconductor-based devices such as photodiodes, avalanche photodiodes, silicon photomultipliers, CCD and CMOS devices as well as PhotoMultiplier Tubes (PMTs) have gained popularity and are widely used. As highly sensitive vacuum phototubes which achieve single-photon sensitivity, PMTs are used in low-light applications where photon counting and high detection efficiency are key requirements. In applications which require 1D or 2D spatial resolution in photon detection, CCD and CMOS sensors are commonly used. Recent advances in semiconductor technology have greatly increased the performance of CCD and CMOS sensors and highly sensitive and granular imaging sensors based on these technologies have become readily available adding to their spread and popularity.

Photon detection devices such as CCD or CMOS imaging sensors have to fulfil a number of requirements depending on the desired application. Important characteristics of imaging sensors include their quantum efficiency, spectral response, gain, dark current and the significance of different contributions to the overall noise of a detection system. The quantum efficiency is a measurement of the sensitivity of a photon detection device defined as the ratio between produced photoelectrons and incident photons. Thus, it measures the fraction of incident photons which trigger the production of an electron. The quantum efficiency typically depends on the wavelength of incident photons resulting in a characteristic spectral response of photon detection devices. To achieve efficient photon detection, the emission spectrum of the light source has to match the wavelength-dependent quantum efficiency of the employed photon detection device as closely as possible. The electrical signal directly produced by incident photons may be orders of magnitude too low in intensity to be detectable. Photon detection devices therefore rely on signal amplification techniques to amplify the primary charge signal to a detectable output signal. The built-in gain of photon detectors is defined as the ratio between the output charge signal of the photon detector



and the charge directly produced by incident photons. The achievable signal-to-noise ratio of photon detectors is determined by the amplitude of the produced signal and the sum of all contributions to the noise level. The total noise can be mainly separated into a constant readout noise contribution and a noise contribution which depends on the exposure time due to the presence of the so-called dark current. In imaging sensors such as CCD or CMOS sensors, the readout noise is a certain random contribution added during each readout cycle of a pixel. It depends on the readout speed of pixels, which is a compromise between the limit to the achievable frame rate at which an imaging sensor can be read out and the readout noise level. While the amplitude of the readout noise is independent of the charge collection time, the noise contribution due to the dark current of photon detectors depends on the exposure time. The dark current is a certain current flowing even in the absence of light mainly due to thermally produced charge carriers and is typically given in electrons per pixel per second. The dark current of imaging sensors can be significantly reduced by sensor cooling and high-performance CCD or CMOS sensors are typically cooled to minimise the dark current contribution to the noise. While the readout noise is typically the dominant noise contribution in the case of short exposure times, noise due to dark current becomes increasingly significant for longer exposure times.

Reading out scintillation light produced in gaseous radiation detectors with high sensitivity, PMTs can be used to collect quantitative information about the emitted light intensity. In addition, they can be used to detect primary scintillation due to the achievable single-photon efficiency and provide timing information with high resolution. In contrast, CCD and CMOS imaging sensors are well-suited to record integrated exposures of emitted secondary scintillation light. Their high granularity allows spatially resolved imaging with good spatial resolution and obtained images can be promptly displayed and used for further analysis without the need for extensive reconstruction algorithms.

### **3.2.1 PMTs**

Combining high gain and a fast response time, PMTs are highly sensitive and versatile photon detectors. They are based on the conversion of incident light to electrons at a photocathode by the photoelectric effect and the multiplication of the primary electrons by secondary emission processes at so-called dynodes. Typical PMTs consist of an evacuated glass tube containing a photocathode and an amplification structure consisting of several dynodes and an anode. The photocathode can be directly deposited on one side of the glass tube. The choice of the composition of this photocathode layer on the entrance window of the device determines the achievable quantum efficiency and the spectral response of a PMT. Photoelectrons produced at the photocathode as a result of incident light are emitted with low energies of several eV. The emitted primary electrons are amplified by a multi-stage multiplication structure taking advantage of secondary emission. In this process, secondary electrons are emitted when electrons of sufficient energy strike the dynodes. Optimised geometries of the dynodes in a PMT result in a maximised number of secondary particles being emitted for each incident electron as well as a high transfer efficiency between dynodes and multiplication of electrons in multiple stages is achieved. By biasing dynodes with increasingly positive voltages, electrons are accelerated from one dynode to the next and produce secondary particles upon impact after gaining sufficient energies from the electric field between dynodes. In a moderate number of amplification steps, this concept allows the achievement of high charge gains of several  $10^7$ . The resulting large number of electrons

is finally collected by an anode and used as output signal of a PMT. The components of a PMT and a typical gain over voltage curve are shown in figure 20.

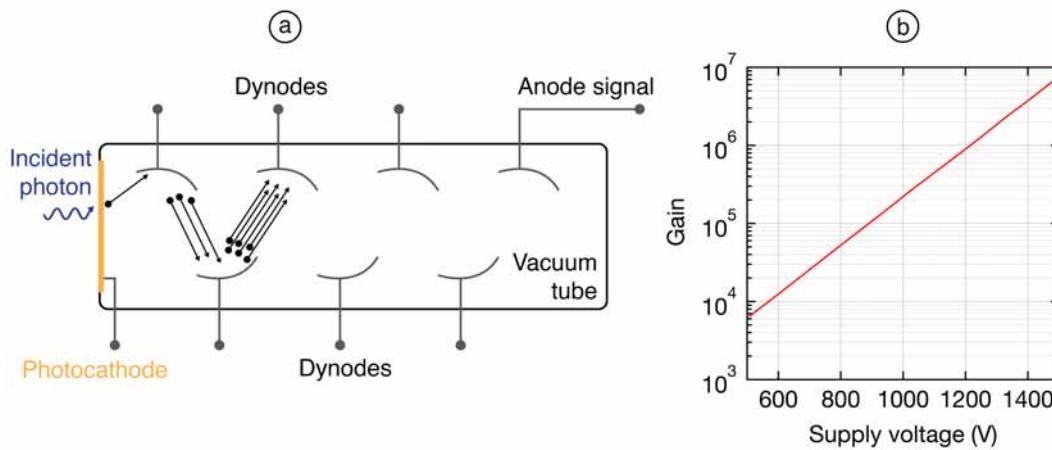


**Figure 20.** Photomultiplier tube: (a) Incident photons produce primary electrons at the photocathode of a PMT. Electrons are multiplied by a multi-dynode amplification structure housed in a vacuum tube before reaching the anode and generating a measurable anode signal. (b) Typical charge gain over supply voltage curve of Hamamatsu R375 2-inch PMT. Adapted from [61].

Even for individual incident photons, the produced output signals can be of significant amplitude and good signal-to-noise ratios are achieved. The sensitivity to single photons enables photon counting with PMTs. In addition, the fast movement of electrons in high electric fields results in a fast detector response and fast signal rise times. PMTs are therefore well-suited for timing applications and to provide trigger signals for slower detectors.

As high-sensitivity photon detectors, PMTs are widely used in particle physics, astronomy and medical imaging. Among numerous other uses, large-scale arrays of PMTs are employed in neutrino physics to detect Cherenkov radiation emitted by highly energetic charged leptons traversing large volumes instrumented by numerous PMTs [62]. In medical imaging, PMTs are used to record flashes of light from scintillators used to detect annihilation light during positron emission tomography.

### 3.2.2 CCD sensors

Imaging sensors based on CCD technology provide high-quality 2D images and are widely used for spatially resolved photon detection in industrial, medical and scientific applications. CCD technology relies on the movement of charge collected in an active region to digitisation electronics and provides an efficient way for reading out a large number of pixels with a limited number of digitisers. The concept of CCDs was introduced in 1969 [63, 64] and soon an experimental realisation demonstrated the applicability of the technology for shift registers and linear imaging devices [65]. Within a decade, CCD imaging sensors with hundreds of thousands of pixels were developed and CCD imaging sensors with several megapixels are readily available by now.

Each pixel in a CCD imaging sensor consists of an epitaxial layer of Si biased into the depletion region, which acts as photosensitive region. Incident photons result in the generation of electron-hole pairs in this region. An applied electric field separates electrons and holes and charge carriers are accumulated at the surfaces of the pixels. The maximum number of electrons which can be collected before thermal equilibrium is reached is called the well depth of the pixel and defines its dynamic range. After the desired exposure time, the

accumulated charge of each individual pixel is read out by a charge amplifier and digitised. The last pixel in a row is connected to a charge amplifier and transfers its charge to it for readout. Subsequently, the charge stored in each pixel is transferred to the neighbouring pixel by biasing gate electrodes in a certain sequence. This shift of the charge from one pixel to the next allows the step-wise readout of the charge of each individual pixel by a single charge amplifier and digitiser. By reading out all pixel in a row and all rows of a 2D CCD imaging sensor subsequently, a 2D image can be recorded with the intensity of each pixel being determined by the corresponding accumulated charge. The pixels and shift registers used for the readout of a CCD sensor are schematically shown in figure 21.

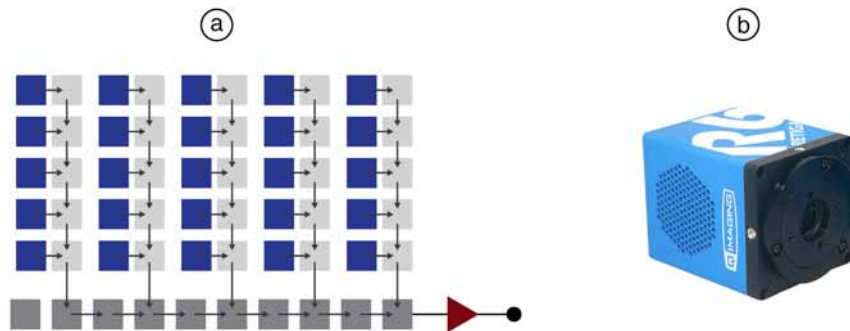


**Figure 21.** CCD imaging sensor: (a) Readout schematic of pixels (blue) of CCD imaging sensor. The electric charge collected within individual pixels is transferred along columns by vertical shift registers (grey) to a horizontal shift register (dark grey). Subsequently, the collected charge is transferred along the horizontal shift register, amplified (red) and digitised by a common analogue-to-digital converter. (b) Commercially available CCD camera. Image from [66].

The process of transferring accumulated charge from one pixel to the next and using only a small number of amplifiers and digitisers for charge readout results in significant times required for the readout of CCD sensors. As a result, the achievable frame rates of CCD sensors are limited and typically reach several tens of Hz. CCD imaging sensors can feature image intensifiers such as micro-channel plates in front of the pixels or electron amplification devices between the pixels and the digitiser to increase the sensitivity of the sensors and enable significantly lower exposure times. Offering high quantum efficiencies and a good linearity of the pixels, CCDs are widely used in professional applications requiring high-quality images. Astrophotography and imaging sensors used in telescopes rely heavily on CCD technology and CCD sensors have also been employed in nuclear physics experiments.

### 3.2.3 EMCCD sensors

In low-light conditions, Electron Multiplying CCD (EMCCD) imaging sensors may be used to achieve signal-to-noise ratios significantly higher than achievable with conventional CCD sensors. This variety of CCD sensors employs impact ionisation to amplify charges before digitisation in order to achieve outstanding sensitivities.

As in conventional CCD imaging sensors, a horizontal shift register collects charges from individual pixels and moves them to a single point of charge-to-voltage conversion and analogue-to-digital conversion. In the case of an EMCCD, however, an additional shift register operated at high voltages is situated between the horizontal shift register and the charge-to-voltage conversion circuit. In this additional shift register, electrons are multiplied

by impact ionisation. A schematic representation of an EMCCD imaging sensor is shown in figure 22.

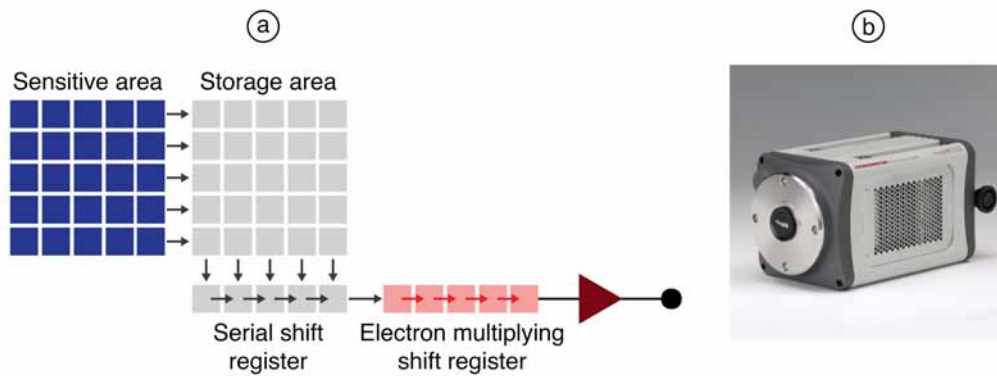


**Figure 22.** EMCCD imaging sensor: (a) Schematic of EMCCD imaging sensor. The charge collected in the active area (blue) is transferred to a storage area (grey). During readout, charges are moved to a serial shift register and amplified by impact ionisation while moving through an electron multiplying shift register (red) before being translated to a voltage. (b) Commercially available EMCCD camera. Image from [61].

Charge amplification by impact ionisation provides gain factors above  $10^3$  in EMCCD imaging sensors and permits imaging even in low-light conditions. The built-in amplification drastically decreases the significance of the read noise in EMCCD imaging sensors to typical values below one electron and permits high signal-to-noise ratios. As individual pixels in EMCCD imaging sensors are typically larger than in conventional CCD imaging sensors, the achievable image resolution of EMCCD cameras is limited.

### 3.2.4 CMOS sensors

In active-pixel sensors, each pixel consists of a photosensitive region and an active amplifier. Based on CMOS technology, this concept permits the construction of imaging sensors with pixels which feature low static power consumption and with low noise characteristics because the collected charge is amplified in each pixel before being moved through shift registers. Since each pixel contains a dedicated amplifier, CMOS sensors require much shorter readout times than passive-pixel sensors such as CCD sensors. This permits significantly higher frame rates and is well-suited for applications requiring fast image acquisition. CMOS sensors are widely used in consumer applications due to the lower manufacturing cost compared to CCD sensors.

The active pixels of CMOS imaging sensors typically consist of a photodiode and multiple transistors for charge readout and resetting of the photodiode. The photodiode is connected to the gate electrode of a source-follower readout transistor used to produce an output signal depending on the accumulated charge in the photodiode. A selection transistor is used to select individual rows during readout. After the readout, each pixel can be reset by applying a voltage to a reset transistor. In 2D active-pixel arrays as used in CMOS imaging sensors, the outputs of all pixels in a row are tied together, while the gates of the selection transistors of all pixels in a column are connected. During readout, a single row is selected and the outputs of all pixel in the row are read out simultaneously by dedicated readout circuitry for each column of pixels. After the readout of all pixels in a row, the pixels need to be reset. The gates of the reset transistors of all pixels in a row are tied together to enable the simultaneous resetting of all pixels in a row. A schematic of the pixels and the connection

lines and transistors used for pixel readout within a CMOS imaging sensor is shown in figure 23.

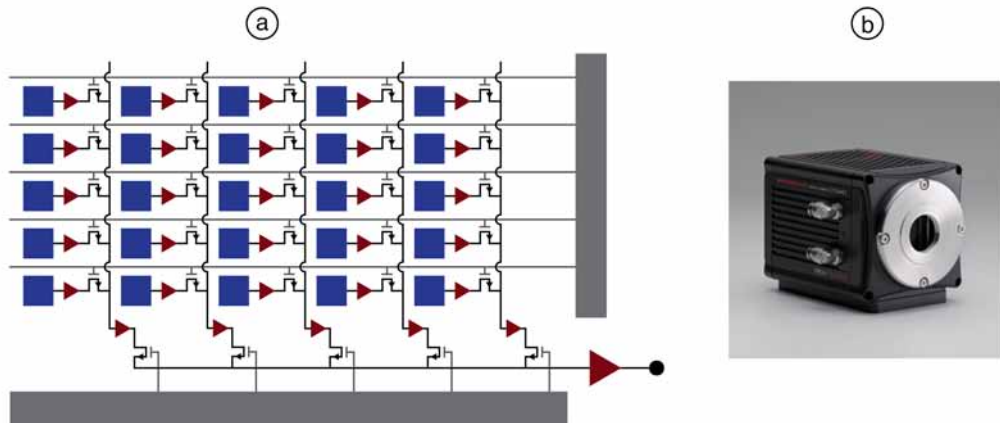


**Figure 23.** CMOS imaging sensor: (a) Readout schematic of pixels (blue) of CMOS imaging sensor. The collected charge is converted to a voltage within each pixel and pixels are read out by selecting a certain row by a transistor and reading out all columns within the selected row. (b) Commercially available scientific CMOS camera. Image from [61].

As the rows of a CMOS sensor are typically read out sequentially, not all pixels of the sensor are exposed simultaneously. This results in a so-called rolling shutter effect. While one pixel row is being read out, other rows are being exposed. After the readout of a row, the next row is read out and the previously read out one may again be exposed. This can lead to distortions and skewed images when imaging moving objects. Additional transistors for each pixel may be used to implement global shutters where the exposure of all pixels in a CMOS sensor happens simultaneously while compromising frame rate capabilities. Alternatively, a global reset of all pixels of an imaging sensor before exposure may be used to minimise the exposure time difference between individual rows of pixels.

### 3.2.5 Comparison of sensitivity of imaging sensors

The different properties of CCD, CMOS and EMCCD imaging sensors may make a certain technology well-suited for a specific application while other use cases may require differing sets of features. In many low-light applications or in quantitative imaging, the achievable signal-to-noise ratio is an important figure of merit. To compare the achievable signal-to-noise ratio in low-light imaging conditions, a quad-GEM detector was used to detect low-energy X-ray photons from an  $^{55}\text{Fe}$  source and the secondary scintillation light produced during electron avalanche multiplication was recorded with different types of cameras facing the bottom electrode of the last GEM of the multiplication stage. A comparison of optically read out images of the secondary scintillation light produced in a GEM-based detector under X-ray irradiation recorded with CCD (QImaging Retiga R6 [66]), CMOS (Hamamatsu ORCA-Flash4.0 V3 C13440-20CU [61]) and EMCCD (Hamamatsu Imagem X2 C9100-23B [61]) cameras is shown in figure 24a.

As the pixel size of CCD and CMOS cameras was significantly smaller than the one of the EMCCD camera, 4x4 pixel binning was used with the CCD and CMOS imaging sensors. This resulted in the effective pixel size and the resolution of the recorded images being approximately equal for the three investigated camera types. The exposure of each frame was chosen to be below 20 ms for all three cameras.

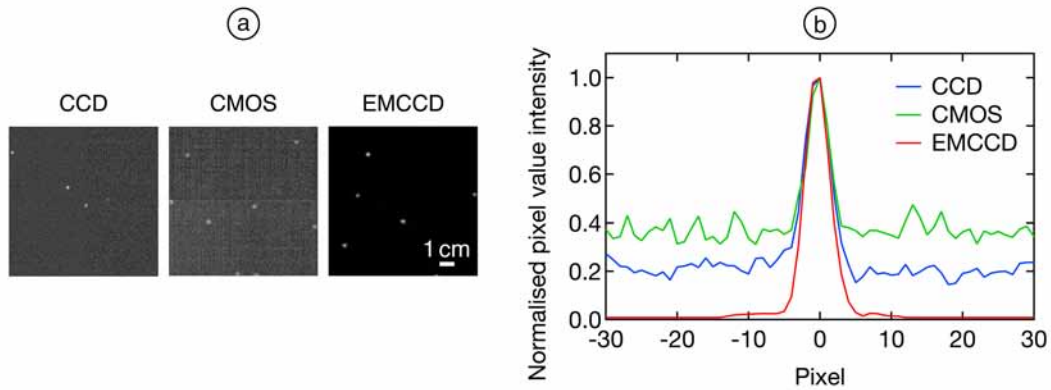


**Figure 24.** Comparison of signal-to-noise ratio with CCD, CMOS and EMCCD cameras: (a) Secondary scintillation light produced in a quad-GEM detector under irradiation with low-energy X-ray photons was optically read out by CCD, CMOS and EMCCD imaging sensors. The brightness scale of each individual image ranged from the minimum to the maximum pixel value intensity in each image. (b) Comparing line profiles of the pixel value intensity of individual signal spots normalised to the maximum pixel value intensity as recorded by the CCD, CMOS and EMCCD imaging sensors shows the significantly lower noise level in the images recorded by the EMCCD imaging sensor.

The signal-to-noise ratio was determined by dividing the averaged maximum pixel brightness above the background level by the standard deviation of the background of the images. In the case of the CCD imaging sensor, a signal-to-noise ratio of about 14 could be achieved. Due to the realisation of binning in the CMOS sensor, a slightly lower signal-to-noise ratio of about 12 could be obtained with the CMOS camera. In the case of the EMCCD camera, a high signal-to-noise ratio of more than 600 could be obtained due to the minimisation of the significance of the read noise by the charge amplification by impact ionisation. The significantly lower relative noise level in the images acquired by the EMCCD imaging sensor in comparison to images acquired by CCD or CMOS imaging sensors is shown in the normalised line profiles of the pixel value intensity of individual signal spots in figure 24b. The EMCCD camera is therefore well-suited for low-light applications requiring high signal-to-noise ratios.

### 3.3 Optically read out detector applications

Optically read out radiation detectors have been employed in a variety of research fields and have been used to meet stringent spatial resolution requirements for decades. Early particle detector concepts such as bubble chambers [67] already used 2D imaging for reading out images of events in the active volume, although they did not rely on the emission of scintillation light but rather recorded microscopic bubbles formed in a superheated liquid when particles traversed and ionised the active medium. Applications of optical readout can be separated into two main categories: highly sensitive photon detection with single-photon sensitivity to detect small signals and spatially resolved photon detection for 2D imaging applications.

The sensitivity of photon detectors such as PMTs to individual photons is used for the detection of low-intensity signals. In the field of neutrino physics, PMTs are used in large-scale detectors with massive active material volumes to detect Cherenkov photons emitted by traversing and interacting particles. PMT-based photon detector modules are used in laboratories such as the IceCube neutrino observatory to instrument large volumes in order

to maximise detection efficiency and probability [62]. Similarly, the Super-Kamiokande neutrino observatory also relies on PMTs for detecting Cherenkov photons with high sensitivity [68]. Arrays of PMTs are also widely used for the readout of TPCs such as Xe-based TPCs used in dark matter experiments like the XENON100 experiment [69]. The excellent sensitivity and time resolution of these photon detectors are used to obtain information about particle drift times and the proportionality of the output signals on the incident intensity of charge is used to extract energy information. While PMTs are ideally suited for low-light applications, they cannot be used for spatially resolved photon detection with high granularity. The use of multiple PMTs arranged in an array can be used to obtain information about the position of incident light but even when employing a centre of gravity algorithm taking advantage of light shared across several PMTs the achievable spatial resolution remains on the scale of millimetres [70].

Detector applications which require excellent spatial resolution with relaxed requirements on photon detection sensitivity can make use of imaging sensors such as CCD or CMOS sensors. Technological advances in semiconductor manufacturing have led to the development of imaging sensors which provide a high number of pixels with low noise characteristics. The low cost per readout channel and the ease of obtaining intuitive visual representations of events of interest make the use of imaging sensors an attractive readout approach for radiation detectors. Recording 2D projections of nuclear recoil events, CCD imaging sensors are at the core of the detection concept of the DMTPC detector, which employs a low-pressure TPC for directional dark matter search [71]. Optically read out TPCs are also used for spectroscopic studies [72] and take advantage of the good spatial resolution provided by imaging sensors. Imaging sensors are also used in astrophysics for photometry applications [73] and for the counting of astronomical objects [74]. The above-mentioned experiments are examples of implementations of detectors relying on photon detection devices which demonstrate the versatility and universality of the approach of the optical readout of radiation detectors.





## CHAPTER 4

# Scintillation studies

Strong secondary scintillation light emission and a scintillation light emission spectrum which is well matched to the quantum efficiency of employed photon detection devices are important aspects determining the achievable image quality in optically read out GEM-based detectors. While many gas mixtures feature scintillation light emission in the UV wavelength range, state-of-the-art imaging sensors are typically optimised for photon detection in the VIS wavelength range. The use of gas mixtures containing  $\text{CF}_4$  permits scintillation light emission in the VIS wavelength range and therefore eliminates the need for wavelength-shifting components or admixtures. The gas composition and operating conditions such as pressure and GEM gain have to be well understood and controlled in order to maximise the intensity of scintillation light recorded by photon detectors used for optical readout.

### 4.1 Secondary scintillation spectra

Secondary scintillation light emission spectra of different gas mixtures were recorded in the UV and VIS wavelength ranges. A detector based on a triple-GEM stack in an UltraHigh-Vacuum-grade (UHV-grade) vessel was operated under X-ray irradiation from an X-ray tube outside of the vessel and the emitted secondary scintillation light was recorded by a spectrometer. The triple-GEM was coupled to a 10 cm long drift volume with a diameter of 10 cm formed by ring-shaped field shaper electrodes used to define a uniform drift field along the length of the conversion volume. X-rays were generated by an X-ray tube with a Ag target located in the axis of the field shaper opposite to the triple-GEM stack and introduced into the detector vessel through a thin metallic window with a diameter of 2 mm. The secondary scintillation light emitted by the GEM was collected by a collimating lens with a diameter of 5 mm located in the gas volume of the detector about 5 mm from the bottom electrode of the third GEM in the stack. The light collected by the lens was guided to an optical fibre-feedthrough by a vacuum-compatible multi-mode optical fibre with a core diameter of 600  $\mu\text{m}$  and a length of about 15 cm. On the outside of the detector vessel, another multi-mode optical fibre with the same core diameter and a length of 1 m guided collected light to a spectrometer. The setup used for recording secondary scintillation spectra is schematically shown in figure 25.

A fused-silica collimating lens suited for a wavelength range from 200 nm to 2000 nm was used. Multi-mode optical fibres with a core thickness of 600  $\mu\text{m}$  compatible with wavelengths from 180 nm to 1150 nm were employed. The fibre on the outside of the detector vessel was covered with black tape to eliminate the leakage of ambient light into the fibre.

A CCD-based compact UV-VIS spectrometer (Ocean Optics FLAME-S-UV-VIS-ES [75]) with a wavelength resolution of better than 0.5 nm and a corrected linearity of better than

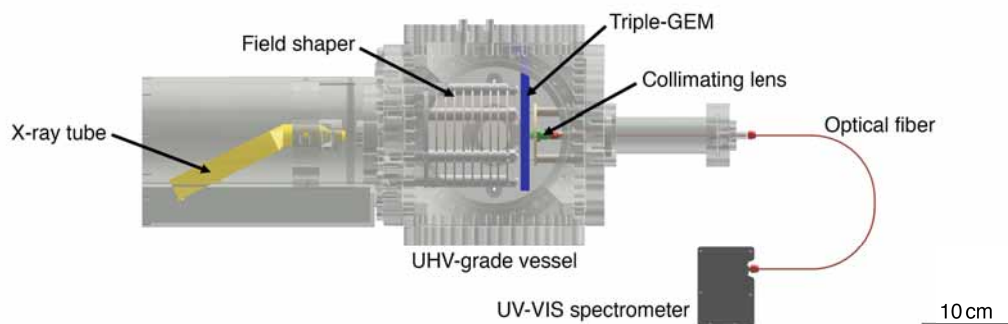


**Figure 25.** Spectroscopy setup: A triple-GEM stack (blue) coupled to a field shaper was integrated in a UHV-grade vessel. An X-ray tube (yellow) with a Ag target was used to irradiate the detector through a thin metallic window and a semi-transparent mesh-cathode. Secondary scintillation light emitted by the triple-GEM was collected with a collimating lens (green) and guided by optical fibres (red) to a UV-VIS spectrometer (dark grey).

99 % was used to record secondary scintillation light spectra. The spectrometer could measure in a wavelength range from 178 nm to 870 and was directly coupled to an optical fibre with SMA-type connectors and featured exchangeable entrance slits to define the light collection and achievable wavelength resolution. The narrowest available entrance slit with a width of 25  $\mu\text{m}$  was chosen for all measurements as it permitted the highest wavelength resolution and the available secondary scintillation light intensity was sufficient.

Secondary scintillation spectra were recorded with a constant exposure time of 10 s. At least 10 individual exposures per measurement point were recorded and averaged. In addition, at least 10 background exposures without the presence of secondary scintillation light were recorded to obtain averaged background information. For each measurement, the averaged background was subtracted from the averaged scintillation light spectrum to obtain an offset-corrected spectrum. The voltage drop across the last GEM and the X-ray tube current were adjusted for each gas mixture to mitigate saturation of the spectrometer.

While the response of the UV-VIS spectrometer was calibrated in wavelength, the response to the light intensity across the accessible range of wavelengths was not. Therefore, the spectroscopy setup was calibrated with a deuterium-halogen absolute irradiance calibration light source. With the spectrometer connected to the fibre-feedthrough by an optical fibre and the collimating lens connected to the other side of the fibre-feedthrough with the shorter vacuum-compatible fibre, the deuterium and halogen lamps of the calibration light source were operated individually and the uncalibrated response of the spectrometer to the two lamps was recorded. From the recorded response and the reference irradiance data of the two lamps, calibration curves were calculated for the UV and VIS ranges and combined to an irradiance calibration of the spectroscopy setup for the full accessible wavelength range. Calibrated secondary scintillation spectra were obtained by multiplying the acquired raw spectra after averaging and background-subtraction with the determined irradiance calibration curve.

The gas composition during measurements was monitored with a Residual Gas Analyser (RGA) sampling the gas in the detector chamber through a small orifice realised by a leak valve as described in section A.6. The RGA was operated at a pressure of about  $5 \cdot 10^{-6}$  mbar. The response of the RGA sampling setup to different gas species was investigated and corrected for as described in A.6. As large systematic errors are expected in the calibration of the RGA response to different gas species and consequently in the gas

composition measurements, the measured fractions of different gas species present only qualitative indications of the investigated gas compositions.

#### 4.1.1 Scintillation of Ar

The emission spectrum of the secondary scintillation light produced by a triple-GEM detector operated in Ar was measured. The recorded scintillation spectrum and the effect of different fractions of CO<sub>2</sub> in the gas on the scintillation spectrum is shown in figure 26. To maximise scintillation light intensity, the triple-GEM stack was operated at a high gain with a voltage drop of 400 V across each one of the first two GEMs in the stack and a voltage drop of 420 V across the third GEM. The X-ray tube irradiating the detector was operated with an acceleration voltage of 20 kV and a current of 200  $\mu$ A. All shown spectra were recorded with the same configuration.

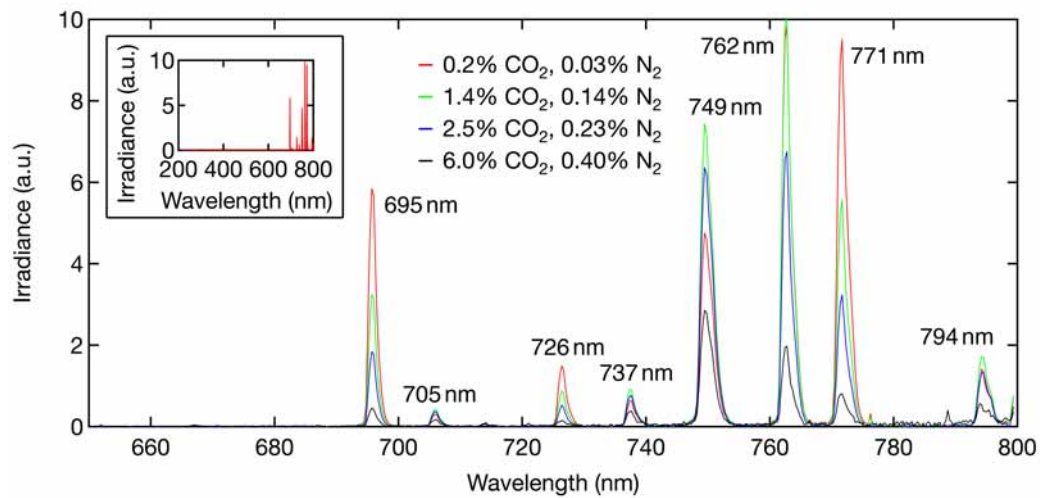


**Figure 26.** Secondary scintillation spectrum of Ar: The monatomic nature of Ar results in sharp emission lines above 695 nm. The relative intensity of emission lines changes with varying CO<sub>2</sub> content. Inset: No significant emission between 200 nm and 695 nm was observed.

In pure Ar gas, no strong secondary scintillation light emission was observed between 200 nm and 695 nm. While Ar features multiple emission lines in the UV wavelength range below 200 nm [76], this range was not accessible with the employed spectrometry setup. As described in section 3.1.1, sharp emission peaks attributed to transitions between different excited states of Ar are observed between 695 nm and 794 nm. The relative intensity of the peaks at 695 nm, 705 nm, 726 nm, 737 nm, 749 nm, 762 nm, 771 nm and 794 nm changes with different fractions of CO<sub>2</sub> and N<sub>2</sub>.

#### 4.1.2 Scintillation of CF<sub>4</sub>

The emission spectrum of a triple-GEM operated in an almost pure CF<sub>4</sub> environment is shown in figure 27. The gas contained small fractions of Ar and N<sub>2</sub> of about 0.5 % each. A high voltage drop of 500 V across each GEM in the triple-GEM stack was chosen to achieve recordable scintillation light intensity. The X-ray tube was operated with an acceleration voltage of 20 kV and a current of 200  $\mu$ A. The achievable gain of the GEM operated in an almost pure quenching gas atmosphere was rather low and resulted in a low scintillation light intensity. The significant noise levels in the UV and NIR wavelength ranges are attributed to the low recorded light intensity.

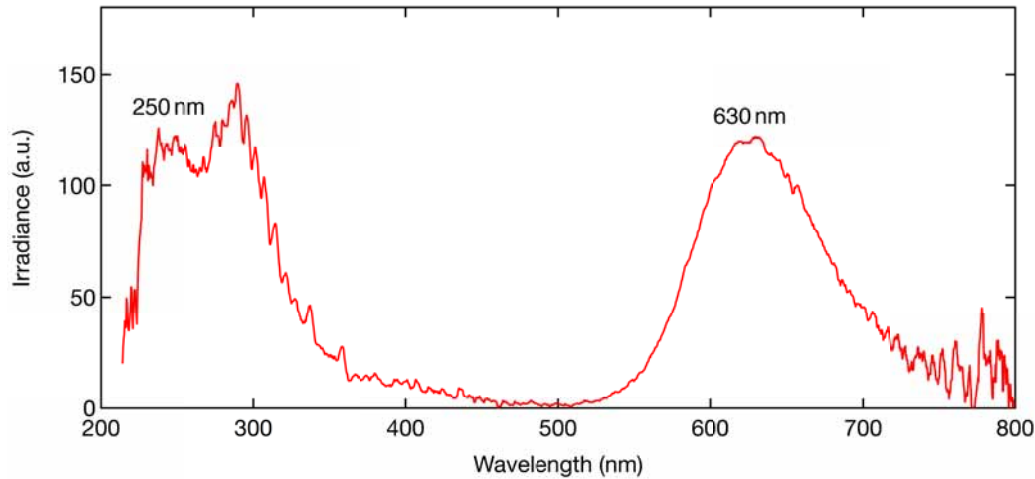


**Figure 27.** Secondary scintillation spectrum of  $\text{CF}_4$ : Secondary scintillation from  $\text{CF}_4$  is characterised by broad emission bands in the UV and VIS ranges focused around wavelengths of 250 nm and 630 nm, respectively. The significant noise level in the recorded spectrum is attributed to the low achievable GEM gain and the resulting low absolute scintillation intensity.

Broad emission bands in the UV and VIS ranges are characteristic for the secondary scintillation light emission of  $\text{CF}_4$ . For the case of almost pure  $\text{CF}_4$ , the maximum intensity of the UV and VIS emission peaks is approximately equal. The VIS emission band peaks at a wavelength of about 630 nm. The double peak structure of the UV emission band was only observed for almost pure  $\text{CF}_4$  and could not be observed in mixtures with higher fractions of Ar. A more detailed description of the scintillation mechanisms leading to the emission spectrum of  $\text{CF}_4$  can be found in section 3.1.1.

### 4.1.3 Scintillation of Ar/ $\text{CF}_4$ gas mixtures

Gas mixtures of Ar and  $\text{CF}_4$  provide stable detector operation conditions with high charge gain values due to  $\text{CF}_4$  acting as a quencher in the mixtures combined with strong UV and VIS emission bands well-suited for optical readout. Secondary scintillation spectra of Ar/ $\text{CF}_4$  gas mixtures with different fractions of  $\text{CF}_4$  are shown in figure 28. The spectra were recorded under X-ray irradiation with an X-ray tube operated with an acceleration voltage of 20 kV and a current of 200  $\mu\text{A}$ . The intensity in the shown spectra is normalised with respect to the amplitude of the peak of the VIS scintillation band at 630 nm.

The scintillation spectra of Ar/ $\text{CF}_4$  gas mixtures in the wavelength range of 200 nm to 800 nm display the combined scintillation properties of Ar and  $\text{CF}_4$ . Strong UV and VIS scintillation bands are attributed to  $\text{CF}_4$  scintillation, while sharp emission lines above 695 nm as shown in the inset in figure 28 are attributed to transitions between different excited states in Ar atoms.

As previously reported, the relative intensity of the sharp Ar emission lines increases with increasing Ar fractions [77, 50]. For mixtures with 5%  $\text{CF}_4$ , the intensity of the main emission lines at 749 nm and 762 nm is significantly higher than the intensity of the VIS emission band. For mixtures with a higher  $\text{CF}_4$  fraction of 20%, the intensity of the strongest Ar emission line at 749 nm is comparable to the peak intensity of the VIS scintillation band.

While the intensity of the UV and VIS emission bands is almost equal for the case of pure  $\text{CF}_4$  as shown in section 4.1.2, the intensity of the UV emission band is significantly lower than the intensity of the VIS emission band in Ar/ $\text{CF}_4$  gas mixtures. With increasing

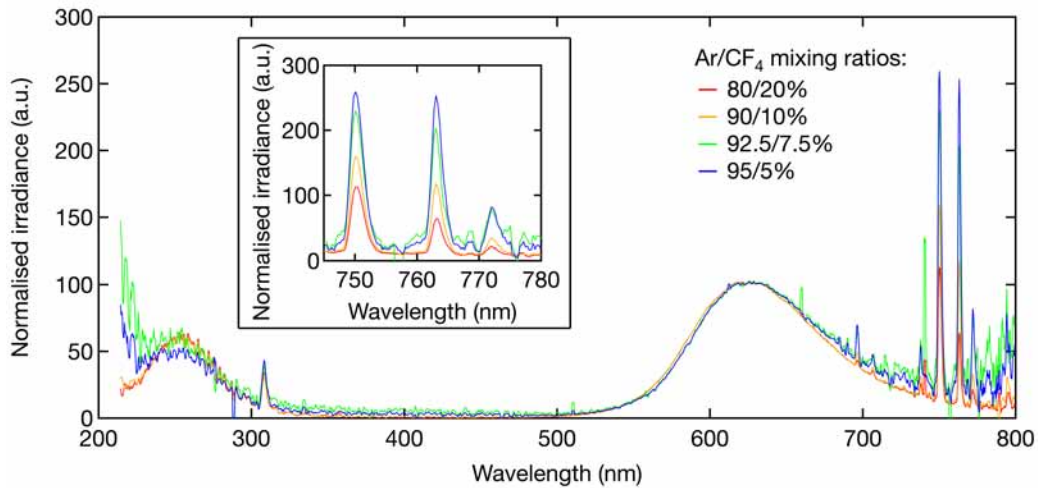


**Figure 28.** Secondary scintillation spectrum of Ar/CF<sub>4</sub> mixtures: CF<sub>4</sub> scintillation emission contributes broad emission bands in the UV and VIS wavelength ranges. Inset: The intensity of the sharp Ar scintillation lines at wavelengths above 695 nm increases relative to the intensity of the CF<sub>4</sub> emission bands with increasing fractions of Ar in the mixtures. Intensity normalised to amplitude of peak at 630 nm.

CF<sub>4</sub> fractions, the relative intensity of the UV emission band with respect to the VIS emission band increases. The double peak structure of the UV emission band observed in pure CF<sub>4</sub> was not present in emission spectra of Ar/CF<sub>4</sub> gas mixtures. The small peak in the emission spectra at around 310 nm is attributed to OH<sup>-</sup> emission from the dissociative excitation of water vapour in the gas mixture [50].

The observed secondary scintillation spectra of Ar/CF<sub>4</sub> gas mixtures as well as the dependence of the amplitude of the sharp emission lines on the Ar content agree well with previously reported measurements [50].

Scintillation light spectra of Ar/CF<sub>4</sub> gas mixtures with 20% of CF<sub>4</sub> at different pressures between 700 mbar and 1000 mbar are shown in figure 29.

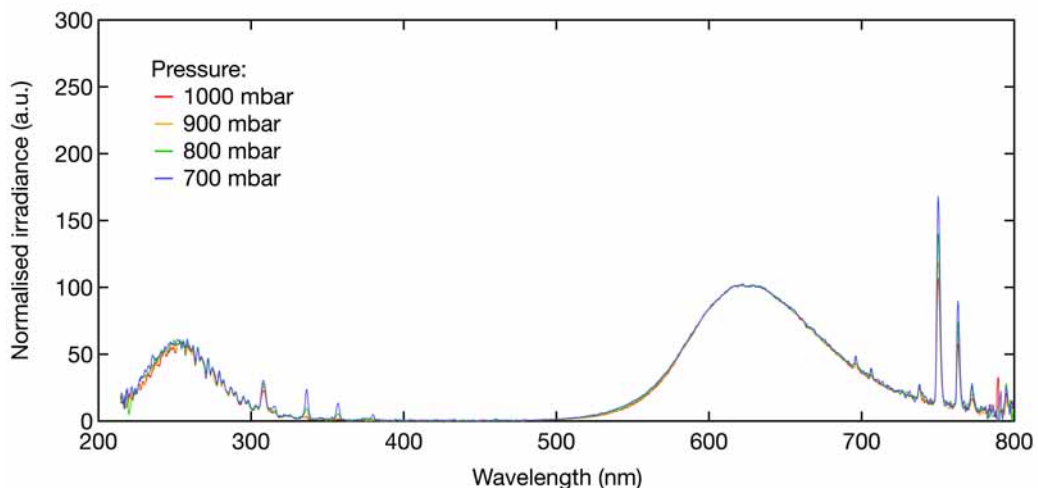


**Figure 29.** Secondary scintillation spectrum of Ar/CF<sub>4</sub> mixtures at different pressures: The position of emission bands and peaks is not modified by pressure variations between 700 mbar and 1000 mbar. Intensity normalised to amplitude of peak at 630 nm.

No clear modifications of the scintillation spectra at different pressures were observed over the covered range of pressures. The slight modifications of the intensity of the Ar emis-

sion lines are attributed to slight changes in the fraction of  $\text{CF}_4$  in the mixtures. The intensity in the shown spectra is normalised with respect to the amplitude of the peak of the VIS scintillation band at 630 nm.

The effect of  $\text{N}_2$  on the scintillation light spectrum of an  $\text{Ar}/\text{CF}_4$  gas mixture with 20 % of  $\text{CF}_4$  is shown in figure 30.

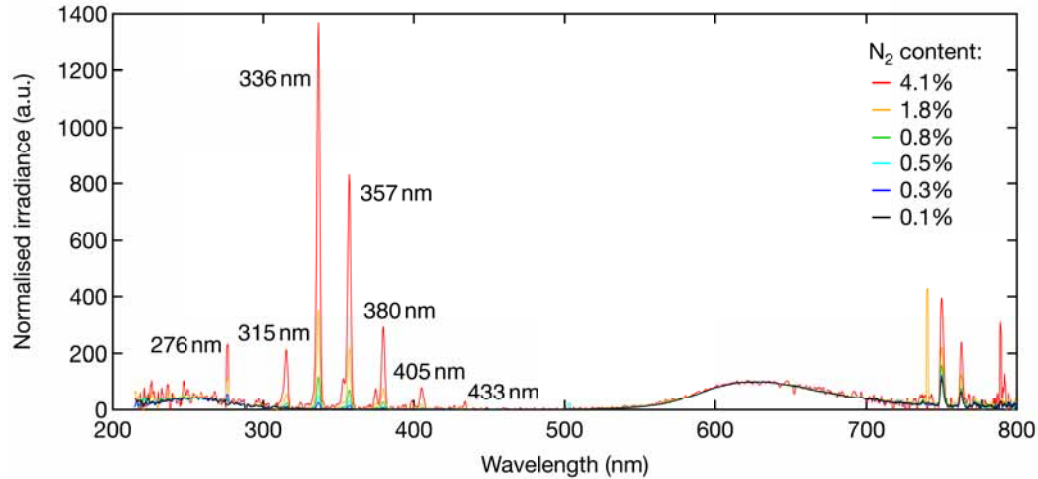


**Figure 30.** Secondary scintillation spectrum of  $\text{Ar}/\text{CF}_4$  with admixtures of  $\text{N}_2$ : The broad emission bands and Ar emission lines of an  $\text{Ar}/\text{CF}_4$  mixture with a mixing ratio of 80/20% are not modified by admixtures of  $\text{N}_2$ . Increasing fractions of  $\text{N}_2$  lead to the appearance of  $\text{N}_2$  emission lines. Intensity normalised to amplitude of peak at 630 nm.

In addition to the UV and VIS emission bands of  $\text{CF}_4$  and the Ar emission lines, sharp  $\text{N}_2$  emission lines in the UV and low-wavelength VIS ranges are observed when  $\text{N}_2$  is present in gas mixtures. Emission peaks at 276 nm, 315 nm, 336 nm, 357 nm, 380 nm, 405 nm and 433 nm are observed with the maximum intensity at 336 nm. These emission lines of  $\text{N}_2$  are attributed to transitions between different energetic states in the electronic-vibrational band systems of  $\text{N}_2$  or  $\text{N}_2^+$  [78].

With increasing  $\text{N}_2$  fractions, the relative amplitudes of the  $\text{N}_2$  emission peaks with respect to the amplitude of the VIS emission band at 630 nm increase significantly. For  $\text{N}_2$  fractions above approximately 1 %, the amplitudes of some  $\text{N}_2$  emission lines surpass the amplitude of the VIS scintillation band of  $\text{CF}_4$ .

#### 4.1.4 Scintillation of $\text{He}/\text{CF}_4$ gas mixtures

The spectra of the secondary scintillation light emitted from a triple-GEM stack operated in  $\text{He}/\text{CF}_4$  gas mixtures with different mixing ratios were recorded. The low density of He makes it an attractive gas choice for detector applications such as beam monitoring, which require a minimisation of the material budget. The GEM was operated at a high gain with voltage drops of about 380 V across each one of the first two GEMs in the stack and a voltage drop of 350 V across the last GEM in the stack. The emission spectra under irradiation with an X-ray tube operated with an acceleration voltage of 20 kV and a current of 100  $\mu\text{A}$  were recorded. To compare emission spectra with different mixing ratios, the intensity was normalised to the peak amplitude of the VIS  $\text{CF}_4$  scintillation band at 630 nm. Secondary scintillation emission spectra of  $\text{He}/\text{CF}_4$  gas mixtures with mixing ratios of 80/20% and 60/40% are shown in figure 31. The investigated mixing ratios were chosen to enable a comparison with previously reported measurements.

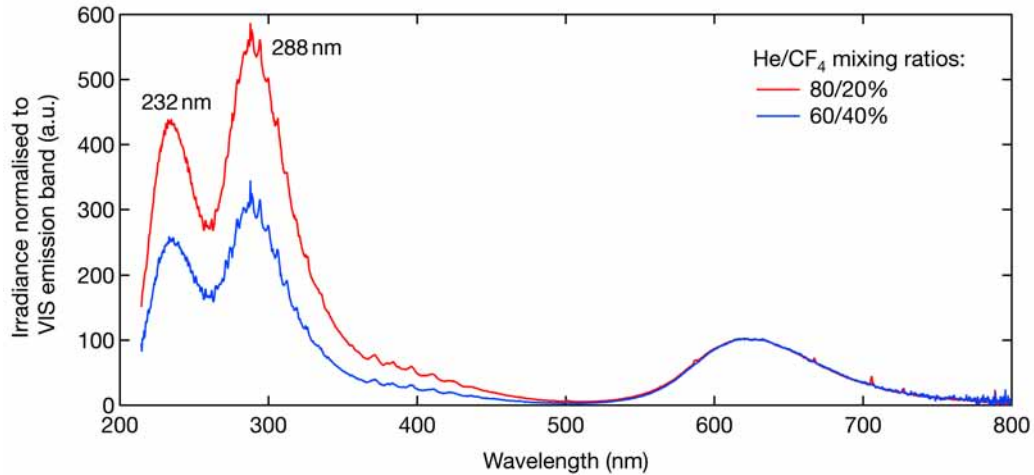


**Figure 31.** Secondary scintillation spectrum of He/CF<sub>4</sub> mixtures: The emission spectrum of He/CF<sub>4</sub> mixtures features two pronounced emission peaks in the UV and a broad VIS emission band. The shown emission spectra with He/CF<sub>4</sub> mixing ratios of 80/20% and 60/40% are normalised to the amplitude of the VIS emission band at 630 nm. The UV emission peaks are more pronounced relative to the VIS emission band for the mixture with a higher fraction of He.

While broad scintillation bands in the UV and VIS wavelength ranges attributed to CF<sub>4</sub> scintillation were observed as in the case of Ar/CF<sub>4</sub> gas mixtures, no sharp emission lines were observed in He/CF<sub>4</sub> gas mixtures with different mixing ratios.

The observed secondary scintillation emission spectrum of an He/CF<sub>4</sub> gas mixture with a mixing ratio of 60/40% agrees well with a previously reported scintillation spectrum of this gas mixture [50], although the peaks in the UV range at 232 nm and 288 nm appear more clearly separated in the measurement shown in figure 31 and the observed ratio between the two peaks is different.

#### 4.1.5 Scintillation of Ne/CF<sub>4</sub> gas mixtures

The spectrum of the secondary scintillation light emitted from a triple-GEM stack operated in a Ne/CF<sub>4</sub> gas mixture with a mixing ratio of 80/20% was recorded. The Ne-based gas mixture provides a high charge gain even at low GEM voltages. The triple-GEM stack was operated at a high charge gain with voltage drops of about 380 V across each one of the first two GEMs in the stack and a voltage drop of 250 V across the last GEM in the stack. The emission spectrum under X-ray irradiation from an X-ray tube operated with an acceleration voltage of 20 kV and a current of 20 μA was recorded. The secondary scintillation spectrum is shown in figure 32.

In addition to the wide CF<sub>4</sub> emission bands in the UV and VIS ranges, the scintillation spectrum of the Ne/CF<sub>4</sub> gas mixture features strong emission lines at 585 nm, 640 nm and 703 nm along with other less pronounced emission peaks, which agrees well with the expected emission spectrum of Ne [79]. As in the observed emission spectra of Ar/CF<sub>4</sub> gas mixtures, the broad emission bands in the UV and VIS wavelength ranges are attributed to CF<sub>4</sub> scintillation and the sharp emission lines are attributed to transitions between different excited states in Ne atoms. The dominant line at 585 nm surpasses the intensity of all other emission lines and bands by more than a factor of four.

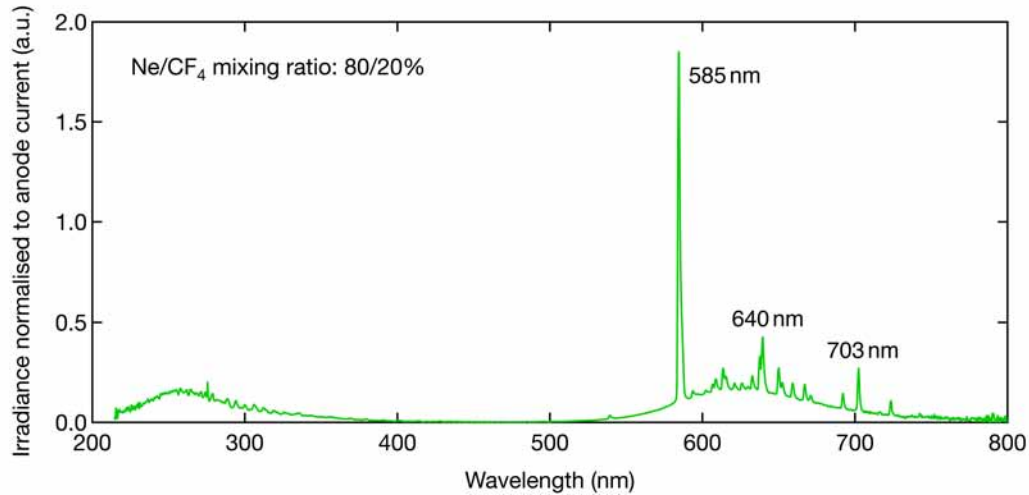


**Figure 32.** Secondary scintillation spectrum of Ne/CF<sub>4</sub>: The emission spectrum of a Ne/CF<sub>4</sub> gas mixture with a mixing ratio of 80/20% features pronounced emission bands in the UV and VIS wavelength ranges and strong emission lines in the VIS wavelength range. The dominant emission lines are at 585 nm, 640 nm and 703 nm.

## 4.2 Light yield

The intensity of the secondary scintillation light emission can be expressed as the light yield  $y_L$ . This number, which can be used to compare the scintillation light emission of different gas mixtures or operating conditions, is defined as the ratio of the number of emitted scintillation photons,  $N_{ph}$ , and the number of secondary electrons produced during electron avalanche multiplication,  $N_e$ , as

$$y_L = \frac{N_{ph}}{N_e} \quad (4.1)$$

The light yield is in units of emitted photons per secondary electron (ph/e<sup>-</sup>). A possibly high light yield enables maximum signal-to-noise ratios in optically read out images. Thus, an optimisation of the operating conditions of optically read out GEM-based detectors for maximum light yield is desirable.

The secondary scintillation light yield was measured by dividing the number of secondary scintillation photons emitted by the third GEM in a triple-GEM stack by the number of secondary electrons produced in the third GEM of the stack. X-rays with a well-defined energy spectrum from an <sup>55</sup>Fe source with an activity of about 1 GBq were introduced into the detector vessel through a thin metallic window. The X-ray source was located in the axis of the field shaper facing the cathode of the detector. Secondary scintillation light was recorded with a 2-inch PMT (Hamamatsu R375 [61]) located on the opposite side of the triple-GEM stack facing the bottom electrode of the third GEM in the triple-GEM stack. The PMT was located outside of the detector vessel behind a deep-UV-grade fused silica viewport in a light shielding tube. The setup for light yield measurements is schematically shown in figure 33.

A shutter between the <sup>55</sup>Fe source and the X-ray window of the detector vessel made of a Cu plate with a 5 mm diameter hole controlled by a linear actuator was used to control the presence of X-rays in the chamber.

The number of secondary electrons produced in the last GEM of the triple-GEM stack was determined by measuring the current on the bottom electrode of the third GEM. The top electrode of the third GEM was grounded and the bottom electrode was powered with



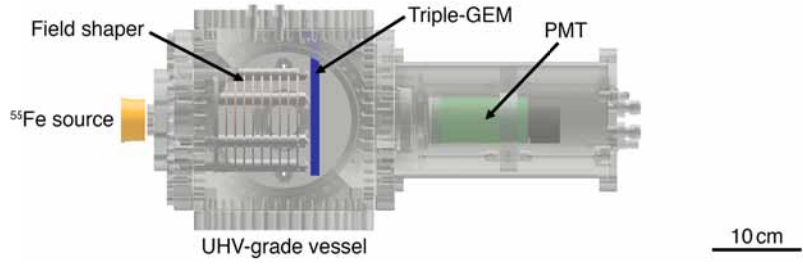


**Figure 33.** Light yield measurement setup: A triple-GEM stack (blue) coupled to a field shaper was integrated in a UHV-grade vessel. X-rays with a well-defined energy spectrum from an  $^{55}\text{Fe}$  source (yellow) were introduced into the chamber through a thin metallic window. Secondary scintillation light emitted by the triple-GEM was measured by a PMT (green) located outside of the detector vessel in a light-shielding tube.

a dedicated power supply channel with a sensitive ammeter and a large resistance on the order of  $1\text{ G}\Omega$  in series. As no anode electrode for charge collection was placed below the triple-GEM stack, all secondary electrons were collected on the bottom electrode of the third GEM and recorded by the ammeter. For each individual measurement point, two current measurements with and without X-rays present in the detector were taken and the difference between these two measurements was recorded as the current due to secondary electrons.

The rate of interactions was determined from recorded PMT signals. With the  $1\text{ GBq }^{55}\text{Fe}$  source placed outside of the detector vessel in the shown configuration, a rate of about  $300\text{ Hz}$  was achieved. The low rate is due to the small size and resulting low geometric acceptance of the thin metallic X-ray window with a diameter of  $2\text{ mm}$  and its attenuation effect and the interaction of X-ray photons in the region between the X-ray window and the cathode of the detector, which is not part of the active volume of the detector.

With the known number of primary electrons of about 220 produced by X-ray photons with an energy of  $5.9\text{ keV}$  from an  $^{55}\text{Fe}$  source interacting in the investigated gas mixtures, the total effective gain of the triple-GEM detector in a certain operating condition could be determined from the measured current and the determined rate of interactions. The total effective gain of the triple-GEM stack was divided by the gain of a single GEM in a given operating condition, which was determined as described in section A.2, to obtain the effective gain of the first two GEMs in the triple-GEM stack. The effective gain of the first two GEMs was then multiplied by the known number of primary electrons of 220 to obtain the number of electrons after the first two multiplication stages,  $n_{e,\text{GEM}1,2}$ . The number of secondary electrons generated during electron avalanche multiplication in the third GEM,  $n_{e,\text{GEM}3}$ , was subsequently determined by the expression  $n_{e,\text{GEM}3} = (G_{\text{GEM}3} - 1) n_{e,\text{GEM}1,2}$ , with the gain of the third GEM,  $G_{\text{GEM}3}$ . Therefore, the number of produced scintillation photons could be normalised to the number of secondary electrons produced in the third GEM, corresponding to the number of ionisation processes occurring during electron avalanche multiplication in the third GEM.

The total number of emitted secondary scintillation photons was extracted from PMT signals. At least  $2 \cdot 10^4$  light pulses were recorded by the PMT for each measurement point. The integrated intensities of the pulses were used to build up an energy spectrum of the recorded signals displaying the typical double-peak structure of the  $^{55}\text{Fe}$  source. The peaks in the spectra were fitted with Gaussian functions and the intensity corresponding to the full energy peak in the  $^{55}\text{Fe}$  energy spectrum was used to determine the emitted

scintillation light intensity. The number of emitted photons was then determined by dividing the intensity corresponding to the full energy peak by the integrated intensity of a single photon event registered by the PMT. The single photon response of the PMT at a certain gain was determined by pulsing a Light Emitting Diode (LED) in the light shielding tube containing the PMT with a pulse generator. Short pulses with amplitudes barely above the threshold for light emission from the LED were used to enable the recording of single photon events by the PMT and determine the integrated PMT signal intensity corresponding to a single detected photon as described in section A.5. The number of emitted scintillation photons was then calculated from the number of photons detected by the PMT by taking into account the geometric acceptance factor of about  $8 \times 10^{-3}$  for the detection of photons emitted from the third GEM in the stack by the PMT and the detection efficiency. The geometric acceptance factor was calculated by ray tracing simulations (F. Resnati) in COMSOL [80] as described in section A.3. The detection efficiency was determined by combining secondary scintillation emission spectra with the wavelength-dependent transmission of the employed viewport and the quantum efficiency of the PMT as described in section A.3.

To determine the light yield as a function of the gain of the last GEM in a triple-GEM stack, the voltage of the first two GEMs was varied to achieve sufficient effective gains of the triple-GEM stack to permit gain measurements. Keeping the transfer field between the second and third GEMs in the stack constant at 1900 V/cm, the voltage drop across the third GEM was varied. For each voltage drop across the third GEM, the voltage supplied to the first two GEMs in the stack was adjusted to achieve total effective charge gain factors of several  $10^3$ . Especially for low voltage drops across the third GEM, the voltage drop across each one of the first two GEMs was chosen to be high. For high voltage drops across the first two GEMs in the stack, the secondary scintillation light intensity produced in electron avalanches in the holes of the first two GEMs contributes significantly to the total scintillation light intensity emitted by the triple-GEM stack. As perforated foils, the GEMs are inherently semi-transparent resulting in some of the secondary scintillation light emitted by the first and second GEMs in the stack passing through the third GEM and being detected by the PMT. To compensate the contribution of the secondary scintillation light from the first two GEMs to the total observed light intensity, the intensity of the secondary scintillation light from the first two GEMs was recorded for each measurement configuration. The third GEM was switched off with no voltage difference between the two electrodes to eliminate its contribution to the total emitted scintillation light intensity. In the same way as for the case of a switched on third GEM, a energy spectrum of detected X-rays was determined from the integrated intensities of PMT signals and the number of detected photons was determined from the intensity corresponding to the location of the full energy peak in the spectrum. Subsequently, the number of secondary scintillation photons originating from the third GEM in the stack was determined by subtracting the light intensity emitted by the first two GEMs from the light intensity emitted by all three GEMs in the stack. Thus, the number of scintillation photons emitted by the third GEM in the triple-GEM stack could be determined even if the scintillation light contribution of first two GEMs was significant. Alternatively, the number of scintillation photons emitted by the third GEM may also be determined by subtracting the scintillation light intensity spectrum recorded with the third GEM switched off from the spectrum recorded with all three GEMs in the triple-GEM stack switched on and subsequently dividing the intensity corresponding to the full energy peak in the resulting spectrum by the integrated intensity of a single photon event.

#### 4.2.1 Light yield of Ar/CF<sub>4</sub>, He/CF<sub>4</sub> and Ne/CF<sub>4</sub> gas mixtures

The secondary scintillation light yields of Ar/CF<sub>4</sub>, He/CF<sub>4</sub> and Ne/CF<sub>4</sub> gas mixtures with different mixing ratios were measured as a function of the gain of the last GEM in a triple-GEM stack in open gas flow mode. A comparison of the secondary scintillation light yields of different gas mixtures in the wavelength range from 200 nm to 800 nm is shown in figure 34.

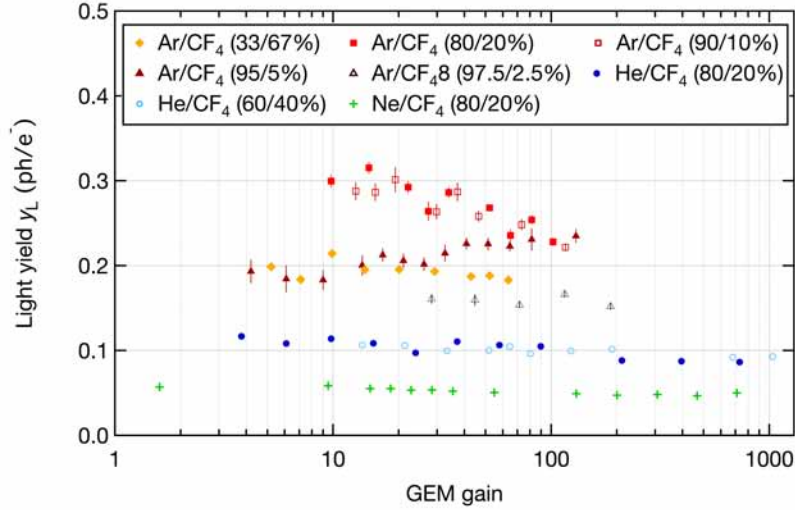


**Figure 34.** Secondary scintillation light yield of different gas mixtures: The measured light yield values vary significantly between different gas mixtures and mixing ratios. The error bars show statistical errors. The systematic errors are estimated to be less than 30%.

The systematic error of the measurement was estimated by changing the geometric acceptance of the PMT by moving it further from the GEM and comparing the observed change in the number of recorded photons with the expected one. In addition, the single photon response of the PMT was determined by two different methods as described in section A.5 to estimate the systematic error arising from the determination of the number of photons by the PMT. The systematic error of the measurements is estimated to be less than 30%.

Ar/CF<sub>4</sub> gas mixtures provided the highest light yield values among the investigated gas mixtures. For mixtures with CF<sub>4</sub> fractions of 10% or 20%, secondary scintillation light yield values of about 0.3 ph/e<sup>-</sup> were obtained for low GEM gain values well below 10<sup>2</sup>. As previously reported for an Ar/CF<sub>4</sub> mixture with a CF<sub>4</sub> fraction of 10% [50], the light yield decreased slightly with higher GEM gains in these mixtures but remained above 0.2 ph/e<sup>-</sup> even at GEM gains of about 10<sup>2</sup>. Ar-based mixtures with higher or lower fractions of CF<sub>4</sub> exhibited lower light yield values, with gas mixtures with a low CF<sub>4</sub> fraction of 2.5% only providing about 0.15 ph/e<sup>-</sup>.

He/CF<sub>4</sub> gas mixtures did not exhibit a light yield as high as the one of Ar/CF<sub>4</sub> gas mixtures. A light yield of about 0.1 ph/e<sup>-</sup> was obtained for a He/CF<sub>4</sub> gas mixture with a CF<sub>4</sub> fraction of 20%.

A Ne/CF<sub>4</sub> gas mixture with 20% of CF<sub>4</sub> provided the lowest number of secondary scintillation photons per secondary electron. For GEM gains ranging from low values below 10 up to several 10<sup>2</sup>, this mixture only provided about 0.05 ph/e<sup>-</sup>.

The obtained light yield values differ significantly from the results reported by Fraga et al. [50] for the GEM scintillation in Ar/CF<sub>4</sub> and He/CF<sub>4</sub> gas mixtures. In the case of He/CF<sub>4</sub> mixtures, the measured light yield values of about 0.1 ph/e<sup>-</sup> are higher than the previously reported values, which may be attributed to the wider wavelength range taken into account.

The measured light yield values of Ar/CF<sub>4</sub> mixtures are about 50 % lower than the previously reported ones. The high reported light yield values above 400 nm for Ar/CF<sub>4</sub> mixtures with 5 % and 10 % of CF<sub>4</sub> of more than 0.5 ph/e<sup>-</sup> could not be reproduced, although the light yield values are expected to be higher in the presented measurements as scintillation light over a wider wavelength range from 200 nm to 800 nm was recorded.

Ar/CF<sub>4</sub> gas mixtures with mixing ratios of 80/20% and 90/10% allow strong secondary scintillation light emission. He/CF<sub>4</sub> and Ne/CF<sub>4</sub> gas mixtures provide higher GEM gains at lower GEM voltages compared to Ar/CF<sub>4</sub> mixtures, which might compensate the lower light yield values of these mixtures and result in total numbers of emitted secondary scintillation photons comparable to those of Ar/CF<sub>4</sub> mixtures. Based on the presented light yield measurements, an Ar/CF<sub>4</sub> gas mixture with a mixing ratio of 80/20% was chosen for the optically read out GEM-based detectors developed and presented within the scope of this work. Besides being an economically efficient option, this mixture provides an emission spectrum with a dominant emission band in the VIS wavelength range and a high secondary scintillation light yield, making it well-suited for optical readout with imaging sensors.

#### 4.2.2 Trend of light yield in sealed detector

The trend of the secondary scintillation light yield of a triple-GEM stack in an Ar/CF<sub>4</sub> gas mixture with a mixing ratio of 80/20% at atmospheric pressure was recorded over an extended period of time in a sealed detector. After extensive gas flushing to achieve a good gas purity in the detector, the gas flow was stopped and the chamber was sealed. The light yield of the triple-GEM operated at a total effective gain of about  $5.5 \times 10^3$  was recorded in intervals of 5 h. The trends of the light yield and the effective GEM gain over 16 days of sealed mode operation are shown in figure 35.

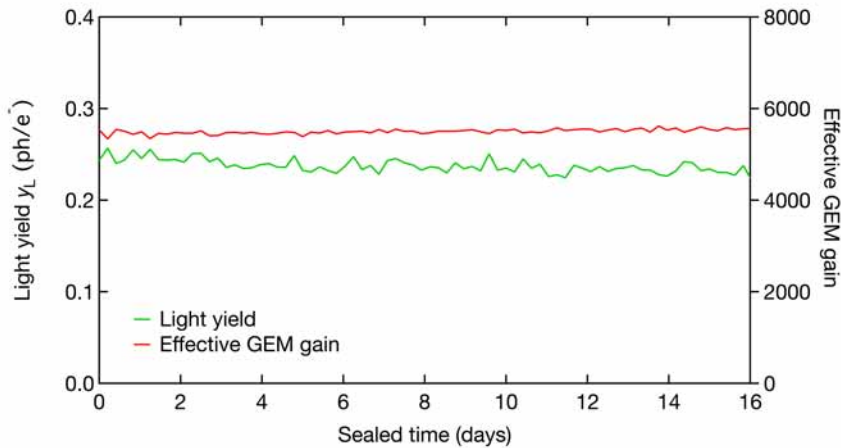


**Figure 35.** Trend of light yield in sealed detector: The light yield of a triple-GEM operated in an Ar/CF<sub>4</sub> gas mixture at atmospheric pressure was recorded in a sealed detector. The overall decrease in the light yield over 16 days was about 6%.

A decrease of the secondary scintillation light yield of about 6 % over 16 days was observed, while the effective GEM gain did not change significantly. The decrease in the light yield is attributed to impurities in the gas due to outgassing from components in the detector vessel despite the usage of low-outgassing materials. As the slight decrease in light yield can be compensated by increasing the gain of the detector, sealed optically read out GEM-based detectors appear feasible. In addition, degradations of the light yield in sealed

detectors due to contamination of the gas might be decreased by using getter pumps to maintain a high gas purity over long periods of sealed mode operation.



## CHAPTER 5

# Optically read out detector concepts

## 5.1 Radiation imaging with optically read out GEM-based detectors

Scintillation light emitted during the electron avalanche multiplication in the holes of GEMs can be recorded with imaging sensors to visualise radiation interacting in the conversion volume of GEM-based detectors. Employing multi-stage amplification structures, the sensitivity of such detectors can be extended to weakly ionising radiation and the use of suitable scintillating gases or gas mixtures enables direct imaging of light produced in amplification structures. Radiographs can be recorded by placing an object of interest between a radiation source and an optically read out GEM-based detector. Furthermore, the concept can also be employed for recording real time images of radiation and to obtain visualisations of radiation events without the need for extensive reconstruction algorithms. The combination of MPGDs with optical readout is also well-suited for applications requiring high spatial resolution and low material budget.

The applicability of optically read out GEM-based detectors to X-ray radiography and fluoroscopy was investigated. Based on multiple radiographs, 3D reconstruction was performed from obtained images. The high achievable sensitivity of detectors based on GEM amplification structures allowed single low-energy X-ray photon sensitivity and energy-resolved imaging was explored.

### 5.1.1 Detector concept and operation

A radiation detector based on a stack of three GEMs as multiplication stage and a cathode defining a conversion volume of several millimetres thickness above the first GEM was placed in an optically transparent gas volume and read out with a CCD camera (QImaging Retiga R6 [66]) positioned below the last GEM [81]. The optically read out GEM-based detector was housed in a transparent gas volume made from polymethylmethacrylate. A 20  $\mu\text{m}$  thick biaxially-oriented polyethylene terephthalate (Mylar) foil coated with 100 nm of Al was used as radiation window to allow low-energy X-ray photons to enter into the detector. Three GEM foils with an active area of  $10 \times 10 \text{ cm}^2$  each were assembled to a triple-layer multiplication stage in the gas volume. GEM foils featuring 70  $\mu\text{m}$  diameter holes with a pitch of 140  $\mu\text{m}$  manufactured by a double-mask etching technique were used. The foils were separated by 2 mm thick transfer gaps between them. The thickness of the conversion layer between the first GEM and the cathode was varied between 2 mm and 10 mm depending on the investigated applications. No anode was used below the triple-GEM stack. The individual

electrodes of the GEMs were contacted by polyimide-insulated wires glued into and leading through the frame of the gas volume. The electrodes were biased with a voltage divider employing high-voltage resistors to define appropriate voltage gradients in the conversion volume and multiplication stage.

A CCD camera was placed outside of the gas volume facing the bottom electrode of the last GEM for recording the emitted scintillation light. A 6-megapixel CCD camera with a  $12.5 \times 10 \text{ mm}^2$  cooled imaging sensor featuring  $4.54 \times 4.54 \text{ }\mu\text{m}^2$  pixels and a nominal read noise of  $5.7 \text{ e}^-$  (rms) was used (QImaging Retiga R6 [66]). To collect secondary scintillation light, a 25 mm focal length lens with a large aperture of  $f/0.95$  was used. Coupling the full active area of the GEM to the imaging sensor resulted in a magnification factor of approximately 10 corresponding to an effective pixel size of about  $45 \times 45 \text{ }\mu\text{m}^2$  on the imaging plane. To enable close distance focusing of the lens, either an additional +3 diopter lens in front of the main lens or a 1 mm spacer between the lens and the camera body was used. The camera was operated with the imaging sensor cooled to  $-20 \text{ }^\circ\text{C}$  by Peltier-cooling to minimise the noise in the recorded images. Depending on the application, binning of pixels or extended integration times were used to achieve sufficient signal-to-noise ratios in the acquired images. The gas volume containing the detector elements was placed in a light shielding box to minimise ambient light leakage to the camera.

The detector was operated in open gas flow mode with an  $\text{Ar}/\text{CF}_4$  gas mixture with a mixing ratio of 80/20% at atmospheric pressure with a flow rate of 5 l/h. The detector was flushed for several hours before operation to ensure a high gas quality.

The gain of the GEMs was adjusted to be compatible with different experimental requirements and enable detection of radiation ranging from low-energy X-rays to highly ionising alpha particles. A tapered voltage biasing scheme based on a resistive voltage divider as shown in figure 36 was used to power the GEMs. The gain of the second and third GEMs in the triple-GEM stack was chosen to be slightly lower than the one of the first GEM because the total amount of charge present in the second and third multiplication stages will be higher. The voltage drop across the second GEM was about 10 % lower than the one across the first one and the voltage drop across the third GEM was about 10 % lower than the one across the second one. For a voltage drop of 400 V across the first GEM in the stack, this resulted in a voltage drop of about 360 V across the second GEM and 325 V across the third GEM. In the case of a detector operated in an  $\text{Ar}/\text{CF}_4$  gas mixture with a mixing ratio of 80/20%, these voltages result in gain values of about 80 for the first GEM, 35 for the second GEM and 15 for the third GEM in a triple-GEM stack.

Transfer field strengths of about 2 kV/cm were employed to effectively collect electrons between individual multiplication stages in the triple-GEM stack in the  $\text{Ar}/\text{CF}_4$  gas mixture. The three 1 M $\Omega$  protection resistors connected in series between the voltage divider and the top electrodes of each of the GEMs were chosen for operation in low-rate environments. For operation in high-rate environments, significantly lower resistor values for these protection resistors should be chosen depending on the total expected charge in the triple-GEM stack.

### 5.1.2 X-ray radiography

X-ray radiography can be used to collect information about internal structures of objects. Employed in fields ranging from medical diagnostics [82] to non-destructive material characterisation, X-ray radiographs are recorded by subjecting a sample to X-ray irradiation and recording the photons traversing the object with a suitable detector located behind the object.



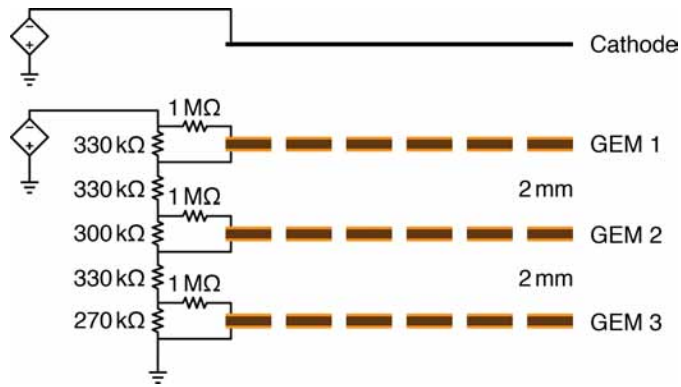


**Figure 36.** Biasing scheme of triple-GEM stack: A voltage divider scheme is used to bias a triple-GEM stack. Slightly lower resistor values across the second and third GEMs in the stack are used to achieve a lower charge gain in subsequent multiplication stages.

A variation of X-ray energies permits probing different depths in samples due to changing absorption characteristics and characteristic absorption lengths.

A triple-GEM-based detector optically read out with a CCD camera was used as an X-ray detector for imaging of biological and non-organic samples under X-ray irradiation from  $^{55}\text{Fe}$  sources or from an X-ray tube with Cu or W targets. A small deceased bat was placed in front of the optically read out GEM-based detector and irradiated with X-rays from an X-ray tube with a W target with high flux. A radiograph of the mammal recorded with an X-ray tube acceleration voltage of 11 kV and an X-ray tube current of 0.5 mA is shown in figure 37.

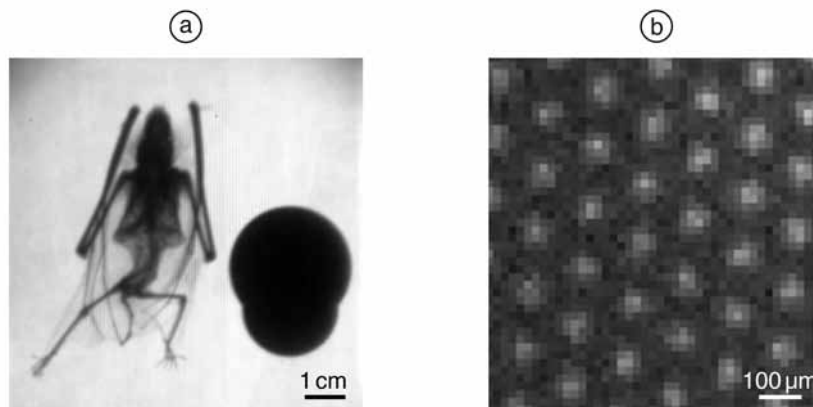


**Figure 37.** X-ray radiograph of bat: (a) X-ray radiograph of bat recorded with an exposure time of 10 s under irradiation with X-rays from an X-ray tube operated with an acceleration voltage of 11 kV and a tube current of 0.5 mA. (b) Close-up view of GEM holes visible as sources of secondary scintillation light.

The acquired image was recorded with an exposure time of 10 s and a pixel binning of 2x2 with the the first two GEMs in a triple-GEM stack operated at a voltage of 400 V each and 350 V across the third GEM. The acquired images demonstrate the imaging capabilities of the optically read out GEM-based detector due to the high pixel count of the employed CCD imaging sensor. Small structures of the animal are visible and the contrast in the images permits a distinction of materials such as bones or skin with different densities [81]. Higher X-ray photon energies result in a deeper penetration into the irradiated material and can be used to resolve internal structures. However, the larger range of photoelectrons released in the conversion volume by photons with higher energies results in decreased image sharpness. The effect of different X-ray photon energies on image sharpness and contrast was

also investigated by recording X-ray radiographs of a miniature drone at different X-ray tube acceleration voltages from 10 kV to 50 kV in steps of 10 kV and comparing central line profiles in the acquired images as shown in figure 38. For higher X-ray energies, the contrast in the images is improved. However, the sharpness is degraded by higher energetic X-rays. This can be attributed to the larger extent of the primary ionisation cluster for higher energetic X-ray photons. At high X-ray photon energies, some X-ray photons might penetrate the object and the detector and reach the imaging sensor of the camera. As a result of direct interaction of X-ray photons with the imaging sensor of the CCD camera which was placed in the axis of irradiation in the presented measurement, some pixels might be directly hit and excited by X-ray photons and give significantly higher readings than neighbouring pixels. These pixels become apparent as sharp spikes in line profiles of the pixel value intensity.

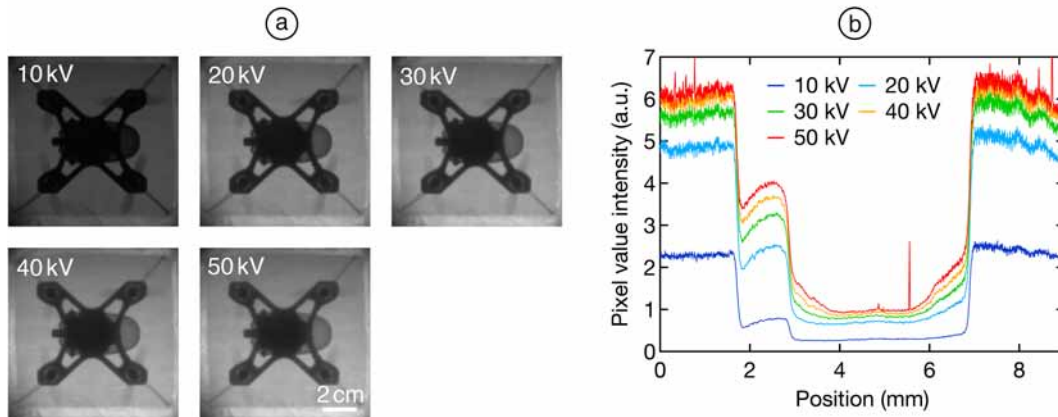


**Figure 38.** Horizontal line profiles of pixel value intensities at different X-ray photon energies: (a) X-ray radiographs of miniature drone recorded with different X-ray tube voltages from 10 kV to 50 kV in steps of 10 kV. (b) Horizontal line profiles of pixel value intensities at different X-ray tube voltages.

The spatial resolution achievable by optically read out GEM-based detectors was studied by determining the edge spread function by imaging a sharp edge under parallel X-ray irradiation. A 100  $\mu\text{m}$  thick Cu foil providing efficient shielding of 8 keV Cu X-rays from an X-ray tube with a Cu target operated with an acceleration voltage of 20 kV located at a distance of about 1 m from the detector was placed directly on top of the cathode of the detector with a thin conversion layer of 2 mm thickness. A radiograph under X-ray irradiation with an X-ray tube current of 1 mA was recorded without pixel binning with an exposure time of 6 s. A triple-GEM stack with a voltage of 400 V across each GEM and a drift gap thickness of 2 mm was used to record images of the sharp edge of the Cu piece. A line profile of the pixel value intensity in the recorded image across the edge of the Cu piece is shown in figure 39.

To determine the spatial resolution, the line profile across the recorded edge was fitted with the error function defined as

$$I(x) = I_0 + \frac{A}{2} \operatorname{erf}\left[\frac{x - x_0}{\sqrt{2}\sigma}\right] \quad (5.1)$$

with the intensity  $I(x)$  at a position  $x$ , the offset intensity  $I_0$ , the amplitude  $A$ , the position of the edge  $x_0$  and the standard deviation  $\sigma$ . From the obtained fit shown in figure 39b, a value for the spatial resolution of  $\sigma = (351 \pm 20) \mu\text{m}$  was obtained. While significantly better values have been obtained with electronic readout using centre of gravity algorithms, the achieved spatial resolution permits accurate imaging and identification of millimetre-scale structures. In electronic readout configurations employing crossed strip readout for 2D position sensi-

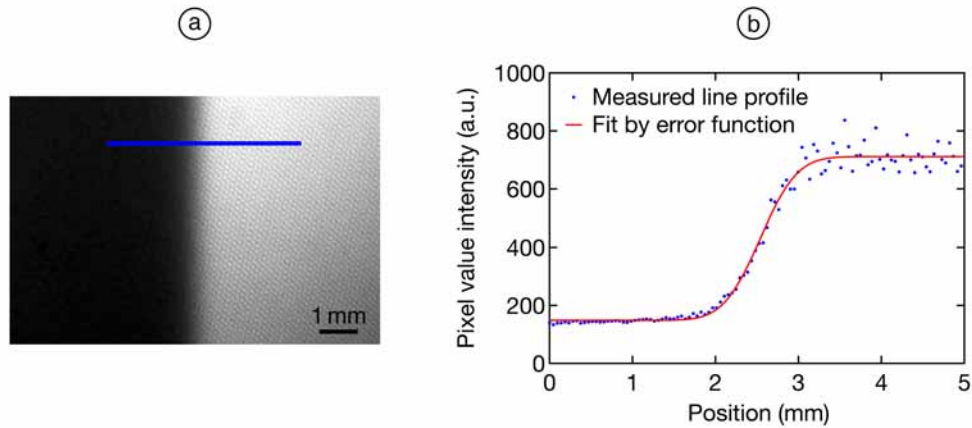


**Figure 39.** Spatial resolution determination by fitting edge profile: (a) Optically recorded image of the edge of a Cu piece under X-ray irradiation. The blue line represents the location of the line profile of the pixel value intensity. (b) Line profile of the pixel value intensity across the edge of a Cu piece. The spatial resolution was determined by fitting an error function to the line profile.

tivity, the high spatial resolution is achieved by performing centre of gravity fitting of induced electronic signals in several neighbouring readout strips resulting in excellent spatial resolutions. The integrating light collection during optical readout of GEM-based detectors by imaging sensors achieves lower spatial resolution due to transversal diffusion of electrons in the drift volume. As no centre of gravity fitting is performed during integrating optical imaging, the diffusion of electrons in the drift region results in reduced image sharpness. Better spatial resolution values may be achieved by identifying single events in images recorded with short exposure times and performing centre of gravity fitting of individual X-ray photon signal spots. Scintillation light readout is inherently insensitive to electronic noise resulting in good signal-to-noise ratios and requires significantly less reconstruction effort in an integrating imaging mode as images are directly available for display and further analysis and no extensive image reconstruction algorithms as used in electronic readout for assembling numerous individual events to an image are necessary.

### 5.1.3 X-ray fluoroscopy

Taking advantage of the frame rate achievable by high-granularity imaging sensors, real-time movies of radiographs of samples under X-ray irradiation can be acquired. This technique known as fluoroscopy is especially useful for online material characterisation and feedback from radiography during dynamic procedures. Acquired images can be directly displayed as no extensive reconstruction is necessary and stored for further analysis. In order to permit real-time fluoroscopy, the exposure time of individual image frames must be kept short and high X-ray fluxes are necessary to obtain sufficient contrast in the individual radiographs. Depending on the readout speed and pixel count, CCD cameras permit frame rates of tens of frames per second while specialised CMOS cameras can achieve hundreds of frames per second. The capability of imaging sensors to collect and record all light arriving within the exposure window makes optical readout well-suited for fluoroscopy as it enables the use of high radiation intensities and thus good signal-to-noise ratios.

Employing the same setup used for X-ray imaging, a triple-GEM-based detector optically read out with a CCD camera was used for X-ray fluoroscopy acquisition. The remote controlled flight of a miniature drone contained in a paper cylinder was recorded in real time. The

drone was irradiated with strong X-ray fluxes from an X-ray tube with a Cu target operated with an acceleration voltage of 10 kV and an X-ray tube current of 10 mA and images with an exposure time of 100 ms were recorded. To achieve sufficient contrast in the individual images despite the short exposure time, 8x8 pixel binning was employed and the triple-GEM was operated at a high gain with a voltage of 400 V across each one of the first two GEMs and a voltage of 350 V across the third GEM in the multiplication stage. Several frames of the obtained X-ray fluoroscopy movie of the flight of a miniature remote-controlled drone are shown in figure 40.

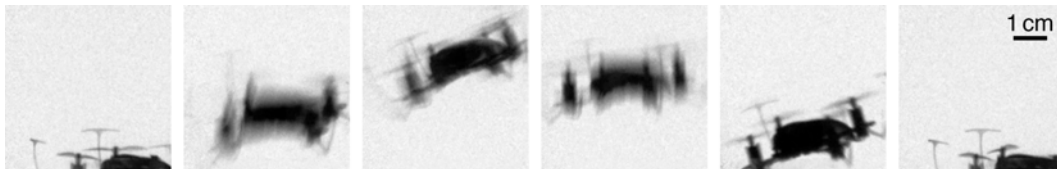


**Figure 40.** Selected frames of X-ray fluoroscopy recording: X-ray radiography images of the flight of a miniature remote-controlled drone were recorded with an optically read out GEM-based detector with a frame rate of 10 Hz. The recorded frames display a high contrast despite the short exposure time of 100 ms per frame.

To achieve higher signal-to-noise ratios or allow shorter exposure times, the intensity of the incident radiation may be increased up to the limit set by the onset of saturation in the GEM stack due to excessive radiation rates. The integrated imaging approach and the immediate availability of images without the need for reconstruction algorithms makes optical readout well-suited for X-ray fluoroscopy applications.

### 5.1.4 X-ray tomography

Acquiring multiple radiographs of the same object from different angles permits 3D reconstruction of the shape of the object. This concept known as tomography is widely used in medical imaging, where multiple X-ray radiographs are assembled to a 3D visualisation by a technique called computed tomography. Using high radiation rates and taking advantage of the integrated full-field imaging capabilities of optical readout, individual 2D images can be recorded rapidly and used for the reconstruction of 3D models.

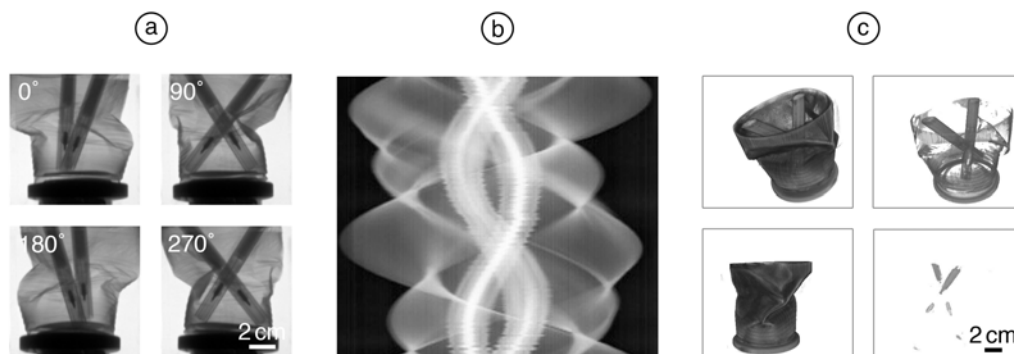


**Figure 41.** X-ray tomography from optically read out images: (a) Selected views of crushed plastic cup containing two pens from different angles. Images were recorded optically with a CCD camera and a background image was subtracted. (b) Example of a sinogram computed from a single radiograph of the object. (c) Views of reconstructed 3D model of crushed plastic cup containing pens with different intensity thresholds to visualise internal features.

An optically read out triple-GEM-based detector was used to acquire multiple radiographic views of an object from different angles [81]. Rotated by a remotely controlled stepper motor, a crushed plastic cup containing two pens was used as a sample to demonstrate the obtainable contrast in acquired images representing different material densities. 200 individual images of the object from angles from  $0^\circ$  to  $360^\circ$  in steps of  $1.8^\circ$  were recorded. A subset of the recorded views of the object is shown in figure 41a. Following image acquisition, sinograms were computed from the images via standard offline image analysis software. An example of the resulting sinograms is shown in figure 41b. The sinograms were subsequently transformed to a 3D model of the original object by a filtered back projection algorithm. Several views of the reconstructed 3D model are shown in figure 41c. Introducing different background thresholds on the images before applying 3D reconstruction algorithms can be used to obtain 3D visualisations of certain features distinguished by image contrast. As an example, high material density regions in the tips of the pens can be selectively shown and reconstructed while hiding the thin plastic cup surrounding them.

### 5.1.5 X-ray fluorescence

Primary X-ray radiation can be used to excite fluorescence radiation from samples [83], which can in turn be used to investigate material compositions. This X-ray fluorescence technique is widely used in art and archaeology for the analysis of paint layers, coins or other artefacts [84]. The two variants of X-ray fluorescence measurements, wavelength-dispersive and energy-dispersive X-ray fluorescence, are also used in a number of other applications including quality control and crystal structure analysis. Their low-energy X-ray detection capability, high-rate compatibility, 2D spatial resolution and scalability to large detection areas make MPGDs well-suited for energy-dispersive X-ray fluorescence analysis [85]. Numerous MPGD-based detectors for X-ray fluorescence analysis have been developed which combine 2D X-ray photon detection with good spectroscopic capabilities for full-field X-ray fluorescence systems [86, 85, 87].

The high achievable gain factors of multi-GEM amplification stages permit the detection of individual low-energy X-ray photons. Operating a triple-GEM amplification stage with an effective charge gain above  $10^5$ , individual X-ray photon events with energies below 5 keV can be unambiguously identified in PMT waveforms and in images obtained with a CCD camera recording the emitted secondary scintillation light [81]. The proportionality between energy deposited in the conversion volume by incident radiation and the number of electrons created during electron avalanche multiplication in gaseous detectors operated in a proportional amplification regime permits the recording of energy spectra of incident radiation from induced electrical signals. Equivalently, the proportional dependence of the emitted number of secondary scintillation photons during amplification on the number of produced electrons allows a determination of the energy deposited in the conversion volume by the incident radiation not only from induced electrical signals but also from the number of emitted photons. When recording emitted secondary scintillation light with a PMT, the integral of PMT signals is a measure of the emitted number of photons. By normalising the PMT response to a known energy such as the full energy peak of an  $^{55}\text{Fe}$  source at 5.9 keV, energy spectra obtained by a PMT as shown in figure 42b can be obtained.

Individual X-ray photon signals can also be identified in CCD images with short exposure times when achieving sufficiently high amplification factors and thus enough scintillation light emission for acceptable signal-to-noise ratios in the optically read out images. Short



**Figure 42.**  $^{55}\text{Fe}$  energy spectra obtained with GEM and PMT: (a) Energy spectrum of  $^{55}\text{Fe}$  obtained from integrating electrical signals read out from the bottom of the third GEM in a triple-GEM-based detector with an energy resolution of 28 % FWHM at 5.9 keV. (b) Energy spectrum of  $^{55}\text{Fe}$  obtained from integrating PMT signals of the secondary scintillation light produced in a triple-GEM-based detector with an energy resolution of 32 % FWHM at 5.9 keV.

exposure times must be used in order to avoid pile-up of multiple photon interaction events in the acquired images. For an  $^{55}\text{Fe}$  source with an activity of approximately 1 GBq placed directly in front of the entrance window of an optically read out GEM-based detector with a 3 mm thick conversion region, exposure times of up to 50 ms resulted in a low number of X-ray photon events present in each individual image with a small number of overlapping events. To increase the signal-to-noise ratio in these images, 8x8 hardware pixel binning was used to effectively increase the pixel size and increase the amount of light collected per read out pixel. An example of a CCD image of several individual low-energy X-ray events from an  $^{55}\text{Fe}$  source recorded with an exposure time of 50 ms is shown in figure 43a.

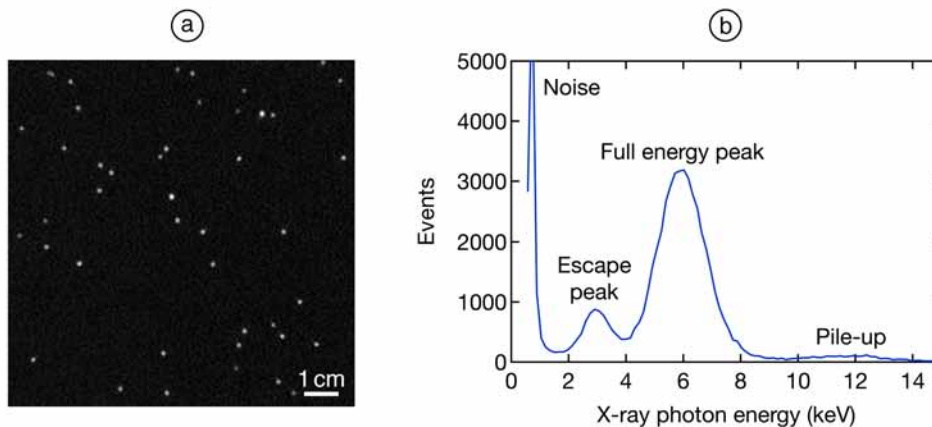


**Figure 43.**  $^{55}\text{Fe}$  energy spectrum obtained from CCD images: (a) Image of multiple X-ray photons from an  $^{55}\text{Fe}$  source interacting in a triple-GEM-based detector optically read out by a CCD camera. The displayed image was recorded with an exposure time of 50 ms and 8x8 pixel binning. (b) Energy spectrum of  $^{55}\text{Fe}$  with an energy resolution of 32 % FWHM at 5.9 keV obtained from integrating the intensity of approximately 65000 X-ray photon signal spots in 5000 individual frames recorded by a CCD camera.

Identifying signal spots in such images, masking them individually and integrating the pixel value intensity around each identified signal spot yields a totally collected light intensity value for each event, which can be directly related to the energy deposited by the incident X-ray photon. An energy spectrum of an  $^{55}\text{Fe}$  source obtained from integrated signal spot

intensities in CCD images recorded with short exposure times is shown in figure 43b. The energy resolution in the obtained spectrum is 32% Full-Width at Half-Maximum (FWHM) at 5.9 keV. A small peak at higher energies resulting from the pile-up of several X-ray photons in the same location in an individual image was observed.

Recording not only the integrated intensity of individual X-ray photon events in CCD images but also their location permits energy-resolved 2D imaging with optically read out GEM-based detectors. This readout approach can be readily scaled to larger or smaller detection areas by the use of suitable lenses and permits the optimisation of area coverage and spatial resolution to meet varying experimental requirements. By encoding incident photon energy in colour channels of images assembled from a high number of individual photon events, different X-ray photon energies can be used to visualise and intuitively identify regions with radiation of certain energies.

X-ray fluorescence imaging takes advantage of the emission of characteristic X-rays from excited materials with X-ray photon energies depending on the energy levels of the excited materials. Recording both energy and location of characteristic X-ray photons emitted from materials excited with X-ray radiation of a higher energy, materials can be distinguished and material-resolved 2D images can be obtained. The energy-resolved 2D imaging achievable with optically read out GEM-based detectors with sufficiently short exposure times can be employed for X-ray fluorescence measurements. A schematic of the experimental setup employed for X-ray fluorescence imaging with a triple-GEM-based detector read out by a CCD camera is shown in figure 44a.

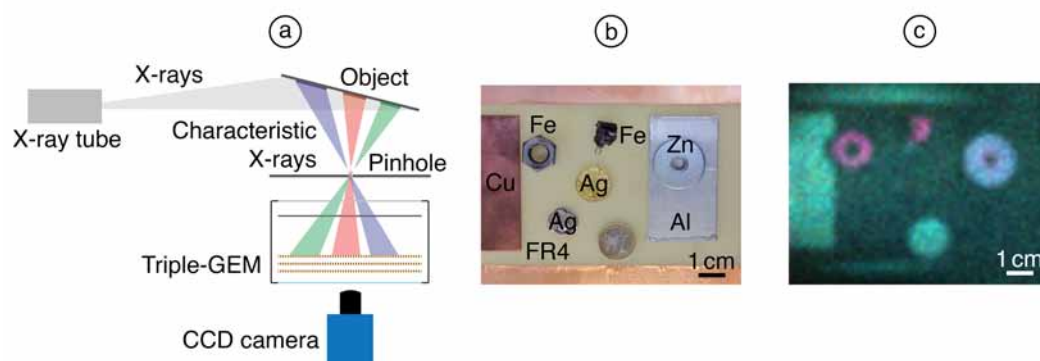


**Figure 44.** X-ray fluorescence imaging with optically read out GEM: (a) X-ray fluorescence setup consisting of an object irradiated with X-rays, a pinhole and an optically read out GEM-based detector. (b) Visible light image of irradiated object consisting of different metals. (c) Colour-coded X-ray fluorescence image permitting the distinction of different metals.

An object composed of different metallic objects composed of Ag, Al, Au, Cu, Fe and Zn as shown in figure 44b fixed to a glass-reinforced epoxy laminate (FR4) plate was placed under an angle in front of an X-ray tube with a W target operated with an acceleration voltage of 20 keV, which was used to excite some of the metals and induce the emission of characteristic X-rays. A millimetre-scale pinhole placed between the excited object and the detector allowed the characteristic X-rays to be recorded in well-defined locations on the active area of the detector corresponding to their origin on the investigated object. In this setup resembling a pinhole camera, the achievable spatial resolution could be improved by using possibly small pinhole diameters. As smaller pinholes also result in a decreased geometrical acceptance of the emitted characteristic X-rays and thus a decreased signal-to-noise ratio of reconstructed energy-resolved images, the pinhole size was chosen to be 2 mm in diam-

eter as a compromise between achievable image sharpness and detectable light intensity. Detected X-ray photon events were recorded by the CCD camera with a short exposure time and 8x8 hardware pixel binning was used. Images were acquired with the maximum achievable frame rate, which was limited to about 20 Hz due to the time required for frame readout from the CCD imaging sensor. Despite the full-field imaging capabilities of optically read out detectors, the limited frame rate of imaging sensors might result in the necessity of long measurement times to collect enough individual exposures for energy-resolved imaging.

The energy of the incident fluorescence photons was determined by integrating the pixel value intensity of each individual signal spot in the recorded CCD images. Assembling the 2D image of the recorded radiation with dots representing each photon event with a colour corresponding to the recorded photon energy according to an arbitrary colour scale, the energy-resolved image shown in figure 44c was obtained. The characteristic X-ray emission energies of different materials allow an interpretation of the energy-resolved image as a material-resolved representation of the studied object [81]. The characteristic X-ray emission energy of Cu at about 8 keV is represented in the image with green colour, while the X-ray photons with energies of about 6.4 keV and 7.06 keV corresponding to characteristic Fe X-ray emission are shown in purple and Zn with an X-ray photon emission peak at about 8.6 keV is shown in blue. Ag and Au have characteristic X-ray energies of 22.1 keV and 68 keV, respectively, which were too high in energy to be excited by incident X-rays from the X-ray tube with a W target operated with an acceleration voltage of 20 kV. While Au also has some lower energy characteristic X-ray energies which could have been excited, emission at these lower energies was likely too low in intensity to be recorded. The achievable resolution of the fluorescence image is limited by the intensity of incoming radiation and the geometric acceptance determined by the pinhole diameter and the experimental setup geometry. Furthermore, parallax-induced broadening due to the conversion of X-rays incident under an angle, which is not always parallel to the electric drift field lines in the conversion volume of the detector, may result in a further loss of spatial resolution and image sharpness.

### 5.1.6 Radiation imaging

Optical readout of scintillation light from gaseous detectors provides 2D projections of events for immediate display without the need for extensive event reconstruction algorithms and is thus well-suited for the identification of radiation events and the distinction of different types of radiation. The tuneable gain of GEMs allows the detection of various types of radiation from MIPs to low-energy photons as well as strongly ionising radiation.

Operating a triple-GEM at high gain, muons can be identified and recorded. A detector with a 10 mm thick drift region and a triple-GEM as amplification stage read out by a CCD camera was operated in a test beam at CERN with a muon beam crossing the active detector volume parallel to the GEM surface. Examples of images of muon tracks exhibiting a characteristic cluster structure with occasional highly energetic electrons originating from the tracks are shown in figure 45.

Although the deposited energy is low, the strong signal amplification achievable by employing a triple-GEM multiplication stage results in high signal-to-noise ratios. The display of radiation events makes the identification of highly energetic electrons possible.

Positioning the detector in a particle beam with the beam perpendicular to the GEM surface permits beam profile monitoring. In order to minimise the exposure of the CCD camera used for optical readout to the particle beam, the CCD camera was placed outside



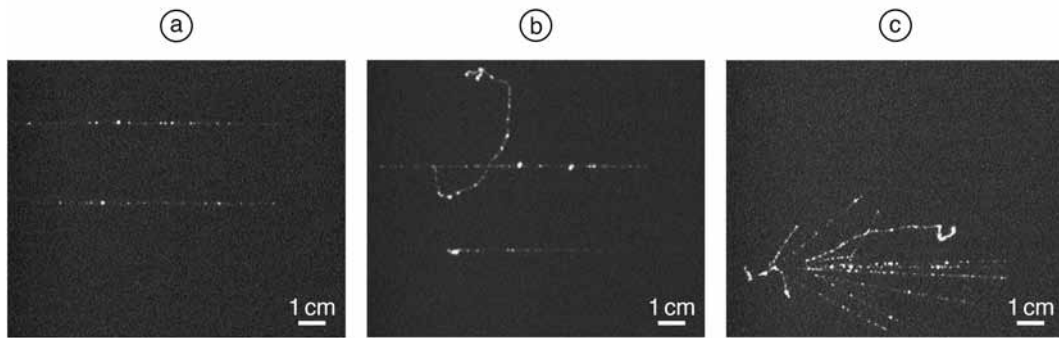


**Figure 45.** Muon tracks and hadronic shower: (a) Tracks of muons showing characteristic cluster structure. (b) Delta ray originating from muon track. (c) Hadronic shower recorded in pion beam.

of the beam axis and scintillation light produced in the GEMs was coupled to the camera via a mirror placed at  $45^\circ$  between the GEM and the camera. The beam profile of a pion beam recorded at CERN is shown in figure 46.

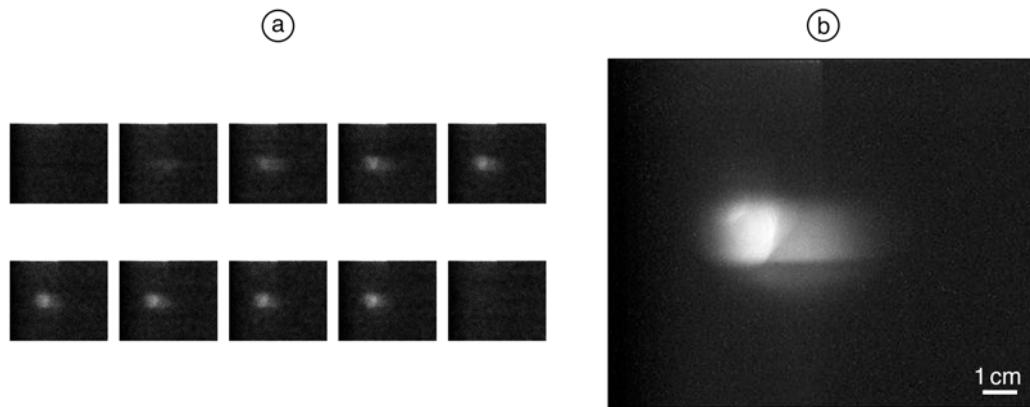


**Figure 46.** Pion beam profile: (a) Ten consecutive exposures with an exposure time of 500 ms per slice displaying the time evolution of a pion beam recorded at CERN during a single spill of the beam. The displayed area is the same as in the integrated image shown on the right. (b) Integrated pion beam profile from 50 spills with an exposure time of 10 s for each spill.

Recording images with an exposure time of 500 ms, changes in the beam profile over the time of a beam spill could be recorded as shown in figure 46a. An integrated beam profile from 50 spills with an exposure time of 10 s per spill is shown in figure 46b [81]. The main beam spot as well as the movement of the beam from right to left during the beginning of each spill due to bending magnet operation procedures can be identified in the recorded images. The immediate visualisation of the beam profile in optically read out detectors makes them well-suited for online beam monitoring. Combined with the low material budget and high signal amplification achievable by gaseous detectors, optically read out detectors using gas as active medium are an attractive technology for versatile online beam monitors.

The large dynamic range of GEM-based detectors allows the detection of a wide range of particles from MIPs to strongly ionising alpha particles or protons. The high spatial resolution achievable by modern imaging sensors permits high signal-to-noise ratios and enables a clear and unambiguous identification of particle track projections. Examples of images of alpha particles with an energy of 6.4 MeV from the decay of  $^{220}\text{Rn}$  recorded with an optically read out detector based on a triple-GEM multiplication stage operated at a moderate gain are shown in figure 47. Alpha particles were emitted by the decay of  $^{220}\text{Rn}$  to  $^{216}\text{Po}$ .  $^{220}\text{Rn}$

was introduced into the detector vessel by flushing the gas mixture used for operating the detector through a cylinder containing  $^{228}\text{Th}$ . The daughter nucleus of  $^{228}\text{Th}$ ,  $^{224}\text{Ra}$ , decayed to  $^{220}\text{Rn}$  emitting alpha particles with an energy of 6.4 MeV and was used as the main source of alpha particles in the detector.

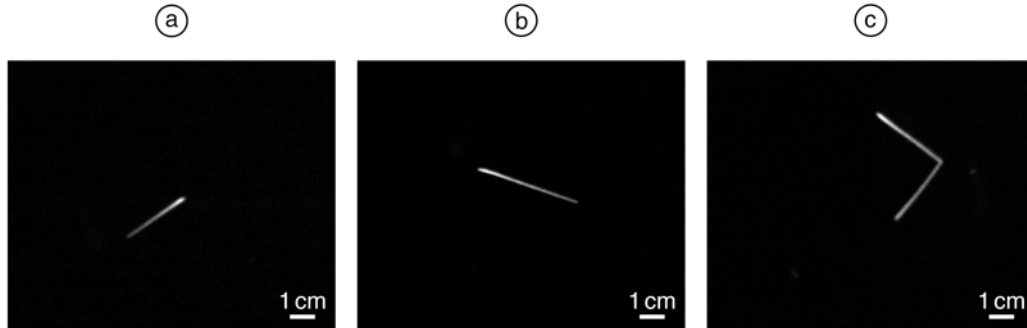


**Figure 47.** Alpha particle tracks from Rn and Po decay: (a, b) Alpha particle tracks from the decay of  $^{220}\text{Rn}$ . (b) Alpha particle tracks from the decay of  $^{220}\text{Rn}$  and the subsequent decay of  $^{216}\text{Po}$ .

The direction as well as the length of the projections of the alpha particle tracks can be determined from the recorded images [81]. Since the detector is operated in a proportional amplification regime and the light yield is thus proportional to the number of primary electrons, the recorded intensity of the scintillation light depends on the charge deposited by the particle traversing the active detector volume. Therefore, a line profile of the pixel value intensity in a recorded image along the track of an alpha particle yields the energy loss curve of the particle. A line profile of the pixel value intensity along an alpha particle track is shown in figure 48. The qualitative shape of the energy loss curve obtained from the line profile of the pixel value intensity agrees well with the expected curve of the energy loss of alpha particles with penetration depth and clearly exhibits a pronounced Bragg peak at the end of the track.

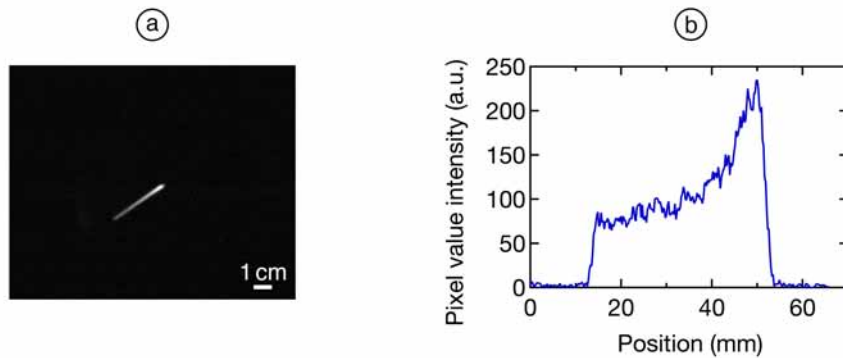


**Figure 48.** Line profile of pixel value intensity along alpha track: (a) Alpha particle track from the decay of  $^{220}\text{Rn}$ . (b) Line profile of pixel value intensity along alpha track in optically read out image.

Besides the identification of individual alpha track events, optical readout is also suited to identify more elaborate events such as subsequent decays of daughter nuclei. The  $^{220}\text{Rn}$  atoms flushed into the gas volume of the GEM-based detectors emit 6.4 MeV alpha particle when decaying to  $^{216}\text{Po}$  with a half life of 55.6 s. With a short half life of 150 ms, the  $^{216}\text{Po}$  atoms decay to  $^{212}\text{Pb}$  emitting another alpha particle with an energy of 6.9 MeV. This prompt subsequent alpha decay can be readily recorded in an optically read out GEM-based detector when choosing exposure times which are sufficiently long to record both consecutive

alpha decays within a single image. Since the  $^{216}\text{Po}$  atom moves along the drift field lines perpendicular to the surface of the GEMs, the alpha tracks from both consecutive decays appear to originate from the same location in the recorded 2D projections as shown in figure 47c. The immediate visual representation of the event obtained from the CCD camera without the need for extensive image reconstruction algorithms allows an intuitive interpretation of such decays. Although this readout approach is only suited for low event rates due to the limited frame rates of imaging sensors, the possibility to adjust the magnification and thus the effective pixel size on the imaging plane by the use of different lenses makes optical readout a versatile readout modality, which can be optimised for a wide range of experimental requirements.

## 5.2 Minimising parallax error with planispherical GEM

While using gas as an active medium in MPGDs permits the construction of low material budget detectors, the low density of the active medium can also be disadvantageous as it results in low interaction probabilities of incident radiation in the active medium and therefore low detection efficiencies. Applications such as X-ray crystallography or X-ray fluorescence, in which X-ray fluxes might be low, rely on maximised detection efficiencies to obtain measurements with acceptable signal-to-noise ratios. An increased interaction probability of incident radiation in the conversion region of gaseous detectors can be accomplished by using high density gases such as Xe, operating the detector at increased pressures or by increasing the thickness of the conversion region. The use of heavier gases as well as high-pressure operation of detectors come with technical difficulties, which make these approaches uneconomical or impractical. While thicker conversion regions can be readily implemented in most gaseous detectors, the uncertainty in the depth of interaction may lead to parallax-induced broadening and a loss of spatial resolution. Incident X-ray photons may interact with the gas anywhere along their path in the conversion region and produce primary electrons in different locations depending on the depth of interaction. For non-parallel X-ray photon fields and parallel drift field lines in the conversion volume, primary electrons will be collected in different locations on the multiplication structure depending on the initial depth of interaction. Therefore, collimated X-ray beams with an incidence angle differing from  $90^\circ$  will be projected onto the 2D readout structure and recorded as extended blurred streaks instead of spatially well-defined spots. In X-ray crystallography, where scattered X-ray photons will enter the detector under different angles, which must be accurately reproduced, the loss of spatial resolution due to the parallax error must be mitigated. Similarly, in X-ray fluoroscopy, where characteristic X-ray photons emitted from the sample pass through a pinhole before reaching the detector, parallax-induced broadening must be avoided to preserve image quality.

The parallax error can be minimised by determining the depth of interaction and reconstructing the incidence angle of a recorded photon. The depth of interaction can be determined from the drift time of the primary electrons for a known drift velocity in a constant drift field. Primary scintillation light emitted during the interaction of the X-ray photon in the active gas volume provides a timestamp of the interaction and can be compared to the time when electrons reach the multiplication structure to determine the drift time and therefore the depth of interaction. Requiring a Xe gas filling and highly sensitive photon detectors for recording the low-intensity primary scintillation light [88], this approach remains technologically challenging and limited to certain application cases.

Alternatively, parallax-induced broadening can also be mitigated by drift field lines radially focused on a point-like source of incident radiation. In radially focused drift fields, primary electrons will continue to drift along the same path as the incident photon and end up in the same location on the multiplication structure independent of the depth of interaction as shown schematically in figure 49.

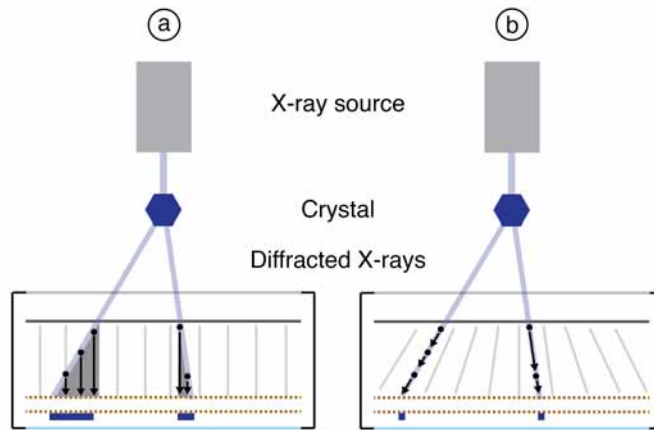


**Figure 49.** Minimisation of parallax error with radial drift field: (a) In gaseous detectors with thick conversion volumes, the parallax error leads to a broadening of signal spots for incident radiation originating from a point-like source. (b) Drift field lines radially focused at the radiation source allow a mitigation of the parallax error and preserve spatial resolution even in off-centre regions of the detector.

This concept has previously been implemented in a detector based on spherical GEMs to create radially focused drift field lines in the conversion volume [89]. However, manufacturing a spherical GEM from a flat GEM foil by deformation under thermal treatment has proven to be complicated and a suitable spherical GEM readout has not been achieved due to technical difficulties associated with this geometry.

Realising a detector which combines radially focused drift field lines to mitigate parallax-induced broadening with a geometry well-suited for optical readout, a prototype detector based on segmented flat GEMs has been realised and successfully operated [90]. The flat detector geometry simplifies manufacturing and graded potentials on ring-shaped segments of the GEM electrodes can be used to create a radially focused drift field suitable for applications requiring thick conversion layers. This planispherical GEM permits the use of thicker drift regions while preserving spatial resolution and compatibility with optical readout.

### 5.2.1 Detector concept

A 10 cm diameter conversion volume with a thickness of 2.5 cm was formed by a segmented circular cathode, a segmented cylindrical field shaper and a segmented circular GEM with a diameter of 10 cm. A dual-GEM multiplication stage was used with a transfer gap thickness of 2 mm between the two GEM foils. The cathode, the field shaper and the GEM electrodes featured 5 segments each, which could be individually biased. On the cathode and the GEM electrodes, ring-shaped segments with widths decreasing from the inside to the outside surround a central circular electrode segment. The different widths of the electrode segments were chosen to achieve drift field lines radially focused on a focal point 10 cm above the cathode with a constant potential difference between neighbouring segments. The drift field lines achieved by the employed electrode geometry were computed with COMSOL [80] (F. Sauli) as shown in figure 50.

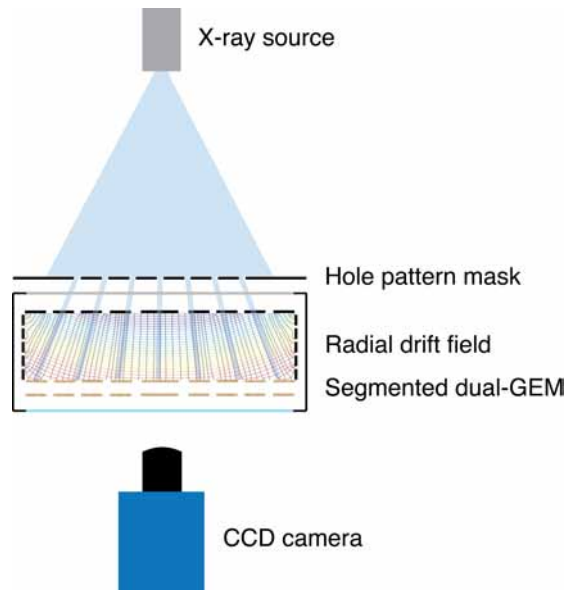


**Figure 50.** Planispherical GEM detector schematic with hole pattern: Segmented electrodes permit a radially focused drift field. A hole pattern mask was placed between the detector and a point-like X-ray source to compare straight and radially focused drift fields.

The detector elements were housed in a circular gas volume manufactured from polyoxymethylene with a polyimide radiation window above the cathode and a borosilicate optical window below the second GEM of the dual-GEM signal amplification stage. Cu tracks on polyimide foils contacting the individual segments of the electrodes were connected to a voltage divider PCB with zero-insertion-force connectors and a powering scheme based on multiple high-voltage channels was used to enable GEM gain adjustments without affecting the drift field lines. The voltage divider PCBs as well as an optional pinhole for X-ray fluorescence measurements were mounted and connected to the main detector volume with 3D printed parts.

The gas inlet was connected to the thin region between the cathode and the radiation window with several holes in the cathode foil outside of the active region permitting gas flow to the conversion volume and through the perforated GEM foils to the outlet connection in the volume between the second GEM and the optical window. The detector was operated with an Ar/CF<sub>4</sub> gas mixture with a mixing ratio of 80/20% in open gas flow mode with a flow rate of 5 l/h to ensure constant high gas purity. Below the detector volume, a light shielding tube housing a CCD camera (QImaging Retiga R6 [66]) for optical readout of the scintillation light produced in the GEM holes was mounted. For operation with radially focused drift field lines, the segments of the electrodes were biased with a potential difference of 34 V between adjacent segments on the GEM electrodes and about 400 V across the GEM foils. Only the first GEM was operated with graded potentials on the individual segments of the electrodes while all segments of the electrodes of the second GEM were biased with the same potential.

## 5.2.2 Minimisation of parallax error

The minimisation of the parallax error with radially focused drift field lines created by segmented electrodes in the developed detector prototype was investigated by comparing the representation of a hole pattern with parallel drift field lines and with radially focused drift field lines. A 100 µm thick Cu foil with 2 mm holes spaced by 5 mm or 10 mm in a crosshair

pattern was placed directly in front of the polyimide radiation window of the detector. An  $^{55}\text{Fe}$  X-ray source collimated with a pinhole in a Cu foil was placed in the focal point of the radially focused drift field lines 10 cm above the cathode. The primary electrons created during ionisation in the drift volume by X-rays passing through the holes of the mask were amplified by the double-GEM multiplication stage and the emitted secondary scintillation light was recorded with the CCD camera facing the bottom of the GEM stack. The setup for measuring the parallax error minimisation capabilities of the detector is schematically shown in figure 50.

Reference measurements of the parallax-induced broadening of the signal spots corresponding to the holes in the mask were recorded by creating parallel drift field lines in the conversion volume by biasing all segments of the cathode and field shaper with the same voltage. An image of the hole pattern acquired with parallel drift field lines is shown in figure 51a and displays increasing parallax-induced broadening in the outward regions of the active area of the detector.

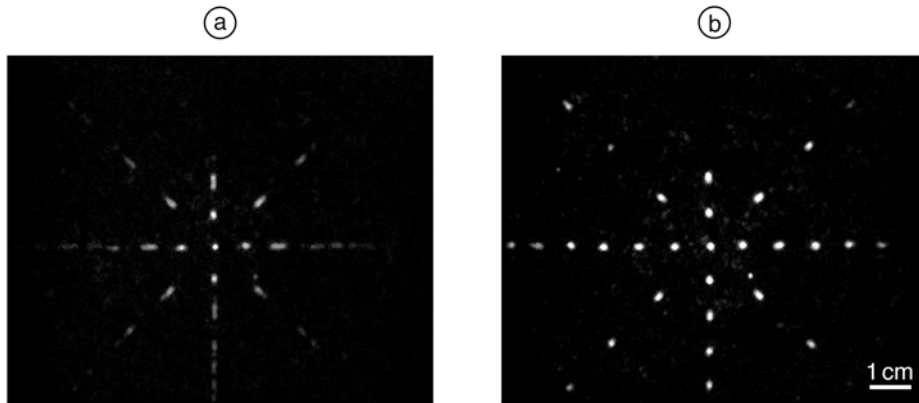


**Figure 51.** Hole pattern representation for different drift fields: In the case of parallel drift field lines, increased parallax-induced broadening leads to a decreased spatial resolution and lower signal-to-noise ratio in the outward regions of the detector. Radially focused drift field lines preserve the spatial resolution and the signal-to-noise ratio across the active area of the detector.

Switching to radially focused drift field lines focused at the point-like radiation source by applying graded potentials on the individual segments of the GEM, the parallax error could be minimised and holes of the mask were correctly represented as localised spots even in the off-centre regions of the detector. As shown in figure 51b, the radially focused drift field lines also resulted in a significantly increased signal-to-noise ratio. The degraded detector response due to the parallax error in the case of parallel drift field lines compared to the preserved signal-to-noise ratio in the case of radially focused drift field lines can also be seen in the horizontal line profiles of the pixel value intensity across the width of the active area as shown in figure 52.

The X-ray fluorescence imaging capabilities of the planispherical GEM-based detector were studied by imaging the characteristic X-ray emission from a Cu grid irradiated with X-rays from an X-ray tube with a W target operated with an acceleration voltage of 20 kV. A  $10 \times 10 \text{ cm}^2$  grid with 2 mm wide Cu lines with a pitch of 10 mm was placed under an angle in front of a 2 mm diameter pinhole in the focal point of the radially focused drift field lines of the planispherical GEM-based detector as shown in figure 53.

Integrated images of the characteristic X-rays emitted by the grid were taken for two different drift field configurations. In the case of parallel drift field lines, the parallax-induced

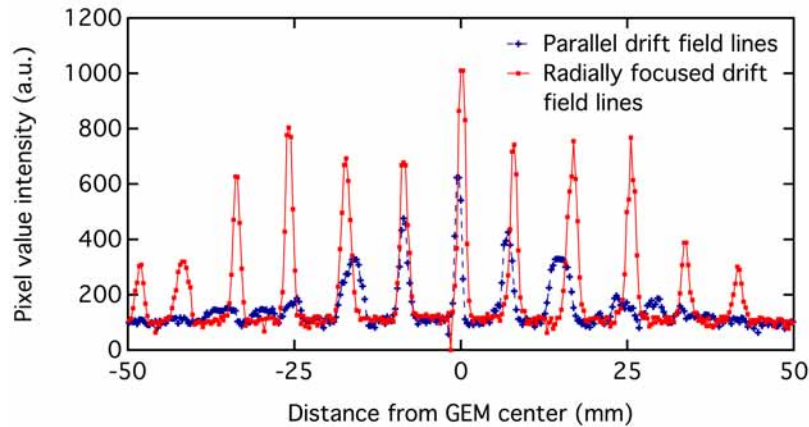


**Figure 52.** Horizontal line profiles of hole pattern: (a) The line profile of the pixel value intensity across the image in figure 51a shows a degradation of the spatial resolution and signal amplitude in off-centre regions of the detector. (b) The line profile of the pixel value intensity across the image in figure 51b taken with radially focused drift field lines demonstrates that parallax-induced broadening can be minimised with radially focused drift field lines. The remaining variations in the observed signal amplitudes may be partly attributed to irregularities of the holes of the mask used for this measurement.

broadening in the outward regions of the detector results in the lines of the grid being washed out in the recorded integrated image shown in figure 54a. The reduced signal-to-noise ratio and the broadening of the signals results in the individual vertical grid lines not being distinguishable anymore in the off-centre regions of the active area. In contrast, when using drift field lines radially focused at the pinhole, the grid lines can be accurately reproduced across the active area of the detector with individual vertical lines remaining separated and distinguishable as shown in figure 54b.

The insulating gaps between the segments of the top electrode of the first GEM result in circular dead regions between segments. Although the insulating regions between segments are only 200  $\mu\text{m}$  wide, the dead regions in the recorded images appear much wider. The width of the circular dead regions in the images might be reduced by minimising the width of the insulating regions between segments. Flood irradiations of the full active area of the detector with a nearly parallel X-ray photon field were used to visualise the effect of graded potentials between neighbouring segments on the width of the gaps between the segments in recorded images. The detector was placed in front of an X-ray tube and irradiated without any collimation to cover the full active area. In the case of parallel drift field lines, all segments of the top electrode of the first GEM were at the same potential and the width of the insulating gaps was reproduced according to the nominal width of about 200  $\mu\text{m}$  as shown in figure 55a. Apart from the profile of the X-ray beam, the response of the detector appeared uniform across the active area. In the case of radially focused drift field lines, the insulating gaps between segments appear significantly wider in recorded images as shown in figure 55b.

Additionally, the inner edges of each ring-shaped sector appear brighter than the outer edges, which can also be seen in the horizontal line profiles of the pixel value intensity across the centre of the flood exposure image recorded with radially focused drift field lines as shown in figure 56.

This imbalance between the brightness of the inner and outer edges of the ring-shaped electrode segments is attributed to the potential difference between neighbouring segments. Outer segments were biased more positively relative to the inner ones resulting in electrons

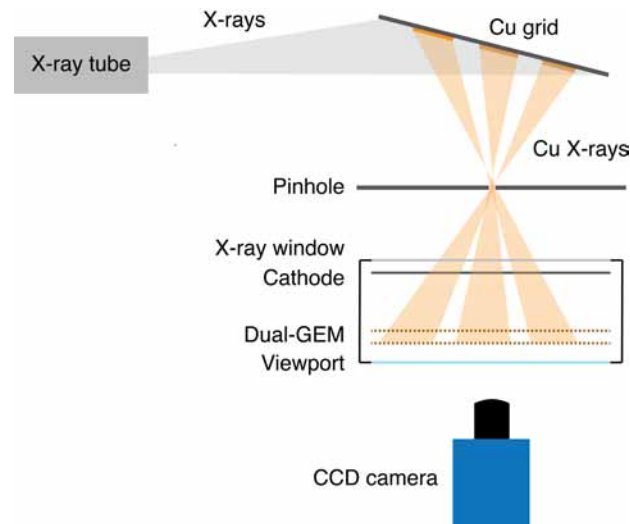


**Figure 53.** Schematic of fluorescence measurements with planispherical GEM: A Cu grid is irradiated with X-rays and the fluorescence X-rays from the Cu grid are focused onto the planispherical GEM-based detector through a pinhole.

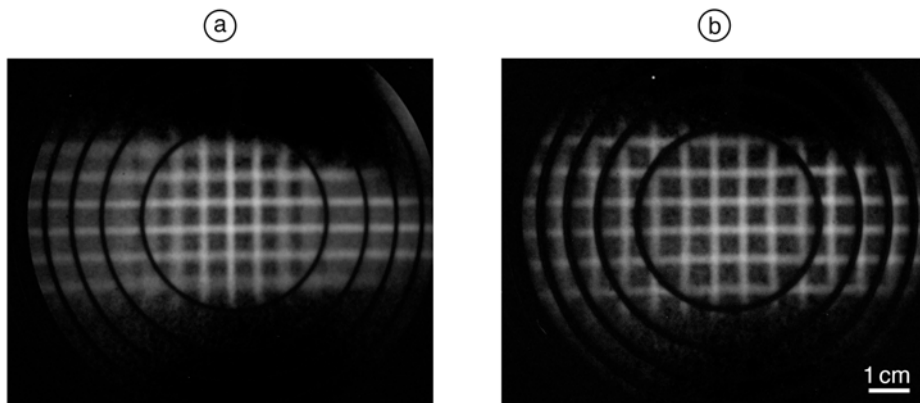


**Figure 54.** X-ray fluorescence measurements with planispherical GEM: (a) In the case of parallel drift field lines, the fluorescence image of a Cu grid appears washed out in off-centre regions and vertical lines become indistinguishable. (b) Drift field lines radially focused at the pinhole permit a preservation of imaging capabilities across the active area of the detector and the lines of the Cu grid are distinguishable even in outward regions of the detector.

close to the insulating gaps between two segments preferably drifting to the outer segment. Therefore, more primary electrons end up at the inner edges of the electrode segments compared to the outer edges of the electrode segments. This behaviour can also be seen by spikes in the horizontal lines profiles of the pixel value intensity across recorded flood exposure images with radially focused drift field lines.

The effect of transferring electrons from a region with radially focused drift field lines to a parallel transfer field between the two GEMs was measured by recording images of flood field irradiations for the three cases of parallel drift and transfer field lines, radially focused drift field lines and parallel transfer field lines and for radially focused drift and transfer field lines. No obvious differences in image quality or in line profiles of the pixel value intensity were observed for parallel or radially focused transfer field lines with the radially focused drift field lines. The effect of the transfer of electrons from a region with radially focused drift field lines to a parallel transfer field as well as the varying electron extraction and collection fields across the active area appear to be negligible. The configuration of radially focused drift field



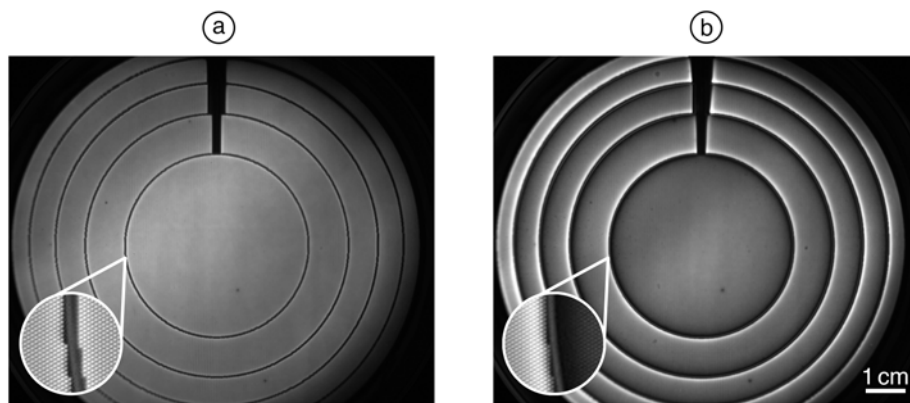


**Figure 55.** Flood exposure images with different drift fields: (a) The pixel value intensity across the surface of the detector operated with parallel drift field lines and all segments of an electrode at the same potential remains approximately constant with some variations due to the beam shape and gain variations across the GEM. Inset: Close-up view of the insulating gap between segments of a segmented electrode showing individual GEM holes. (b) In the case of radially focused drift field lines, the potential differences between neighbouring segments of a segmented electrode leads to an unbalanced electron collection with electrons being preferably collected at the inner borders of each segment. Inset: Close-up view of the insulating gap between segments of a segmented electrode showing individual GEM holes.

lines and parallel transfer field lines between the GEM foils was chosen for operation as it results in a simpler powering scheme without requiring different potentials on all electrode segments of the second GEM.

The dual-GEM multiplication stage could achieve sufficient gains to record single low-energy X-ray photon events with low signal-to-noise ratios. Operating both GEMs with a potential difference of more than 400 V between the electrodes of each foil, individual 5.9 keV X-ray photon events could be observed in images recorded with the CCD camera with short exposure times. This enables energy-resolved imaging and can be applied for X-ray fluorescence measurements. Therefore, the planispherical GEM-based detector combines energy-resolved imaging capabilities with minimised parallax-induced broadening due to radially focused drift field lines. Additional multiplication stages can be added to increase the signal-to-noise ratio of individual X-ray photon events and to improve the sensitivity of the detector.

The minimisation of the parallax-induced broadening demonstrated by the presented planispherical GEM-based detector paves the way for applying optically read out gaseous detectors to applications such as X-ray crystallography or fluorescence, which require thick conversion regions. Guiding electrons along radially focused drift field lines in the conversion volume preserves the angular information of the incident radiation and results in more accurate representations of the incident X-ray photon field. The spatial resolution and the signal-to-noise ratio are significantly better preserved when employing radially focused drift field lines than in the standard case of parallel drift field lines in the conversion volume.

Optical readout is well-suited for X-ray crystallography because it is compatible with high particle rates and all incident light in the exposure window will be collected and recorded in integrated diffraction pattern images. While only limited energy resolution was achieved with optically read out GEMs, optical readout also presents an attractive readout modality for X-ray fluorescence as it enables full-field energy-resolved imaging. The planispherical GEM-based detector can be scaled up in size and the use of suitable lenses enables the optical readout of larger detectors. The high spatial resolution achievable by imaging sen-

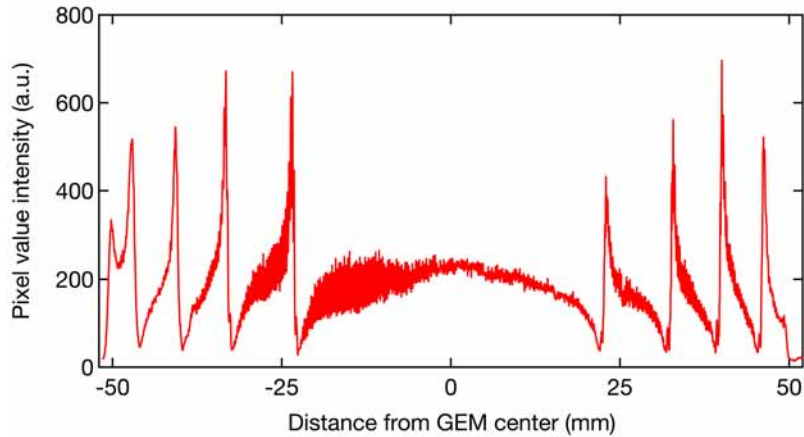


**Figure 56.** Line profile across flood exposure image for radially focused drift field lines: The horizontal line profile of the pixel value intensity across the flood exposure image shown in figure 55b taken with radially focused drift field lines shows unbalanced electron collection around the insulating gaps between individual segments of the segmented GEM electrodes.

sors is a key advantages of optical readout for such a detector for X-ray crystallography or fluorescence applications and the sensitivity of the detector to low-energy radiation may be extended by adding additional amplification stages.

### 5.3 Event reconstruction in an optically read out TPC

Augmenting 2D projections with associated depth information, TPCs enable 3D particle track reconstruction [91]. The versatility of TPCs has made them a widely used concept in particle detection and many varieties of TPC geometries and readout schemes have been developed and used. The TPC used in the ALICE experiment [92] at the LHC at CERN and the one used in the STAR experiment [93] at the RHIC at BNL are examples of currently operating large-scale TPCs. Large TPCs have also been at the core of previous experiments such as the ALEPH [94] and DELPHI [95] experiments at the LEP at CERN. Future experiments in a variety of research fields are also centred around TPCs such as the NEXT experiment for neutrinoless double beta decay search [96], liquid Xe based TPCs searching for nuclear recoils resulting from scattering dark matter particles [69], the DMTPC project focused on directional dark matter search [71] or for the tracking of heavy ions at the SuperFRS [36] at FAIR.

Optical readout is well-suited for reading out MPGD detectors at the endcaps of TPCs. The high spatial resolution and the economically efficient scalability of this readout approach can be used to realise optically read out TPCs based on amplification technologies such as GEMs. While 2D projections of particle tracks are obtained from optically read out images of the secondary scintillation emitted during avalanche multiplication in the GEMs, depth of interaction information such as from fast photon detectors can be used to enable 3D particle track reconstruction [97]. Optically read out TPCs are used in applications ranging from proton spectroscopy [72] and the study of two-proton decays [98] to studies in nuclear astrophysics with gamma-ray beams [99, 100] to directional dark matter search [71]. The high granularity of imaging sensors is also well-suited for the study of rare events such as low-energy nuclear recoils in the search for dark matter and is exploited by the CYGNUS collaboration in a proposed high-resolution TPC based on optical readout [101].

An optically read out GEM-based TPC was developed for studies of the applicability of optical readout to particle track reconstruction [102] and a readout scheme compatible not only with straight particle tracks but with more complex particle trajectories was demonstrated.

### 5.3.1 Detector concept

A TPC based on optically read out GEMs was realised and employed for 3D event reconstruction. The detector was based on a UHV-grade vessel housing a circular field shaper and a triple GEM-stack as shown in figure 57.

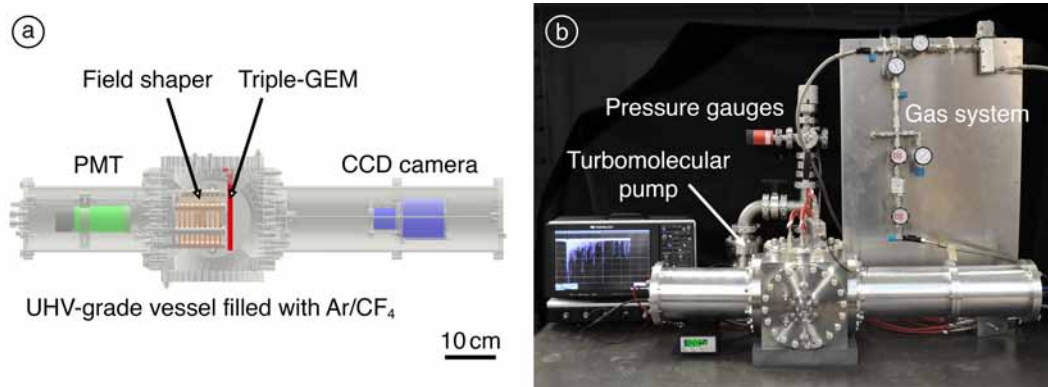


**Figure 57.** Optically read out TPC: (a) Schematic of the optically read out GEM-based TPC. A CCD camera faces the bottom of a triple-GEM stack. A PMT faces the conversion volume formed by a field shaper. The field shaper and the GEMs are housed in a UHV-grade vessel. (b) Optically read out TPC setup with turbomolecular pump for cleaning of the vessel and gas system for controlled filling of the chamber.

The chamber containing the detector elements was built from CF160 stainless steel components and had a volume of approximately 8 l. Two optical viewports located at opposite sides of the cubical vessel were facing the drift volume and the bottom of the GEM-stack. A 2-inch PMT (Hamamatsu R375 [61]) and a CCD camera (QImaging Retiga R6 [66]) were placed in front of the viewports and housed in attachable Al tubes for light shielding. The chamber was connected to a vacuum pumping system consisting of a rotary vane pre-pump and a turbomolecular vacuum pump. The pressure inside the chamber was monitored by multiple pressure and vacuum gauges including a combined Pirani-type and capacitive gauge, a combined Pirani-type and cold cathode gauge and a capacitive high pressure transducer to continuously cover all pressure regimes from high vacuum to several bar overpressure. Additionally, a gas monitoring and recirculation system consisting of multiple monitoring devices, valves to control the gas flow and a getter cartridge were connected to the vessel to provide information about the gas flow and pressure when filling or flushing the vessel as well as to allow gas purification during sealed mode operation.

A stainless steel mesh was used as a cathode at the top of the active region. The adjacent field shaper with a diameter of 10 cm and a length of 10 cm consisted of multiple ring-shaped Cu electrodes, which were interconnected with a chain of resistors inside the vessel to achieve the desirable potential gradient over the whole length of the drift region. The GEM electrodes were individually connected to Safe High Voltage (SHV) feedthroughs and biased with a resistor-based voltage divider located outside of the vessel. The  $10 \times 10 \text{ cm}^2$  active area GEMs were glued onto ceramic frames and mounted in a triple-GEM stack with 2 mm transfer gaps between the individual foils.

Aiming at long-term sealed mode operation of the device as well as high gas purity, a special focus was put on the selection of materials to be placed in contact with the gas volume. Low-outgassing materials such as ceramic frames and PolyEther Ether Ketone (PEEK) plastic were used for mechanical support structures for the detector elements and only metallic gaskets and all-metal valves were used for sealing the chamber as well as the associated vacuum and gas systems. While polyimide is not well-suited for low-outgassing environments, electrical connections inside the chamber were made by polyimide-insulated wires to achieve good high-voltage insulation. Clamping was used to mitigate the use of solder in the chamber.

### 5.3.2 Detector operation

Prior to gas filling, the vessel was pumped to pressures below  $1 \times 10^{-5}$  mbar by a turbo-molecular pump backed by a rotary vane pump. Extended pumping for several days was used to minimise contamination of the gas due to outgassing from detector components or adsorbed gases. Mass flow controllers were used to mix the desired gas mixtures from pure gases and stainless steel gas pipes were used for all connections from the gas bottles to the detector vessel. After cleaning the chamber and prior to gas filling, input gas lines were purged with a gas flow of 5 l/h. Subsequently, the chamber was filled with the same gas flow rate up to atmospheric pressure. After filling, the chamber was flushed with the desired gas mixture for several hours to ensure high gas purity. The detector was then operated either in sealed or open gas flow mode depending on the performed measurements.

The individual electrodes of the three GEMs used as multiplication and scintillation stages in the detector were biased with a resistor-based voltage divider. The top electrode of the third GEM in the stack was grounded to permit easy tuning of the gain of the third GEM by varying the positive bias voltage of the bottom electrode without changing the transfer field or any other voltage gradients in other amplification stages. Operated at voltage drops of approximately 400 V across each GEM, the triple-GEM achieved gains of  $10^3$  to  $10^4$ . The field shaper was biased by applying negative bias voltages on the cathode mesh and the bottom ring-shaped electrode with the equal resistors interconnecting all ring-shaped electrodes of the field shaper resulting in a linear voltage drop along the field shaper. Limited by the high-voltage stability of the 10 kV-SHV-feedthrough used to bias the cathode, a maximum drift field of 500 V/cm could be achieved. Typically, the detector was operated with drift fields ranging from 100 V/cm to 300 V/cm although much lower drift fields were explored as well.

The PMT was operated with a moderate negative voltage of 1000 V corresponding to a gain of about  $5 \times 10^5$  as this provided sufficient dynamic range to detect single photon signals as well as record high-intensity secondary scintillation pulses from alpha track events.

Event reconstruction studies of the TPC were performed using signals from alpha particles, which provide a high signal-to-noise ratio due to their high energy loss in the gas. The straight tracks of alpha particles with energies of several MeV can be unambiguously identified and reconstructed and were therefore well-suited for establishing event reconstruction capabilities of the TPC. Alpha particles from the decay of  $^{220}\text{Rn}$  to  $^{216}\text{Po}$  were introduced into the TPC as described in section 5.1.6.

The primary scintillation light emitted by particles interacting in the conversion volume as well as the secondary scintillation light emitted during electron avalanche multiplication in the triple-GEM stack were registered by a PMT and recorded with an oscilloscope trig-

gering on the high-intensity secondary scintillation signals. The output signal of the PMT was also connected to a Nuclear Instrumentation Module-based (NIM-based) discriminator, which generated a NIM-level pulse when the signal crossed a certain threshold amplitude. The generated pulse was used to trigger the oscilloscope and acquire the waveform from the PMT. Simultaneously, the pulse from the discriminator was used to control the image acquisition with the CCD camera. The CCD camera used for recording the scintillation light emitted during electron avalanche multiplication was operated in bulb triggering mode, which allowed direct control of the shutter operation with external Transistor-Transistor Logic (TTL) signals. In bulb triggering mode, the shutter of the camera opened when the level of the TTL signal changed from a low to a high level and remained open until the signal changed back to a low level. With a response time of the shutter of approximately  $100\ \mu\text{s}$  after the change of the level of the trigger signal, the external TTL triggering of the camera allowed direct control of the shutter operation. The shutter of the camera was opened as soon as the system was ready for a new event after processing the previous one. It remained open until an event was registered by the PMT and was closed by the pulse generated by the discriminator from a PMT signal crossing the set threshold. This resulted in exposure times varying from event to event depending on the random occurrence of alpha decays in the active volume of the detector. In addition to the PMT waveform being recorded and the CCD exposure being stopped as soon as an event was registered, the acquired data was transferred to an online analysis script or saved for later offline reconstruction depending on the operation mode of the TPC.

### 5.3.3 Live event reconstruction

Augmenting the 2D projections of events obtained from the images recorded by the CCD camera with timing information from the PMT permitted 3D event reconstruction in the optically read out TPC. For highly ionising particles like alpha particles, the primary scintillation in the drift volume was sufficiently strong to be measured with the PMT. As the primary scintillation light pulse occurred upon interaction of the incident particles in the drift volume, it was used to determine the time  $t_0$  of the occurrence of an event in the TPC. The secondary scintillation light was emitted only after electrons have drifted towards and reached the GEMs and the time between primary and secondary scintillation light therefore corresponds to the drift time of the electrons. With a known drift velocity for a specific electric field strength in the drift region, this time difference between primary and secondary scintillation could be converted into depth of interaction information. The emission of primary scintillation light is a fast photon production mechanism and previous studies of the time spectra of scintillation light emission from pure  $\text{CF}_4$  and  $\text{Ar}/\text{CF}_4$  gas mixtures have shown that typical effective lifetimes of the involved excited states are on the order of 5 ns to 10 ns [46, 103]. Compared to the much longer electron drift times in the TPC, the decay times of the excited states leading to scintillation light emission do not significantly contribute to the uncertainty in the determination of Z-coordinates from time differences between primary and secondary scintillation signals.

Combined with 2D information from CCD images, this readout approach provided 3D information of events in the TPC and permitted 3D reconstruction of particle tracks. An example of an image of an alpha track recorded in the optically read out TPC is shown in figure 58a. The high granularity of the employed imaging sensor provides a 2D projection of the event with high spatial resolution and the strong signal amplification and associated

high scintillation light intensity achieved by the triple-GEM multiplication structure resulted in a high signal-to-noise ratio.

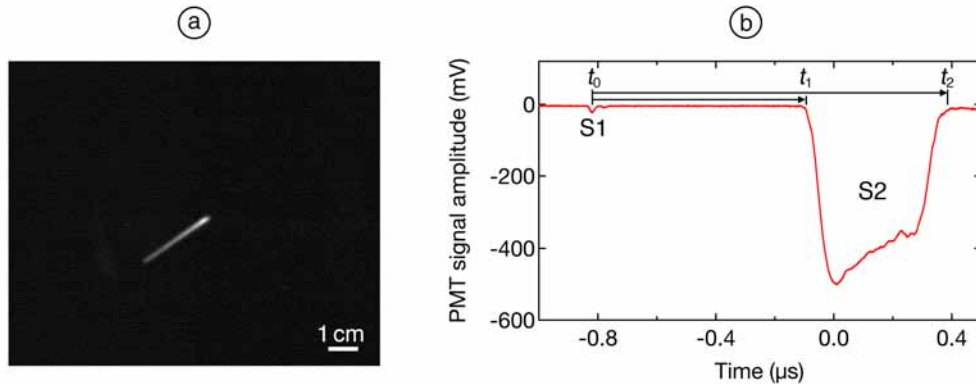


**Figure 58.** Image of alpha particle track and PMT waveform: (a) An optically read out image provides X-Y-information for track reconstruction with high spatial resolution. (b) The signal from a PMT is used to determine the track inclination and the depth of interaction from the time difference between the time  $t_0$  of the primary (S1) scintillation signal and the times  $t_1$  and  $t_2$  of the beginning and end of the secondary (S2) scintillation pulse, respectively.

An example of an acquired PMT waveform is shown in figure 58b. In the shown example, the primary scintillation signal with a low amplitude occurred about  $t_0 = 0.8 \mu\text{s}$  before the secondary scintillation pulse, which exhibits a significantly higher amplitude and width. Multiplying the time difference  $\Delta t_1 = t_1 - t_0$  between the primary scintillation and the beginning of the secondary scintillation pulse with the drift velocity of electrons in the drift region yields the Z-coordinate of the track point closest to the surface of the GEMs. Similarly, multiplying the time difference  $\Delta t_2 = t_2 - t_0$  between the primary scintillation and the end of the secondary scintillation pulse with the drift velocity of electrons in the drift region yields the Z-coordinate of the track point farthest from the surface of the GEMs. While these two coordinates provide information about the absolute position of the track in the drift volume and its extent along the Z-axis, they do not suffice to unambiguously reconstruct the track. To combine the Z-coordinates of the farthest and closest track points with the start and end points of the track in the CCD images to a 3D reconstructed event, the obtained Z-coordinates must be assigned to the start and end points of the track in the 2D projections. This requires knowledge of the orientation of the track, i.e. the orientation of the trajectory of the detected particle. The Bragg curve of the energy loss of a particle along its path in the active detection volume can be used to determine the orientation of the track and resolve any residual ambiguity in the track reconstruction from a combination of a 2D projection with depth of interaction information from the PMT. The energy loss profile along the track can be determined from a PMT waveform as well as from a CCD image as shown in figure 59.

The secondary scintillation light signal in the PMT waveform of a fully contained alpha particle exhibits a pronounced peak at either the beginning or the end of the pulse. The structure encoded in the secondary scintillation light corresponds to the energy loss of the particle and can be used to determine if the end of the trajectory of the particle denoted by the Bragg peak of maximum energy loss occurred at the beginning or the end of the secondary scintillation signal. A Bragg peak at the beginning of the secondary scintillation signal denotes a particle trajectory oriented towards the surface of the GEMs, while a Bragg peak at the end of the secondary scintillation signal corresponds to a particle trajectory oriented towards the cathode. Similarly, a line profile of the pixel value intensity along a

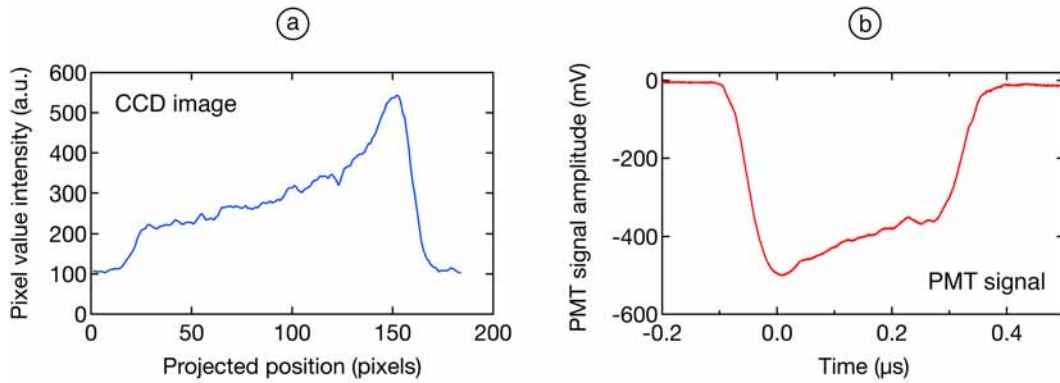


**Figure 59.** Energy loss profiles along alpha track: (a) A line profile of the pixel value intensity along the alpha track from figure 58a shows the Bragg peak at the end of the track. (b) The structure visible in the PMT waveform of the secondary scintillation allows a determination of the orientation of the trajectory of the observed alpha particle.

particle track in an image recorded by the CCD camera also yields the energy loss curve of the particle and exhibits a pronounced Bragg peak at one end of the track. Combining the knowledge of the orientation of the track from the structure of the secondary scintillation peak with the identification of the end of the track in the CCD image, an unambiguous assignment of the closest and farthest Z-coordinates of the particle track to the beginning and end points of the track in the 2D projection is possible and permits a determinate 3D reconstruction of the event. A visualisation of exemplary reconstructed alpha tracks is shown in figure 60.

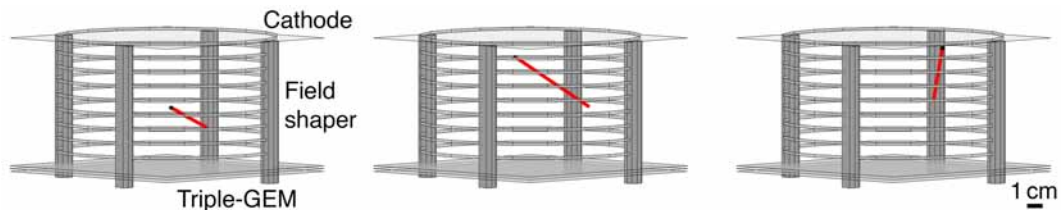


**Figure 60.** Reconstructed alpha tracks: Exemplary 3D reconstructions of alpha tracks (red) from CCD images and PMT waveforms visualised in the field shaper of the optically read out TPC. The black dot denotes the starting point of the alpha track.

The data acquisition and event reconstruction workflows were automated to permit live 3D reconstruction and online event display [102]. Once the processing of the previous event was completed, a data acquisition and control script notified other components of the data acquisition system about its readiness for a new event through a microcontroller used to send an enable signal to the NIM-based electronics. The NIM-based electronics were used to control the shutter of the camera and the triggering of the oscilloscope. This opened the shutter of the camera which remained open until an event was registered by the PMT. Upon the registration of an event, the shutter of the camera was closed, the acquisition of the PMT waveform by the oscilloscope was triggered and the data acquisition script was notified of the presence of new data through a microcontroller used as an interface between analogue TTL signals and the digital control software. Subsequently, the acquired image from the CCD camera and the acquired PMT waveform were transferred to the data acquisition script. Employing the described event reconstruction algorithm, the 2D projection from the image and timing information from the PMT waveform were assembled to a 3D reconstruction of the event and the event was displayed on-screen. Once reconstruction and display were completed, the system was ready for the next event. Limited by the transfer of

data from the oscilloscope and the CCD camera to the computer, a rate of approximately one to two displayed events per second could be achieved. The rate of displayed events may be significantly increased by employing a camera with a lower readout time, faster data acquisition links and optimised event reconstruction algorithms.

The reconstructed tracks of alpha particles from the decay of  $^{220}\text{Rn}$  flushed into the detector vessel were used to measure the distribution of track lengths in the optically read out TPC. After 3D reconstruction of events, the length of the track was calculated and the distribution of obtained alpha track lengths is shown in figure 61.

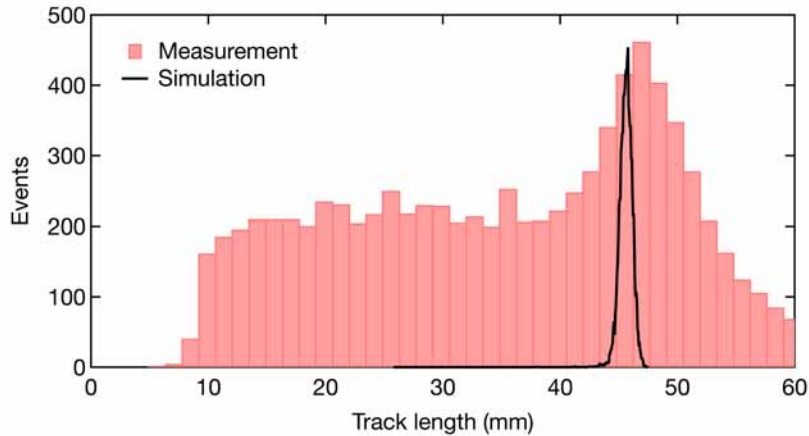


**Figure 61.** Reconstructed track lengths of alpha particles: The measured track length distribution of reconstructed tracks of alpha particles with an energy of 6.4 MeV in an Ar/CF<sub>4</sub> gas mixture with a mixing ratio of 80/20% at atmospheric pressure exhibits a maximum at around 45 mm, which is in agreement with the simulated track length distribution. Shorter track lengths correspond to partially contained tracks.

The distribution of alpha track lengths exhibits a maximum at track lengths of about 45 mm with a lower and approximately constant number of tracks with shorter track lengths and some reconstructed tracks with longer lengths. The randomness of the origins of the trajectories of the alpha particles resulting from the use of the gaseous  $^{220}\text{Rn}$  source leads to a high number of events not being fully contained in the active volume of the detector. The parts of the tracks of these events registered by the detector resulted in the events with short track lengths. Below 10 mm track length, the employed reconstruction algorithm could not perform 3D event reconstruction with acceptable confidence and these events were excluded from further analysis. The peak in the track length distribution at around 45 mm corresponds to the tracks of fully contained alpha particles. The expected length of the tracks of the 6.4 MeV alpha particles from the decay of  $^{220}\text{Rn}$  in the Ar/CF<sub>4</sub> gas mixture with a mixing ratio of 80/20% used in the detector was calculated with a simulation in Geant4 [104] (G. Galgóczi) and is shown in figure 61. The observed peak in the experimentally obtained distribution of track lengths of the alpha particles agrees well with the simulated track length, which confirms the correct operation of the detector and validates the event reconstruction algorithm. The appearance of some longer track lengths in the observed distribution is attributed to shortcomings of the reconstruction algorithm and the consecutive alpha decay of the decay product of  $^{220}\text{Rn}$ ,  $^{216}\text{Po}$ . If the decay of  $^{216}\text{Po}$  occurs shortly after the initial decay of  $^{220}\text{Rn}$ , alpha particles emitted by both decays might be recorded within the same CCD image. The algorithm used to determine 2D projections of tracks was not suited to disentangle such events which might result in some overestimated track lengths.



### 5.3.4 Combined optical and electronic readout

Combining the 2D projection of particle trajectories obtained from optically read out images of the scintillation light produced during electron avalanche multiplication in the GEM-based multiplication stage of an optically read out TPC with timing information from a PMT permits 3D event reconstruction of events with measurable primary scintillation intensity and straight particle trajectories. For weakly ionising particles which do not produce primary scintillation light of detectable intensity or more complex trajectories, the depth of interaction information required for 3D event reconstruction cannot be obtained from the time difference between primary and secondary scintillation signals. Therefore, event reconstruction in the optically read out TPC is limited to highly ionising straight particle tracks like alpha particle tracks when relying on the time difference between primary and secondary scintillation signals for the determination of the depth of interaction of the measured particle. To overcome this limitation, the Z-coordinates needed to go from a 2D event projection to a 3D reconstructed event representation can be obtained from the arrival time of the electrons at the multiplication stage at one end of the TPC. However, CCD, CMOS or EMCCD imaging sensors do not provide sufficient frame rates for a determination of the difference in the arrival time of electrons along the track of particles which should be detected. With frame rates of tens or hundreds of frames per second, even modern imaging sensors are much too slow to record multiple frames per event, which would allow a determination of the arrival times of electrons from different locations along the particle trajectory in the active volume of the detector. Fast readout electronics as used in the conventional electrical readout of MPGDs, however, are capable of recording the arrival time of electrons with sufficient temporal resolution to determine the depth of interaction along the trajectory of a particle. By combining the high spatial resolution provided by optical readout with the fast readout speed of electrical readout, 3D event reconstruction can be performed without the need for timing information from PMT waveforms. To permit the reconstruction of more complex particle trajectories, electrical signals used for depth of interaction determination must be recorded with associated coarse position information. This can be achieved by a segmented anode with limited granularity below the triple-GEM multiplication stage used in the optically read out TPC. Electrons produced during avalanche multiplication in the holes of the GEM will induce electrical signals in an anode placed below the last GEM in the multiplication stage when moving from the holes of the last GEM towards the anode. These induced signals can be picked up and recorded with amplifying electronics and an oscilloscope or dedicated readout electronics. The arrival time of the electrical signals allows a determination of relative Z-coordinates of the track of the detected particle as shown conceptually in figure 62.

Spatial granularity in the electrical readout of an anode below the triple-GEM stack can be achieved by a pixelated anode or anodes with strips in one or two dimensions. To permit electrical signal readout and simultaneous recording of secondary scintillation light from the GEM by a camera, a transparent anode needs to be used. Combining electrical conductivity and optical transparency in the VIS wavelength range, Indium Tin Oxide (ITO) can be used to manufacture transparent anodes. ITO layers can be easily deposited by evaporation or sputtering and are widely used as transparent electromagnetic shielding. The deposited ITO layer thickness can be tuned to achieve desired values of sheet resistivity as well as optical transparency with 25 nm thick layers exhibiting a typical sheet resistivity of  $100 \Omega/\square$  and thicker layers of 450 nm exhibiting a significantly lower sheet resistivity of  $4 \Omega/\square$ . The

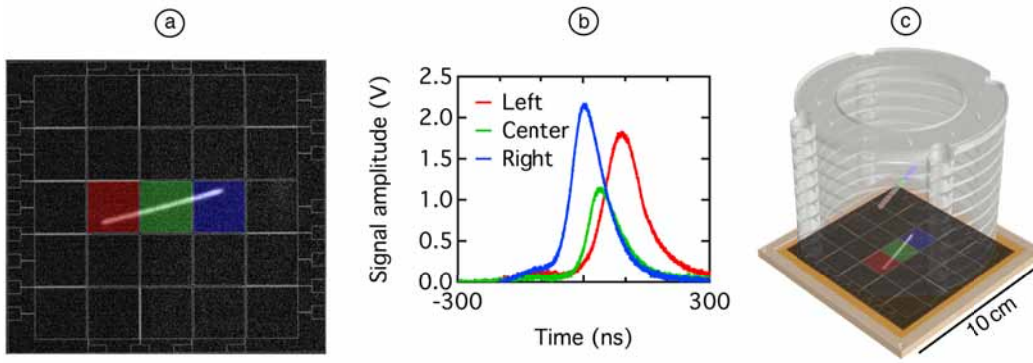


**Figure 62.** Combined optical and electronic readout for track reconstruction: (a) An optically read out 2D image provides a high spatial resolution 2D projection of a particle track. A pixelated anode pattern is shown as overlay and three hit and electronically read out pads are identified by colour. (b) Electronic signals from three central pads corresponding to the coloured pads in the optical image display differences in signal arrival time which translates to relative depth information between different sections of the track. (c) Schematic visualisation of particle track reconstructed from a combination of optically obtained 2D information and depth information extracted from electronically read out signals.

wavelength-dependent optical transparency of ITO films depends mostly on the film thickness with thicker layers exhibiting some undulation as shown in figure 63.

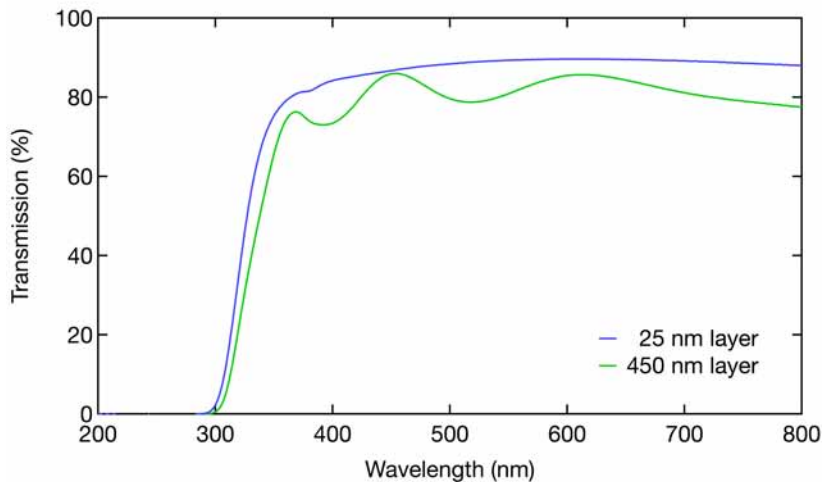


**Figure 63.** Optical transmission of ITO films: ITO films exhibit a maximum optical transparency of about 80 % in the VIS wavelength range. The transparency drops sharply below 350 nm and thicker layers display undulation of the transparency with wavelength and an overall decreased optical transparency. The transparency of ITO films on 1.1 mm thick glass substrates was measured for wavelengths ranging from 200 nm to 800 nm.

The properties of ITO have previously been used in optically read out GEM-based detectors for electrical signal collection and recording of energy spectra by a transparent anode [105]. However, using unstructured full-plane anodes, the depth information encoded in the arrival times of the electrical signals could not be associated with 2D information from the optical readout.

Taking advantage of micro-fabrication techniques, structured anodes for combining optical and electrical readout in an optically readout TPC were manufactured [106]. Commercially available, ITO-coated glass substrates with a substrate thickness of 1.1 mm and an ITO-layer thickness of nominally 25 nm corresponding to a sheet resistivity of  $100 \Omega/\square$  were used as base material. Pixelated anodes with  $5 \times 5$  pads with dimensions of  $2 \times 2 \text{ cm}^2$  each

were manufactured from these ITO-coated glass plates with dimensions of  $11 \times 11 \text{ cm}^2$ . The ITO-coated glass plates were covered with a UV-sensitive photoresist by spin coating. Subsequently, the pad pattern was exposed with a direct laser lithography system achieving a spatial resolution of  $2.5 \mu\text{m}$  before the photoresist was developed to expose regions which should be insulating and free of ITO. The ITO film in the exposed regions was removed by etching in hydrochloric acid (HCl) with a concentration of 32%. The 25 nm thick layer of ITO was etched and completely removed in the exposed regions by this solution in less than 1 min. Finally, the remaining photoresist was removed in an acetone bath and the anodes were cleaned with isopropanol and dried in flushing  $\text{N}_2$ .

The patterned ITO-based anodes were glued onto ceramic frames to be mounted below the triple-GEM stack in the multiplication stage of the optically read out TPC. An induction gap thickness of 5 mm between the last GEM and the anode was chosen for high-voltage stability and ease of connectivity. The 25 pads of the pixelated anode were connected to contact pads outside of the active area of the anode by narrow ITO-based tracks with a width of  $200 \mu\text{m}$ . While 16 pads on the outside of the active region were connected to contact pads with short tracks, longer tracks in between pads were used to contact the inner pads. The pad pattern and the corresponding connection pads are shown as an overlay on the ITO anode mounted in the TPC in figure 64.

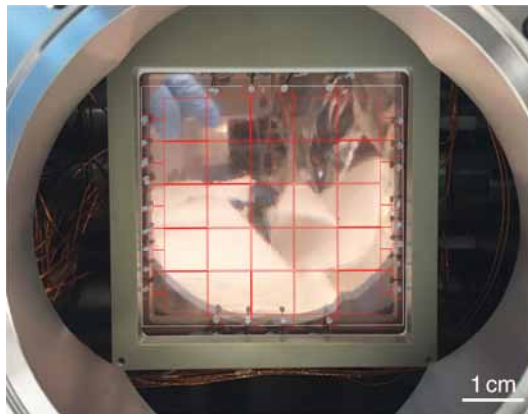


**Figure 64.** ITO pad anode: The view into the TPC as seen by the CCD camera shows the ITO pad anode mounted below a triple-GEM stack. The pad pattern and the connection pads corresponding to individual pads are shown as an overlay in red.

The narrow track width combined with the thin ITO-layer used for the conductive paths between anode pads and contact pads resulted in series resistances of about  $2.5 \text{ k}\Omega$  for the outer pads and up to  $17.5 \text{ k}\Omega$  for the inner and central pads. The anode pads were electrically connected to the outside of the detector vessel by coaxial, polyimide-insulated cables leading from the contact pads on the ITO-based anode to a multi-pin electrical feedthrough. After fixing the insulation of the coaxial cables to the ceramic frame holding the ITO-based anode with two-component adhesive for mechanical stability, the central contacts of the coaxial wires were electrically connected to the contact pads on the anode with Ag-loaded adhesive. The shields of the individual coaxial cables were connected together, grounded and connected to a solid ITO-frame on the outside of the anode around the active area to minimise coupling to potential sources of electronic noise. Outside of the detector vessel, the readout electronics were connected to the multi-pin feedthrough with a custom adapter PCB with the possibility for adding series resistances and capacitive voltage dividers for each individual readout channel.

Electrical signals from the pads of the ITO-based anodes were read out with a readout hybrid board based on the APV25 ASIC [107] connected to the RD51 scalable readout system [108], both of which were developed for the electrical readout of MPGD-based detectors. While the employed APV25 ASIC was capable of reading out up to 128 channels, only 25 channels were used for reading out the structured transparent anode with  $5 \times 5$  pads. The ASIC requires an external trigger signal to begin data acquisition, which was supplied by a NIM-level pulse from a discriminator generated when the high-intensity secondary scintillation pulse of an event in the detector was registered by the PMT. Signal waveforms of all 25 channels were acquired in 27 time bins with a width of 25 ns each resulting in a width of the acquisition window of 675 ns. For the electron drift velocity of 8 cm/ $\mu$ s in an electric drift field of 300 V/cm this corresponds to a maximum recordable drift distance of 5.4 cm. For this electron drift velocity, the 25 ns width of the time bins in the employed APV25 ASIC corresponds to a Z-depth range of 2 mm and limits the achievable Z-resolution of the TPC.

The same signal used for triggering electrical data acquisition by the APV25 ASIC was used to stop the exposure of the CCD camera achieving synchronisation of electrical and optical readout. Therefore, for each recorded electrical signal, a corresponding image was recorded by the CCD camera, which permitted direct mapping of electrical signals to optical images for 3D reconstruction by reconstruction algorithms.

To achieve high signal-to-noise ratios in the optically obtained images, the triple-GEM multiplication stage had to be operated at moderate to high gain factors in order to provide ample scintillation light intensity. This also created a large number of secondary electrons inducing large-amplitude signals in the anode. Consequently, the limited dynamic range of the employed APV25 ASIC was often exhausted, which resulted in the saturation of readout channels. To mitigate this saturation, capacitive voltage dividers were used on each readout channel to attenuate the signals reaching the APV25 ASIC. Trials showed that high attenuation factors of several  $10^3$  were necessary for recording electrical signals from alpha particles without saturation and an attenuation factor of  $4.7 \times 10^3$  was chosen and realised on the adapter PCB between the electrical feedthrough and the APV25-based hybrid board by a 100 pF series capacitor and a 470 nF capacitor to ground on each readout channel. Additionally, the differences in the series resistances between individual readout channels resulting from the different lengths of ITO-tracks connecting the anode pads to the contact pads were compensated by adding additional series resistances of 7.5 k $\Omega$  or 15 k $\Omega$  for each channel to equalise the total series resistance between each anode pad and the APV25 ASIC to approximately 17.5 k $\Omega$ .

Event reconstruction of particle tracks from 2D projections obtained with a CCD camera and timing information from the electrical signals from the ITO-based pixelated anode was performed by an offline event reconstruction algorithm. The maximum amplitude of the waveform recorded for each anode pad was extracted and pads with a maximum signal amplitude above a certain threshold were identified as hit pads. For each of these hit pads, the arrival time of the signal was extracted by 30% constant fraction discrimination with linear interpolation on the rising edge of the waveforms to account for varying pulse rise times for signals with different maximum amplitudes. The time at which the signal crossed 30% of the maximum amplitude was used as a measure for the arrival time of the signal. The differences in the arrival time of the electrical signal between different pads were converted to differences in the depth of interaction by multiplying the time differences by the drift velocity of electrons in the applied drift field. While this procedure yields information about the relative depth of interaction between pads, it does not provide absolute depth of interaction

information. An example of the relative depth information of the track of an alpha particle obtained from an ITO-based anode with pads is shown in figure 65a.

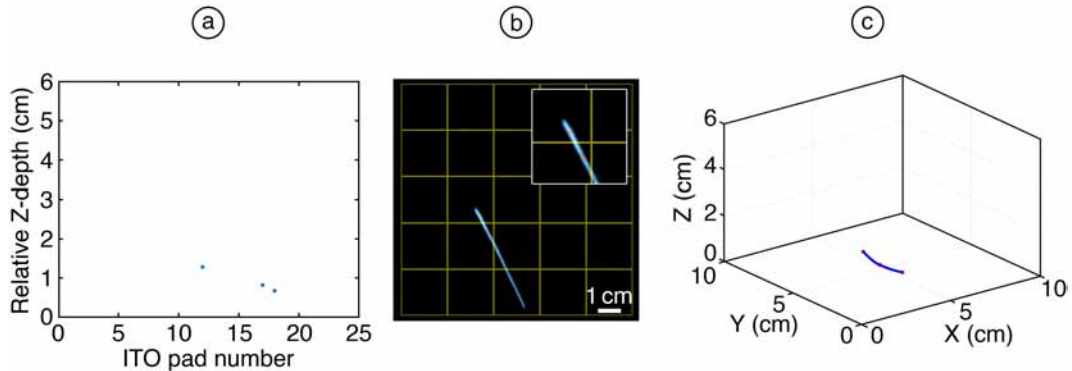


**Figure 65.** 3D reconstruction with ITO pad anode: (a) Relative depth information on several pads determined from electronic signals read out by APV25 ASIC. (b) Optical image of 2D track projection with ITO pad anode pattern shown as overlay (yellow). Inset: Identified bright pixels (blue) and hit locations within each pad (red). (c) 3D visualisation of reconstructed track.

The 2D projection of the track was obtained from the optically read out image of the secondary scintillation light. The image acquired by the CCD camera was filtered with a median filter to remove hot pixels and the background offset determined by the mean value of randomly sampled pixels was subtracted. The randomly selected pixels were also used to determine the standard deviation of the background of the image and a binary version of the image was obtained from comparing the pixel value intensity of each pixel with a threshold value several standard deviations above the mean value of the background. To combine the depth of interaction times obtained by electrical readout with the 2D projection, the hit positions of the tracks on the anode pads had to be identified. Since only a single depth of interaction value was available for each anode pad with an area of  $2 \times 2 \text{ cm}^2$ , this depth of interaction value had to be assigned to a specific 2D point along the track for 3D reconstruction. From the known location and extent of each of the anode pads in the optically obtained images, the bright pixels within each pad were identified in the obtained binary image and the mean values of the X and Y-coordinates of all bright pixels within each pad were determined and used as the 2D hit location within a certain pad as shown in figure 65b. The depth of interaction information for each hit pad from the electrical signals was assigned to the 2D hit location of the track segment within each pad. This procedure resulted in some 3D points along the track with 2D information obtained from an optically readout picture and depth information obtained from electronic signals. Subsequently, 3D tracks were reconstructed by cubic spline interpolation between the determined 3D points. An example of a reconstructed track of an alpha particle is shown in figure 65c. The presented method allows the determination of the inclination of particle tracks without relying on information from a PMT. However, without an absolute electron drift time obtained from the time difference between primary and secondary scintillation signals, no absolute depth coordinates can be determined. The developed transparent ITO-based anodes with multiple pads present a first step towards transparent anodes for optically read out GEM-based TPCs. The large pad size of  $2 \times 2 \text{ cm}^2$  of the ITO pad anode resulted in a very low number of electronically read out channels being hit in a single event. Consequently, the determination of relative Z-coordinates from the arrival times of electrons at different pads of the anode was rather coarse resulting in a poor resolution in the Z-coordinate of the reconstructed tracks.

Higher granularity ITO-based anodes with smaller pads or strips may be used to extend the reconstruction capabilities of the optically read out TPC to more complex particle trajectories. Following the initial results from the ITO pad anode, an ITO strip anode with higher granularity was developed. Building upon the experience of electrical signals being attenuated by the high resistance of the ITO tracks in the case of the ITO pad anode, a thicker ITO layer was used as base material for an ITO strip anode. A 450 nm thick ITO layer on a 1.1 mm glass substrate with a nominal sheet resistivity of  $4 \Omega/\square$  was used as base material for an ITO strip anode. A strip pattern of 48 strips with a width of 1.5 mm and a pitch of 2 mm covering the  $10 \times 10 \text{ cm}^2$  active area of the GEMs in the optically read out TPC was manufactured in a similar way to the ITO pad anode. The thicker ITO layer required significantly longer etching times and electrical insulation between individual strips could only be obtained after 17 min of etching in HCl with a concentration of 32%. The structured ITO strip anode was then glued onto a ceramic frame and fixed to a connection PCB, which was used to connect individual ITO strips to the readout channels of an APV25 hybrid board with a capacitive voltage divider on each individual channel. As Z-connection tape, elastomeric connectors and Ag-loaded adhesive did not succeed in creating reliable electrical connections between ITO strips and the connection PCB, individual wires were soldered to the connection PCB and bent to mechanically contact ITO strips and the electrical connection was ensured by Ag-loaded adhesive between individual wires and ITO strips. The ITO strip anode is shown in figure 66 along with the connections between the readout PCB and the individual ITO strips.

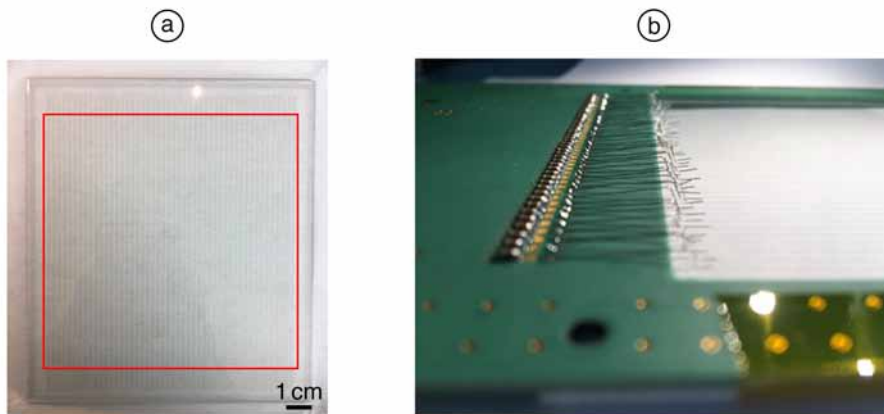


**Figure 66.** ITO strip anode: (a) ITO strip anode on glass substrate with active area shown by red overlay. (b) The connections between the ITO strip anode and the connection PCB were made with wires and Ag-loaded adhesive.

The ITO strip anode was mounted in the optically read out TPC after the triple-GEM multiplication stage with an induction gap thickness of 4 mm. Optical images of the scintillation light produced in the GEM multiplication stage were recorded through the ITO strip anode with a CCD or EMCCD camera (Hamamatsu ImagEM X2 C9100-23B [61]) operated in bulb mode with external triggering as in the case of the ITO pad anode described above. Obtained optical images displaying 2D projections of events were processed by subtracting an averaged background image and by median filtering the image with each pixel being assigned the median value of a  $4 \times 4$  neighbourhood to correct for hot pixels. In the case of readout with an EMCCD camera, an electron multiplier gain of  $10^3$  and no pixel binning were used for recording projections of alpha particles. For other types of radiation events such as cosmic events, the maximum electron multiplier gain of the EMCCD camera of

$1.2 \times 10^3$  was used. After image processing, the strip pattern of the anode was overlaid on the image and bright pixels within each strip were identified. The mean values of the X and Y-coordinates of the bright pixels within each strip were calculated and used as strip hit locations. An example of the image processing and analysis steps performed for each event is shown in figure 67.

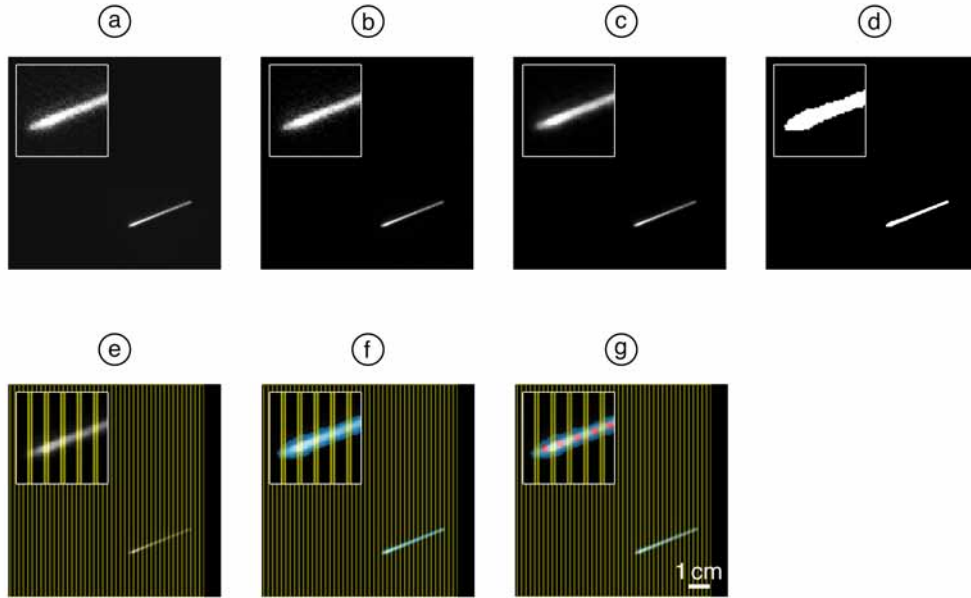


**Figure 67.** Image processing and analysis for reconstruction with ITO strip anode: (a) Raw image of event recorded by camera. (b) Image with averaged background image subtracted. (c) Median filtered image to correct for outliers. (d) Binary image obtained with threshold of several standard deviations above the background level. (e) Pattern of ITO strip anode shown as overlay (yellow). (f) Bright pixels identifying track shown in blue. (g) Strip hit locations determined from mean X and Y-coordinates of bright pixels within each strip shown in red.

Electronic signals from the ITO strips of the anode read out by an APV25 ASIC were used to determine relative Z-depth information to be assigned to the determined hit locations on each strip. An example of the waveforms on different strips of a single event of an alpha track in the TPC is shown in figure 68a.

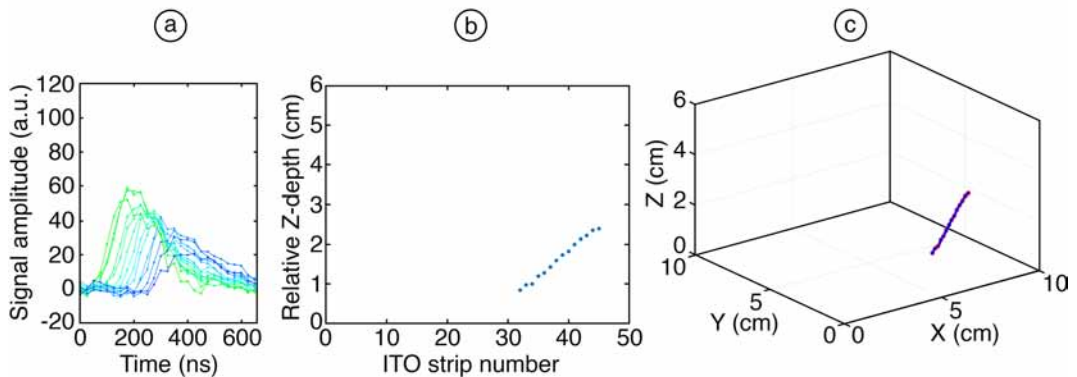


**Figure 68.** Electronic signals and 3D reconstruction with ITO strip anode: (a) Waveforms of electronic signals from individual anode strips. (b) Relative Z-depth information on different strips from electronic signals. (c) 3D visualisation of alpha track with 2D projection from optical image and relative Z-depth information from electronically read out signals.

The arrival time of electronic signals was determined by constant fraction discrimination at 30 % with linear interpolation on the rising edge of the waveforms. The differences in arrival time were then translated to differences in Z-depth. An example of the obtained Z-depth for each hit strip is shown in figure 68b. Assigning the Z-depth information of hit strips to the 2D hit locations extracted from the optically read out image as shown in figure 67g, a 3D visualisation of an alpha track as shown in figure 68c could be obtained with a much better resolution than in the case of the ITO pad anode.

For reconstructing 3D tracks of alpha particles with the ITO strip anode, electronic signals were recorded with a capacitive voltage divider with an attenuation factor of  $10^2$  between individual ITO strips and readout channels of the APV25 ASIC to mitigate saturation of readout channels. During manual contacting of ITO strips and mounting of capacitive dividers, some shorts between neighbouring strips resulted in several channels not responding correctly as shown in figure 69a. Nevertheless, the majority of ITO strips responded properly and could be used for electronic signal readout. The employed attenuation factor of  $10^2$  was sufficient to minimise the saturation of the readout channels of the APV25 ASIC with only a small fraction of electronic signals saturating the readout electronics as shown in figure 69b.

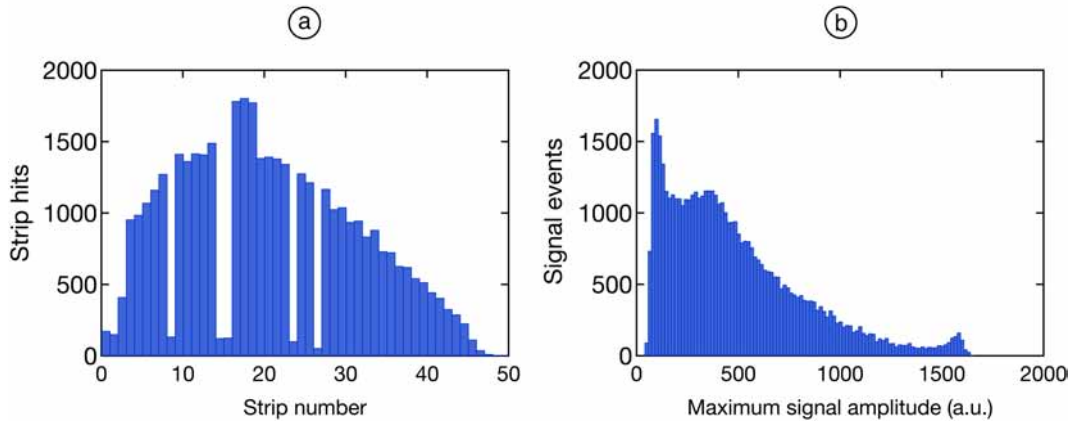


**Figure 69.** Hits per strip and signal amplitude on ITO strip anode: (a) The distribution of hits per strip on the ITO strip anode shows some dead channels. (b) The histogram of the maximum signal amplitude on the ITO strip anode for  $5 \times 10^3$  alpha particle events recorded with an attenuation factor of  $10^2$  displays some minor saturation.

The combination of high-resolution 2D projections from optically read out images and Z-depth information from an ITO strip anode with moderate granularity permitted accurate 3D reconstruction of particle tracks with good resolution [106]. Similarly to the 3D reconstruction performed with a combination of data from a CCD camera and a PMT, the distribution of track lengths of alpha particles flushed into the TPC could be measured. The distribution of track lengths of alpha particles with an energy of 6.4 MeV from the decay of  $^{220}\text{Rn}$  in the GEM-based TPC is shown in figure 70.

As in the case of reconstruction from CCD and PMT data, the track length distribution exhibits a peak corresponding to fully contained alpha tracks and a large fraction of shorter track lengths attributed to partially contained alpha tracks. The shift towards shorter track lengths might be attributed to missing Z-depth information from some ITO anode strips due to contacting issues between several ITO strips and readout channels of the APV25 ASIC.

In addition to permitting 3D reconstruction of straight tracks, the ITO strip anode extended the reconstruction capabilities of the GEM-based TPC to more intricate track geometries. Employing the same reconstruction methods as used for alpha particle tracks, cosmic events



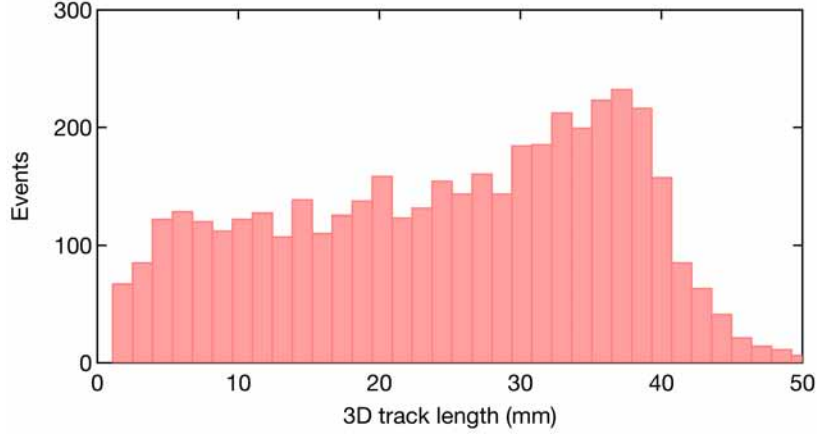


**Figure 70.** Alpha track length from 3D reconstructions with ITO strip anode: Fully contained alpha tracks exhibit a track length of approximately 4 cm. The shoulder at lower track lengths is attributed to partially contained alpha particles.

with curved or more complex tracks could be reconstructed. Some examples of 3D tracks of cosmic events obtained from combining the 2D track projections recorded with an EMCCD camera with the Z-depth information from electronically read out ITO anode strips are shown in figure 71 along with the corresponding images of the 2D track projections.

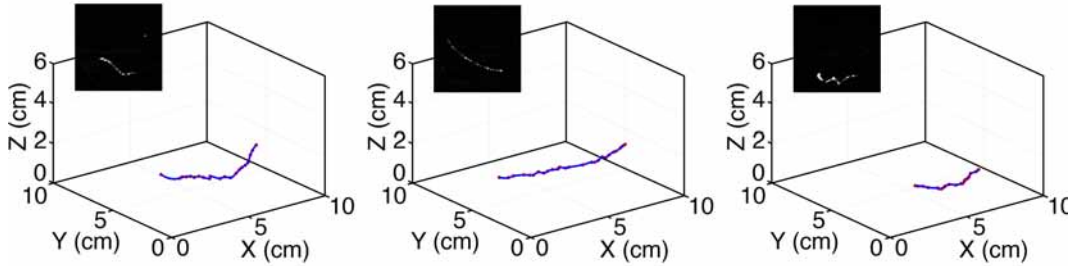


**Figure 71.** Reconstructed cosmic events: The combination of optical readout with electronic readout of an ITO strip anode permitted 3D reconstruction of cosmic events.

The arrival times of charge signals electronically read out from the ITO strip anode provide relative Z-information for particle track reconstruction. If the time  $t_0$  of the passing of a track in the active volume of the TPC can be determined, the reconstruction of the absolute Z-position of the track may be possible. For particles which can traverse multiple layers of detectors, external scintillators or other detector technologies around the TPC may provide  $t_0$  information. In the case of highly ionising particles like alpha particles, primary scintillation light emission might be sufficiently strong to be detected and used as  $t_0$  information. In the presented optically and electronically read out TPC, PMT waveforms displaying both primary and secondary scintillation pulses were used to determine absolute depth information for alpha particle tracks in addition to relative Z-information from electronically read out charge signals. An example of absolute alpha particle track reconstruction is shown in figure 72. The time difference  $\Delta t$  between the primary scintillation signal and the leading edge of the secondary scintillation pulse is multiplied by the electron drift velocity of  $8 \text{ cm}/\mu\text{m}$  to determine the Z-coordinate of the end of the particle track closest to the triple-GEM stack. In the shown example, a time difference of  $\Delta t = 612 \text{ ns}$  corresponds to a distance of  $4.89 \text{ cm}$  from the triple-GEM stack. Together with the relative Z-information from the readout of charge

signals and the optical image, a 3D alpha track reconstruction with absolute positioning along the Z-axis could be obtained.

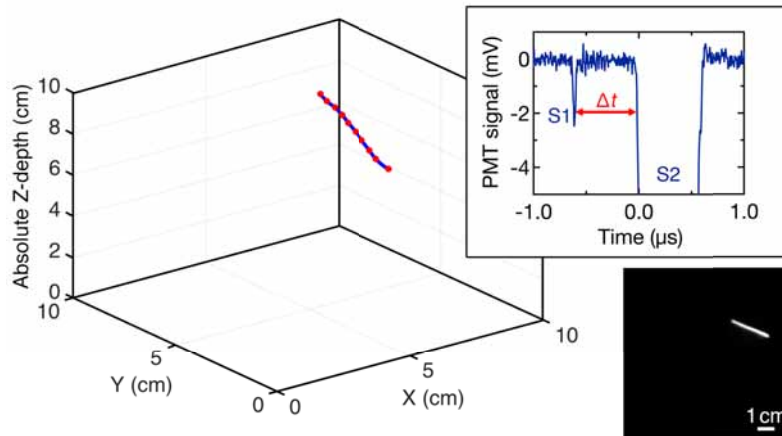


**Figure 72.** Reconstruction of absolute Z-coordinates with PMT waveform: Alpha track reconstructed from combining a 2D image and the relative Z-information from arrival times of charge signals with drift time information from a PMT waveform (shown in inset). The time  $\Delta t$  between primary scintillation (S1) and secondary scintillation (S2) pulses corresponds to the drift time of the primary electrons produced closest to the triple-GEM stack.

While the 1D strips of the ITO strip anode might not be sufficient to provide unambiguous Z-depth information in some cases of complex particle track geometries, the concept can be readily extended to 2D electronic readout with 2D ITO strips or a combination of wires and ITO strips in different directions. In addition, the use of readout ASICs with better time sampling capabilities might be used to achieve better Z-resolutions in the TPC.

The simultaneous optical and electronic readout permits 3D reconstruction of particle tracks from high spatial resolution 2D projections and electron arrival times while requiring only a low number of electronic readout channels. This readout concept extends the reconstruction capabilities of optically read out TPCs to more complex particle trajectories.

## 5.4 Dose imaging detector for hadron therapy

Radiation treatment of cancerous tissue has become an important cornerstone of modern oncology. In multimodal treatments, radiation therapy is either used to treat residual disease after the majority of the tumour has been surgically removed or before surgery to cause shrinkage of soft-tissue tumours and make them easier to remove [109]. While conventional X-ray based irradiation treatments often strongly affect neighbouring healthy tissue, hadron therapy aims to minimise radiation exposure of surrounding tissue by taking advantage of the dose depth curve of protons or carbon ions. X-ray photons might interact strongly with tissue before reaching the depth of the tumour to be treated. By contrast, protons and carbon ions traverse a certain amount of tissue with limited energy deposition before losing all residual energy in a well-defined region. The Bragg peak of the dose depth curve allows control over the depth of maximum energy deposition during radiation treatments and is exploited to selectively target cancerous tissue while minimising exposure to surrounding regions. A schematic comparison of the dose depth curves of X-rays and protons is shown in figure 73.

The dose delivery capabilities of hadron therapy have led to the establishment of numerous proton and carbon therapy facilities. With currently about 50 hadron therapy centres in

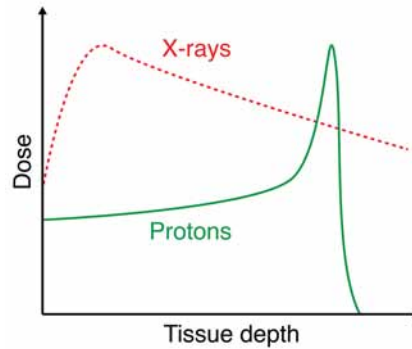


**Figure 73.** Dose depth curve comparison: While X-rays deposit a significant amount of energy at low tissue depth, protons traverse the outer tissue layers and deposit the most energy in a well-defined depth denoted by the Bragg peak.

operation around the world, a total of about  $1.5 \times 10^5$  patients have been treated with proton beams and more than  $2 \times 10^4$  have been treated with carbon ions [110].

The 3D distribution of deposited dose is outlined by physicians in patient-specific treatment plans created after identifying the spatial extent of the cancerous tissue with suitable imaging techniques. Computer tomography and magnetic resonance imaging are used to define the tissue volume which should be irradiated with a certain amount of dose [109]. The total dose that the tumour should be irradiated with is delivered in multiple treatment sessions, so-called fractions. Typically, tumours are treated with 20 to 40 fractions with a dose of about 2 Gy each [109].

Extensive quality assurance measurements are performed at radiotherapy facilities prior to patient treatments to verify that deposited dose distributions agree with treatment plans and ensure patient safety and treatment efficiency. In addition, the totally deposited dose must be accurately monitored to ensure that the actually delivered dose matches the prescribed dose to within 2.5% of the prescribed dose [109]. State-of-the-art detectors for these quality assurance tests have several shortcomings including poor spatial resolution in detectors based on ionisation chambers or high material budget. Therefore, commonly used instruments have to be used before patient treatments and do not allow online monitoring of the actually deposited dose distribution.

To overcome this limitation, a proton beam monitoring detector based on an optically read out GEM and an ionisation chamber has been developed. With gas as an active medium and the use of thin beam windows and electrodes to achieve low material budget, the developed detector meets material budget requirements for an online detector and combines accurate total dose measurement with an ionisation chamber with high spatial resolution dose distribution imaging by an optically read out GEM. The possibility of coupling scintillation light produced in the beam path to an imaging sensor located outside of the beam path with a mirror makes optical readout well-suited for a low material budget beam monitoring detector. In this way, the imaging sensor does not contribute to the material budget in the beam path and is not directly exposed to the beam, thus minimising radiation-induced damages. Aiming at a spatial resolution of several hundred  $\mu\text{m}$ , the dose imaging detector can also be used for beam profile and position monitoring. A dosimetry system based on an optically read out GEM-based detector has previously been developed for pre-treatment dose verification in hadron therapy and operation in carbon beams has been demonstrated successfully [111].

Recording the dose distribution deposited during treatments with an optically read out GEM can provide high spatial resolution 2D visualisations. In current scanning proton beam facilities, ionisation chambers read out with segmented anodes are used to monitor the position of the beam and the dose delivered during scanning of the pencil beam. Commonly, multiple ionisation chamber layers with readout strips in different directions or ionisation chambers with pixelated readout are used to achieve limited 2D dose imaging capabilities. However, the reconstruction of the dose distribution from dose profiles projected onto readout strips may introduce significant inaccuracies and ambiguities. Figure 74 schematically shows the limitations in the dose distribution reconstruction for the case of orthogonal readout strips with widths of 2 mm. The pixel value intensities in the dose distribution image shown in figure 74a were projected in software to horizontal and vertical slices and the resulting slice profiles are shown in figure 74b. Subsequently, a simple back-projection algorithm was used to compute the reconstructed dose distribution image shown in figure 74c, which shows that the dose distribution cannot be accurately determined from slice profiles.

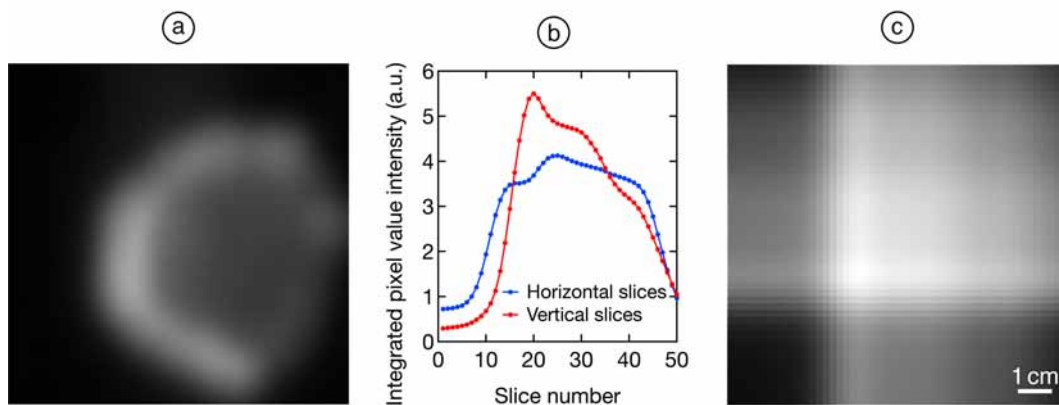


**Figure 74.** Dose distribution reconstruction from slices: (a) Dose distribution of single irradiation layer in proton therapy treatment recorded by optical readout. (b) Profiles of dose distribution projected to vertical and horizontal slices with widths of 2 mm. (c) Dose distribution reconstructed from slice profiles shown in (b).

The reconstruction of the dose distribution may be significantly improved by employing multiple ionisation chamber layers with different readout geometries. Different readout strip orientations, narrower readout strips or pixelated readout may be used to achieve more accurate dose distribution images. A dose distribution reconstructed from two orthogonal slice profiles with slice widths of 1 mm as shown in figure 75a exhibits better granularity than the one reconstructed from slice profiles with slice widths of 5 mm as shown in figure 75b. While pixelated readout as shown in figure 75c results in more accurate dose distributions with less ambiguities, the large size of individual readout pixels limited by the use of ionisation chamber arrays to the scale of several mm still cannot provide dose distributions with high spatial resolution.

An optically read out dose imaging detector can provide high spatial resolution 2D dose distribution information by taking advantage of the high pixel count of state-of-the-art imaging sensors. The pixelated readout approach can resolve potential ambiguities in intricate 2D dose distributions while preserving high granularity in the acquired images. Due to the limited frame rate of imaging sensors, optical readout is not suited for fast feedback and control of scanning pencil beams, which is done with ionisation chambers read out at several tens of

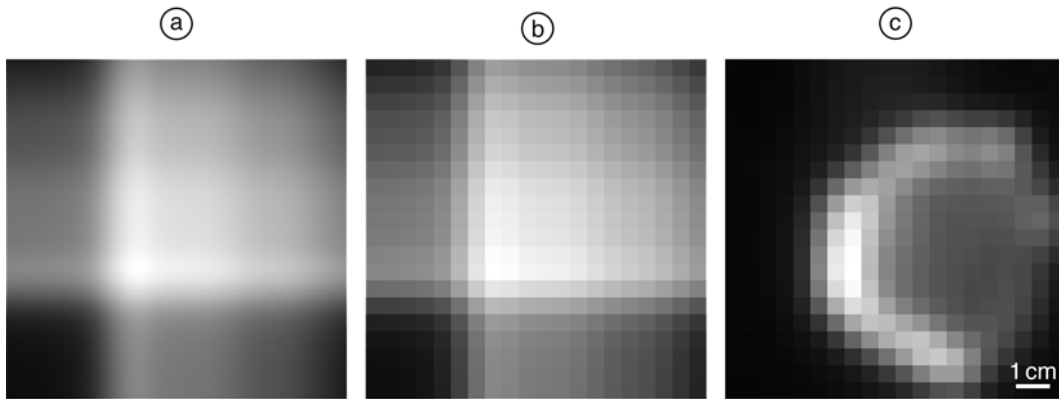


**Figure 75.** Dose imaging comparison: (a) Dose distribution reconstructed from projections in horizontal and vertical slices with widths of 1 mm. (b) Dose distribution reconstructed from projections in horizontal and vertical slices with widths of 5 mm. (c) Dose distribution recorded with pixels with a size of  $5 \times 5$  mm.

kHz in some dose delivery systems [112]. However, optical readout can provide integrated dose distribution information to verify delivered treatment plans.

#### 5.4.1 Detector concept and operation

An optically read out proton beam monitoring detector combining an ionisation chamber with a GEM-based detector with an active detector area of  $10 \times 10 \text{ cm}^2$  was developed and operated. The detector elements were housed in a UHV-grade vessel with beam windows. To minimise material budget in the beam path, thin foils were used as beam windows and as electrodes of the active detector elements. Both beam entrance and exit windows consisted of 15 cm diameter aluminised Mylar foils mounted with In wire seals to flanges on both sides of the detector vessel. The ionisation chamber was formed by a thin Al foil cathode and an aluminised Mylar foil anode mounted with a 15 mm gap onto a PEEK frame. Using the cathode of the ionisation chamber as drift electrode, a single-GEM-based detector was mounted with a 5 mm drift gap adjacent to the ionisation chamber. To record the scintillation light produced during electron avalanches in the single GEM foil with a CCD camera, a thin mirror made from aluminised Mylar foil was mounted under a  $45^\circ$  angle. Light generated in the GEM holes is reflected by the mirror to a CCD camera (QImaging Retiga R6 [66]) mounted orthogonally to the beam axis. In addition to coupling the light from the GEM to a camera outside of the beam path, the mirror also allowed focusing the camera on the surface of the GEM to achieve high spatial resolution across the entire active area of the detector. The proton beam monitoring detector is schematically shown in figure 76.

Electrical connections to the electrodes in the detector vessel were made with polyimide-insulated wires leading from GEM contacts and the common cathode and ionisation chamber anode to SHV-feedthroughs mounted on CF40 flanges. Gas inlet and outlet were realised with vacuum-grade valves and a combined Pirani-type and capacitive pressure gauge was used to monitor gas pressure in the detector. As the beam entrance and exit windows had a low but disruptive light transmission, light shielding was achieved by opaque, black paper shields in front of the beam windows.

Prior to gas filling and operation, the detector chamber was pumped to a pressure below  $5 \times 10^{-4}$  mbar with a turbomolecular pump. As excessive differential pressure between the pumped vessel and the environment might break the thin beam windows, protective pump-

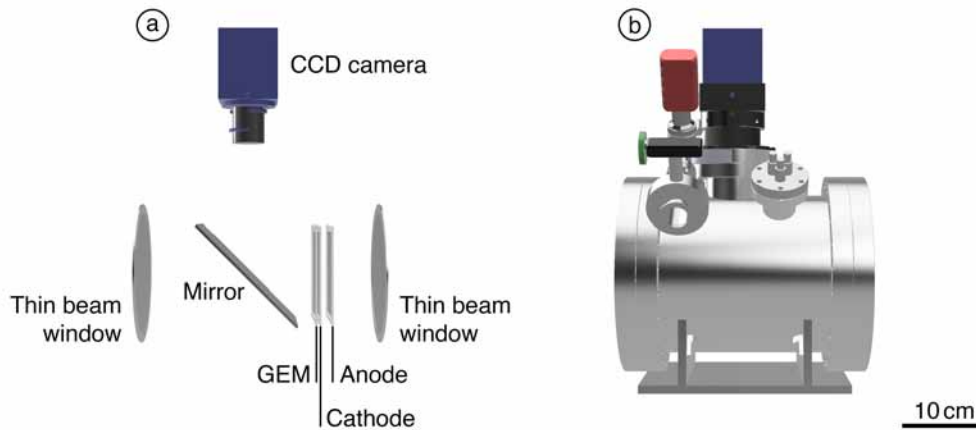


**Figure 76.** Proton beam monitor schematic: (a) An ionisation chamber and a GEM sharing a common thin foil cathode are placed in the beam path between two thin foil beam windows. Light produced in the GEM is coupled to a CCD camera by an thin mirror. (b) The detector components are housed in a UHV-grade vessel with electrical feedthroughs and gas ports.

ing caps were mounted outside of the beam windows. Pumping these caps separately permitted keeping the pressure differences between the two sides of the beam windows always below 20 mbar thus preserving the integrity of the thin foil windows. After prolonged pumping and cleaning of the chamber, it was filled with an Ar/CF<sub>4</sub> gas mixture with a mixing ratio of 80/20% at atmospheric pressure and flushed for several hours before operation. The use of materials selected for their low outgassing rate and a UHV-grade vessel with metallic seals allowed for extended sealed mode operation with a moderate decrease in scintillation light yield. Nevertheless, the detector was operated in open gas flow mode to ensure a constant and high level of gas purity.

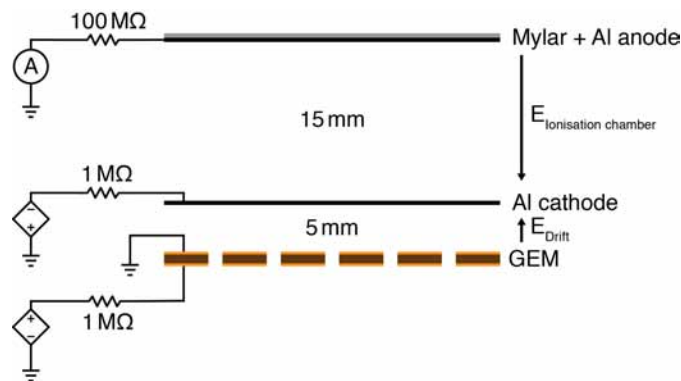


**Figure 77.** Electrical schematic of dose imaging detector: The ionisation chamber and the GEM share a common cathode. The cathode is biased to negative high voltage, the top electrode of the GEM is grounded and the anode of the ionisation chamber as well as the bottom electrode of the GEM are individually biased to positive high voltages. The current on the anode of the ionisation chamber is measured by an ammeter.

The common cathode and the bottom electrode of the GEM were powered with individual channels of a high-voltage power supply as shown in figure 77. The top electrode of the GEM was grounded, while the anode of the ionisation chamber was connected to ground with a 100 MΩ resistor and a high-resolution ammeter in series. The cathode was biased at -1000 V while the positive biasing voltage applied to the bottom electrode of the GEM was adjusted from 0 V to 440 V to adjust the gain of the detector. This flexibility in the gain of the

GEM enabled the operation of the detector in a wide range of operating regimes ranging from the detection of low-energy X-rays for calibration and response characterisation tests to recording high-intensity clinical proton beams.

#### 5.4.2 Material budget

To enable an operation of the dose imaging detector during treatment irradiations as on-line dose distribution monitoring instrument, the impact of the detector on beams passing through it must be minimised. The significance of different materials in the path of beams in hadron therapy can be expressed as Water Equivalent Thickness (WET). Therefore, the impact materials with different stopping power values, densities and thicknesses have on particle beams can be expressed as the equivalent thickness of water, which has the same attenuation effect on the beams. The WET  $t_W$  can be calculated from the thickness  $t_M$  of a certain material as

$$t_W = t_M \frac{\rho_M \overline{S_M}}{\rho_W \overline{S_W}} \quad (5.2)$$

with the density of the material  $\rho_M$ , the density of water  $\rho_W$ , the mean stopping power  $\overline{S_M}$  of the material for particles such as protons with certain energies and the corresponding mean stopping power of water  $\overline{S_W}$  [113].

The material budget of the presented dose imaging detector was kept to a minimum by using possibly thin foils as detector elements in the beam path. A single GEM foil made of a polyimide foil with a thickness of 50  $\mu\text{m}$  and two Cu electrodes with a thickness of 5  $\mu\text{m}$  each were used as signal amplification stage. An Al foil with a thickness of 20  $\mu\text{m}$  was used as the cathode shared by the GEM detector and the ionisation chamber. Mylar foils with a thickness of 20  $\mu\text{m}$  each and an Al-coating with a thickness of about 100 nm were used as anode electrode for the ionisation chamber, as mirror and for the two beam windows of the chamber resulting in a total of four Al-coated Mylar foils in the assembly. An Ar-based gas mixture was used in the detector vessel with a total thickness of 30.8 cm in the beam path. The materials used in the detector and corresponding thicknesses and values for the stopping power for protons with an energy of 100 MeV,  $S_{p,100\text{MeV}}$ , are shown in table 5.1 along with the individual WET contributions.

Material	Density (kg/m <sup>3</sup> )	$S_{p,100\text{MeV}}$ (MeV cm <sup>2</sup> /g)	Thickness ( $\mu\text{m}$ )	WET ( $\mu\text{m}$ )
Mylar	1380	6.791	92	118
Polyimide	1420	6.681	50	65
Al	2700	5.678	20.3	42
Cu	8960	4.852	10	59
Ar	1.784	5.213	308000	392

**Table 5.1.** Material budget of dose imaging detector and contributions to WET. The stopping power values for protons with an energy of 100 MeV are taken from [114].

The total WET of the detector is about 680  $\mu\text{m}$ . The Z-depth of energy deposition in proton therapy treatments is known with a precision on the order of 1 mm. The attenuation due to the material budget of the detector would therefore be acceptable for online operation in proton beams enabling online dose imaging.

While the attenuation of beams passing through the dose imaging detector might be minimal, multiple scattering in the detector components might result in a broadening of the profile of particle beams. To minimise broadening due to multiple scattering, the WET of the detector should be further decreased with a focus on decreasing the thickness of metals such as Cu as much as possible. The thickness of the Cu electrodes of the GEM might be significantly reduced and thicknesses around 1  $\mu\text{m}$  may be readily reached by etching of Cu. GEMs with Cr-based electrodes and only thin Cu grids for electrode rigidity are being developed [23] and might also be used to minimise the material budget of GEM-based detectors. Furthermore, the use of He instead of Ar in the gas mixture of the detector might allow a further decrease in the WET of the device. With the geometry and all other components unchanged, switching from Ar to He, the total WET can be decreased from 680  $\mu\text{m}$  to less than 400  $\mu\text{m}$  due to the low density of He.

### 5.4.3 Detector response

The linearity of the detector response and the gain of the GEM for different voltages were verified under irradiation with an X-ray tube and during proton beam irradiation. The current measured at the anode of the ionisation chamber was recorded, while the integrated pixel value intensity of the beam spot in the images obtained by the CCD camera was taken as a measure of the light intensity produced during avalanche multiplication in the GEM. The effective gain of the GEM was estimated by comparing the current in the ionisation chamber and the current measured at the bottom electrode of the GEM and correcting for the different thicknesses of the ionisation chamber and the drift region coupled to the GEM in a proton beam. The measurement was not corrected for differences in beam energy loss between the adjacent ionisation chamber and drift regions. As the proton beam energy loss in the thin cathode foil between them and the ionisation chamber gas volume is negligible and the depth dose over material thickness curve of the proton beams can be approximated as constant in the corresponding material thickness range, no correction for beam energy loss was necessary in the GEM gain estimation.

The gain of the single GEM increases exponentially with voltage across the GEM and reaches a value slightly above 50 at 375 V across the GEM as shown on figure 78. This is sufficient for imaging proton beams even at low beam intensities of 0.1 nA nozzle beam current and the exponential gain over GEM voltage curve verifies that no saturation in the response of the detector occurs.

The linearity of the detector response under X-ray irradiation was verified as shown in figure 79. The ionisation chamber current increased linearly with the irradiation intensity up to high X-ray irradiation rates with an X-ray tube current of 20 mA.

In order to be able to rely on the images recorded with the CCD camera for a determination of the dose distribution, the recorded light intensity must correspond to the observed ionisation chamber current. A scatter plot of the integrated light intensity from CCD camera images as a function of the recorded ionisation chamber current under proton beam irradiation is shown in figure 80.

The displayed data points were recorded at proton beam energies ranging from 60 MeV to 226 MeV and nozzle beam currents ranging from 0.1 nA to 2 nA, thus covering the full accessible beam energy and nozzle beam current range in the clinical facility the detector was tested in. The linear relationship between the recorded light intensity in CCD images



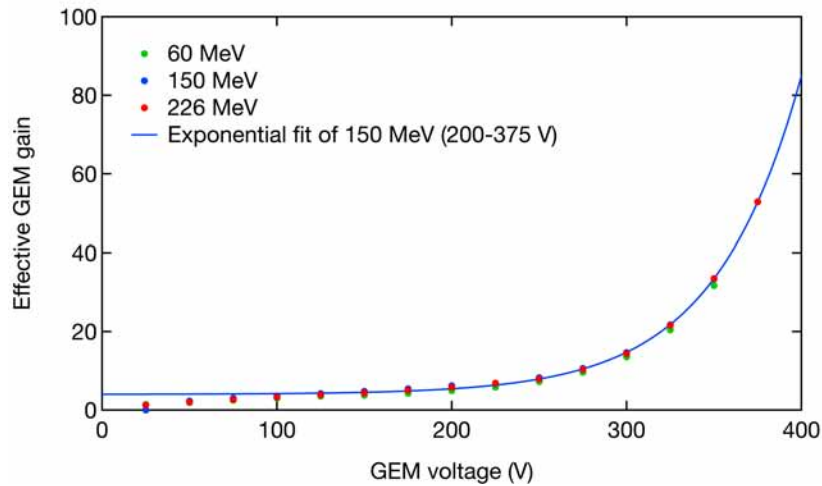


**Figure 78.** GEM gain in proton beam: The effective gain of the GEM operated in the proton beam depends exponentially on the GEM voltage.

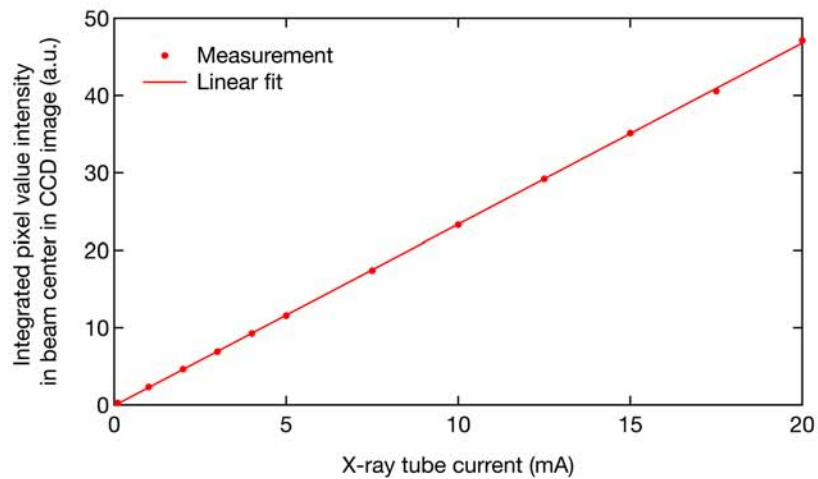


**Figure 79.** Linearity of CCD response under X-ray irradiation: The integrated pixel value intensity in the centre of the beam profile in CCD images depends linearly on the X-ray tube current.

and the ionisation chamber current allows a determination of the spatial distribution of the deposited dose by using CCD images as 2D dose maps.

The ionisation chamber current measures the dose deposited by proton beams in the 15 mm thick active gas volume between the common cathode and the anode of the detector. The energy deposited in this gas volume depends on the energy-dependent stopping power of protons in the gas. Measuring the ionisation chamber current as a function of nozzle beam current for different beam energies, the linear relationship with different slopes for five beam energies ranging from 60 MeV to 226 MeV as shown in figure 81 could be observed.

The slope of the ionisation chamber current as a function of the beam current reflects the stopping power of protons in the gas used in the detector and agrees well with the nominal stopping power curve for protons in Ar, as shown in figure 82.

The stability of the ionisation chamber current in sealed mode operation was investigated under constant irradiation with a  $^{90}\text{Sr}$  source. The trend of the ionisation chamber current over 60 h as shown in figure 83 displays less than 1 % of variation. Therefore, the ionisation chamber can be used as a stable and reliable way of monitoring the totally deposited dose across the full active area even in a sealed detector with gradually decreasing gas quality.

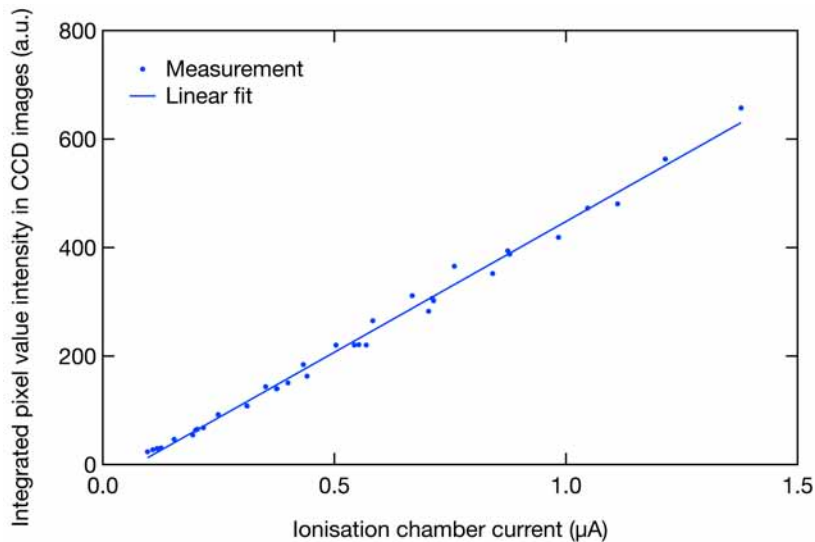


**Figure 80.** Correlation between ionisation chamber current and CCD response: The integrated pixel value intensity from CCD images depends linearly on the recorded ionisation chamber current. The displayed data points were recorded at different beam energies and nozzle beam currents.

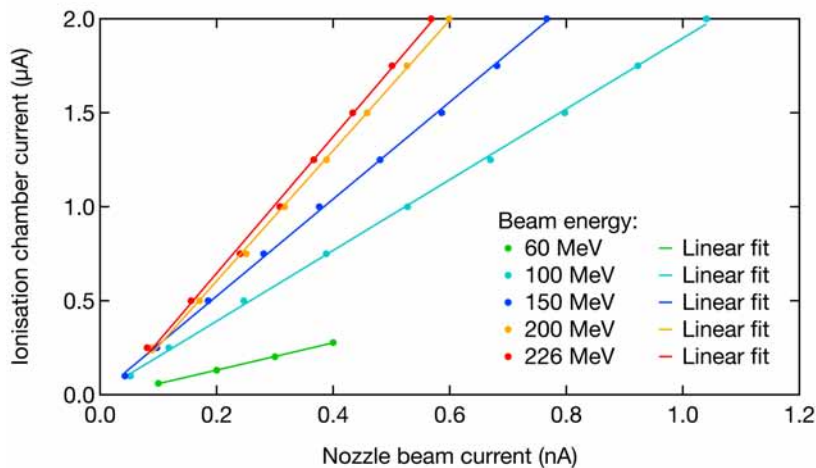


**Figure 81.** Ionisation chamber current for different beam currents: The ionisation chamber current at a given beam energy depends linearly on the nozzle beam current. The slope of the linear dependence increases with higher beam energies.

In the clinical environment, the deposited dose is expressed as Monitoring Units (MUs), which is an arbitrary unit corresponding to a certain amount of deposited charge in reference ionisation chambers in the beam nozzle. Therefore, the ionisation chamber in the presented detector is well-suited as an absolute dose monitor as it employs the same detection principle as the dose reference for clinical treatments. Combining the verified correspondence between the integrated pixel value intensity from CCD images with the ionisation chamber current and therefore the amount of deposited dose, the relationship between the integrated light intensity and the deposited MUs shown in figure 84 was measured.

The direct proportionality between the recorded light intensity and the deposited charge verifies the applicability of the optically read out images as representations of the deposited dose distribution for a totally deposited dose of up to 30 MU, which corresponds to the upper limit of dose commonly delivered in an individual layer of a clinical irradiation. The linear relationship holds true for the full range of proton beam energies from 60 MeV up to

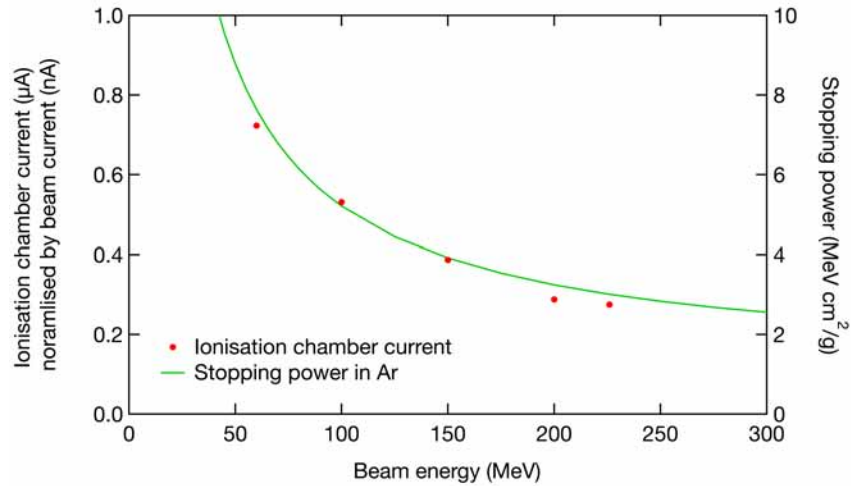


**Figure 82.** Ionisation chamber current for different beam energies: The dependence of the ionisation chamber current on the beam energy agrees well with the trend of the stopping power of protons of different energies in Ar.

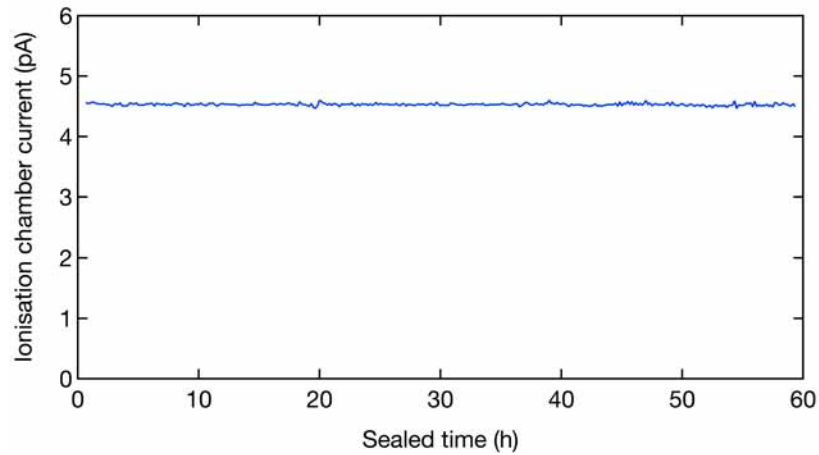


**Figure 83.** Stability of ionisation chamber current: The ionisation chamber current under irradiation with a <sup>90</sup>Sr source displayed less than 1 % of variation over 60 h of sealed detector operation.

226 MeV when operating the GEM at a moderate voltage of 300 V. This corresponds to an effective gain of approximately 13. However, at a GEM voltage of 400 V corresponding to a high charge gain of more than 50, a saturation in the detector response is observed as the recorded light intensity does not depend linearly on the deposited MUs anymore.

As the beam delivery system uses possibly high nozzle beam currents in order to minimise the time needed to deliver a certain amount of MUs, the deviation from the linear behaviour at a few MUs for a GEM voltage of 400 V is attributed to a saturation originating from excessively high currents in the GEM at a high beam current and strong amplification in the GEM. Operating the GEM at a moderate voltage of 300 V mitigates this saturation behaviour and preserves the linear relationship between the recorded light intensity and the deposited MUs up to 30 MU. Since the corresponding effective gain of 13 is high enough to record images of low-intensity proton beams, operating the GEM at 300 V is sufficient for the full range of accessible beam parameters and was chosen as a maximum GEM voltage for proton beam tests of the presented detector.

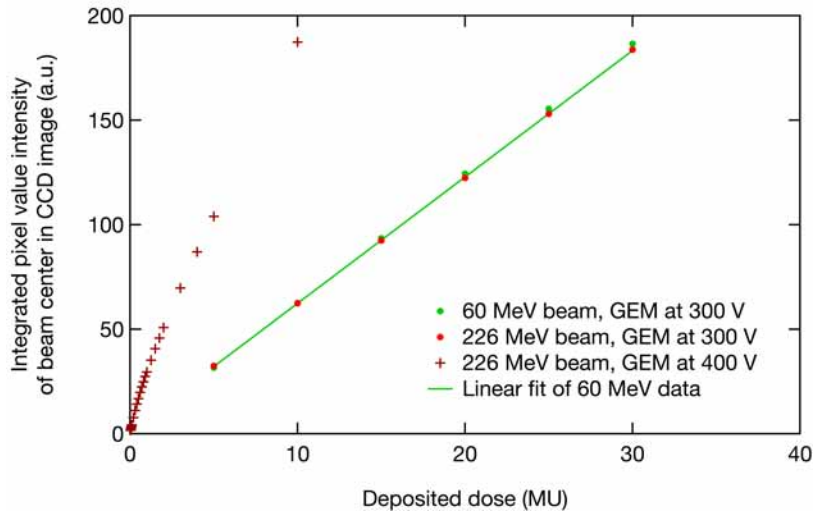


**Figure 84.** Integrated light intensity for different deposited doses: At high charge gains, the recorded light intensity saturates and does not depend linearly on the deposited dose. At a lower GEM voltage of 300 V, a linear relationship between the recorded integrated light intensity and the deposited dose holds true for different beam energies.

#### 5.4.4 Beam profile monitoring

The high-resolution images obtained with the CCD camera are well-suited for beam profile monitoring and may be used to measure and validate the profiles of proton pencil beams [81]. This may be used for machine parameter validation and pre-treatment beam profile checks. Operating the detector with a low GEM voltage of 200 V and recording images of proton pencil beams with an exposure time of 2 s, beam profile images as shown in figure 85 were obtained.

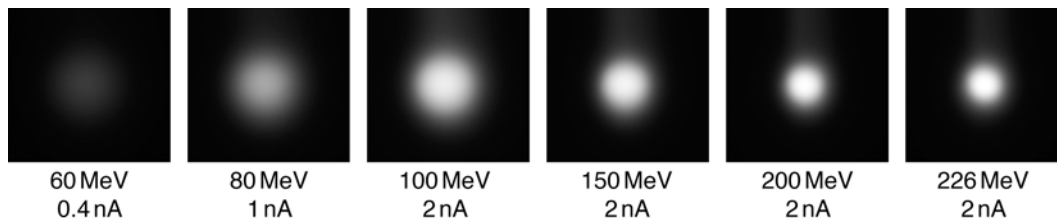


**Figure 85.** Images of proton beams with different energies: The optically read out images of the intensity distribution of proton beams of different energies ranging from 60 MeV to 226 MeV display a trend towards narrower beam profiles with higher beam energies.

Beam profiles were recorded for proton beam energies ranging from 60 MeV to 226 MeV and the highest obtainable nozzle beam current was chosen for each beam energy. While 2 nA of nozzle beam current could be delivered by the machine for energies above 100 MeV only 0.4 nA and 1 nA nozzle beam current could be delivered for 60 MeV and 80 MeV proton beams, respectively. The images recorded by the CCD camera show a trend towards narrower beam profiles with increasing beam energies. In figure 86, the horizontal and vertical line profiles of the pixel value intensities in the recorded beam profile images show that the Gaussian shape of the beam profile is preserved from the lowest to the highest accessible beam energies, with the width of the beam profiles decreasing for higher beam energies. Fitting the horizontal beam profiles with a Gaussian function and using the standard deviation determined by the Gaussian fit function to measure the width of the beam profile, the

width of the beam profile at a beam energy of 60 MeV was determined to be 7.8 mm. The width decreases with increasing beam energy and reaches 3.2 mm at a beam energy of 226 MeV. According to information received from the clinical test facility, the expected beam width at 60 MeV is 7.1 mm, while the beam at 226 MeV should be 2.9 mm wide. Therefore, the measured values are approximately 10 % higher than the nominal beam width values. This overestimation may be due to the detector not being placed exactly in the isocenter of the proton beam during the beam tests, where the nominal reference values were measured. Additionally, the reference values were measured in a calibrated and commissioned clinical room, while the measurements with the presented detector were performed in a dedicated research room, for which no reference measurements were available. Nevertheless, the observed trend towards narrower proton beams for higher beam energies and the recorded Gaussian profiles of the proton pencil beams demonstrate the applicability of the presented detector for proton beam monitoring.

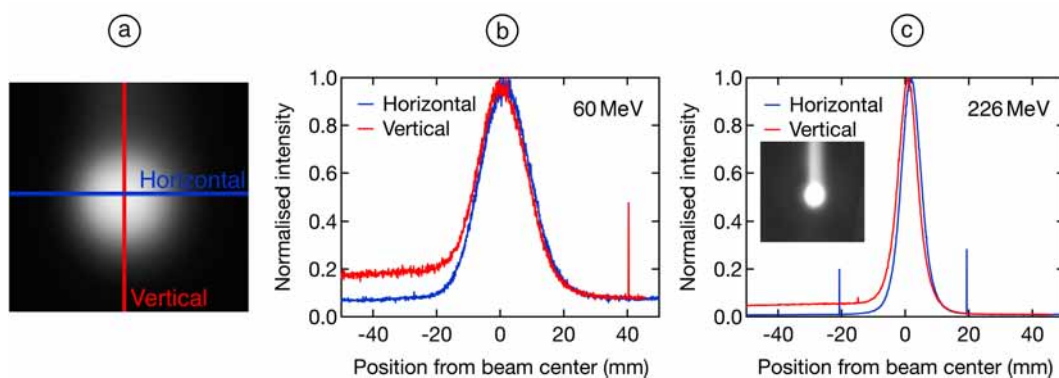


**Figure 86.** Proton beam profiles at different beam energies: (a) Horizontal and vertical line profiles of the pixel value intensity in CCD images were used to determine the beam profile at different beam energies. (b) The horizontal and vertical beam profiles for a beam with an energy of 60 MeV show a Gaussian shape with a width of 7.8 mm. (c) The horizontal and vertical beam profiles for a beam with an energy of 226 MeV show a Gaussian shape with a width of 3.2 mm. Inset: Reflections above the main beam spot are visible and contribute to the observed offset in the vertical beam profiles.

The vertical line profiles shown in figure 86 display a significant offset in the pixel value intensity value at negative positions corresponding to the region above the main beam spot. This offset is present for all investigated beam energies and reaches up to 20 % of the maximum peak amplitude for low beam energies. Due to the asymmetry of this offset, it is attributed to reflections between the bottom surface of the GEM and the mirror. Scintillation light emitted during avalanche multiplication in the GEM may be reflected back onto the GEM by the mirror and reach the camera after additional reflections contributing to a non-zero offset outside of the main beam spot. These reflections in the region above the main beam spot can be seen in the inset of figure 86c, which displays a beam profile with a limited pixel value range to visualise the reflections. To eliminate these reflections, a non-reflective GEM electrode coating or an adjusted placement of detector and readout elements may be used.

#### 5.4.5 Dose depth curve measurement

In addition to the 2D beam profile information provided by optically read out images of the proton pencil beam, the sum of the pixel intensities in the recorded pictures provides a measurement of the energy deposited in the active drift volume of the detector during the

exposure time. The energy deposited by the proton beam strongly depends on the material it has traversed before. As a quantitative comparison, the released energy normalised to the maximum intensity as a function of the traversed material expressed as water equivalent depth is described by the dose depth curve for a certain incident beam energy. Placing solid absorber blocks with a density comparable to water in front of the detector and measuring the totally released energy at specific absorber thicknesses corresponding to tissue depth by integrating the pixel value intensity in obtained images, a dose depth curve for a 150 MeV proton beam was measured. In total, 16 measurement points corresponding to water equivalent depths ranging from 0 cm to 15.9 cm were recorded. The GEM was operated at a voltage of 200 V and CCD images were recorded with an exposure time of 2 s. A low beam intensity of 0.1 nA nozzle beam current was sufficient to achieve images with high signal-to-noise ratios. The measured dose depth curve agrees well with a reference curve provided by the clinical facility as shown in figure 87.

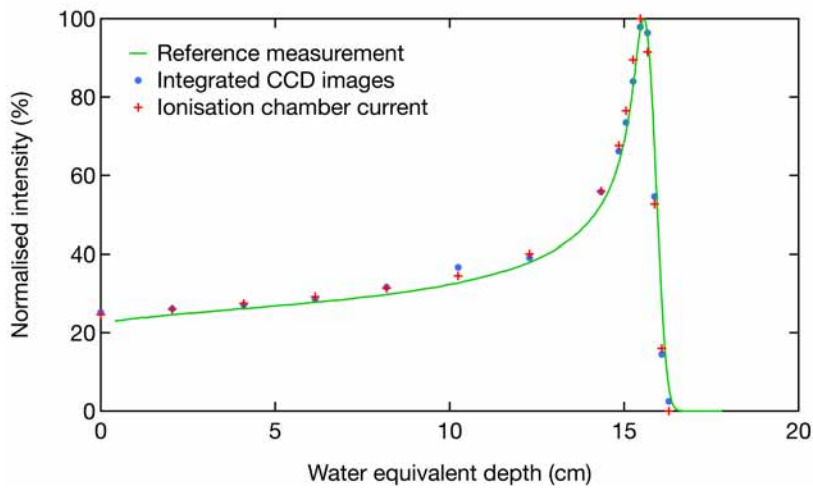


**Figure 87.** Dose depth curve of 150 MeV proton beam: The dose depth curves obtained from the integrated pixel value intensity from CCD images as well as from the ionisation chamber current agree well with a clinical reference measurement.

The ratio of the deposited energy without absorbers to the maximum amplitude of the dose depth curve of approximately 1:4 as well as the location of the Bragg peak defined as the water equivalent depth for which the dose depth curve reaches 80 % of its maximum on the falling slope at 15.8 cm agree well with the reference values provided by the proton therapy facility where the tests were carried out. As the totally recorded light intensity is directly related to the ionisation chamber current, the dose depth curve can also be measured from ionisation chamber current measurements taken with different absorbers in front of the detector and dose depths curves obtained from these two methods are in good agreement.

The achievable accuracy in measuring the deposited dose as a function of water equivalent depth depends on the similarity of the energy loss of protons in the medium used for detection to the energy loss in water. The ratio between the proton stopping power of Ar/CF<sub>4</sub> mixtures and water changes within several percent with proton energy [115]. Thus, Ar-based mixtures are not well-suited for recording dose depths curves. Mixtures of He and CF<sub>4</sub>, however, can be used to achieve stopping powers matched to the proton stopping powers in water and are consequently better suited for accurate dose depth measurements with gaseous detectors [115].

### 5.4.6 Dose imaging

The 2D imaging capabilities of the presented detector can be used to obtain high spatial resolution dose distribution maps of scanning pencil beam irradiations. During treatments of cancerous tissue, a certain amount of dose is delivered according to a patient-specific treatment plan developed by doctors. Imaging technologies are employed before the treatment to gather information about the 3D shape of the cancerous tissue, which should be irradiated. To selectively deliver the dose to the desired locations with minimal exposure to surrounding healthy tissue, the Bragg peak of the proton pencil beam is shifted to the desired tissue depth by absorbers added between the gantry nozzle and the patient or by adjusting the energy of the proton beam for each irradiation layer. Additionally, the pencil beam is deflected by magnets to scan the area which should be irradiated. Once all tissue in a certain depth has been irradiated, the proton beam energy or the absorber thickness is changed to tune the Bragg peak to a different depth and the cancerous tissue in this depth is irradiated. Recording CCD images showing the 2D dose distribution on each layer of a multi-layer treatment plan irradiation, a 3D map of the deposited dose can be built and used to verify that the deposited dose distribution agrees with the one outlined by the patient-specific treatment plan. The dose distribution in 29 layers of a patient treatment plan recorded with the optically read out dose imaging detector is shown in figure 88a. The beam energy was changed between individual layers with a maximum proton beam energy of 118 MeV. In total, 325 MU were delivered in 29 layers. A visualisation of the 3D dose distribution obtained from rendering a 3D volume from the 29 layers at a fixed arbitrary Z-spacing is shown in figure 88b. This visualisation does not take into account the energy deposited on other layers during irradiations of deeper regions.

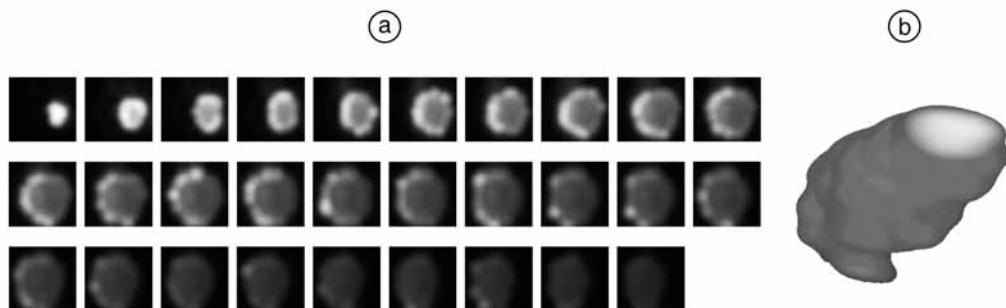


**Figure 88.** Dose distribution of treatment plan: (a) Dose distribution of 29 individual layers of patient treatment plan. (b) 3D visualisation of dose distribution of patient treatment plan.

The distribution of the totally deposited dose over the 29 layers of irradiation can be extracted from the integrated pixel value intensity for each acquired image. Comparing the deposited charge per irradiation layer with the nominal values outlined by the treatment plan, a good agreement between the recorded and the expected distributions as shown in figure 89 is achieved.

The hybrid detector concept combining an optically read out GEM for dose imaging with an ionisation chamber for absolute dose measurements provides high spatial resolution dose maps as well as stable and accurate dose monitoring capabilities. The detector is well-suited for online beam monitoring applications due to the low material budget achieved by using gas as an active medium and thin foils in the beam path. The optical readout provides images of the dose distribution without the need for extensive reconstruction algorithms

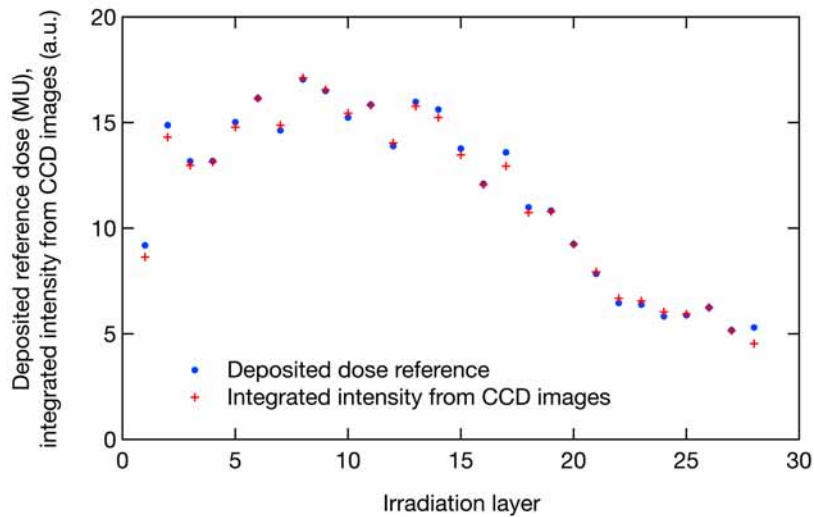


**Figure 89.** Deposited dose per irradiation layer: The recorded total pixel value intensity per irradiation layer agrees well with the nominal distribution of deposited dose per layer for 29 layers in a patient treatment plan irradiation.

and the tuneable signal amplification of the GEM permits an operation of the detector in a wide range of applications. The versatility and the spatial resolution achievable with optically read out GEMs makes dose imaging detectors based on this concept a promising approach for machine parameter verification and patient-specific treatment plan validation in hadron therapy and can improve the accuracy and resolution of dose distribution measurements while retaining online monitoring capabilities.







## CHAPTER 6

# Conclusions

Optical readout presents a versatile readout modality for radiation detectors and provides intuitive visualisations with high granularity. Taking advantage of modern imaging sensors, which feature sensitive pixels with low noise characteristics, high-resolution images with good signal-to-noise ratios can be acquired. By simultaneously collecting all photons arriving at the pixels of an imaging sensor during the exposure window, optical readout is efficient in recording integrated full-field images. As light can be guided and manipulated by optical components such as mirrors or lenses on its path from the detector to the imaging sensor, the effective pixel size on the imaging plane can be varied and optimised and optical readout devices can be placed in favourable locations for specific applications.

The spectra of the secondary scintillation light emitted by GEM-based detectors operated in gas mixtures containing  $\text{CF}_4$  feature ample UV and VIS emission bands. The VIS scintillation band centred around 630 nm is compatible with the wavelength-dependent quantum efficiency of CCD, EMCCD or CMOS imaging sensors and makes the use of wavelength shifters in such gas mixtures obsolete. The spectra of the scintillation light emitted by GEM-based detectors in  $\text{Ar}/\text{CF}_4$ ,  $\text{He}/\text{CF}_4$  and  $\text{Ne}/\text{CF}_4$  gas mixtures with different mixing ratios were measured and sharp emission lines characteristic for the present noble gas species were observed in addition to the above-mentioned emission bands. The secondary scintillation light yield of gas mixtures was compared and an  $\text{Ar}/\text{CF}_4$  gas mixture with a mixing ratio of 80/20% was found to provide the highest light yield of about 0.3 scintillation photons per secondary electron among the investigated mixtures.

The applicability of optically read out GEM-based radiation detectors was investigated and prototype detectors optimised for various studies were developed. Imaging capabilities were demonstrated by recording X-ray radiographs and the integrated full-field imaging capabilities provided by optical readout were shown to be well-suited for X-ray fluoroscopy. 2D images of tracks of alpha particles and muons were acquired and enabled an intuitive identification and interpretation of radiation events.

An optically read out GEM-based TPC was developed to study the possibility of 3D reconstruction from optically recorded 2D images and associated depth information. High-granularity 2D images enabled accurate track reconstruction and line profiles of pixel value intensities in images could be matched with PMT waveforms for unambiguous determinations of alpha track orientations. Primary and secondary scintillation light signals were observed by a PMT and could be used to extract absolute depth information. To extend the track reconstruction capabilities of optically read out TPCs to more intricate, curved particle tracks, an ITO-based transparent anode was developed. This strip anode permitted simul-

taneous electronic and optical readout and enabled the reconstruction of complex particle tracks.

The emitted secondary scintillation light intensity corresponds to the energy deposited by incident radiation in GEM-based detectors operated in a proportional amplification regime. Images of individual low-energy photons interacting in a triple-GEM-based detector were recorded and the deposited energy was extracted from pixel value intensities in the optically read out images. An energy resolution of about 30 % FWHM at 5.9 keV was achieved, which is comparable to the one achieved with electronic readout. Full-field X-ray fluorescence measurements with an optically read out GEM-based detector were performed and energy-resolved 2D images could be reconstructed and used for material distinction. In addition, a concept for mitigating the parallax-induced broadening of signal spots in X-ray fluorescence or crystallography measurements with gaseous detectors with thick drift regions was tested. A planispherical GEM-based detector prototype employing radially focused drift field lines was developed and shown to effectively minimise parallax-induced broadening and preserve good signal-to-noise ratios even in off-centre regions of the active area.

An optically read out detector prototype for beam monitoring applications in hadron therapy was developed with a total material budget below 0.7 mm WET due to the usage of thin foils as detector components and windows. Secondary scintillation light emitted by a GEM was coupled to a camera outside of the beam path by a mirror. Combining an optically read out GEM with an ionisation chamber, this detector provides high-resolution dose distribution images as well as accurate and stable total dose monitoring capabilities. The detector was tested in a clinical environment in a proton therapy facility and beam profile monitoring, dose depth curve recording and treatment plan visualisation were demonstrated.

While optical readout might not be able to compete with electronic readout for some applications requiring high frame rates or large-area coverage, the ongoing development of novel imaging sensors could overcome some of these limitations. With ever-increasing pixel sensitivities and numbers of pixels, future imaging sensors might push back the frontiers of recordable phenomena and lead to the application of optical readout of radiation detectors in an increasing number of fields and experiments.

Versatile detectors capable of visualising radiation ranging from MIPs to strongly ionising particles and particle beams can be realised by combining the high dynamic range of GEM-based detectors with the granularity and sensitivity of imaging sensors. This makes optical readout an attractive readout modality for applications ranging from high energy physics to nuclear physics experiments as well as beam monitoring for medical applications.





## APPENDIX A

# Experimental details

### A.1 Quantum efficiency of CCD, EMCCD and CMOS imaging sensors

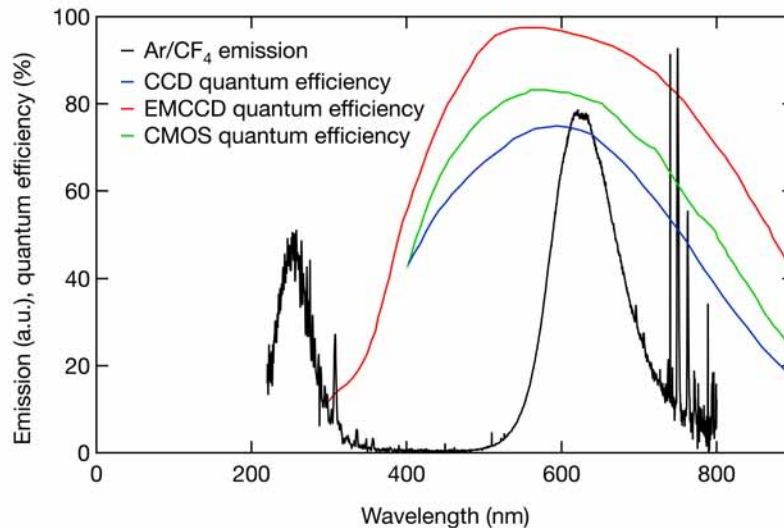


**Figure 90.** Wavelength-dependent quantum efficiencies of imaging sensors: CCD, EMCCD and CMOS imaging sensors are optimised for highest quantum efficiency in the visible wavelength range. The quantum efficiency curves of the shown imaging sensors are well-suited to record the visible scintillation band of Ar/CF<sub>4</sub> gas mixtures.

A comparison of the quantum efficiency curves of CCD (QImaging Retiga R6 [66]), EMCCD (Hamamatsu ImagEM X2 C9100-23B [61]) and CMOS (Hamamatsu ORCA-Flash4.0 V3 C13440-20CU [61]) imaging sensors is shown in figure 90. The quantum efficiency of the CCD imaging sensor peaks at 595 nm with a maximum value of 75 %. The CMOS quantum efficiency reaches a maximum value of 83 % at a wavelength of about 565 nm. The EMCCD camera provides a high quantum efficiency of more than 90 % over a wavelength range between 490 nm and 690 nm, with a peak quantum efficiency of more than 97 % at 560 nm.

### A.2 GEM gain measurement

The effective charge gain of a GEM can be measured as a function of the voltage across the GEM by measuring the current of secondary electrons leaving the holes of the GEM and comparing it with the primary ionisation current in the drift volume. A single GEM foil

was placed in a gas volume with a Cu-based cathode to define a drift field in a drift gap with a thickness of 3 mm. No anode was placed below the GEM to ensure that secondary electrons generated during electron avalanche multiplication will be collected by the bottom electrode of the GEM. The cathode was powered with a negative voltage to define the drift field in the conversion region. The top electrode of the GEM foil was grounded and the bottom electrode of the GEM was powered with a positive voltage to define the voltage drop across the GEM. An ammeter was placed between the bottom electrode of the GEM and the power supply channel to measure the current reaching the bottom electrode of the GEM with a 25 kΩ resistor in series between the GEM and the ammeter.

For different drift fields ranging from 50 V/cm to 2000 V/cm, the voltage drop across the GEM was varied from 0 V up to 400 V or 500 V and the current on the bottom electrode of the GEM was recorded. The detector was irradiated by an X-ray tube with a Cu target operated with an acceleration voltage of 20 kV and a current of 0.2 mA or 1 mA. The X-ray tube was placed about 50 cm from the detector to achieve an approximately flat beam profile across the active area of the detector. The irradiated area was defined by a cutout in a Cu foil mounted in front of the detector to a circular area of about 30 cm<sup>2</sup>. Even for the highest used irradiation rate of about 300 MHz corresponding to a primary ionisation current of  $I_0 = 10$  nA, the interaction rate per mm<sup>2</sup> of 100 kHz/mm<sup>2</sup> was in a regime where no modifications of the gain due to high charge densities are expected [6]. An exemplary measurement of the currents on the bottom electrode of the GEM as a function of the voltage drop across the GEM for different drift fields measured in an Ar/CF<sub>4</sub> gas mixture with a mixing ratio of 80/20% is shown in figure 91.

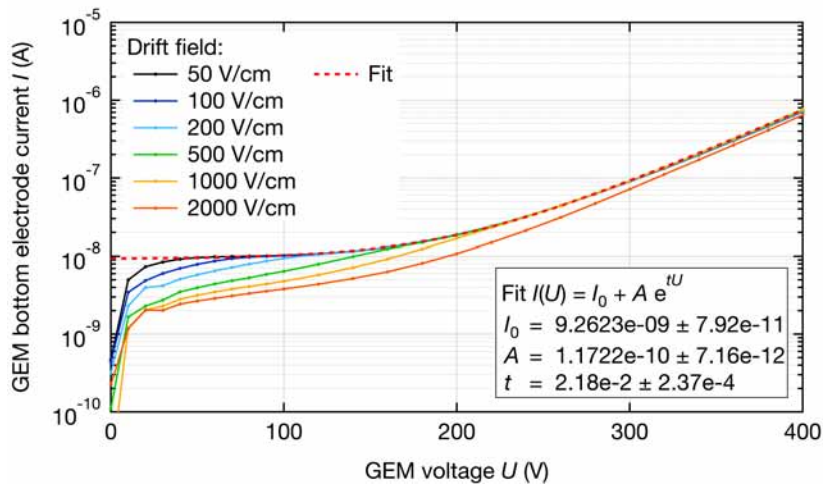


**Figure 91.** GEM gain measurement: The current measured at the bottom electrode of a single GEM increases exponentially with the voltage drop across the GEM for moderate and high voltages. At low voltages, the primary electron current  $I_0$  results in a current offset. The ratio between the GEM current and  $I_0$  is the gain of the GEM. At high drift fields, primary electrons might not be fully collected into the holes of the GEM. The shown measurements for different drift fields were measured with a single GEM in an Ar/CF<sub>4</sub> gas mixture with a mixing ratio of 80/20% irradiated with X-rays from an X-ray tube operated with an acceleration voltage of 20 kV and a tube current of 1 mA.

At low GEM voltages, primary electrons from the drift region might not be collected into the holes of the GEM with full efficiency. For higher drift fields, higher GEM voltages are necessary to achieve full primary electron collection efficiency. The approximately constant current for GEM voltages between 50 V and 100 V for the lowest drift field of 50 V/cm signals good electron collection efficiency before the onset of significant avalanche multiplication. In



this range of voltages, the primary ionisation current is collected into the holes of the GEM and recorded on the bottom electrode of the GEM. For a higher voltage drop across the GEM, electron avalanche multiplication sets in and the recorded current rises exponentially with the voltage drop across the GEM. Fitting the recorded currents with an exponential function  $I(U) = I_0 + A e^{tU}$  with the current  $I$  and the GEM voltage  $U$ , allows an extraction of the primary ionisation current  $I_0$ . In the presented case, a primary ionisation current of about  $I_0 = 9.2$  nA was measured.

By dividing the current  $I(U)$  at a certain voltage  $U$  by the primary ionisation current  $I_0$ , the effective charge gain  $G(U)$  can be determined as  $G(U) = \frac{I(U)}{I_0}$ .

For higher drift field strengths, higher GEM voltages are needed to achieve full primary electron collection efficiency. For drift fields of several hundred V/cm, full primary electron collection efficiency might not be achieved before the onset of electron avalanche multiplication. Therefore, the primary ionisation current was extracted from measurements at a low drift field of 50 V/cm. For drift fields of 50 V/cm to 1000 V/cm, full primary electron collection efficiency is achieved around or below a voltage drop of 250 V across the GEM as can be seen from the overlap of the measured current curves for higher voltages. In the case of a high drift field of 2000 V/cm, the high field strength might result in some primary electrons impinging on the top electrode of the GEM and not being available for electron avalanche multiplication. This effect leads to lower currents being measured in the case of a high drift field strength.

### A.3 Photon detection efficiency

#### Spectral detection efficiency

The efficiency for the detection of emitted scintillation photons by a PMT depends on the emission spectrum of the investigated gas mixture, the transmission of all elements in the optical path from the triple-GEM where scintillation light is emitted to the PMT and the quantum efficiency curve of the employed PMT (Hamamatsu R375 [61]). The detection efficiency  $D$  for emitted secondary scintillation photons was determined for the setup used for light yield measurements by taking into account the emission spectrum  $E(\lambda)$  normalised to the total scintillation light emission for the wavelength range of 200 nm to 800 nm of the employed gas mixtures, the wavelength-dependent transmission  $T(\lambda)$  of the deep-UV-grade fused silica viewport and the quantum efficiency  $QE_{\text{PMT}}(\lambda)$  of the PMT, which also depends on the wavelength  $\lambda$ . The emission spectrum, viewport transmission and PMT quantum efficiency are shown in figure 92.

The detection efficiency was calculated by integrating the contributions over the investigated range of wavelengths as

$$D = \int E(\lambda) \times T(\lambda) \times QE_{\text{PMT}}(\lambda) d\lambda \quad (\text{A.1})$$

For the case of an Ar/CF<sub>4</sub> gas mixture with a mixing ratio of 80/20% as shown in figure 92, a detection efficiency of  $D = 11.36\%$  was determined by numeric integration in steps of 0.5 nm over a wavelength range from 200 nm to 800 nm. For He/CF<sub>4</sub> gas mixtures, detection efficiencies of  $D = 17.38\%$  and  $D = 16.33\%$  for mixing ratios of 80/20% and 60/40%, respectively, were determined. For a Ne/CF<sub>4</sub> gas mixture with a mixing ratio of 80/20%, a detection efficiency of  $D = 12.86\%$  was calculated.

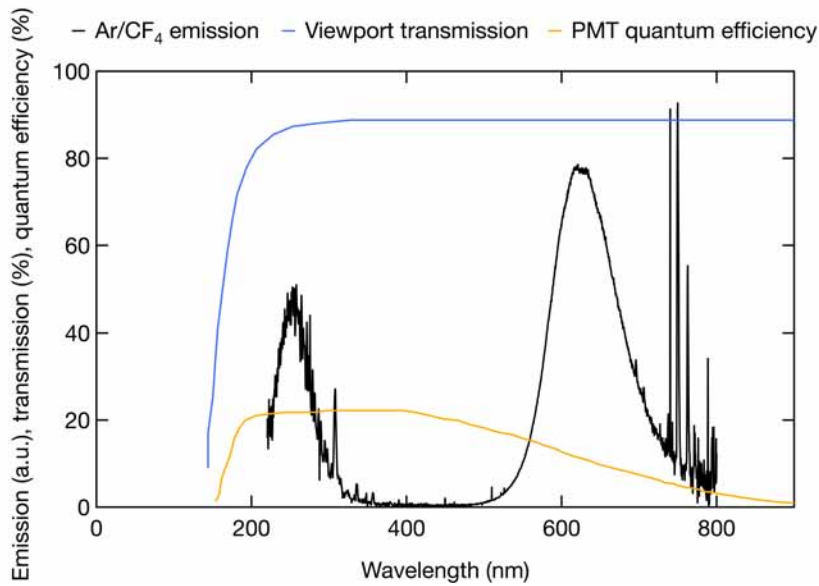


**Figure 92.** Spectral detection efficiency of secondary scintillation photons by PMT: The high transmission of the deep-UV-grade fused silica viewport permits secondary scintillation light from both UV and visible emission bands to reach the PMT. The quantum efficiency of the PMT permits detection of UV and visible photons.

### Geometric detection efficiency

The geometric acceptance factor for the detection of scintillation photons emitted from the last GEM in a triple-GEM stack in the setup used for light yield measurements was determined from the profile of employed X-ray beams and the geometric acceptance for photons in certain regions of the active area of the detector. The profile of the X-ray beam from an <sup>55</sup>Fe source was recorded by optical readout of the emitted secondary scintillation light with a CCD camera. An example of the distribution of X-rays across the active area of the GEM as used for light yield measurements is shown in figure 93a.

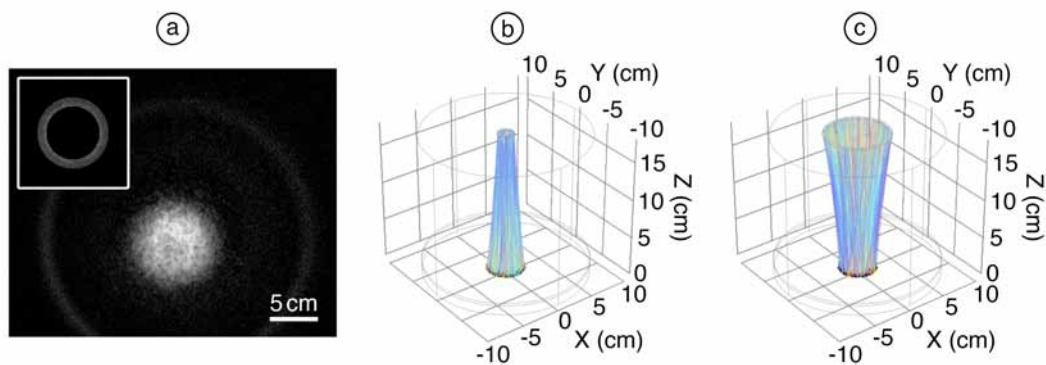


**Figure 93.** Determination of geometric photon detection efficiency by PMT: (a) Optically read out image of X-rays from collimated <sup>55</sup>Fe source interacting in GEM-based detector for light yield measurements. Inset: The relative radial intensity distribution of the source was determined by integrating the intensity in rings with a width of 5 mm with increasing inner diameters. (b) Ray tracing simulation to determine the geometric acceptance factor for photons emitted in a 5 mm wide ring with 5 mm inner diameter. (c) Ray tracing simulation to determine the geometric acceptance factor for photons emitted in a 5 mm wide ring with 35 mm inner diameter.

The radial intensity distribution of the X-ray beams was determined by integrating the pixel value intensity in rings with a width of 5 mm with increasing inner diameters ranging

from 0 mm to 45mm to obtain intensity profiles of the X-ray flux detected by the triple-GEM stack.

The ratio between the number of recorded photons and the originally emitted number of secondary scintillation photons was determined with a ray tracing simulation (F. Resnati) implemented in COMSOL [80]. Photons originating in a certain ring-shaped region on the active area of the GEM with random orientations were produced. The number of photons reaching the 2-inch diameter active detection area of the PMT located about 13 cm from the last GEM in the triple-GEM stack was recorded. The simulation was repeated for different ring-shaped regions of photon emission from the GEM plane with ring widths of 5 mm and inner ring diameters increasing from 0 mm to 45 mm corresponding to the regions used in the determination of the radial X-ray beam profiles. For each measurement point,  $10^4$  photons were produced and used to determine the fraction of photons reaching the PMT active area. Examples of ray tracing simulations for two selected ring-shaped regions of photon emission are shown in figures 93b and 93c.

The total geometric acceptance  $G$  for secondary scintillation photons from the GEM by the PMT was subsequently calculated by the expression

$$G = \sum_{r_i} \frac{I_{r_i}}{I_t} G_{r_i} \quad (\text{A.2})$$

with the integrated pixel value intensity  $I_{r_i}$  in an optical image of the X-ray beam profile for a ring-shaped region with an inner diameter of  $r_i$ , the total sum of the integrated intensities of all ring-shaped regions,  $I_t$ , and the fraction of photons produced in a certain ring-shaped region reaching the PMT active area,  $G_{r_i}$ , as determined from the ray tracing simulation. For the light yield measurements performed with an  $^{55}\text{Fe}$  source, a geometric acceptance factor for the detection of secondary scintillation photons from the third GEM in a triple-GEM stack by the PMT of  $G = 0.8\%$  was determined. The error in the determination of the geometric acceptance factor is estimated to be less than 10 %.

## A.4 PMT dynamic range

The dynamic range of the 2-inch PMT (Hamamatsu R375 [61]) used for light yield measurements was determined by increasing the gain of a triple-GEM stack resulting in increasing numbers of secondary scintillation photons being recorded by the PMT and plotting the trend of the PMT response and the gain of the triple-GEM stack. The PMT was operated at a voltage of 1000 V corresponding to a nominal gain of about  $10^5$ . The voltage of the third GEM in the stack was fixed at 420 V and the voltage of the first two GEMs was varied over a voltage range from 340 V to 430 V across the first GEM. The PMT response under irradiation with X-rays from an  $^{55}\text{Fe}$  source was determined by building energy spectra from the integrated signal intensities in PMT waveforms and using the location of the full energy peak in the energy spectrum of  $^{55}\text{Fe}$  as an indication for the PMT response. The PMT response and the total effective GEM gain of the triple-GEM stack over the covered range of voltages across the first GEM in the stack is shown in figure 94.

The total effective gain of the GEM increases exponentially over the full range of voltages. The PMT response also increases exponentially with the voltage drop across the first two GEMs up to an integrated PMT signal intensity of about  $4 \times 10^{-9}$  V s corresponding to about 400 detected photons. Above this value, the response of the PMT deviates from the

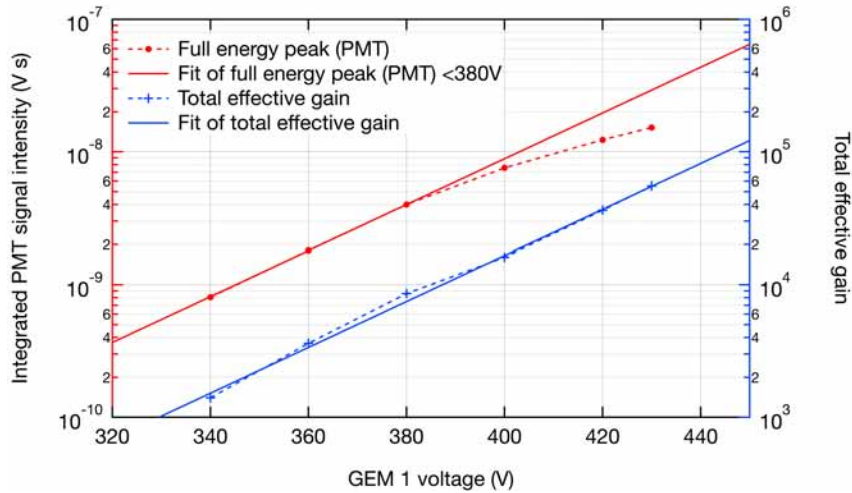


**Figure 94.** Linearity of PMT and GEM responses: With a fixed voltage drop of 420 V across the third GEM in a triple-GEM stack, the voltage drop across the first two GEMs was varied and the PMT response and triple-GEM gain were measured. The total effective gain of the triple-GEM stack increases exponentially with increasing voltage drops across the first two GEMs. The integrated PMT signal intensity for X-ray signals from an  $^{55}\text{Fe}$  source increases exponentially up to an integrated intensity of about  $4 \times 10^{-9}$  V s and deviates from the exponential trend for higher detector gains. This behaviour for higher PMT signal intensities indicates saturation of the PMT.

exponential trend indicating saturation of the PMT response. Therefore, the gain of the GEM was adjusted during quantitative measurements to mitigate PMT saturation.

## A.5 PMT single photon response

To enable a determination of the number of photons detected by the employed PMT (Hamamatsu R375 [61]), the response of the PMT to a single photon was recorded. The PMT was operated with a total voltage of 1000 V inside a light shielding tube. An LED connected to a pulse generator was placed in the light shielding tube with the PMT and powered with short voltage pulses with a width of 20 ns and an amplitude of about 4.6 V. The response of the PMT was recorded by an oscilloscope triggering on the pulses from the pulse generator and the integrated signal intensity from the PMT waveforms was recorded. A distribution of the integrated signal intensity recorded by the PMT in this configuration is shown in figure 95.

Although the obtained distribution of integrated PMT signal intensities does not exhibit a clearly pronounced peak apart from the dominating noise peak around 0 V s, additional Gaussian peaks corresponding to one and two photon events could be determined by curve fitting. The resulting curve consisting of three Gaussian curves fits the observed distribution well. The single photon intensity could subsequently be extracted from the difference between the noise level and the peak of the Gaussian curve corresponding to single photon events detected by the PMT. For a PMT voltage of 1000 V corresponding to a nominal PMT gain of about  $10^5$ , an integrated PMT signal intensity for single photon events of  $I_{\text{ph}} = 1.07 \times 10^{-11}$  Vs was determined.

The integrated intensity of single photon events detected by the PMT was determined by a second method for verification. The integrated intensity of the single photon response detected by the PMT was recorded and the total voltage applied to the PMT was varied from 1150 V to 1400 V. The acquired data points were fitted by an exponential function, which was subsequently used to extrapolate the single photon response of the PMT at a voltage

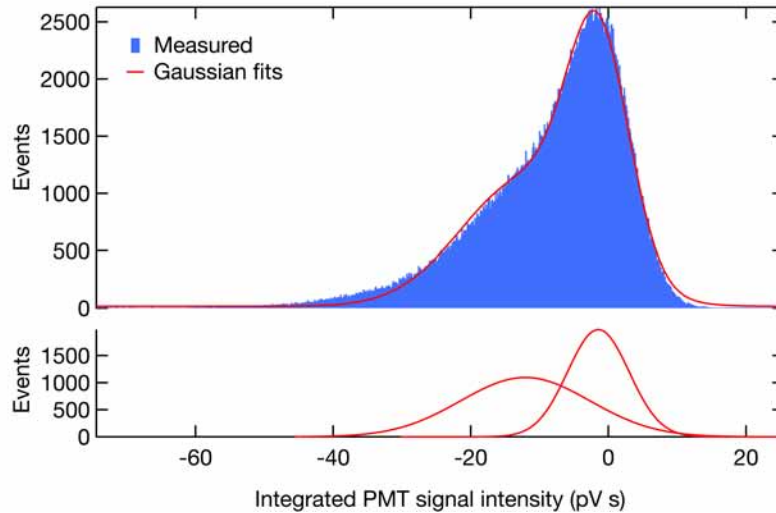


**Figure 95.** Single photon response of PMT: An LED located in the light shielding tube housing the PMT was powered with short voltage pulses with a width of 20 ns and an amplitude of about 4.6 V to emit a low number of photons. Triggering on the electronic pulses, signals from the PMT operated at 1000 V in coincidence with the pulses sent to the LED were recorded. The intensity of PMT signals was determined by integrating waveforms and the distribution of PMT signal intensities was plotted (top). The distribution of intensities was fitted with multiple Gaussian curves corresponding to PMT signals for zero, one, and two photon events (bottom). The difference between the peak positions for zero and one photon events was used as single photon response of the PMT.

of 1000 V as shown in figure 96. The determined value deviates from the one determined by the above-mentioned method by about 14 %, which contributes to the statistical error of the light yield measurements.

## A.6 Residual gas analyser setup

An RGA (SRS RGA100/2 [116]) was used to measure gas compositions and impurities in the optically read out detectors. The permitted operating pressure of the RGA of up to about  $1.3 \times 10^{-4}$  mbar [116] is not compatible with the pressure commonly used in GEM-based detectors. Therefore, a sampling system was implemented to allow the RGA to operate at about  $5 \times 10^{-6}$  mbar and sample from gas volumes at pressures of around 1 bar.

The head of the RGA was mounted to a sampling volume based on a CF40 6-way cross continuously pumped by a turbomolecular pump. The pressure in the sampling volume was monitored by a cold cathode gauge and kept below  $1 \times 10^{-5}$  mbar. Due to the gas species dependence of the response of the cold cathode gauge, its reading was only used to estimate the approximate pressure in the sampling volume. Base pressures below  $1 \times 10^{-8}$  mbar were achieved after prolonged pumping. The low-pressure sampling volume was connected to a high-pressure volume through a manual all-metal leak valve. The high-pressure volume was either connected to the detector vessel with a CF40 bellow or connected in series in open gas flow mode operation between the detector outlet and the gas exhaust. This sampling method permitted the flow of a small quantity of gas from the high-pressure volume to the sampling volume through the leak valve to allow a characterisation of the gas composition by the RGA. The sampling setup is schematically shown in figure 97.

Examples of gas species spectra recorded by the RGA for vacuum and for an Ar/CF<sub>4</sub> gas mixture with a mixing ratio of 80/20% are shown in figure 98.

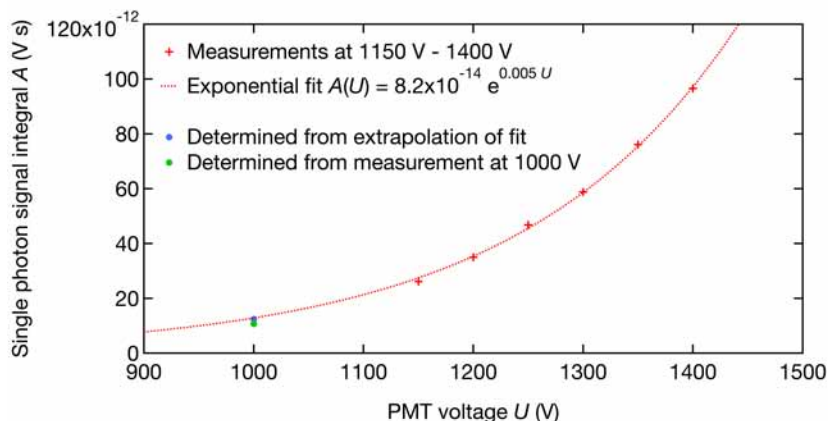


**Figure 96.** Extrapolation of single photon response of PMT: The single photon response was determined as a function of the total voltage applied to the PMT. The measured integrated intensities of single photon signals detected by the PMT for voltages from 1150 V to 1400 V were fitted with an exponential function and the obtained parameters were used to extrapolate the single photon response at a PMT voltage of 1000 V. The measured single photon response at a PMT voltage of 1000 V is shown for comparison and deviates from the extrapolated value by about 14 %.

## Gas species dependence of RGA response

The sampling of gas from a high-pressure volume to the RGA sampling volume depends on the gas flow through the leak valve. Due to the small size of the opening used to permit some gas flow through the leak valve, the conductance of the leak valve might not be independent of the gas species. Different gases might traverse the leak valve more or less uninhibited resulting in a misrepresentation of the gas composition in the high-pressure volume in the low-pressure sampling volume and therefore in distorted gas composition measurements acquired by the RGA. For small orifices, the conductance  $C$  in the molecular flow regime is defined as

$$C = A \sqrt{\frac{kT}{2\pi m}} \quad (\text{A.3})$$

with the cross section of the orifice  $A$ , the Boltzmann constant  $k$ , the temperature of the gas  $T$  and the molecular mass of the gas species  $m$  [117]. Therefore, gases with low molecular masses will be overrepresented in the sampling volume and in spectra recorded by the RGA with respect to gases with higher molecular masses.

As the shape and dimensions of the opening of the leak valve are not known and other aspects of the sampling system might also have an effect on the gas species-specific response of the RGA, a calibration of the RGA response with gas mixtures with well-known mixing ratios was performed. An Ar/CF<sub>4</sub> gas mixture with a mixing ratio of 80/20%, an Ar/CO<sub>2</sub> gas mixture with a mixing ratio of 70/30% and a Ne/CO<sub>2</sub>/N<sub>2</sub> gas mixture with a mixing ratio of 85.7/9.5/4.8% were used to determine correction factors for different gas species relative to the response of the RGA to Ar.

The validity of the gas species-specific correction factors for the RGA response for different leak valve settings, varying pressures in the high-pressure volume and changing mixing ratios was investigated. Only small variations of the response for different mixing ratios in an Ar/CF<sub>4</sub> gas mixture were observed. The correction factor for CF<sub>4</sub> relative to Ar varied by up to 30 % when decreasing the pressure in the high-pressure volume from 1 bar to 100 mbar. A strong change in the required correction factor for the RGA response to CF<sub>4</sub> was also

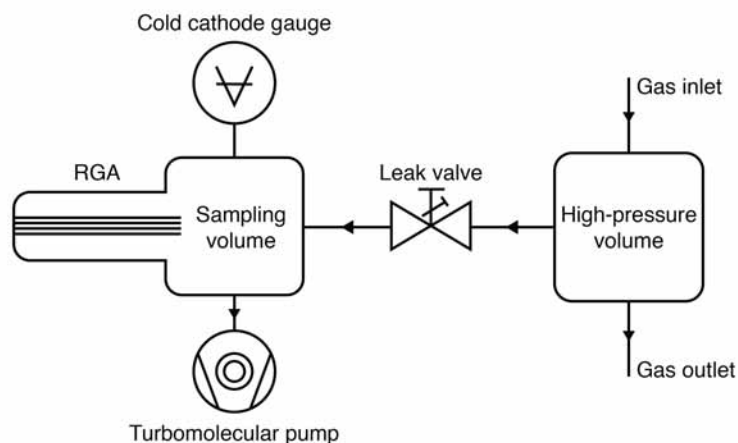


**Figure 97.** RGA setup for sampling from high-pressure volume: The RGA measures the gas composition in a sampling volume, in which a pressure of about  $5 \times 10^{-6}$  mbar is maintained by a turbomolecular pump and monitored by a cold cathode gauge. Gas from a high-pressure volume at around 1 bar is sampled through a leak valve. The detector vessel is connected to the gas inlet of the high-pressure volume in the RGA sampling setup and gas exits through the gas outlet to an exhaust.

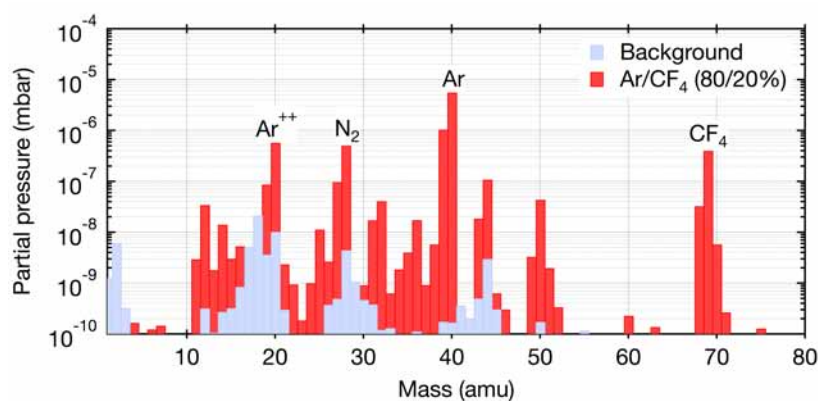


**Figure 98.** RGA spectra: The RGA provides spectra showing partial pressure as a function of atomic mass. The background spectrum was measured in vacuum and shows residual contamination of the system. After subtraction of the background, the spectrum of an Ar/CF<sub>4</sub> gas mixture with a mixing ratio of 80/20% shows pronounced Ar and CF<sub>4</sub> peaks at 40 amu and 69 amu, respectively, a less abundant Ar<sup>++</sup> peak at 20 amu and some residual contamination with N<sub>2</sub> at 28 amu.

observed when changing the size of the orifice between the high-pressure volume and the sampling volume by varying the leak valve setting. To be able to use the determined correction factors, the same leak valve setting was used for calibration and measurements. As the pressure in the detector vessel was kept constant at around 1 bar for the majority of measurements, the dependence of the RGA response on the pressure in the high-pressure volume did not distort partial pressure measurements.





## References

- [1] H. Kolanoski et al. *Teilchendetektoren*. Springer Berlin Heidelberg, Berlin, Heidelberg, 2016.
- [2] C. A. Klein. Bandgap Dependence and Related Features of Radiation Ionization Energies in Semiconductors. *J. Appl. Phys.*, 39(4):2029–2038, 1968.
- [3] M.J. Berger et al. XCOM: Photon Cross Sections Database. <https://www.nist.gov/pml/xcom-photon-cross-sections-database>, Accessed: 2018-02-22.
- [4] F. Sauli. *Gaseous Radiation Detectors*. Cambridge Monographs on Particle Physics, Nuclear Physics and Cosmology. Cambridge University Press, Cambridge, 2014.
- [5] V. Peskov et al. The study and optimization of new micropattern gaseous detectors for high-rate applications. *IEEE Trans. Nucl. Sci.*, 48(4):1070–1074, 2001.
- [6] P. Thuiner. *Ion space-charge effects in multi-GEM detectors : challenges and possible solutions for future applications*. PhD thesis, Technische Universität Wien, 2016.
- [7] M. Titov et al. Micro-Pattern Gaseous Detector Technologies and RD51 Collaboration. *Mod. Phys. Lett. A*, 28(13):1340022, 2013.
- [8] A. Oed. Detectors for thermal neutrons. *Nucl. Instruments Methods Phys. Res. Sect. A*, 525(1-2):62–68, 2004.
- [9] E.M. Bazelyan et al. *Spark Discharge*. CRC Press, 1997.
- [10] F. Sauli. Principles of operation of multiwire proportional and drift chambers. Technical report, CERN, Geneva, 1997.
- [11] E. Rutherford et al. An Electrical Method of Counting the Number of Alpha-Particles from Radio-Active Substances. *Proc. R. Soc. A Math. Phys. Eng. Sci.*, 81(546):141–161, 1908.
- [12] G. Charpak et al. The use of multiwire proportional counters to select and localize charged particles. *Nucl. Instruments Methods*, 62(3):262–268, 1968.
- [13] A. Oed. Position-sensitive detector with microstrip anode for electron multiplication with gases. *Nucl. Instruments Methods Phys. Res. Sect. A*, 263(2-3):351–359, 1988.
- [14] J. Schmitz. *The Microstrip Gas Counter and its application in the ATLAS inner tracker*. PhD thesis, NIKHEF-H, 1994.

- [15] B. Mindur et al. Performance of a Micro-Strip Gas Chamber for event wise, high rate thermal neutron detection with accurate 2D position determination. *J. Instrum.*, 9(12):P12004–P12004, 2014.
- [16] Y. Giomataris et al. MICROMEGAS: a high-granularity position-sensitive gaseous detector for high particle-flux environments. *Nucl. Instruments Methods Phys. Res. Sect. A*, 376(1):29–35, 1996.
- [17] J. Melai et al. A UV sensitive integrated Micromegas with Timepix readout. *Nucl. Instruments Methods Phys. Res. Sect. A*, 628(1):133–137, 2011.
- [18] F. Sauli. GEM: A new concept for electron amplification in gas detectors. *Nucl. Instruments Methods Phys. Res. Sect. A*, 386(2-3):531–534, 1997.
- [19] F. Sauli. The gas electron multiplier (GEM): Operating principles and applications. *Nucl. Instruments Methods Phys. Res. Sect. A*, 805:2–24, 2016.
- [20] D. Mörmann et al. Evaluation and reduction of ion back-flow in multi-GEM detectors. *Nucl. Instruments Methods Phys. Res. Sect. A*, 516(2-3):315–326, 2004.
- [21] K. Ikematsu. Development of large-aperture GEMs as a gating device of the ILC-TPC for blocking positive ion feedback. In *2014 IEEE Nucl. Sci. Symp. Med. Imaging Conf.*, pages 1–4. IEEE, 2014.
- [22] A. Bondar et al. Light multi-GEM detector for high-resolution tracking systems. *Nucl. Instruments Methods Phys. Res. Sect. A*, 556(2):495–497, 2006.
- [23] B. Mindur et al. Performance of a GEM detector with copper-less foils. *J. Instrum.*, 12(09):P09020–P09020, 2017.
- [24] R. Chechik et al. Thick GEM-like hole multipliers: properties and possible applications. *Nucl. Instruments Methods Phys. Res. Sect. A*, 535(1-2):303–308, 2004.
- [25] T. Fujiwara et al. Fine-pitch glass GEM for high-resolution X-ray imaging. *J. Instrum.*, 11(12):C12050–C12050, 2016.
- [26] T. Fujiwara et al. Gas scintillation glass GEM detector for high-resolution X-ray imaging and CT. *Nucl. Instruments Methods Phys. Res. Sect. A*, 850(January):7–11, 2017.
- [27] F. D. Amaro et al. The Thick-COBRA: a new gaseous electron multiplier for radiation detectors. *J. Instrum.*, 5(10):P10002–P10002, 2010.
- [28] R. Bellazzini et al. The WELL detector. *Nucl. Instruments Methods Phys. Res. Sect. A*, 423(1):125–134, 1999.
- [29] A. Rubin et al. First studies with the Resistive-Plate WELL gaseous multiplier. *J. Instrum.*, 8(11):P11004–P11004, 2013.
- [30] T. Alexopoulos et al. A spark-resistant bulk-micromegas chamber for high-rate applications. *Nucl. Instruments Methods Phys. Res. Sect. A*, 640(1):110–118, 2011.
- [31] M. Byszewski et al. Resistive-strips micromegas detectors with two-dimensional readout. *J. Instrum.*, 7(02):C02060–C02060, 2012.
- [32] D. Attié et al. Piggyback resistive Micromegas. *J. Instrum.*, 8(11):C11007–C11007, 2013.

- [33] A. Bamberger et al. Resolution studies on 5GeV electron tracks observed with triple-GEM and MediPix2/TimePix-readout. *Nucl. Instruments Methods Phys. Res. Sect. A*, 581(1-2):274–278, 2007.
- [34] A. Bressan et al. Two-dimensional readout of GEM detectors. *Nucl. Instruments Methods Phys. Res. Sect. A*, 425(1-2):254–261, 1999.
- [35] B. Ketzer et al. Performance of triple GEM tracking detectors in the COMPASS experiment. *Nucl. Instruments Methods Phys. Res. Sect. A*, 535(1-2):314–318, 2004.
- [36] F. García et al. A GEM-TPC in twin configuration for the Super-FRS tracking of heavy ions at FAIR. *Nucl. Instruments Methods Phys. Res. Sect. A*, 884(December 2017):18–24, 2018.
- [37] J. Derré et al. Spatial resolution in Micromegas detectors. *Nucl. Instruments Methods Phys. Res. Sect. A*, 459(3):523–531, 2001.
- [38] F. Sauli. Radiation imaging with gaseous detectors. *Nucl. Instruments Methods Phys. Res. Sect. A*, 878:1–9, 2017.
- [39] S.P. George et al. Particle tracking with a Timepix based triple GEM detector. *J. Instrum.*, 10(11):P11003–P11003, 2015.
- [40] H. van der Graaf. GridPix: An integrated readout system for gaseous detectors with a pixel chip as anode. *Nucl. Instruments Methods Phys. Res. Sect. A*, 580(2):1023–1026, 2007.
- [41] M. Campbell et al. Detection of single electrons by means of a Micromegas-covered MediPix2 pixel CMOS readout circuit. *Nucl. Instruments Methods Phys. Res. Sect. A*, 540(2-3):295–304, 2005.
- [42] T. Alexopoulos. The micromegas project for the ATLAS upgrade. In *2013 IEEE Nucl. Sci. Symp. Med. Imaging Conf. (2013 NSS/MIC)*, pages 1–7. IEEE, 2013.
- [43] A Colaleo et al. CMS Technical Design Report for the Muon Endcap GEM Upgrade. Technical Report September, CERN, Geneva, 2015.
- [44] P. Gasik. Building a large-area GEM-based readout chamber for the upgrade of the ALICE TPC. *Nucl. Instruments Methods Phys. Res. Sect. A*, 845:222–225, 2017.
- [45] G. G. Barnaföldi et al. Portable cosmic muon telescope for environmental applications. *Nucl. Instruments Methods Phys. Res. Sect. A*, 689:60–69, 2012.
- [46] A. Morozov et al. Effect of the electric field on the primary scintillation from CF<sub>4</sub>. *Nucl. Instruments Methods Phys. Res. Sect. A*, 628(1):360–363, 2011.
- [47] V.M. Gehman et al. Fluorescence efficiency and visible re-emission spectrum of tetraphenyl butadiene films at extreme ultraviolet wavelengths. *Nucl. Instruments Methods Phys. Res. Sect. A*, 654(1):116–121, 2011.
- [48] A. Pansky et al. The scintillation of CF<sub>4</sub> and its relevance to detection science. *Nucl. Instruments Methods Phys. Res. Sect. A*, 354(2-3):262–269, 1995.
- [49] A Morozov et al. Secondary scintillation in CF<sub>4</sub> : emission spectra and photon yields for MSGC and GEM. *J. Instrum.*, 7(02):P02008–P02008, 2012.

- [50] M.M.F.R. Fraga et al. The GEM scintillation in He-CF<sub>4</sub>, Ar-CF<sub>4</sub>, Ar-TEA and Xe-TEA mixtures. *Nucl. Instruments Methods Phys. Res. Sect. A*, 504(1-3):88–92, 2003.
- [51] L.M.S. Margato et al. Performance of an optical readout GEM-based TPC. *Nucl. Instruments Methods Phys. Res. Sect. A*, 535(1-2):231–235, 2004.
- [52] H. Natal da Luz et al. GEM operation in CF<sub>4</sub>: Studies of charge and scintillation properties. In *2008 IEEE Nucl. Sci. Symp. Conf. Rec.*, pages 2650–2652. IEEE, 2008.
- [53] E. Seravalli. *A Scintillating GEM Detector for 2D Dose Imaging in Hadron Therapy*. PhD thesis, Technische Universiteit Delft, 2008.
- [54] L. G. Christophorou et al. Electron Interactions With Plasma Processing Gases: An Update for CF<sub>4</sub>, CHF<sub>3</sub>, C<sub>2</sub>F<sub>6</sub>, and C<sub>3</sub>F<sub>8</sub>. *J. Phys. Chem. Ref. Data*, 28(4):967–982, 1999.
- [55] U. Müller et al. Further studies of the continuous UV emission produced by electron impact on CF<sub>4</sub>. *Zeitschrift für Phys. D Atoms, Mol. Clust.*, 24(2):131–139, 1992.
- [56] L. C. Lee et al. Fluorescence from extreme ultraviolet photoexcitation of CF<sub>4</sub>. *J. Chem. Phys.*, 85(11):6294–6300, 1986.
- [57] K. Furuya et al. Fragment ion-photon coincidence investigation of carbon tetrafluoride by controlled electron impact. *J. Phys. B At. Mol. Opt. Phys.*, 34(8):1405–1413, 2001.
- [58] M. Tsuji et al. Dissociative excitation of CF<sub>4</sub>, CCl<sub>4</sub>, and chlorofluoromethanes by collisions with argon and helium active species. *J. Chem. Phys.*, 97(1):245–255, 1992.
- [59] J. E. Hesser et al. Radiative Lifetimes of Ultraviolet Molecular Transitions. *J. Chem. Phys.*, 45(8):3149–3150, 1966.
- [60] N. Washida et al. Emission spectra of CF<sub>3</sub> radicals. IV. Excitation spectra, quantum yields, and potential energy surfaces of the CF<sub>3</sub> fluorescences. *J. Chem. Phys.*, 78(3):1025–1032, 1983.
- [61] Hamamatsu Photonics K.K. Hamamatsu. <https://www.hamamatsu.com>, Accessed: 2017-10-23.
- [62] R. Abbasi et al. The IceCube data acquisition system: Signal capture, digitization, and timestamping. *Nucl. Instruments Methods Phys. Res. Sect. A*, 601(3):294–316, 2009.
- [63] W. S. Boyle et al. Charge Coupled Semiconductor Devices. *Bell Syst. Tech. J.*, 49(4):587–593, 1970.
- [64] W. Boyle et al. Three dimensional charge coupled devices. In Intergovernmental Panel on Climate Change, editor, *Clim. Chang. 2013 - Phys. Sci. Basis*, pages 1–30. Cambridge University Press, Cambridge, 1974.
- [65] M. F. Tompsett et al. Charge coupled 8-bit shift register. *Appl. Phys. Lett.*, 17(3):111–115, 1970.
- [66] QImaging Corporation. QImaging. <https://www.qimaging.com>, Accessed: 2017-10-23.

- [67] D. A Glaser. Some Effects of Ionizing Radiation on the Formation of Bubbles in Liquids. *Phys. Rev.*, 87(4):665–665, 1952.
- [68] K. Bays et al. Supernova relic neutrino search at super-Kamiokande. *Phys. Rev. D*, 85(5):052007, 2012.
- [69] E. Aprile et al. The XENON100 dark matter experiment. *Astropart. Phys.*, 35(9):573–590, 2012.
- [70] J. Koide et al. Improvement of Spatial Resolution of Time-Resolved MA-PMT Camera for Imaging of TRU Elements. In *2016 IEEE Nucl. Sci. Symp. Med. Imaging Conf. Room-Temperature Semicond. Detect. Work.*, pages 4–7. IEEE, 2016.
- [71] G. Sciolla. The DMTPC project. *J. Phys. Conf. Ser.*, 179:012009, 2009.
- [72] M. Pomorski et al. Proton spectroscopy of  $^{48}\text{Ni}$ ,  $^{46}\text{Fe}$ , and  $^{44}\text{Cr}$ . *Phys. Rev. C - Nucl. Phys.*, 90(1):014311, 2014.
- [73] F. N Owen et al. CCD surface photometry of radio galaxies - I. FR class I and II sources. *Mon. Not. R. Astron. Soc.*, 238(2):357–378, 1989.
- [74] S. P. Driver et al. Multicolour faint galaxy number counts with the Hitchhiker parallel CCD camera. *Mon. Not. R. Astron. Soc.*, 266(1):155–178, 1994.
- [75] Ocean Optics Inc. Ocean Optics. <https://oceanoptics.com>, Accessed: 2018-02-22.
- [76] Joseph M Ajello et al. Study of electron impact excitation of argon in the extreme ultraviolet : emission cross section of resonance lines. *J. Phys. B*, 23:4355–4376, 1990.
- [77] E Seravalli et al. 2D dosimetry in a proton beam with a scintillating GEM detector. *Phys. Med. Biol.*, 54(12):3755–3771, 2009.
- [78] T. Waldenmaier et al. Spectral resolved measurement of the nitrogen fluorescence emissions in air induced by electrons. *Astropart. Phys.*, 29(3):205–222, 2008.
- [79] J.E. Sansonetti et al. Handbook of Basic Atomic Spectroscopic Data. <https://www.nist.gov/pml/handbook-basic-atomic-spectroscopic-data>, Accessed: 2017-12-04.
- [80] COMSOL Inc. COMSOL. <https://www.comsol.com>, Accessed: 2017-05-18.
- [81] F. M. Brunbauer et al. Radiation imaging with optically read out GEM-based detectors. *J. Instrum.*, 13(02):T02006, 2018.
- [82] E. Krestel. *Imaging systems for medical diagnostic*. Siemens Aktiengesellschaft, Berlin and Munich, 1990.
- [83] R. Glocker et al. Quantitative Röntgenspektralanalyse mit Kalterregung des Spektrums. *Ann. Phys.*, 390(8):1089–1102, 1928.
- [84] M. Mantler et al. X-ray fluorescence spectrometry in art and archaeology. *X-Ray Spectrom.*, 29(1):3–17, 2000.

- [85] J.F.C.A. Veloso et al. Gaseous detectors for energy dispersive X-ray fluorescence analysis. *Nucl. Instruments Methods Phys. Res. Sect. A*, 878(August):24–39, 2018.
- [86] J.F.C.A. Veloso et al. Energy resolved X-ray fluorescence imaging based on a micropattern gas detector. *Spectrochim. Acta Part B At. Spectrosc.*, 65(3):241–247, 2010.
- [87] A. Zielińska et al. X-ray fluorescence imaging system for fast mapping of pigment distributions in cultural heritage paintings. *J. Instrum.*, 8(10):P10011–P10011, 2013.
- [88] G. Charpak et al. The scintillating drift chamber: A new tool for high-accuracy, very-high-rate particle localization. *Nucl. Instruments Methods*, 126(3):381–389, 1975.
- [89] S. D. Pinto et al. First results of spherical GEMS. In *IEEE Nucl. Sci. Symp. Med. Imaging Conf.*, pages 1877–1880. IEEE, 2010.
- [90] F.M. Brunbauer et al. The planispherical chamber: A parallax-free gaseous X-ray detector for imaging applications. *Nucl. Instruments Methods Phys. Res. Sect. A*, 875:16–20, 2017.
- [91] D. R. Nygren. The Time Projection Chamber - A New 4pi Detector for Charged Particles. In *eConf*, volume C740805, pages 58–78, 1974.
- [92] J. Alme et al. The ALICE TPC, a large 3-dimensional tracking device with fast readout for ultra-high multiplicity events. *Nucl. Instruments Methods Phys. Res. Sect. A*, 622(1):316–367, 2010.
- [93] K.H. Ackermann et al. The forward time projection chamber in STAR. *Nucl. Instruments Methods Phys. Res. Sect. A*, 499(2-3):713–719, 2003.
- [94] W.B. Atwood et al. Performance of the ALEPH Time Projection Chamber. *Nucl. Instruments Methods Phys. Res. Sect. A*, 306(3):446–458, 1991.
- [95] C. Brand et al. The DELPHI time projection chamber. *Nucl. Instruments Methods Phys. Res. Sect. A*, 283(3):567–572, 1989.
- [96] D. Lorca et al. The NEXT experiment: A high pressure xenon gas TPC for neutrinoless double beta decay searches. *Nucl. Instruments Methods Phys. Res. Sect. A*, 718:387–390, 2013.
- [97] P. Fonte et al. Beam test of an imaging high-density projection chamber. *Nucl. Instruments Methods Phys. Res. Sect. A*, 283(3):658–664, 1989.
- [98] M. Ówiok et al. Optical time projection chamber for imaging of two-proton decay of Fe nucleus. *IEEE Trans. Nucl. Sci.*, 52(6):2895–2899, 2005.
- [99] M. Gai et al. An optical readout TPC (O-TPC) for studies in nuclear astrophysics with gamma-ray beams at HI $\gamma$ S 1. *J. Instrum.*, 5(12):P12004–P12004, 2010.
- [100] W. R. Zimmerman et al. Unambiguous Identification of the Second 2+ State in  $^{12}\text{C}$  and the Structure of the Hoyle State. *Phys. Rev. Lett.*, 110(15):152502, 2013.
- [101] D. Pinci et al. Cygnus: development of a high resolution TPC for rare events. In *Eur. Phys. Soc. Conf. High Energy Phys.*, number July 2017, pages 0–5, 2017.

- [102] F.M. Brunbauer et al. Live event reconstruction in an optically read out GEM-based TPC. *Nucl. Instruments Methods Phys. Res. Sect. A*, 886:24–29, 2018.
- [103] Jinliang Liu et al. Primary scintillation characteristics of Ar+CF<sub>4</sub> gas mixtures excited by proton and alpha particles. *Nucl. Instruments Methods Phys. Res. Sect. A*, 694:157–161, 2012.
- [104] S. Agostinelli et al. Geant4 - a simulation toolkit. *Nucl. Instruments Methods Phys. Res. Sect. A*, 506(3):250–303, 2003.
- [105] T. Fujiwara et al. High-photon-yield scintillation detector with Ar/CF<sub>4</sub> and glass gas electron multiplier. *Jpn. J. Appl. Phys.*, 55(10):106401, 2016.
- [106] F. M. Brunbauer et al. Combined Optical and Electronic Readout For Event Reconstruction in a GEM-based TPC. *IEEE Trans. Nucl. Sci.*, 65(3):1–1, 2018.
- [107] M.J. French et al. Design and results from the APV25, a deep sub-micron CMOS front-end chip for the CMS tracker. *Nucl. Instruments Methods Phys. Res. Sect. A*, 466(2):359–365, 2001.
- [108] S Martoiu et al. Development of the scalable readout system for micro-pattern gas detectors and other applications. *J. Instrum.*, 8(03):C03015–C03015, 2013.
- [109] H. Paganetti. *Proton Beam Therapy*. IOP Publishing, Bristol, 2016.
- [110] M. Dosanjh. From Particle Physics to Medical Applications. In *Phys. World Discov.* IOP Publishing, Bristol, 2017.
- [111] E. Seravalli et al. A scintillating gas detector for 2D dose measurements in clinical carbon beams. *Phys. Med. Biol.*, 53(17):4651–4665, 2008.
- [112] S. Giordanengo et al. The CNAO dose delivery system for modulated scanning ion beam radiotherapy. *Med. Phys.*, 42(1):263–275, 2014.
- [113] R. Zhang et al. Calculation of water equivalent thickness of materials of arbitrary density, elemental composition and thickness in proton beam irradiation. *Phys. Med. Biol.*, 54(6):1383–1395, 2009.
- [114] M.J. Berger et al. ESTAR, PSTAR, and ASTAR: Computer Programs for Calculating Stopping-Power and Range Tables for Electrons, Protons, and Helium Ions. <http://physics.nist.gov/Star>, Accessed: 2017-11-08.
- [115] D. Nichiporov et al. Characterization of a GEM-based scintillation detector with He-CF<sub>4</sub> gas mixture in clinical proton beams. *Phys. Med. Biol.*, 61(8):2972–2990, 2016.
- [116] Stanford Research Systems Inc. Stanford Research Systems. <http://www.thinksrs.com>, Accessed: 2017-11-24.
- [117] Pfeiffer Vacuum GmbH. Introduction to Vacuum Technology. [www.pfeiffer-vacuum.com](http://www.pfeiffer-vacuum.com), Accessed: 2017-11-22.





## Abbreviations

<b>MIP</b>	Minimum Ionising Particle
<b>MPGD</b>	MicroPattern Gaseous Detector
<b>PCB</b>	Printed Circuit Board
<b>MSGC</b>	Micro-Strip Gas Counter
<b>Micromegas</b>	Micro-Mesh Gaseous Structures
<b>GEM</b>	Gaseous Electron Multiplier
<b>TPC</b>	Time Projection Chamber
<b>LHC</b>	Large Hadron Collider
<b>NSW</b>	New Small Wheel
<b>ASIC</b>	Application-Specific Integrated Circuit
<b>UV</b>	UltraViolet
<b>VIS</b>	Visible
<b>CF<sub>4</sub></b>	Tetrafluoromethane (carbon tetrafluoride)
<b>NIR</b>	Near-InfraRed
<b>CCD</b>	Charge-Coupled Device
<b>CMOS</b>	Complementary Metal-Oxide-Semiconductor
<b>PMT</b>	PhotoMultiplier Tube
<b>EMCCD</b>	Electron Multiplying CCD
<b>UHV</b>	UltraHigh-Vacuum
<b>RGA</b>	Residual Gas Analyser
<b>LED</b>	Light Emitting Diode
<b>Mylar</b>	Biaxially-oriented polyethylene terephthalate
<b>FWHM</b>	Full-Width at Half-Maximum
<b>FR4</b>	Glass-reinforced epoxy laminate
<b>SHV</b>	Safe High Voltage
<b>PEEK</b>	PolyEther Ether Ketone
<b>NIM</b>	Nuclear Instrumentation Module
<b>TTL</b>	Transistor-Transistor Logic
<b>ITO</b>	Indium Tin Oxide
<b>HCl</b>	Hydrochloric acid
<b>WET</b>	Water Equivalent Thickness
<b>MU</b>	Monitoring Unit



# Curriculum Vitae

## Florian Maximilian Brunbauer

Date of birth: October 30, 1992  
Place of birth: Linz, Austria  
Nationality: Austrian  
florian.brunbauer@me.com

**Address**  
Peuerbachstraße 1  
4040 Linz  
Austria

## Education

### **Doctoral programme in Engineering Sciences with specialisation in Technical Physics**

Technische Universität Wien, Vienna, Austria - 2015-2018  
Doctoral thesis "Applications of gas scintillation properties in optically read out GEM-based detectors" conducted at CERN, Geneva, Switzerland

### **Master's programme Technical Physics**

Technische Universität Wien, Vienna, Austria - 2014-2015  
Master's thesis "Electronic Transport Phenomena in Al Nanowires and Al-Ge-Al Nanowire Heterostructures" conducted at Institute of Solid-State Electronics  
Graduated with distinction

### **Bachelor's programme Technical Physics**

Technische Universität Wien, Vienna, Austria - 2011-2014  
Bachelor's thesis "Residual Resistance Ratio Measurements of Niobium Films" conducted at Institute of Atomic and Subatomic Physics

Kollegium Aloisianum, Linz, Austria - High school diploma 2011  
Graduated with distinction

Lassen Union High School, Susanville, CA, USA - High school diploma 2010

## Experience

Tutor in experimental physics and programming, Technische Universität Wien, Vienna, Austria - 2014-2015

Project work on "Molecular Beam Monitor Testing and Operation", Technische Universität Wien, Institute of Applied Physics, Vienna, Austria - 2014

Project work on "Neutroninterferometry with a Skew-Symmetric Perfect-Crystal Interferometer", Technische Universität Wien, Institute of Atomic and Subatomic Physics, Vienna, Austria - 2013

Cooperation Associate, CERN, Geneva, Switzerland - 2014

Summer Student, CERN, Geneva, Switzerland - 2014

Internship in steel production, voestalpine AG, Linz, Austria - 2013

Internship in software development, voestalpine AG, Linz, Austria - 2008

Mobile application development - 2008-present